UNIVERSITAT DE BARCELONA

Activity Mediated Interactions in Soft Matter

Structure, Interactions, and Phase Transitions

Joan Codina Sala

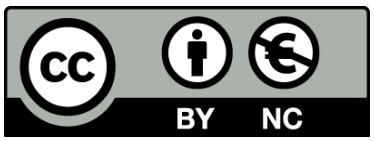

Activity Mediated Interactions in Soft Matter

Structure, Interactions, and Phase Transitions

Joan Codina Sala

Ph.D. Thesis
Ph.D. advisor: Ignacio Pagonabarraga Mora
Barcelona, June 2018
Programa de Doctorat en Física
Departament de Física de la Matèria Condensada
Facultat de Física
Universitat de Barcelona

Contents

Preface

This thesis presents my PhD research in Physics, performed under the supervision of Ignacio Pagonabarraga at the University of Barcelona between November 2013 and June 2018. It covers the majority of the research performed during the aforementioned time interval. However, the funding grant which I enjoyed during the PhD imposed the teaching in several undergraduate courses in Physics.

What is in this thesis

The first topic of this thesis concerns the emergent interactions in an active particle's suspension. This research originated from a joint discussion with Jure Dobikar and Ignacio Pagonabarraga, corresponds to Chapter 2 in this thesis, and is currently being prepared for puclication. The interest in the properties of an active bath of active brownian particles, reported in Chapter 1, comes from a detailed study of the active bath of Chapter 2, and the parallel interest in the topic of Demian Levis, and published in [Levis et al., 2017].

The second concerns the emergent interaction of spheres in a horizontally vibrated granular media. Given my previous experience in the extraction of effective emergent forces in out-of-equilibrium systems, from a discussion with Iker Zuriguel, we defined and studied a model of shaken grains in Chapter 3, and is currently being prepared for publication.

Finally, the third topic of my thesis concerns the emergent structures in bath of photocatalytic apolar particles in a suspension of passive colloids. This stems from previous experiments of Fernando Martínez-Pedrero in Pietro Tierno's laboratory at Universitat de Barcelona, and later continued by Helena Massana-Cid. This work is now submitted for publication.

1 General Introduction

In this introductory chapter we present the reader the content needed in order to understand and assess the research presented in this thesis. We define soft active matter and present several model systems widely used in the research community, with special emphasis in the ones used in the following chapters – colloidal and granular. We then present different models for active matter and outline the simulation methods we use along this thesis. After presenting the theoretical models of active matter, we review the sate of the art and place the contributions of the present thesis in this rapidly growing field.

In this work we study, mainly by means of computer simulations, the interaction between passive particles mediated by active and activated agents. On one hand, we study active agents such as individual self-propelled particles, and autophoretic colloids. On the other hand, we study activated particles, which is the case of millimetric grains. While active and activated particles move regardless of noise and thermal fluctuations we distinguish between active and activated agents according to the origin of the activity.

Activated particles move due to external forcing. Examples of activated particles are sand grains, that move when shaking or tilting the container; and magnetic colloids that solidly rotate and drift following external magnetic fields. In general, a system of activated particles moves as a response of an external forcing. Active particles, on the contrary, have an inherent capacity to convert energy from internal sources or the surrounding medium into directed motion or stress generation in the medium. Examples of active particles include self-catalytic colloids, which convert chemical products to generate chemical imbalances that stir the neighbouring fluid;

and bumper-cars that convert electric energy into self-propulsion. Active and activated agents exhibit a persistent motion which is ultimately responsible for the out-of-equilibrium nature of the systems.

Despite the apparent differences between all sorts of active and activated systems we can model their key features and behaviours with simple models that are subject to further modifications to differentiate into the specifics of each system under consideration.

1.1 Soft Matter

In this thesis we present active systems in the context of soft matter. Soft matter is the field of condensed matter physics that studies systems whose interactions are in the range of the thermal energy $E = k_B T$, the structures involved span from several nanometres to micrometres, and slow temporal dynamics, from seconds to hours. The contrast between solid state physics and soft matter is clear when comparing the typical energies and length involved. In solid state, the length between interacting objects are in the Ångstrom scale $L \approx 10^{-10}\ m$, and ionic and covalent bond energies are $E \approx 100\ k_B T$, this combination leads to a typical stiffness of the order of $k \approx Nm^{-1}$. In soft matter, instead, typical stiffness values are in the order of $k \approx k_B T/L^2 \approx 10^{-9}\ Nm^{-1}$. In soft matter systems, thermal fluctuations play a vital role and lead to self assembly, and the formation of malleable and deformable materials. The length scale involved in soft matter does not permit a detailed molecular description, for instance a volume of $1\ \mu m^3$ contains approximately $\sim 10^8$ water molecules. Models need to coarse grain the molecular details and incorporate the essentials: the diffusion introduced by the molecular collisions, and the interactions between constituents. Among the most studied soft matter systems we find polymer solutions an polymer melts, dispersions of colloids of different sizes, shapes and interactions with the solvent, liquid crystals, and the structures formed by amphiphilic molecules: vesicles, membranes, micelles, etc.

1.1.1 Colloids

Colloids are small solid particles, or fluid droplets, dispersed in other fluids. The diameters of colloids typically range from several nanometres to micrometres, much larger than the atomic since, and hence constituted by millions or billions of molecules. Large ensembles of colloids follow the assumptions posed by statistical mechanics. Therefore, equal interaction potentials in molecular systems, and colloidal systems give rise to equal behaviours. This equivalence is largely exploited in colloidal science to tune the colloidal interactions to construct analog models for molecular interactions, and unlike molecular ensembles visible through microscopy.

Colloids immersed in a fluid are subject to hydrodynamics. At the colloidal level

Stokes hydrodynamic equations are a suitable approximation since the Reynolds number is $Re = LU/\nu << 1$. In the low Reynolds number viscosity prevails over inertial effects, and for a sphere of radius R moving at velocity U the fluid generates a drag force opposing to the movement of magnitude $F = 6\pi\eta R\gamma U = \gamma U$, with η the viscosity of the fluid. A spherical particle in a viscous fluid will only travel at constant velocity U if, and only if, it is pushed by a constant force $F = \gamma U$. The reverse is true, the application of a force of magnitude F on a colloidal particle results in a velocity $U = \gamma^{-1}F$, or introducing the mobility factor, $U = \mu F$. In the low Reynolds fluids particles follow Aristotelian physics.

In the colloidal scale the fluid is treated as a continuum with the corresponding hydrodynamic equations. The details of the molecules of the fluid, though, are not lost. Diffusion is the signature of the molecular jiggling and random collisions with the colloids. For an equilibrium fluid, the Stokes-Einstein equation applies and relates the magnitude of thermal fluctuations of the particle to the dissipation $D = k_B T\gamma^{-1} = \mu k_B T$, where $k_B T$ is the thermal energy. The colloidal models that appear in this thesis incorporate thermal fluctuations in the form of translational diffusions on the colloids, and additionally the equivalent diffusion in its fluctuations in the rotations.

Colloid interactions

As previously introduced, colloids are constituted by chunks of matter, millions of atoms. The electric nature of the atoms introduce long range induced dipolar interactions between pairs. The addition of interactions pairs of atoms of different colloids gives rise to an overall interaction between the colloids, the dispersion forces. Dispersion forces are attractive long range forces [Hunter, 2001] that solely depend on material properties, the shapes of the bodies, and thermal fluctuations. The details of the material properties are condensed into the Hamaker constant, $A \approx 10K_B T$. For a pair of spheres, dispersion forces decay as $\sim d^{-6}$ while the decay is $\sim d^{-1}$ for close spheres.

In colloidal dispersions, electrically charged particles are not rare. Charges introduce structure to the fluid ions and, thus interactions between pairs. Altogether, electric interactions and dispersion forces, constitute the DLVO potential of interaction between colloids. But the colloidal world is much richer and colloids may be fabricated out of ferromagnetic, paramagnetic and superparamagnetc materials. Magnetic colloids interact like micrometric magnets and, additionally, respond to external magnetic fields.

Furthermore, colloids may be highly modified. Nanotechnology permits the covering and coating of colloid surfaces with molecules, docking sites to attach to other molecules, or even other colloids. In Janus colloids, for instance, the surface of the particle has spatial dependent properties: half-silica, half-platinum colloids make excellent candidates for microswimmers and will be presented in 1.2.5.

1.1.2 Polymers and Liquid Crystals

Polymers are elongated and/or branched molecules. Dispersed in a solvent, and as a function of their interaction, polymers structure and entangle themselves. Polymers in "good" solvents swell at high temperatures and form compact structures. At low temperatures polymers in "good" solvents extend. The opposite behaviour is observed for "poor" solvents.

Depending on the constituents of the polymer the, presence of large region with apolar sites, or just the contrary regions rich in charges, introduce additional interactions with the dispersing fluid. A polymer immersed in water will favour interactions between water and polar sites (hydrophilic sites) wile the apolar sites will be hydrophobia, they will be energetically penalized. For large enough polymers, such as proteins, hydrophilic regions are on average located at the external part of the protein while the hydrophobic parts are hidden far from the water. Shorter molecules with a combination of hydrophobic, and hydrophilic sites, give rise to mesoscopic arrangements of the polymers, the self-assembly of polymers, into micelles, membranes, and double membranes, see Figure 1.1. This structures play a vital role in biology, cells are enclosed by a bilayer membrane.

Shape asymmetries may lead to large structures with long range position corre-

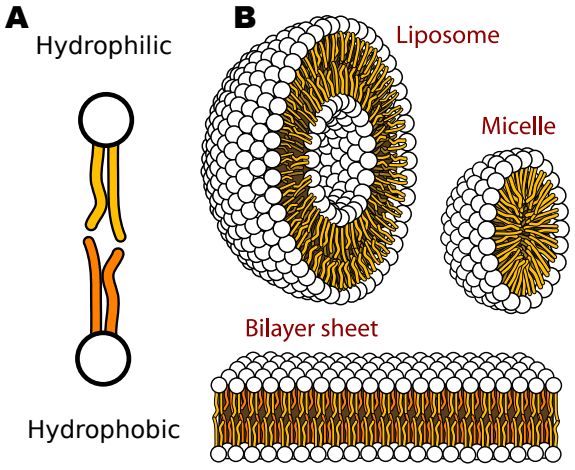

Figure 1.1 | Self assembly of amphiphilic polymers. **A** Amphiphilic polymers with hydrophilic white beads, and hydrophobic tails. **B** Different self assembly structures where hydrophobic tails hide from the water in the exterior. A liposome is a spherical shell constituted by two polymer units, it encloses a water region which can be further used for nano technological applications. A micelle is a sphere of polymers that exposes all hydrophylic beads to the exterior and hides the hydophobic tails. Finally a bilayer, a membrane. Image from Mariana Ruiz Villarrea.

lations in a direction but short range correlations in other ones, and even give rise to several structural phase transitions. Liquid crystals present such anisotropic

behaviour with the coexistence of crystal, and fluid properties in the different axes of symmetry, see Figure **??**

1.1.3 Depletion forces

Excluded volume interactions are relevant in colloidal mixtures, and specially between colloids and coiled polymers. We consider a binary mixture of large spheres suspended in dilute suspensions of non absorbing polymers, micelles, or smaller hard spheres in equilibrium. Coiled non-absorbing polymers, of typical size defined by the radius of gyration $2R_g$, are free to interpenetrate but its centre of mass cannot approach to a distance closer to R_g of the surface of each colloid due to repulsive interactions, this leaves an excluded volume corona of thickness R_g surrounding each colloid. In Figure 1.2 we present the excluded volume coronas for polymers for different colloidal configurations. First, when the colloid-colloid distance $d > \sigma + 2R_g$ the total excluded volume of the system corresponds to addition of each corona. Then, when the colloid-colloid distance $\sigma < d < \sigma + 2R_g$ excluded volume coronas overlap and the overall excluded volume for the polymers is reduced, and the total entropy of the colloids increase. Configurations with touching colloids are entropically favoured, and thus more probable. Second, colloidal particles at close distances from walls obtain a reduction of the overall excluded volume for the polymers following the same principles, see Figure 1.2. In thermal equilibrium this gives rise to the so called depletion forces. A detailed analysis of this interactions is found in [Mao et al., 1995].

A mechanical interpretation of the problem is also feasible in terms of the van'Hoff's polymer osmotic pressure $\Pi = \rho k_B T$, where ρ is the density of the polymer. For an isolated colloid the density of surrounding polymers is isotropic, and so is the pressure on the surface of the colloid. However, when the excluded volume coronas overlap, polymer concentration in the inner region drops, and thus there is an osmotic pressure imbalance that keeps colloids in contact.

In dense binary mixtures of colloids with size ratio $\sigma_a/\sigma_b \approx 10$ experiments in [Dinsmore et al., 1997] showed the emergence of depletion force in thermal equilibrium. Microscopy images shown in Figure 1.3 correspond to the the focal plane in the dispersion just close to the confining wall of the system. At zero concentration of small particles we large colloids diffuse to the wall and diffuse back to the bulk of the fluid. Then a small fraction of small particles was added to the large colloidal dispersion and large particles that approach to the wall diffuse there, due to depletion interactions with the wall for longer times, until they diffuse back to the fluid, there is an observational increase of particles close to the walls. Finally, at higher concentrations of smaller particles large particles that approach the wall reside there for even longer times and diffuse in the plane close to the wall and colloid-colloid depletion interactions contribute to the formation of a dense aggregate of large particles.

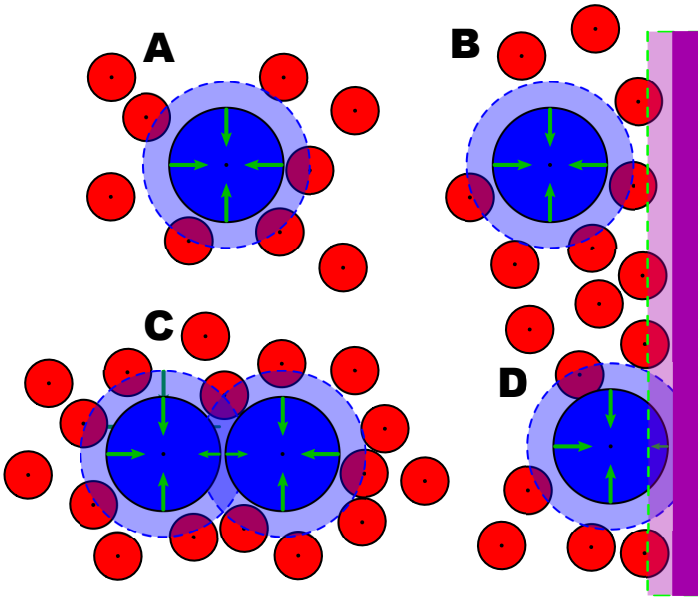

Figure 1.2 | Schematic representation of a mixture of large and small disks, and a wall. In **A**, and **B** the excluded volume coronas of the colloids do not overlap arrows represent an isotropic osmotic pressure. In **C** excluded volume coronas of the colloids overlap, the osmotic pressure of the polymers is no longer isotropic, and depletion appears. In **D** The excluded volume corona of the colloid overlaps with the excluded region of the wall. Osmotic pressure on the colloid is not isotropic and generates depletion pushes the colloid towards the wall.

To summarise, depletion forces are short ranged, act at separation distances comparable to the small particles, and are the order of the thermal energy.

1.1.4 Critical Casimir forces

Casimir forces were first predicted in 1948 [Casimir, 1948] in the context of quantum electrodynamics theory. For a pair of parallel conducting plates, at close distances, the selection of fluctuating modes of the electromagnetic fields generates an imbalance of energy density in the internal region relative to the external and a force emerges. More recently, a model for thermal charge particles on parallel plates has reported the emergence of Casimir-like thermal interactions [Lu et al., 2015].

In 1978, Fisher and de Gennes predicted [Fisher and Gennes, 1978], and later refined [de Gennes, 1981], the thermal analogous of the QED Casimir forces in soft matter close to a critical point, critical Casimir forces. Like their QED counterpart, critical Casimir forces, rely on the confinement of fluctuations, and the difference in mode selection in confinement compared to unbounded scenarios. Second order

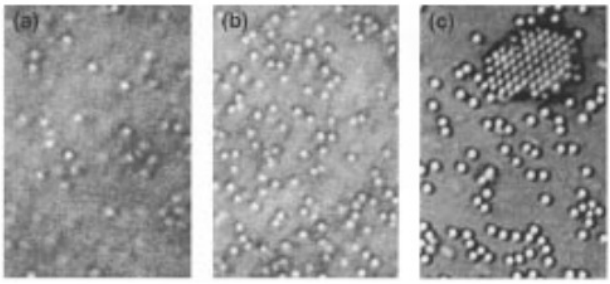

Figure 1.3 | Optical micrographs of colloidal beads of size $\sigma_a = 0.8\ \mu m$ and concentration $\phi = 0.02$ at a glass wall. **A** with no small spheres, colloids diffuse stay in the focal plane for few seconds, and away from the focal plane. **B** small particles $\sigma_b = 0.07\ \mu m$, at concentration $\phi_b = 0.08$, are introduced and the concentration of large colloids close to the wall increases, colloids diffuse close to the wall for several minutes prior escaping to the bulk. **C** increasing the density of small particles to $\phi_b = 0.16$ interactions between type a particles increase and crystalline structures form. Figure from [Dinsmore et al., 1997]

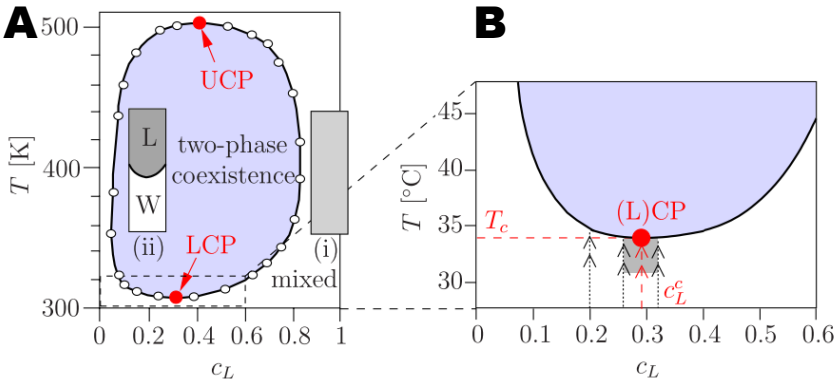

Figure 1.4 | Water and Lutidine (W+L) phase diagram extracted from [Gambassi et al., 2009]. In the colored region in **A** W+L fluid phase separates, and two critical points can be observed. **B** close to the low temperature critical point LCP, $T_c = 34.1^\circ\ C$, lutidine is miscible in water. For $T > T_c$ an initial concentration C_1 separates into a rich water phase in, and a rich lutidine phase.

phase transitions in liquids near the critical temperature, T_c, were predicted to be good candidates in which experiments could observe, and measure critical Casimir forces. For liquid crystals, [Ziherl et al., 1999] predicted critical Casimir forces between parallel plates arising from the isotropic wetting transition, and [Uchida, 2001] for the isotropic-lamelar transition. However, fluctuation forces in liquid crystals are difficult to measure and differentiate from the background dispersion forces [Ziherl and Muševič, 2001].

Recently, [Hertlein et al., 2008] measured critical Casimir forces for colloids close to walls, and between pairs of colloids [Paladugu et al., 2016] in water-lutidine binary mixtures. A binary fluid system is constituted by two different species at a temperature T. Such a system may undergo a second order phase separation between mixed, and demixed states. Temperature determines the miscibility of one fluid into the other. In Figure 1.4 we present the phase diagram for a binary fluid, water and lutidine from experiments in [Vnuk, 1983, Beysens and Estève, 1985], as a function of fraction of lutidine c_L, and temperature T. The critical point $(C_c,\ T_c)$ determines whether lutidine is miscible in water or the system phase separates. Below the critical temperature lutidine is miscible in water and the system remains mixed, above it the system demixes. And, near the critical point, the characteristic length of order parameter fluctuations [Kadanoff et al., 1967].

Water-lutidine phase diagram presents two critical points, one at $T \approx 300K$, and a second at $T \approx 500K$. The first critical point is just a few degrees above room, and thus an ideal candidate for experiments in the laboratory.

1.2 Active Soft Matter

We move from the introduction to soft matter and emergent interactions in thermal equilibrium to active matter to a sustained out-of-equilibrium. In this regime energy needs to flow from the outside of the system to the agents of the system or be converted from an internal source, and finally be dissipated at the active particles's level. Now we consider actuated systems which do not have the intrinsic mechanism to convert energy from a source but are collectively forced from the exterior of the system. We briefly review colloidal magnetic systems, and granular vibrated matter. Then, we introduce active systems that intrinsically, and locally, convert energy to disturb the environment. We briefly review bacteria, active colloids, and active liquid crystals.

1.2.1 Magnetic Colloids

Ferromagnetic, and super paramagneteic particles, in the microscale, constitute magnetic colloids. In suspension magnetic colloids diffuse due to thermal fluctuations and, additionally, magnetically interact through dipole-dipole interactions. Magnetic interactions are intrinsically anisotropic, and decay algebraically with the

distance d^{-3}. Anisotropy in the interaction favours parallel alignments between magnetic dipoles, and for spherical particles it favours the formation of chains. Even though, the equilibrium, and metastable structures of small aggregates is still a matter of interest in the statistical mechanics community [Hernández-Rojas et al., 2016].

Magnetic colloids respond under external magnetic fields and, by introducing a periodic variation of the fields, a large variety of scenarios appear. At low Reynolds regime, the collection of movements that result in swimming must take into account the celebrated scallope theorem [Purcell, 2014,Lauga, 2011]. Experiment presented

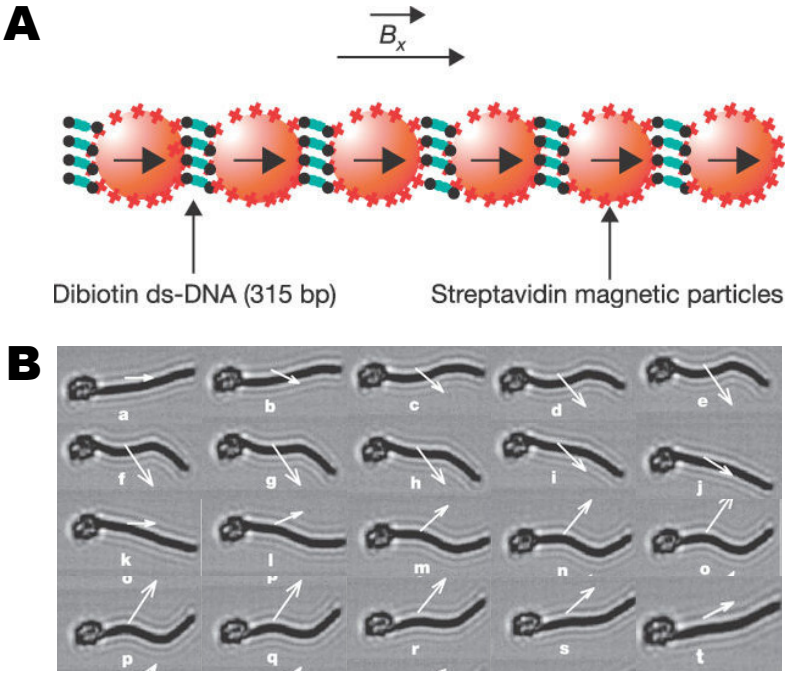

Figure 1.5 | Magnetic Swimmer. **A** DNA joined magnetic particles constitute the filament which is attached to a large object, in this case red blood cell. **B** a time dependent magnetic field generates a beat pattern on the filament which ultimately propels the swimmer. Extracted from [Dreyfus et al., 2005].

in [Dreyfus et al., 2005] assembled, by means of DNA connections, magnetic colloids in a long chain, see Figure 1.5, and finally the chain was then attached to an inert colloid. By a prescribed variation of an external magnetic field the response of each particle in the chain depends on the distance from the passive bead. After a whole cycle the particle propels a certain distance, and thus is able to swim by periodically forcing the system.

The wall effect has also been exploited to construct magnetic swimmers. The

confinement breaks a spatial symmetry of the system and more simple objects may propel such as paramagnetic joined doublets of different size under a precessing magnetic field [Tierno et al., 2008], or even simpler systems such as magnetic worms where precessing magnetic fields induce an angular rotation to each particle [Martinez-Pedrero et al., 2015].

1.2.2 Vibrated grains

An astonishing feature appears when shaking granular materials [Aranson and Tsimring, 2006, Jaeger et al., 1996]. Under external vibration the resulting granular material lies in a hybrid state between a solid and a liquid, the fluidization regime. When the local density exceeds a critical value [Reynolds, 1885] the, the system is resistant to shear deformations like a solid, while below this density the system flows. In a vertically agitated container vertical movements accelerate the particles against gravity, which accelerates them down. The energy output at the bottom and the cooling in the walls introduce typical hydrodynamic instabilities, the formation of rolls [Gallas et al., 1992], shown in Figure 1.6.

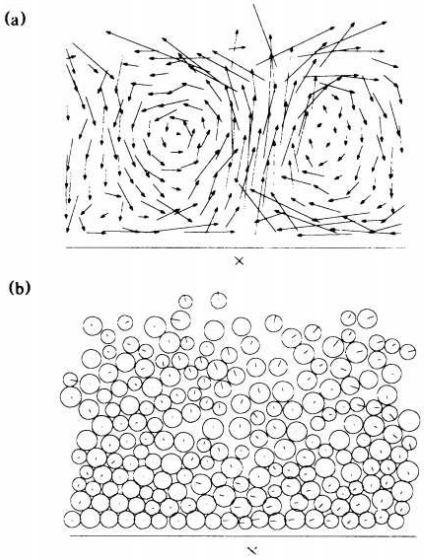

Figure 1.6 | Fluidization of a granular media. (a) trajectories of particles depicting the characteristic convection rolls in vertically fluidized granular systems. In (b) the state of the system, images from [Gallas et al., 1992]

Granular vibrated systems have also explored quasi two dimensional systems when considering granular monolayers. A vertically shaken granular monolayer will not set convective rolls, since there is no bulk of granular, but achieve self-propulsion for grains designed with certain asymmetries [Deseigne et al., 2010]. Granular monolayers have also been horizontal, and circularly shaken and conduced to equally astonishing results [Daniels et al., 2009, Mullin, 2000]. Granular, regardless of the material details, experience mechanical friction with either the

container surfaces, and other grains. Thus granular models need to introduce energy dissipation in collisions. As a final remark, note that typical accelerations in granular media compete with gravity. In experiments, gravity is difficult to switch off and some tests need to be performed in situations of microgravity to completely exclude gravitational effects present in the Earth surface.

1.2.3 Activity in living systems

In the biological world we find active matter at all its scales. In the interior of cells there are complex molecules, organelles, and cytoplasm, a crowded media. The diffusion though the cytoplasm is a slow and non-directed mechanism to transport vital chemicals or organelles from the place where they are produced or stored to the where they are needed. Interestingly, evolution has achieved the equivalent of motorways. Immersed in the cellular interior one finds microtubules, a hard tubular structure made out of tubuline, a protein. Kinesins, molecular motors, run on these structures. Kinesins are anchored to the surface of the microtubule by a pair of feet. At each foot the reaction of ATP molecules, the energy coin in the cell, attaches or detaches the foot from the tubuline molecules. When the foot detaches it diffuses in a preferential direction, for the microtubule has an electric polarization. The attachment and detachment dynamics of the feet allows kinesins to walk on microtubules, and more importantly apply a force on their cargo. Groups of kinesins, whose size is approximately $10m$, are able to attach to cargo lipid vesicles, carrying all sorts of molecules, and transport them along large distances such as the axon of neurons, millimetric lengths.

1.2.4 Bacteria and cells

From the nanometric world of the molecules we jump into the micrometric world. *Escherichia coli*, and many more bacteria and algae, are propelled by flagella [Berg, 2008]. Molecular motors at the bacterial wall of *E. coli* at the roots of the flagella induce a circular motion to it. A counter-clockwise rotation to the bunch of helical flagella results into the formation of a large rotating helix that propels *E. coli*. However, the clockwise rotation of the flagella results into a chaotic arrangement of the flagella and induces a random rotation to the body of *E. coli*, see Figure 1.7. By switching long runs and random reorientations [Son et al., 2013], *E. coli*, effectively diffuses with a diffusion constant one hundredfold its thermal diffusion constant. Finally, by fine tunning the run time, *E. coli*, manages to direct its motion towards chemical gradients to either follow increasing concentration of food or to scape to decreasing concentrations of toxic chemicals.

Here we introduce a scenario in which the origin of the activity is in the nanometric scale, the conversion of chemical energy into rotatory motion of the motor attached to the flagella. The theoretical or computational study of propulsion in

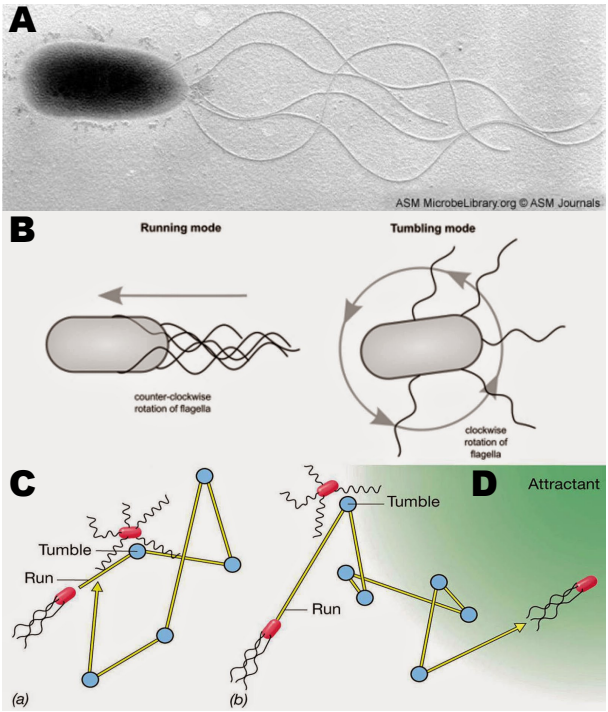

Figure 1.7 | *E. coli* and Run-and-Tumble. A An electron microscope image of an *E. coli* with a differentiated main body, and a bunch of flagella. **B** The different configuration for the flagella for CCW rotations (left) that translate into directed motion, and CW rotations (right) that translate into a random reorientation. **C** The run-and-tumble mechanism. Combining a series of runs and tumbles *E. coli* performs a large scale diffusive motion. **D** Adapting the runtimes *E. coli* changes the effective diffusion and is able to follow chemical gradients.

microorganisms and its collective effects generally disregards the details of the origin of the propulsion. The difference in size, and the large amount of constituents involved leads to the coupling of millions of constituents with the final point of achieving propulsion. Thus, to study the behavior of self-propelled microorganisms activity is entered though surface fluid velocities, propulsion velocities of the agents, and stress generation in hydrodynamic models.

Propulsion is not constrained to the microscopic world. Large multicellular organisms, animals, are able to either swim, fly or run. Once again the propulsion comes from an inverse cascade of active processes from the cellular level, to tissues and finally to the whole of the organism.

The idea of a unit propelling at a given velocity, and subject to random reorientations, or orientation with the neighbours is a constant over all length scales. But activity is not an exclusive feature of living organisms. Artificial active systems have been trendy in the laboratories for the last decades and here we present: colloidal particles, micro robots, and polymers that have been engineered to achieve self-propulsion.

1.2.5 Active Colloids

We have previously presented colloidal particles in Section 1.1.1. Nowadays, colloids can be engineered in detail to the surface level. For instance, Janus particles, spherical or rod-like micro particles are half coated with different materials. It is interesting to consider Janus particles in a chemical solution with chemical reactions occurring only, or with different intensity, in one of the halves. This happens in platinum coated particles in a rich H_2O_2 (hydrogen peroxide) environment. Platinum catalyzes the dissociation of H_2O_2 and thus a chemical imbalance appears. The gradient of chemical products is sustained by the constant chemical activity on the catalysing site. Gradients near surfaces are known to couple to the fluid and generate flows proportional to the gradient of chemicals. By this mechanisms, and integrating the overall velocity on the Janus particle we obtain neat propulsion of the particle, for a detailed list of artificial self-propulsion mechanisms see [Bechinger et al., 2016].

Janus particles that consume H_2O_2 constantly produce oxygen gas which eventually forms macroscopic bubbles that destroy the colloidal arrangements or the colloidal structures achieved in the experiment. An alternative to hydrogen peroxide is the aforementioned water-lutidine mixture. For temperatures below T_c a Janus with half a gold coating diffuses thermally. Once the sample is illuminated, the golden face of the colloid absorbs light and locally heats the water-lutidine fluid to $T > T_c$ and leads to water lutidine demixing only on the gold coated side. Due to the appearance of chemical gradients the particle propels and the water lutidine separated that remains behind mixes once again when it cools to the bath temperature $T < T_c$. This system does not present gas generation, and what is even more, the used fuel regenerates. Furthermore, the velocity of the Janus colloids depends on the light intensity, see Figure 1.8.

Self-propelled colloids are subject to thermal fluctuations. In the low Reynolds regime, stokes equations, and fluctuation dissipation theorem imposes a diffusion constant D_t for spatial random movements, and a rotational diffusion constant D_r, for random solid rotations. The diffusion constants for a spherical colloid are:

$$D_t = \frac{k_B T}{6\pi\eta R}, \qquad D_r = \frac{k_B T}{6\pi\eta R^3} \tag{1.1}$$

where $k_B T$ is the thermal energy, η the viscosity of the medium, and R the radius

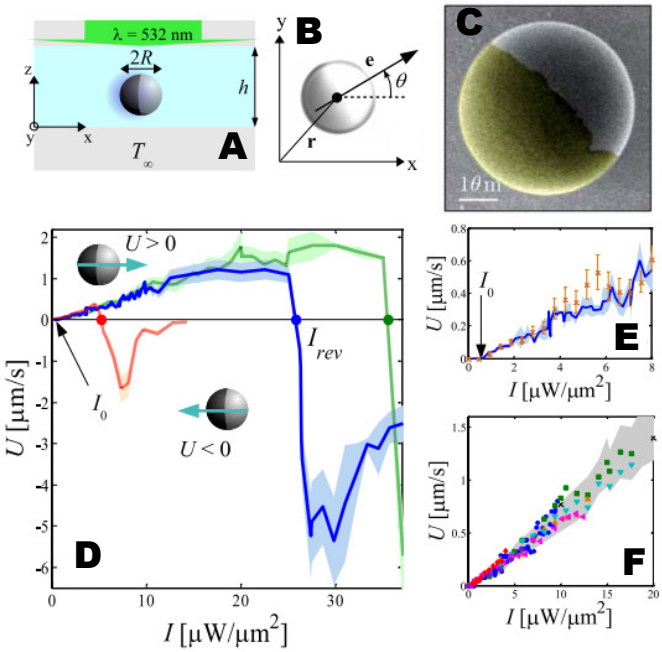

Figure 1.8 | Janus particles. **A** The particle in the bath, and **B** the diagram of an active Janus, from [Gomez-Solano et al., 2017]. A microscopy image of a gold coated Janus colloid from [Volpe et al., 2011]. **D-F** Velocity of Janus self-propelled colloids in a critical water-lutidine binary mixture tunned by light intensity.

of the colloid. The Langevin equations for the equations of Brownian motion are $\dot{\boldsymbol{r}} = (2D_t)^{1/2}\boldsymbol{\xi}$. The solution to the equations predicts an averaged mean squared displacement, in two dimensions, $\Delta r^2(\Delta t) = 4D_t\Delta t$ for a time interval Δt.

Active particles, however, propel in a defined axis of symmetry of the colloid indicated by the unit vector $\hat{\boldsymbol{n}}$. Equation 1.1 already introduces fluctuations of the orientation of the sphere. For passive colloids, though, this has no effect in the displacement of the particle, but now propulsion couples fluctuations on the orientation of the colloid $\hat{\boldsymbol{n}}$ to the swimming direction, and hence to the trajectory of the colloid.

For a colloid swimming at velocity v_a the simplest equation of motion for the center of mass includes the velocity in the direction of the orientation, and the diffusion $\dot{\boldsymbol{r}} = v_0\hat{\boldsymbol{n}} + (2D_t)^{1/2}\xi$. And in two dimensions the orientation is equally described by the angle θ. The evolution of the angle is then described by the diffusion equation $\dot{\theta} = (2D_r)^{1/2}\nu_i$. The details to incorporate self propulsion in a Brownian model are given in Section 1.3.2.

The solution for the mean squared displacement when propulsion is considered

is richer than the correspondent to brownian motion

$$\Delta r^2 = 4D_t\Delta t + \frac{v_a^2}{2D_r^2}\Big[2\Delta t D_r + \exp\big(-2\Delta t D_r\big) - 1\Big] \tag{1.2}$$

The temporal dependence of Δr^2 on the elapsed time has two limiting regimes. First, at times shorter than the typical diffusion time $\Delta t << \Delta_r^{-1}$ the behavior of the active particle is ballistic[1] $\Delta r^2 = v_0^2\Delta t^2$. For larger times, the diffusion in the orientation reorients the particle, and with a characteristic time D_r^{-1} it displaces a distance of the order $v_0 D_r^{-1}$. The long time limit of (1.2) gives $\Delta r^2 = 4D_t\Delta t + v_0^2 D_r^{-1}\Delta t$. The linear behavior on Δt defines an effective diffusive motion with $D_{eff} = D_t + v_0^2/(4D_r)$. In experiments [Howse et al., 2007], analysed the trajectories of catalytic Janus particles for different H_2O_2 concentrations and obtained both the ballistic-diffusive crossover and the increase of the particle velocity increasing the concentration of chemicals, see Figure 1.9.

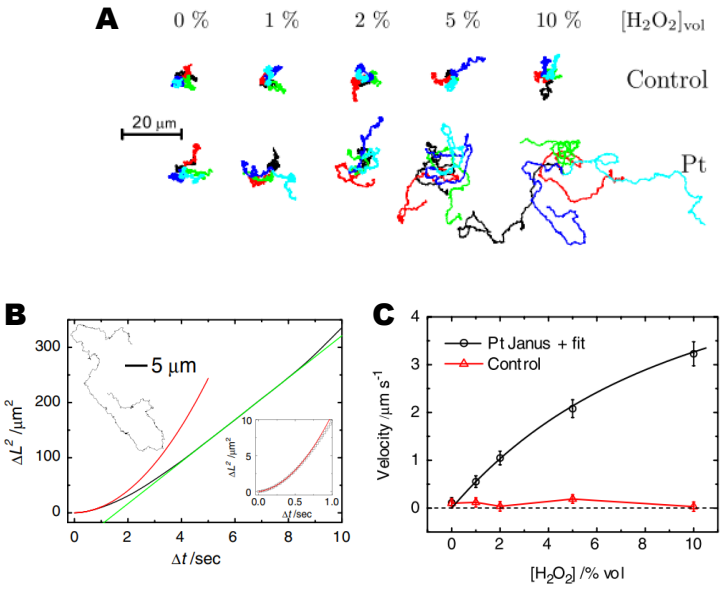

Figure 1.9 | Diffusion of self-propellent active colloids. **A** Trajectories of the active particles for different H_2O_2 concentrations. **B** Mean Squared Displacement for active particles. In green a linear regime for diffusion, in red a parabolic dependence on Δt to reflect the ballistic behavior below D_r^{-1}. **C** Velocity of self-propulsion for increasing concentrations of the reactant chemicals. Images from [Howse et al., 2007]

Activity, though, is not only the ability of the Janus particle to translate the

[1] We deliberately do not include in this limit the discussion of the relation between the diffusion time R^2/D_t, and the rotational dime D_r^{-1} which leads to a crossover between the ballistic behavior presented and the simple thermal diffusion, which in turn is expected at times $\Delta t > R^2/D_t$ [Huang et al., 2011]

chemical reaction into its own propulsion but capacity to sustain the chemical imbalance away from its surface. A spherically symmetric catalytic sphere will not be able to achieve a velocity in a persistent direction, unless the spacial symmetry is broken – still the system is far from equilibrium. Several scenarios have been proposed to induce propulsion to symmetric active particles. First, [Michelin and Lauga, 2014] predicted that a finite Pe distorts the chemical profile and thus gain production. Second, the coupling of two apolar active particles gives rise to an approaching pair velocity. What is even more, for apolar active particles [Colberg and Kapral, 2017] observe the formation of pairs that self-propel and act as a polar particle.

1.3 Models for dry Active Matter

In the last section we have presented several scenarios where, by different means, microscopic particles gain propulsion. We have seen the essential role of hydrodynamics in the development of the motion at the local scale. At the larger scale, we are interested in the effects that propulsion introduces to soft matter, and to capture the basic physics that emerges from the persistence of motion, we consider physical models that do not include hydrodynamic interactions between particles[2], and generally omit the surrounding fluid. In this section we present the two most fundamental and simple models commonly used to study active particles that incorporate fluctuations, and propulsion. The first, the Vicsek model, incorporates propulsion alignment. The second, the Active Brownian Particle (ABP) model, additionally incorporates excluded volume interactions. In this thesis we have worked with a variation of ABP particles that incorporate a Vicsek-like alignment interaction.

1.3.1 The Vicsek Model

A first fundamental aspect of self-propulsion is the behaviour of the propelling direction. In 1995 Vicsek, *et al.* [Vicsek et al., 1995] proposed a model where point particles had an associated propulsion direction, constant velocity, and orientations where subject to random noise and alignment. Years later this model, the Vicsek model, has lead to the broad field of collective motion [Vicsek and Zafeiris, 2012]. And variations of the original model have been proposed to study from cell colonies [Szabó et al., 2006] to bird flocks [Cavagna et al., 2010].

In the Vicsek model positions $\boldsymbol{r}$ and orientations θ of particles are updated from a their values at time t to their values at times $t + 1$ following simple kinematic

[2]However, a complete model of the system needs hydrodynamics and research in wet active systems has also captured large attention [Marchetti et al., 2013].

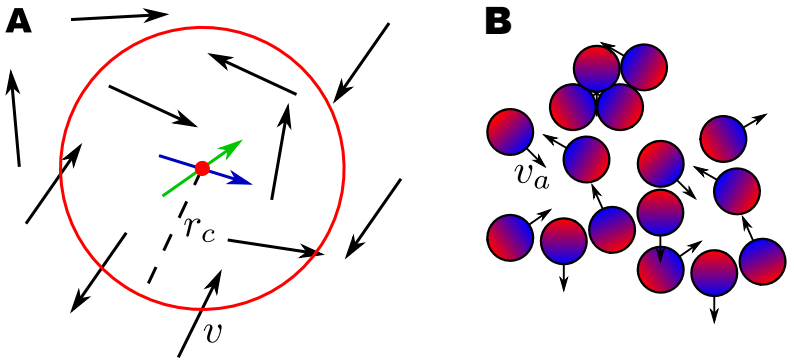

Figure 1.10 | Dry Active Particles. **A** The Vicsek model. **B** The Active Brownian Particle model

rules.

$$\begin{aligned}\theta_i(t+1) &= \arg\left(\sum_n \exp(i\theta_n(t))\right) + \eta \\ \boldsymbol{r}(t+1) &= \boldsymbol{r}(t) + v(\cos\theta_i, \sin\theta_i)\end{aligned} \tag{1.3}$$

where the orientation updates to the average orientation of the neighbours within a distance r_c, η is a random uniform number in the range $[-\eta/2, \eta/2]$ that stands for the strength of orientation fluctuations, and v_a is the propulsion magnitude.

The competition between alignment with neighbours and noise drives the whole system either to a state with zero global polarization or a polarized state. The Vicsek model is simple and incorporates three key ingredients in systems of active particles: propulsion, alignment, and random fluctuations.

1.3.2 Active Brownian Particles

A second fundamental aspect of self-propelled particles is excluded volume interactions. Active Brownian Particles (ABPs) were born from a system equilibrium brownian repulsive spheres with translational and rotational diffusions at a finite temperature, T. The system is then modified by the propulsion at constant velocity v_a in the direction defined by the director $\hat{\boldsymbol{n}}$.

$$\begin{aligned}\frac{\boldsymbol{r}_i(t)}{dt} &= v_a\hat{\boldsymbol{n}}_i + \mu\boldsymbol{F}_i^c + \sqrt{2\mu k_B T}\boldsymbol{\xi}_i \\ \frac{d\hat{\boldsymbol{n}}_i}{dt} &= \sqrt{2\mu_r k_B T}\hat{\boldsymbol{n}}_i \times \boldsymbol{\nu}_i\end{aligned} \tag{1.4}$$

Interactions are introduced by the conservative force $\boldsymbol{F}^c$ that guarantees excluded volume. Fluctuation dissipation theorem connects thermal mobilities μ_t, and

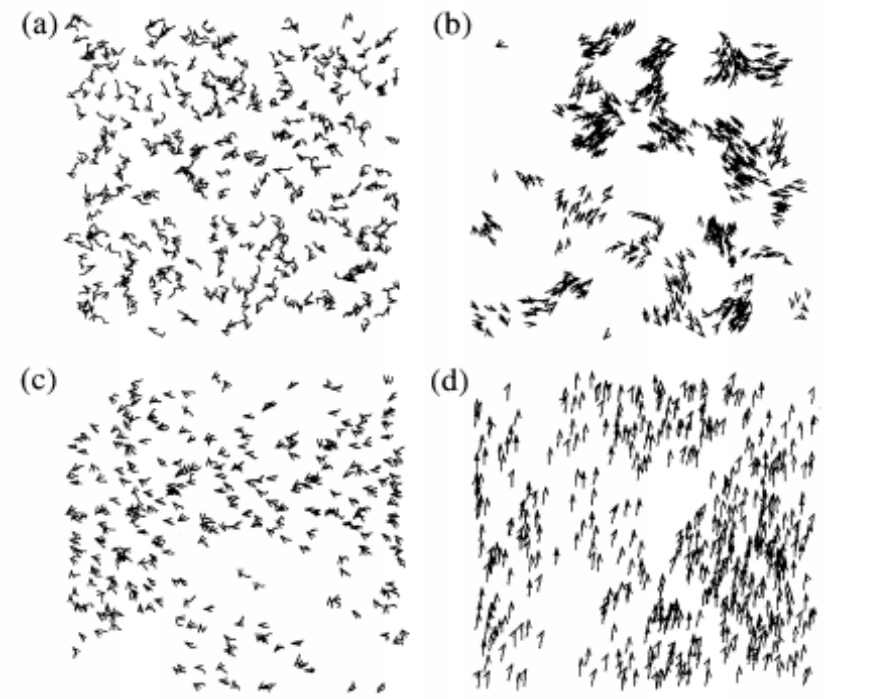

Figure 1.11 | Snapshots of the system with an arrow denoting the propulsion direction preceded by a line indicating the trajectory for the last time steps. At different noise amplitudes and particle density from [Vicsek et al., 1995].

μ_r to the diffusion constants $\mu k_B T$. Diffusion of the orientation vector is introduced by the second equation in (1.4), where $\boldsymbol{\nu}$, is vectors with random components drawn from a Gaussian distribution with zero mean and unit variance. The cumbersome equation involving the vectorial product may be translated to the angles that define $\hat{\boldsymbol{n}}$ in the unit sphere. For two dimensions it is common to use $\hat{\boldsymbol{n}} = (\cos\theta, \sin\theta)$, and thus rewrite the equation for the angle $d\theta_i(t)/dt = (2\mu_r k_B T)^{1/2}\nu_i$.

Systems combining self-propulsion, and excluded volume are known to experience a Motility Induced Phase Separation (MIPS) [Tailleur and Cates, 2008, Cates and Tailleur, 2015]. At large values of propulsion velocity, and moderate densities, the system phase separates into a high density aggregate in coexistence with a low density gas, see Figure 1.12. Colliding APBs reduce their velocities, in a cluster of ABPs incoming gas particles collide and stay in the surface until their diffusion orients them to fly away, unless they get trapped by more incoming particles [Hagan and Baskaran, 2016]. The balance between APBs going in the aggregate and APBs going out determines whether the aggregate grows in time or evaporates.

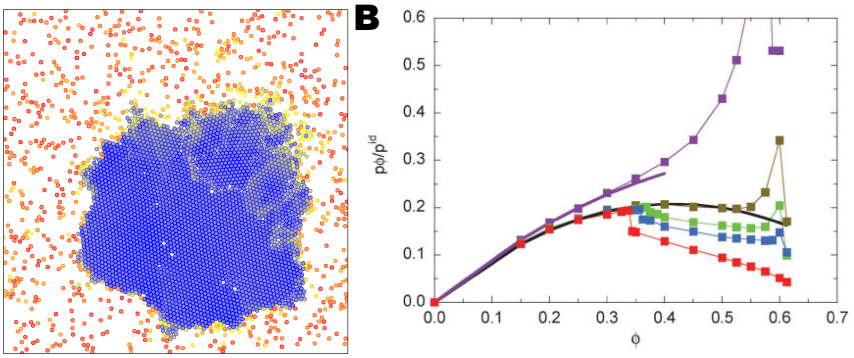

Figure 1.12 | MIPS, and pressure for ABP. Active particles collide and get trapped. **A** System of ABPs that has undergone MIPS. In colors we denote the average centre of mass displacement of each particle, red for particles moving at v_a, and blue for particles moving at ≈ 0. **B** Active pressure measured across MIPS. The pressure drop appears in the density in which MIPS is triggered in the gas phase. In different colors the propulsion velocity for increasing values from purple to red. Green, blue, and red measures show a pressure drop, data from [Winkler et al., 2015b].

Recently, a lot of effort in the community has been devoted to understand the details of the phase separation. In this process, the concept of active pressure [Takatori et al., 2014, Takatori and Brady, 2016] as an equation of state for ABPs has appeared [Solon et al., 2015c, Solon et al., 2015a]. The results, though, included a pressure drop that could not be properly understood and was assumed to by a trace of the intrinsic activity of the problem. In Chapter 1 we have devoted to this problem and have helped in the interpretation of this pressure drop by identifying the existence of a metastable state in the previously though ABP gas phase. With this results, the MIPS phase transition for ABPs is a non-equilibrium transition with all the features of first order phase transitions in equilibrium.

1.4 Interactions in active and Passive systems

From the seminal work of Wu and Libchaber [Wu and Libchaber, 2000] the interest in the introduction of active agents in passive suspensions has increased. Wu and Libchaber prepared a suspension of *E. coli* in a horizontal interface between two fluids. Once confined in the interface the suspension behaves in a quasi-two dimensional space, and thus justifies the interest in two dimensional models of active particles. At large concentration of bacteria hydrodynamics destroyed orientation correlations and the system of active particles behaved like an active gas. A detailed analysis of bacterial bath has later revealed the development of chaotic flows and given rise to the exploration of the so called active turbulence [Dunkel et al., 2013]. In Figure 1.13 we observe the colloids, inclusions of 10 μm of diameter, in the dense bacterial suspension.

The mean squared displacement of the inclusions reveals a late time diffusive behaviour. At early stages in the measurements colloids are advected by the bacteria. At longer times angular diffusion, in the bacteria, reorients the pushing direction and, effectively, the inclusion's trajectories diffuse in the interface.

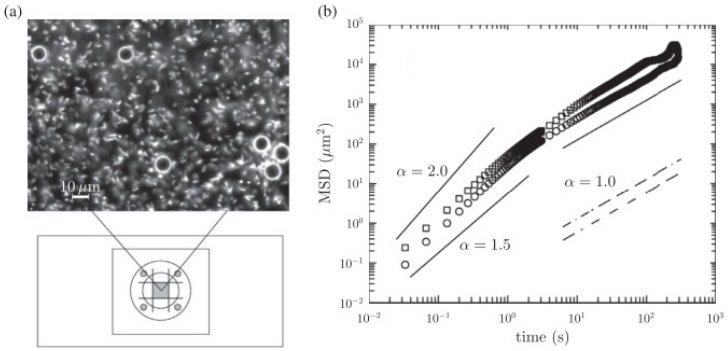

Figure 1.13 | Enhanced diffusion of passive colloids in a bacterial bath. **A** An image of the system with passive colloids, note the trimer of inclusions. **B** the MSD of inclusions with diameters 4.5 (circles), and $10\ \mu m$ reveals a ballistic to diffusive crossover with an effective diffusion constant given induced by bacteria in the bath. Dashed lines correspond to the thermal diffusion for beads of 4.5, and $10\ \mu m$ diameters, image from [**?**, wu2000]

1.4.1 Dilute suspensions

The introduction of an effective temperature explains the movements of single inclusions in active suspensions. The situation, however, gains interest as the concentration of passive particles increase. The sole introduction of an effective temperature does not respond to the fundamental question on whether passive-passive interactions are modified in a medium with active particles.

An important step to resolve this question was the work in Rome by [Angelani et al., 2011]. In a suspension of active particles the pair correlation function of large passive colloids. For an equilibrium dilute suspension of large passive particles in a suspension of dead active particles (this translates into a mixture of large and small passive colloids) depletion forces are expected to emerge between large colloids, and thus giving a strong signal in the pair correlation function at a distance of an inclusion diameter, and then then a decay to zero with a typical decaying distance comparable to the size of the small colloids.

For living bacteria, or active particles, authors reported a decrease of the peak of the $g(r)$ at contact, and additional peaks extending to larger distances, see Figure 1.14. The decrease of the first could be associated to a repulsive active deple-

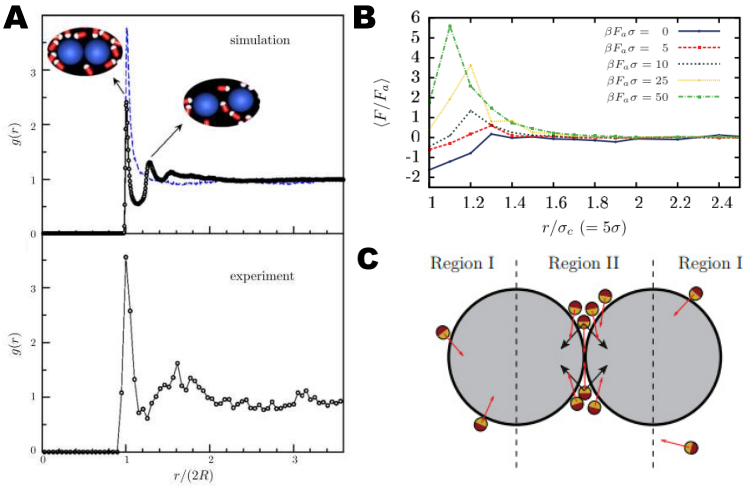

Figure 1.14 | Active particles in a complex environment. **A** Active particles in a suspension of passive colloids. The curves are the extracted pair correlation functions between colloids, image from [Angelani et al., 2011]. **B** Active particles interacting with a pair of colloids [Harder et al., 2014a]. **C** physical mechanism for active depletion interactions. ABPs are captured in the wedge and push colloids apart.

tion competing interaction. Then, the formation of multiple peaks correspond to favoured configurations with whole active particles in the inner region between inclusions. This open problem on emergent interactions between passive particles arouse our interest, and motivated this thesis.

In parallel to the development of this thesis results reported in [Harder et al., 2014a], and illustrated in Figure 1.14, explained the repulsion between spheres immersed in a suspension of ABPs. For disks at contact the geometry of the system facilitated the confinement of active particles and thus promoted the accumulation of particles in the newly formed wedge. The resulting forces were repulsive, as opposed to well known equilibrium depletion forces. The analysis of the interaction force of pairs of inclusions in a suspension of ABP particles is found in Chapter 2 of this thesis as well as an extension of it to ABP with aligning interactions.

1.4.2 Geometrical constrains

In the bulk active particles travel free and only interact in particle-particle collisions. The limiting scenario presented for the interaction between low concentration of passive colloids and active particles is easily explained in terms of an enhancement of the diffusion of the passive colloids, but the situation gains interest when the situation is reversed. In a crowded colloidal suspension the addition of a few active particles has a remarkable effect. As presented in Figure 1.15**A**, active particles push and compress the surrounding passive colloids, and thus generating fomenting

crystalline order among them [Kümmel et al., 2015]. This contrasts with the idea of an increase of the effective temperature, but resembles the effects already seen in binary mixtures of particles at different temperatures [Weber et al., 2016].

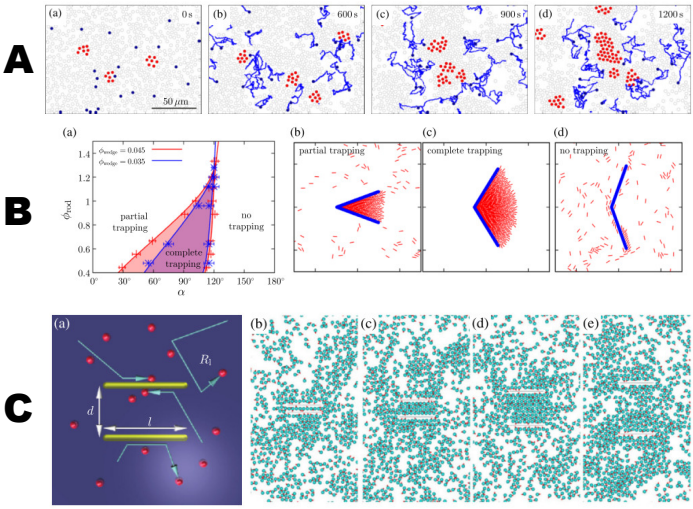

Figure 1.15 | Active particles in a complex environment. **A** A dilute suspension of active particles in a dense colloidal dispersion, from [Kümmel et al., 2015]. **B** Active particles in a geometrical confining object, from [Kaiser et al., 2012]. **C** Active particles interacting with a two rods system, images from [Ray et al., 2014], and [Ni et al., 2015]

The introduction of solid objects in the system may introduce large consequences in the movement of particles. A solid wall prevents movements in its perpendicular direction, active particles colliding with a wall will move along it until a fluctuation in the orientation reorients the particle. For elongated particles the situation is more dramatic since particle wall interaction will align the particle parallel to the wall [Elgeti and Gompper, 2009]. The interaction between active particles and walls results in a wall accumulation of particles [Elgeti and Gompper, 2013]. However, when hydrodynamic interactions are introduced in the problem, the scattering of individual particles depends on the details of the propulsion [Lushi et al., 2017].

Active particles in suspension with solid wedge shaped passive objects get trapped in a more dramatic manner. As presented in Figure 1.15**B** the asymmetry in the allows the deflection of active particles travelling from left to right, they collide with the surface of the wedge and escape. For particles travelling from right to left the collision with the walls of the wedge deflects them to the central region of the wedge where particles from the other arm also converge [Kaiser et al., 2012].

Active particles in a suspension with large fixed rods, as presented in Figure 1.15**C**, generate a dense region of active particles pushing the walls inside and a dense region outside. As a function of the distance between plates an oscillating attractive-repulsive force emerges in the suspension that extends to long ranges, further than equilibrium depletion forces. This situation has also been reported for interactions between ABPs and pairs of close spheres [Harder et al., 2014a]. The wedge between spheres confines a large population of ABPs that constantly push the spheres apart. For fixed spheres this leads to a repulsion force between spheres that ranges several ABP diameters. It is not clear, though the effect of alignment between active particles how this interaction between spheres may change. The introduction of alignment between particles has been considered in Chapter 2 in order to consider induced interactions between passive particles in an active fluid with aligning interactions.

1.4.3 Diffusophoretic interactions

When we introduced active colloids in section 1.2 we stated the existence of non-Janus, apolar, active particles, where the symmetry in the chemical reactions is not broken on the surface of the spheres. This leads to activity but not propulsion. In a series of experiments [Palacci et al., 2014] uncovered an attractive interaction between apolar active particles, see Figure 1.16. The interaction can bee understood by the production of long range decaying concentration profiles of chemical products, [Soto and Golestanian, 2014a]. The interaction of particles with the profiles distort the chemical fields and finally induce diffusophoretic velocity fields on the surfaces of apolar particles, see Figure 1.16.

The appearance of long range attractive interactions in an active system is a matter of great interest since there is no evident counterpart of these interactions in equilibrium, except for gravitation – for which no proper thermodynamic limit can be defined. Out of equilibrium, though such long range interactions are feasible. As it has already been mentioned lots of efforts have been invested in the study of interactions between active and passive objects but activity entered almost always in the form of a propulsion. In this thesis we propose a new scenario where activity is introduce by apolar particles which induce long range interactions to distant colloids, we have extended the previous models to interactions between particles of different sizes and activities. This discussion can be found in Chapter 5 of this thesis.

1.4.4 Interactions in a granular bath

The introduction of grains of different physical properties in a fluidized granular media introduces some interactions that we want to emphasize before the conclusion of the introduction. First, the introduction of large grains in the fluidized granular medium introduces the Brazil nut effect [Möbius et al., 2001]. In vertical shaking the large body experience a buoyant vertical force that pushes it to the upper

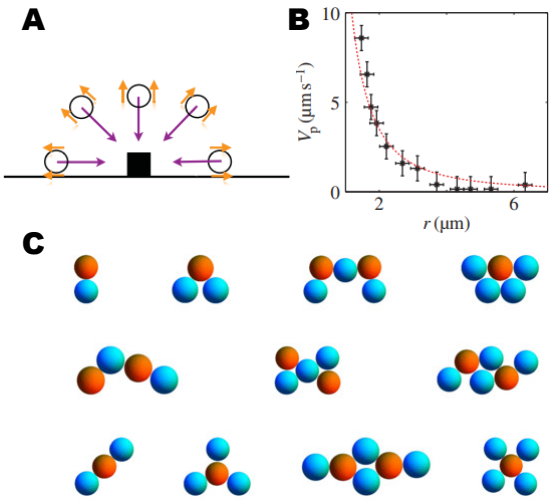

Figure 1.16 | Diffusophoretic interactions induced by apolar active particles. **A** An apolar particle (black) induces velocity flows on the surface (orange arrows) of passive particles (white) which acquire a velocity (purple arrow) towards the apolar particle. **B** Relative velocities of passive particles as they approach the apolar particle [Palacci et al., 2014]. **C** typical clusters in the computational model proposed by [Soto and Golestanian, 2014a] for dilute mixtures of apolar particles with different surface activities.

surface of the container [Huerta et al., 2005]. This effect has also been reported in swirling [Aumaître et al., 2001a], and horizontal [Schnautz et al., 2005] agitations of the granulars.

In horizontally vibrated granular monolayers a mixture of grains and spheres phase separate and form patterns of stripes perpendicular to the shaking direction [Aranson and Tsimring, 2006, Reis et al., 2006]. This separation of grains and spheres was experimentally analysed in its most simple variant [Lozano et al., 2015]. Experiments with two spheres in a shaken granular bed reported an increase of the probability to measure the pair of particles at contact with large residence times. This had lead to the interpretation of increase of the probability as an emergent interaction between the two spheres induced by the granular bath. The interest in this problem has lead us to replicate this problem computationally, and has become Chapter 3 of this thesis.

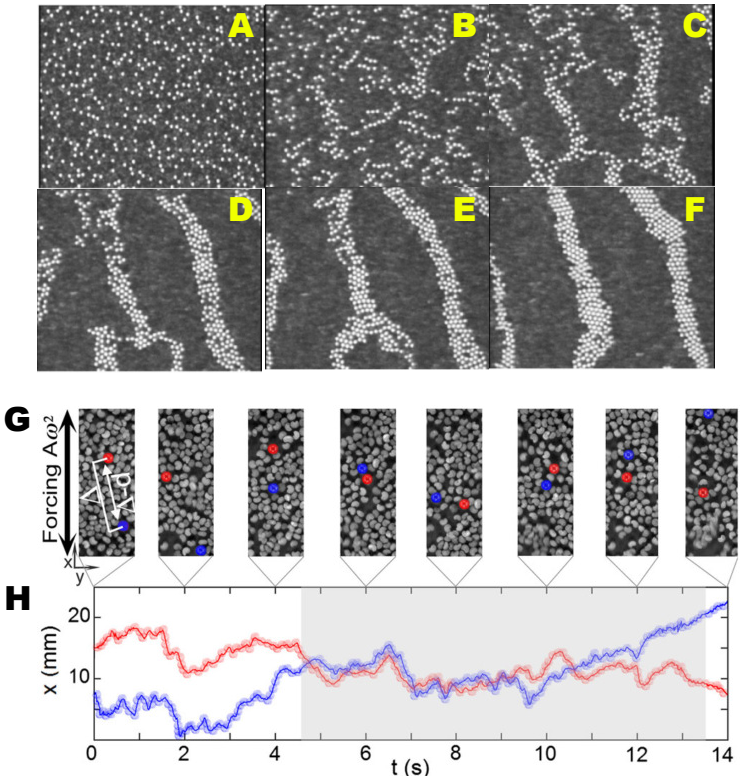

Figure 1.17 | Sphere segregation in a horizontally vibrated granular monolayer, images from [Reis et al., 2006]. **A-F** the stripe formation in a mixture of grains and spheres. **G-H** Trajectory of a pair of spheres in a granular monolayer, images and data from [Lozano et al., 2015].

2 Active Brownian Particles

Active Brownian Particles, ABP, constitute the minimal model for dry active matter. The key ingredients for the active agents being: excluded volume, propulsion, and thermal fluctuations. The competition between propulsion and repulsion leads to a non-equilibrium phase transitions. In this Chapter we introduce the ABP model, the active pressure as a contribution to the total pressure of the system as the Equation of State to assess various open problems regarding pressure measurements across MIPS, and to stablish parallels with equilibrium first order phase transitions.

2.1 Self propelled particles

An agent that extracts energy from the medium and converts it into directed motion is considered to be a self propelled particle. Traditionally, nonequilibrium statistical mechanics has focused on the kinetics of relaxation to thermal equilibrium, and temporal correlations in equilibrium. A self-propelled particle, on the contrary, keeps a sustained out-of-equilibrium nature.

The concept of active system involves a reservoir of free-energy, either internal or external. For living organisms ATP molecules inside cells sustain motor activities and propel the organism. Living self-propelling particles include swimming bacteria, crawling cells, swimming fishes, and flying birds. In the general introduction to this thesis we have introduced artificial, human made, system that self-propel. In the microscopic scale we encounter colloids that asymmetrically trigger chemical reactions on their surface. The coupling of the chemical field gradients on the immediacies of the particles induces a fluid flow that translates into a global translational velocity of the particle. This phoretic mechanism, diffusophoresis,

introduced in more detail in Chapter 5.

At microscopic scales, we encounter vibrated granular systems. An asymmetric design of the contact surface of the grains permits the rectification of vibratory movements of the base, and translate into a translational velocity of the particle. To summarise, self-propelled particles convert a local free-energy source into directed motion, along this thesis we introduce self-propulsion on the particles as a constant velocity v_a on a preferential direction $\hat{\boldsymbol{n}}$. The sustained energy flux converted into motion and ultimately dissipated in the viscous drag, locally breaks energy conservation law.

2.1.1 Langevin Equations for SPP – The ABP model

In this Chapter we focus on SPP in the micrometric scale. SPPs are immersed in a fluid in the Stokes regime, particles experience a drag froce proportional to the radius, and its velocity $F_d = 6\pi\eta R v$. In addition, a spherical particle of radius R in a viscous fluid at temperature T experiences a brownian motion of with a diffusion constant $D = k_B T/(6\pi\eta R)$, where η is the fluid viscosity. Introducing typical numbers to the diffusion relation we obtain diffusions of the order of $D \approx 0.2\ \mu m^2 s^{-1}$. This result translates into a mean squared displacement of the particle size in times of the order of the second. Diffusion needs to be incorporated to the equations, and thus the use of models based on Landevin equations has spread in the community. This models that do not include explicitly hydrodynamics are labelled as dry models.

However, a Langevin description of SPPs coexists with models that solve SPPs while considering a full hydrodynamic description of the system, the wet models. This models need to solve the motion of both particles, and the embedding fluid. Nowadays, a large collection of models are generally used in the literature, such as boundary elements methods [Ishikawa et al., 2006], multiparticle collision dynamics [Zöttl and Stark, 2014, Yang et al., 2014], Lattice-Boltzmann [Llopis and Pagonabarraga, 2010], and force coupling methods [Delmotte et al., 2015].

In this Thesis we have specially focused on the effects of bare propulsion and activity in the emergent forces between passive particles. For this reason, we have opted for a Langevin description of active particles.

The centre of mass position vector $\boldsymbol{r}$ for a diffusive Brownian particle of diameter σ moving in a viscous fluid with viscosity η, and diffusion constant $D_T = k_B T\gamma$ can be modelled with the following Langevin stochastic equation,

$$m\frac{d\boldsymbol{r}^2}{dt^2} = -\gamma\frac{d\boldsymbol{r}}{dt} + \boldsymbol{F}^c + \sqrt{2\gamma k_B T}\boldsymbol{\xi}_i \tag{2.1}$$

where we introduce a conservative interaction force $\boldsymbol{F}^c$ acting on particles coming from either an external potential or interactions with other particles in the system. Dividing the equations by $\gamma\sigma$ we identify the characteristic timescales of the different processes. For a microscopic particle the typical size is of the order of

the micrometer $\sigma \approx 10^{-6}\ m$, and mass $m \approx 10^{-18}\ kg$. With a drag coefficient $\gamma = 6\pi\eta\sigma/2$ the inertial timescale is $\tau_i \approx m/(\gamma L) \approx 10^{-5}\ s$. The diffusion time $\tau_d = (K_B T/\gamma)^{-1/2} L^{-1} \approx 0.5s$. For interactions of the order $10K_B T/L$, the interaction timescale is $\tau_{int} = (10K_B T/(\gamma L^2)) \approx 0.1\ s$. At this scales we observe that inertial effects occur faster than any other phenomena. The system is overdamped, thus we neglect inertial effects in the system. For microscopic systems we further omit accelerations in the scope of this thesis. And present the equation in the form

$$\frac{d\boldsymbol{r}}{dt} + \gamma^{-1}\boldsymbol{F}^c + \sqrt{2\gamma^{-1}k_B T}\boldsymbol{\xi}_i \tag{2.2}$$

where we an now define the mobility $\mu = \gamma^{-1}$, and by the Stokes-Einstein relation $D = \gamma^{-1}k_B T$. Finally, to model the propulsion of a SPP we introduce a velocity v_a at each particle along a characteristic direction, the orientation, defined by $\hat{\boldsymbol{n}}$. Now the orientation plays a role in the temporal evolution of the centre of mass since v_a couples orientation and propulsion. For this reason we need to incorporate the diffusion effects on the orientation. Overall, evolution of both position, and orientation follow of each i-th particle we write an overdamped Langevin equation.

$$\begin{cases} \dfrac{d}{dt}\boldsymbol{r}_i(t) = v_a\hat{\boldsymbol{n}}_i(t) + \mu_t\boldsymbol{F}_i^c(t) + \sqrt{2D_t}\boldsymbol{\xi}_i \\ \dfrac{d}{dt}\hat{\boldsymbol{n}}_i(t) = \sqrt{2D_r}\hat{\boldsymbol{n}}_i \times \hat{\boldsymbol{\nu}}_i \end{cases} \tag{2.3}$$

With v_a the propulsion velocity, μ_t the thermal mobility, $D_t = \mu_t K_B T$, and $D_r = \mu_r K_B T$ the translational and rotational diffusion constants, and $\boldsymbol{\xi}_i$, and $\boldsymbol{n}u_i$ two vectors whose components are drawn from Gaussian distributions, with zero mean and unit variance. We keep the interaction force $\boldsymbol{F}^c$ on each particle to introduce either external interactions, or interactions between particles. For a system evolving in two dimensions, which is typically the experimental scenario with SPPs precipitated on the surface of the experimental set-up or particles in the interface between two fluids, orientation vector is equivalently defined by the angle θ, $\hat{\boldsymbol{n}} = (\cos\theta, \sin\theta)$. The vectorial equation for the orientation in (2.3) translates into a simpler scalar equation for θ.

$$\frac{d}{dt}\theta_i(t) = \sqrt{2D_r}\nu_i(t) \tag{2.4}$$

With $\nu_i(t)$ a random real with a Gaussian distribution, zero mean value and unit variance. This, the equations for the centre of mass, and the orientation of the particle constitute the model of an Active Brownian Particle (ABP).

The interest for ABPs is not only purely theoretical. This out-of-equilibrium model has aroused attention and we there are broad applications in experimental systems. Janus colloids [Ginot et al., 2015], shaken grains [Briand and Dauchot, 2016]. Even the dynamics of $+1/2$ topological defects on active nematics [Keber et al., 2014, Ellis et al., 2017] may be modelled by ABP. An active nematic behaves as a mixture of active particles, $+1/2$ topological defects, and passive particles,

$-1/2$ topological defects, with and long range elastic force, due to the elastic properties of the polymers, and the complete annihilation at contact.

In recent years the study of Active Brownian Particles (ABP) has extended in the out of equilibrium community as a prototypical model for dry SPPs. An initial, and general, model for ABP considered a collection of Brownian diffusive particles with the ability to store energy from the environment [Schweitzer et al., 1998]. More recently, the community has focused on ABP that convert the internally stored energy into movement, a propulsion v_a relative to the medium. Thus, ABP incorporate an additional degree of freedom: the orientation $\hat{\boldsymbol{n}}$.

The ABP model does not introduce chemical reactions, mechanical movements nor hydrodynamic interactions, which are responsible for the propulsion; we introduce it only by means of a constant velocity, or force, on the particle. To get further details on derivations of the velocities of active particles see Chapter 5, and specially [Golestanian et al., 2007].

2.1.2 Time Reversal Symmetry

A system of ABPs is intrinsically out-of-equilibrium. We examine this feature by an inspection of the violation of the time reversal symmetry in ABP interactions. According to Noether's Theorem, energy is conserved if the system is invariant under temporal symmetries. The non-conservation of energy must be accompanied by the violation of time reversal symmetry, and detailed balance [de Groot and Mazur, 1984] is not fulfilled. To exemplify the time reversal violation, in Figure 2.1, we sketch the evolution of a pair of colliding particles with a finite volume.

In a pair collision between two diffusing bodies with repulsive interactions particles that interact are repelled after the collision. In a pair collision between SPPs, as seen in Figure 2.1, the persistence of motion opens a new scenario. Particles collide and repel each other. The propulsion of both particles keeps pushing and then particles stay bonded together. The system stays trapped at contact until thermal fluctuations on the orientation of particles gradually reorient the propulsion direction and particle escape is possible. If we were to describe the time reversed scenario we would encounter a different scenario. Two particles collide and a rapid sliding occurs into a fixed position then stay bounded for a random time. With no previous notice the attractive bond between particles breaks and particles fly away. The time reversed scenario cannot be described by the same physics, so time reversal symmetry is broken in pair collisions between self propelled particles.

The violation of time reversal symmetry is also seen in collisions between active particles and obstacles or wall, see Figure 2.1. The increase of residence time on the walls leads to the accumulation of active particles [Elgeti and Gompper, 2013], and the capture of ABP in wedges [**?**].

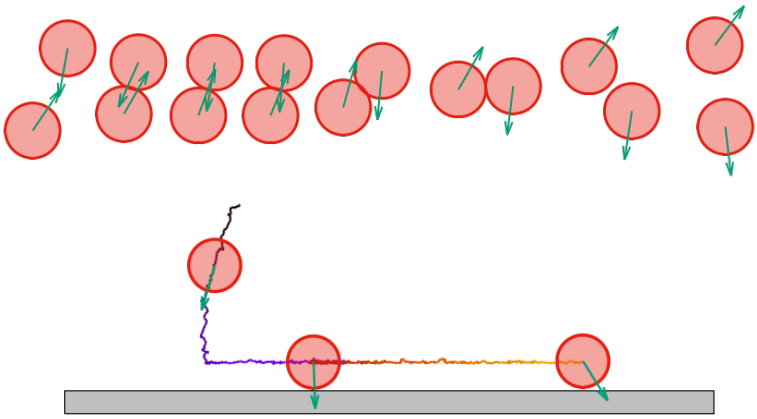

Figure 2.1 | Time Reversal Breaking in SPPs. **A** Collision between two self propelled particles. Pictures of the pair are taken at equal time intervals. Particles collide and stay pushing until diffusion changes the direction of the orientations. **B** Collision of an ABP with a wall. The solid line marks the trajectory of the trapped particle.

The intrinsic out-of-equilibrium nature of self-propelled particles can be extended a step further. We can devise funnelled walls that induce a density imbalance in the system [Galajda et al., 2007, Lambert et al., 2010] or by a combination of funnelled walls drive the system into a state with macroscopic fluxes of momentum, as reported in [Cates, 2012]. The asymmetry of confinement as been recently exploited to power micromotors from a bacterial bath [Angelani et al., 2009, Vizsnyiczai et al., 2017]. Dented asymmetric rotors were used by [Di Leonardo et al., 2010] to convert active motion from a bacterial bath into continuous rotation of a passive body. Finally, [Vizsnyiczai et al., 2017] have 3D printed a huge bacterial powered structure.

Interactions between SPP and walls are illustrated in Figure 2.1**B**. The asymmetry of the funnels in Figure 2.2 exploits the SPP-wall interactions. Active particles follow the walls and encounter the route from the left to the right side of the box with higher probabilities than particles travelling from the right to the left side of the box. The combination of funnel walls in 2.2**C** separates two regions in the box: the left wall generates a spontaneous flow from left to right while the bottom funnel wall a flow from top to bottom. The combination of the two walls generates a steady clockwise circulation of active particles in the system.

The experimental realization of moving wedges in an active turbulent flow from [Kaiser et al., 2014, Kaiser et al., 2015], altogether with the self-starting asymmetrically dented wedges [Angelani et al., 2009] present a practical exploit of the tendency of SPP to follow walls and their force transmission, which for

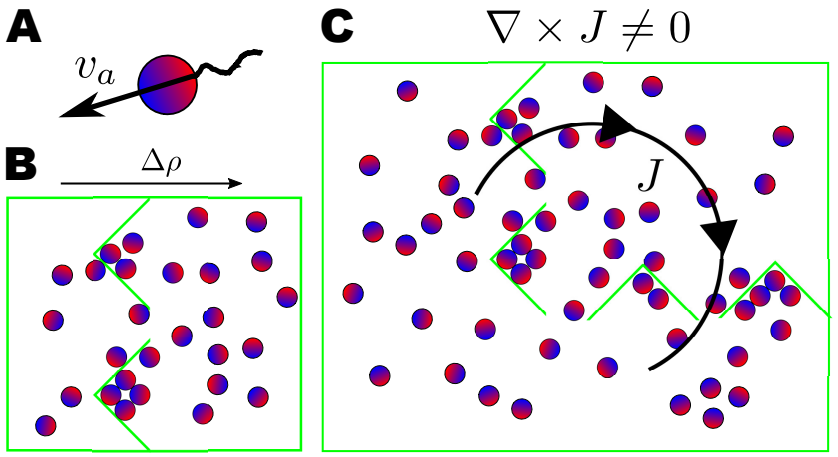

Figure 2.2 | Funneling ABPs. A A Self Propelled particle with swimming velocity v_a. **B** A wall of funnels induces a flux of particles from the left box to the right box until a density imbalance is reached, based on [Galajda et al., 2007, Galajda et al., 2008]. **C** A combination of funnel walls generates a sustained flux of SPPs, based on [Lambert et al., 2010, Cates, 2012].

non-fixed objects translates into motion. Di Leonardo's group [Vizsnyiczai et al., 2017] have engineered 3D arrays of micromotors that trap *E. coli* to power the rotors and finally extract directed motion.

2.1.3 Motility Induced Phase Separation in ABPs

In ABP pair collisions velocities of colliding particles in the radial direction mutually compensate and the total velocity of the pair decreases. In this situation more incoming particles will difficult the escape of already entrapped particles, and thus start the formation of a large macroscopic cluster driven by the Motility Induced Phase Separation (MIPS) [Tailleur and Cates, 2008, Cates and Tailleur, 2015]. In ABP systems with repulsive interactions the locally averaged velocity of the system is a decreasing function of the local density $v(\rho)$. This feature emerges from the intrinsic out-of-equilibrium nature of the particles, and thus leads to a non-equilibrium phase separation.

To illustrate this density phase separation we have prepared a system of $N = 4000$ ABPS at a moderate packing density, see Figure 2.3. At early stages from the start of the computation the system forms clusters that capture and slow down particles. This clusters grow in time and finally lead to a steady state where the system is separated into a dense, and a dilute regions.

In a coloured scale we measure the average velocity of ABPs, the displacement over a diffusion time unit, with $v(\rho)$ a decaying function of ρ, the local density. The simple functional form $v(\rho) = v_0 - \zeta\rho$ is easily tested and responsible of this

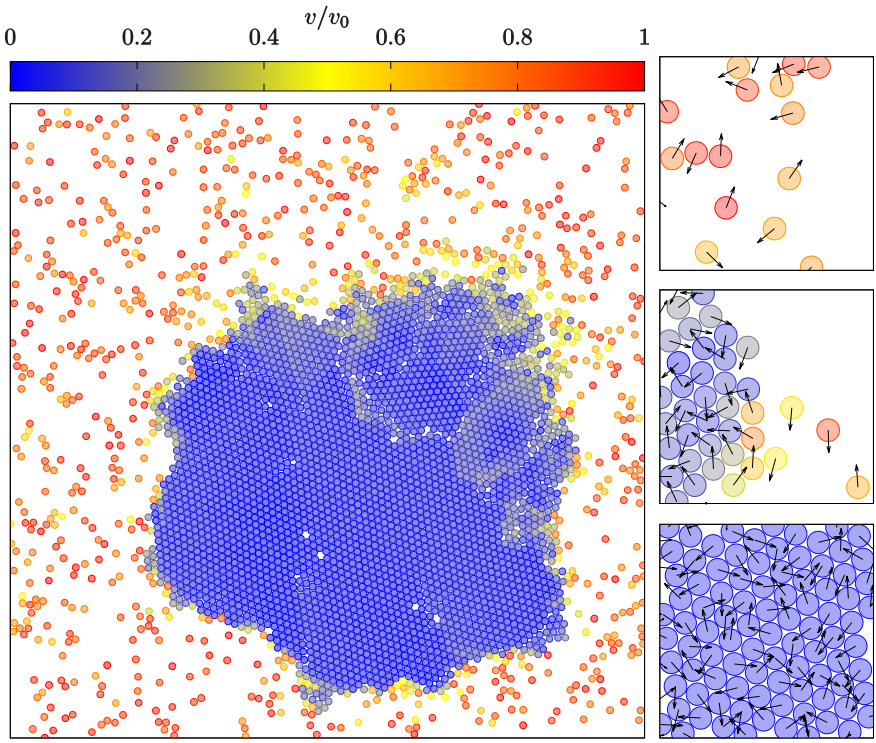

Figure 2.3 | Motility Induced Phase Separation for ABPs. A system of 4000 particles undergoing a MIPS transition. In the dilute regime active particles move at great velocities $v \approx v_0$, and orientations are randomized. An increase of the density reduces the local value of the velocity $v(\rho) = v_0 - \zeta\rho$. Close to the surface the velocity drops and orientations are mainly pointing inwards for trapped particles. Inside the dense phase $v \approx 0$ and orientations are randomized.

striking out-of-equilibrium phenomenon. The denser a system is, the lower the local velocity is. The persistence of motion in the direction of the orientation $\boldsymbol{n}$ leads to a slow down of the local density, as clearly depicted in Figure 2.3. Active Brownian particles in a dense phase push between them in such a way that their velocities cancel each other and the local velocity averages to zero.

To treat this out-of-equilibrium phase transition the concept of pressure has been recently extended to capture the self-propulsion [Takatori et al., 2014]. For systems with no aligning interactions the total pressure, active and passive contributions, has been identified to define the equation of state of the system. In this context, pressure is the appropriate measure to characterize the phase transition. In this Chapter we settle different open questions regarding the interpretation of this phase transition and show that MIPS is fully consistent with the first-order phase transition scenario. We bring out the existence of a metastability region with an hysteresis-loop around

the coexistence pressure. We show that the pressure drop [Winkler et al., 2015a] associated to a non-equilibrium signature of the transition is in fact a result of pressure measurements in a metastable state of ABPs.

2.2 Active Brownian Particles

Equation (2.3) unambiguously defines ABPs but the model still has some fine details that need to be settled. Fist we discuss the relationship between translational, and rotational diffusion constants. Then we define a repulsive interaction between pairs of particles. Finally, we introduce dimension-less numbers to fully characterize the ABPs.

2.2.1 Dimensionless relevant parameters

The equations of motion present several terms, and timescales. In this section we define a set of characteristic numbers which relate the relative strength of each term in the equations. Thermal fluctuations on a sphere define a relation between translational and rotational mobilities. For a system of ABPs we introduce the same ratio, so that the system maintains the equilibrium limit $v_a \to 0$. Equilibrium fluctuations on a sphere of diameter σ couples the mobilities so that $\mu_t = \mu_r\sigma^2/3$. This relation corresponds to the relation between diffusion constants $D_t = D_r\sigma^2/3$. We define as unit length the size of each ABP, σ. To define a time unit we use the inverse of rotational decorrelation time $T = D_r^{-1} = (\mu_r k_B T)^{-1}$.

$$\frac{1}{\sigma D_r}\frac{d}{dt}\boldsymbol{r}_i = \frac{v_0}{\sigma D_r}\hat{\boldsymbol{n}}_i + \frac{\mu_t}{\sigma D_r}\boldsymbol{F}_i^c + \sqrt{2D_t/(\sigma^2 D_r)}\frac{1}{D_r^{1/2}}\boldsymbol{\xi}_i(t) \tag{2.5}$$

Note that $\boldsymbol{\xi}_i(t)$ has units of $t^{-1/2}$. Using the relation between mobilities of spheres of diameter σ in a Stokes regime $\mu_t = \sigma^2\mu_r/3$, and combined with $D = \mu k_B T$, we relate the translational mobility to the rotational diffusion coefficient $\mu_t/(\sigma D_r) = \sigma/(3k_B T)$ and also $D_t/(\sigma^2 Dr) = 1/3$,

$$\begin{aligned}\frac{d\boldsymbol{r}(t)}{dt} &= Pe\hat{\boldsymbol{n}}_i(t) + \frac{\epsilon}{3}\boldsymbol{F}_i^c(t) + \sqrt{2/3}\boldsymbol{\xi}_i(t)\\ \frac{d\theta_i}{dt} &= \sqrt{2}\nu_i(t)\end{aligned} \tag{2.6}$$

Where we introduce the Péclet number Pe that compares the reorientation time to the swimming time. The highest the value of Pe the longer is the persistence swimming length of an ABP. In the literature, though the are two coexisting definitions for the Péclet number, either $Pe = v_0\sigma/D_r$ as found in [Winkler et al., 2015a], or $Pe = 3v_0/(\sigma D_r)$ like in [Solon et al., 2015d]. In addition, we introduce ϵ as the characteristic energy of the interaction. In our modelling of ABPs we introduce

either a conservative repulsion WCA potential (2.7), or a model of hard disks[1]

$$F_{ij}^{c}(\sigma, r) = -\frac{d}{dr}U_{wca} = \frac{24\epsilon k_B T}{\sigma}\left[2\left(\frac{\sigma}{r}\right)^{13} - \left(\frac{\sigma}{r}\right)^{7}\right]\hat{\boldsymbol{r}}, \text{ for } r < 2^{1/6}\sigma \quad (2.7)$$

with $r = |\boldsymbol{r}_i - \boldsymbol{r}_j|$ and the unit vector $\boldsymbol{r}_{ij} = (\boldsymbol{r}_i - \boldsymbol{r}_j)/r$, and $r < 2^{1/6}\sigma$ the cutoff for repulsive interactions.

The scope of this chapter is to study the system at different values of Pe, and packing density $\phi = N\pi\sigma/(4L^2)$, for systems with periodic boundary conditions (PBD), and systems with geometric confinement. For the pairs $(\phi,\ Pe)$ we determine whether the system phase separates, and the correspondent value of the total pressure $p(Pe;\ \phi)$

2.2.2 Phase diagram of ABP

To determine the phase diagram for ABP we introduce the calculation of the binodal lines. The binodal line corresponds corresponds to a structural measure of the system. In a system at steady state we define local measures of the density, ρ, and with this construct the probability distribution of the local densities $P(\rho)$. The identification of maxima in the $P(\rho)$ curves allow us to define the coexistence densities in the system. To measure $P(\rho)$ we define a virtual grid on the system to extract, at the measuring time, the occupation fraction of each cell. The total occupation of each cell is then processed into the $P(\rho)$.

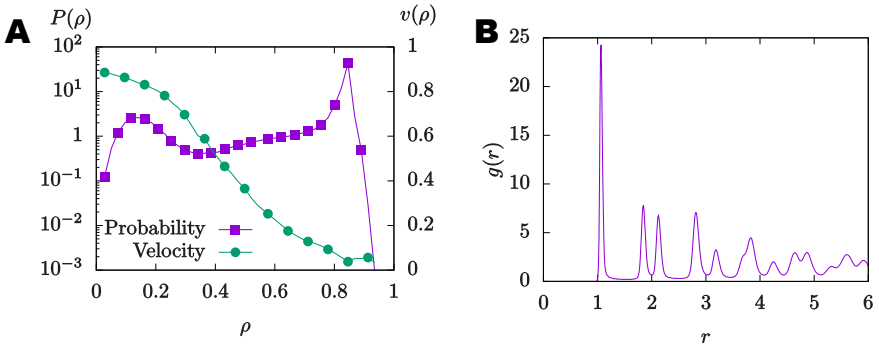

Figure 2.4 | Density dependent velocity, and local structure of ABPs. In **A** we plot the velocity as a function of the local density, and the local density distribution $P(\rho)$ of a system of Active Brownian Particles. In **B** we plot the averaged pair distribution function of ABP at short distances. The first peaks correspond to the hexagonal lattice.

To determine the maxima in $P(\rho)$ we prepare an equilibrium configuration ABPs at packing fraction $\phi = 0.45$, and PBC, we quench it into various activities

[1] For hard-disks the energy scale ϵ cannot be defined.

Pe. In Figure 2.4 we have prepared a system of $N = 4000$ ABPs at $\phi = 0.45$, and quench it to $Pe = 60$. Once the system has undergone MIPS and is in a steady phase separated state we begin the computation of the local density to construct $P(\rho)$. Additionally, we measure the averaged velocity of ABPs in the lattice sites as the total displacement over a diffusion time to illustrate the $v(\rho)$ dependence, also in Figure 2.4. Additionally, we compute the pair distribution function of ABPs in the system to extract the $g(r)$ in Figure 2.4 whose peaks correspond to the first neighbours distances of an hexagonal crystalline structure. At long distanes, though the signal is gradually lost due to the contribution of the gas phase, and the presence of topological defects in the dense phase, see Figure 2.3 for a representative high density ABP crystalline structure.

Now, we proceed to systematically characterize the coexistence densities of ABPs for different values of the Pe number. We have systematically run simulations with $N = 2000$ ABP at various Pe, ϵ, and for Hard Disks. Hard Disk ABPs have been introduced via a Monte Carlo even driven algorithm, as done in [Scala et al., 2007, Ni et al., 2013, Levis and Berthier, 2014]. In Figure 2.5 the vertical arrow represents the quench from the equilibrium system at $Pe = 0$ to a finite Pe where statistics are carried out. Above a critical Pe, the local density probability, $P(\rho)$, develops two peaks: at low density $\phi_{low} = \phi_g$ which corresponds to a gas phase of ABP; and at high density $\phi_{high} = \phi_f$, which corresponds to the high density fluid of ABP. After the activity quench, ABP with different stiffness exhibit the same qualitative phase behaviour: above a critical Pe they undergo MIPS if its bulk density is large enough.

In a ϕ-Pe map, see Figure 2.5 the collection of $\phi_g(Pe)$, and $\phi_f(Pe)$, see Figure 2.4, constitute a pair of lines, the low, and the high density binodal lines. Additionally we locate the pair of coordinates that define the onset of MIPS in red points in Figure 2.5, this collection of points correspond to the spinodal line of the phase transition. To identify the onset of MIPS at a given Pe we prepare equilibrium systems at surface density ϕ and quench them into Pe. Once in the steady state we measure the probability that a particle belongs to the largest cluster Ψ, as defined by a cut off distance $r_c = 1.05\sigma$. At low densities of ABPs we expect a value $\Psi \approx 0$. At constant activity Ψ monotonically increases as we increase the packing fraction of active particles. The onset of the transition is visible from an abrupt increase of Ψ. To clearly identify the onset of MIPS we define the second moment of the Ψ distribution in the form of a susceptibility $\chi = \left\langle \Psi^2 \right\rangle - \left\langle \Psi \right\rangle^2$, see Figure 2.6.

Susceptibility χ shows a peak at the onset of MIPS, ϕ_n, thus providing a criterion to locate the transition in the ϕ-Pe phase diagram, the spinodal line. The collection of onset densities is identified by red symbols in the Phase Diagram in Figure 2.5. By means of mechanical measures, the active pressure, [Winkler et al., 2015a, Patch et al., 2017], the onset of MIPS is easily identified by pressure drop located precisely at ϕ_n, both in $d = 2$, and in $d = 3$, we plotted the density of the pressure drop in blue points in the Phase Diagram in Figure 2.5. The match of

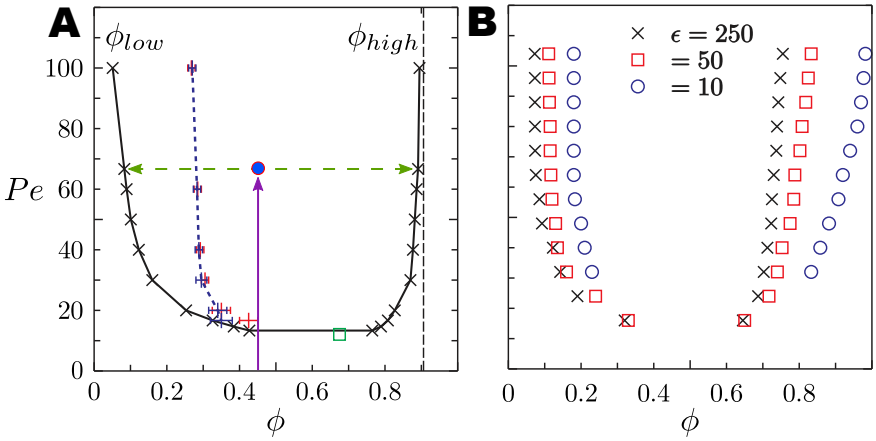

Figure 2.5 | Phase Diagram of MIPS. ϕ-Pe phase diagram of ABP after a $Pe \neq 0$ quench with PBCs. **A** Diagram for ABP Hard Disks. The binodal line is dedined by black cosses. In blue dashed lines the onset of MIPS as defined by χ. **B** Binodals for ABP with WCA repulsive interactions.

the density of the pressure drop and the onset of MIPS is clear and confirms the previously reported origin in the onset of the MIPS transition for activity quenches.

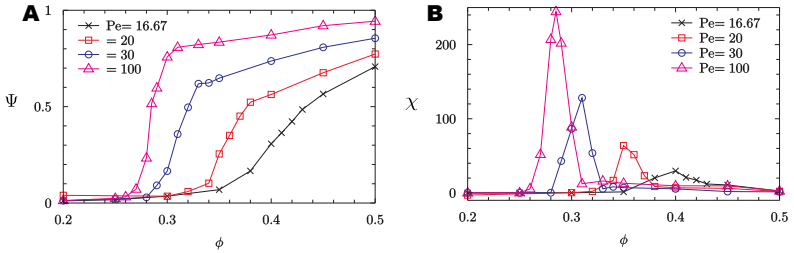

Figure 2.6 | Onset of MIPS. Determination of the transition onset at constant Pe in $N = 4000$ ABP Hard Disks. **A** fraction of particles in the largest cluster. **B** Second moment of Ψ, the position of the peak determines the spinodal density ϕ_n.

Finally, we comment on the density shift, and the opening of the branches observed in Figure 2.5 for ABPs interacting via WCA potentials at different ϵ.

2.2.3 Stiffness of ABPs

In the equations of motion for the ABP we introduced the WCA repulsive interaction characterized by the repulsion energy ϵ. The relation between the characteristic repulsion and the propulsion determines the typical distance between two colliding active disks. While the divergence of WCA guarantees the excluded volume below

a certain threshold. Nevertheless, the smaller the quotient ϵ/Pe the closer active disks can approach. From this competition we extract two major consequences.

First, for low values of ϵ/Pe the peaks of the pair distribution function widen. The characteristic distances between colliding particles presents a larger dispersion. The maximum of the pair distribution function typically goes to lower r, and decreases.

Second, the decrease in the rigidity of particles facilitates the scape of collid-

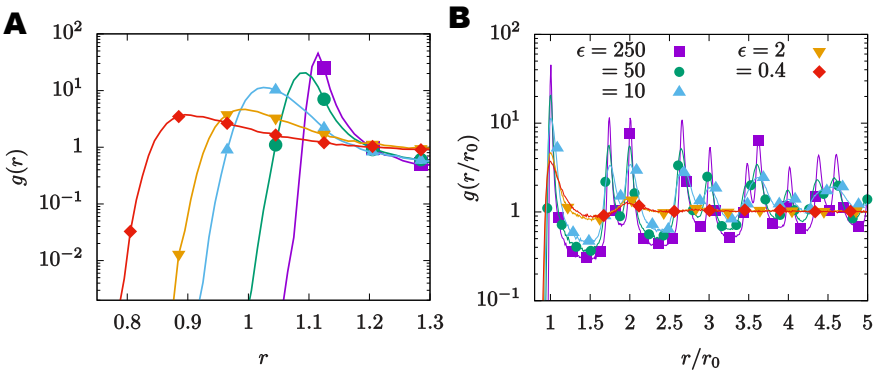

Figure 2.7 | Pair correlation functions for ABPs of different stiffness. Pair correlation functions $g(r)$ for systems of Active Brownian Particles at $Pe = 30$, and $\phi = 0.35$ for different values of the repulsive energy ϵ. In plot **A** We observe the displacement of the contact distance r_0 to decreasing values of r. In **B** we plot the $g(r/r_0)$ to compare the periodicity and the hexagonal structure for $\epsilon > 2$. At $\epsilon < 10$ we do not observe neither MIPS nor hexagonal order.

ing particles. As seen in Figure 2.7 the decrease of the rigidity also destroys the crystalline-like structure of the dense phase of ABPs.

For this reason once the phase separation occurs there is a shift to higher densities at lower values of ϵ. This effect is then magnified in the dense region where it shows the dependence on the Pe. In a dense region we locate more particles per unit area and thus ϕ_f increases.

2.3 Active Pressure

We have introduced the Mobility Induced Phase Separation and its general features. There are strong evidences to associate its major characteristics to an equilibrium First Order Phase Transitions. In this section we introduce the concept of Active Pressure as a state function for ABP.

We consider N self-propelled particles of diameter σ in a 2d surface $S = L \times L$, with number density $\rho = N/S$ and packing fraction $\phi = \pi\sigma^2\rho/4$. The model is

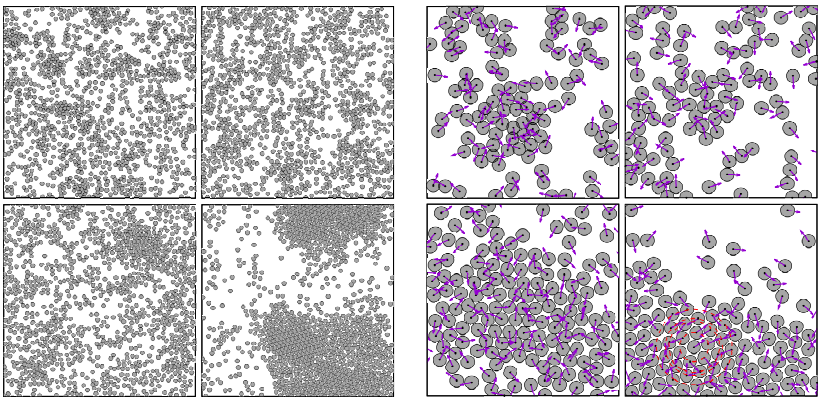

Figure 2.8 | Crystaline structure in MIPS. Local structure of the dense phase for different values of the repulsion energy ϵ at $\phi = 0.35$, and $Pe = 30$. Low values of ϵ prevent the density separation. For $\epsilon = 10$ the separation still occurs but hexagonal ordering is rapidly lost. For $\epsilon = 250$ we draw some coordination rings to appreciate the hexagonal structure surrounding a particle.

defined by the ABP overdamped Langevin equations for each particle at position $\boldsymbol{r}_i = (x_i, y_i)$

We project the equations of motion of ABPs onto the positions $\boldsymbol{r}_i$ and average over independent realisations of the noise to obtain:

$$\frac{1}{2}\frac{d}{dt}\left\langle \boldsymbol{r}_i^2(t)\right\rangle = v_0\left\langle \hat{\boldsymbol{n}}_i\cdot\boldsymbol{r}_i\right\rangle + \mu_t\left\langle \boldsymbol{F}_i^c(t)\cdot\boldsymbol{r}_i(t)\right\rangle + \sqrt{2D_t}\left\langle \boldsymbol{r}_i(t)\boldsymbol{\xi}_i(t)\right\rangle \tag{2.8}$$

In this stage of the computation we need to incorporate the periodic boundary conditions. The computation of interactions take into account the minimum distance between particles. Initially, all particles are in the so-called primary box at positions $|x_i|, |y_i| < L$, and their positions in the periodically replicated boxes at positions $\boldsymbol{r}_i + \boldsymbol{R_u}$ where $\boldsymbol{R_u} = (u_x\hat{\boldsymbol{e}}_x + u_y\hat{\boldsymbol{e}}_y)$ with $u_x, u_y \in \mathbb{Z}$. After a finite time, the particles may have escaped the primary box and $|x_i|, |y_i|$ may be arbitrary large. We introduce periodic boundary conditions in the interactions so that the distance between particles corresponds to the minimum distance between virtual pairs.

$$d(\boldsymbol{r}_i, \boldsymbol{r}_j) = \|\boldsymbol{r}_i - \boldsymbol{r}_j - \boldsymbol{u}L\| = \|\Delta\boldsymbol{r}_{ij}\|, \quad \text{with} \quad \boldsymbol{u}_\alpha = \text{int}\left(\frac{r_i^\alpha - r_j^\alpha}{L/2}\right) \tag{2.9}$$

The total force acting on a particles is

$$\boldsymbol{F}_i^c = \sum_{j\neq i}\boldsymbol{F}_{ij}\left(\boldsymbol{r}_i - \boldsymbol{r}_j - \boldsymbol{R_u}\right) \tag{2.10}$$

The summation of the force over all particles and applying Action-Reaction for the

interparticle interaction

$$\sum_i \boldsymbol{r}_i \boldsymbol{F}_i^c = \frac{1}{2}\sum_i \sum_{j\neq i} \boldsymbol{r}_i \cdot \boldsymbol{F}_{ij} + \sum_j \sum_{i\neq j} r_j \cdot \boldsymbol{F}_{ji} = \frac{1}{2}\sum_i \sum_{j\neq i} \boldsymbol{r}_i \cdot \boldsymbol{F}_{ij} - \sum_j \sum_{i\neq j} r_j \cdot \boldsymbol{F}_{ij} \tag{2.11}$$

Now summing equation (2.8) and adding and subtracting the projection of the pair force on the vector $\boldsymbol{R_u}$ to keep $\boldsymbol{r}_i - \boldsymbol{r}_j$ in the primary box

$$\begin{aligned}\frac{1}{2}\sum_i \frac{d}{dt}\left\langle r_i^2(t)\right\rangle =& v_0 \sum_i \left\langle \boldsymbol{n}_i \cdot \boldsymbol{r}_i\right\rangle + \frac{\mu_t}{2}\sum_{i,j,\alpha}\left\langle F_{ij}\left(\boldsymbol{r}_i - \boldsymbol{r}_j - \boldsymbol{R}_u\right)\right\rangle + \\ &+ \frac{\mu_t}{2}\sum_{i,j,\alpha}\left\langle \boldsymbol{F}_{ij}\cdot \boldsymbol{R_u}\right\rangle + \sum_i \left\langle \boldsymbol{\xi}_i \cdot \boldsymbol{r}_i\right\rangle\end{aligned} \tag{2.12}$$

At long times, and assuming a diffusive behaviour of active particles we introduce an effective diffusion constant $\left\langle \boldsymbol{r}_i^2(t)\right\rangle = 2\cdot 2Dt$, where we explicitly state $d = 2$.

$$2ND = v_0 \sum_i \left\langle \boldsymbol{r}_i \cdot \hat{\boldsymbol{n}}_i\right\rangle + \frac{\mu_t}{2}\sum_{i,j,\alpha}\left\langle \boldsymbol{F}_{ij}^c \Delta \boldsymbol{r}_{ij}\right\rangle + 2ND_0 + \frac{\mu_t}{2}\sum_{i,j,\alpha}\left\langle \boldsymbol{F}_{ij}^c \cdot \boldsymbol{R_u}\right\rangle \tag{2.13}$$

Equation (2.13) introduces a collection of either internal and external virial functions:

$$G^i(t) = \frac{v_0}{2\mu_t}\sum_i \boldsymbol{n}_i(t)\cdot \boldsymbol{r}_i(t) + \frac{1}{4}\sum_{i,j,\alpha}\boldsymbol{F}_{ij}^c \Delta \boldsymbol{r}_{ij} \tag{2.14}$$

$$G^e(t) = -\frac{1}{4}\sum_{i,j,\alpha}\boldsymbol{F}_{ij}^c \cdot \boldsymbol{R_u} \tag{2.15}$$

Then, the instantaneous internal, and external pressure is

$$\Pi^i(t) = \rho k_B T + G^i(t)/S =, \quad P^i = \lim_{t\to\infty}\left\langle \Pi^i(t)\right\rangle \tag{2.16}$$

$$\Pi^e(t) = \rho D - G^e/S, \quad P^e = \lim_{t\to\infty}\left\langle \Pi^e(t)\right\rangle \tag{2.17}$$

The internal pressure in the system has a thermal source $P_0^i = P_0 = \rho k_B T$ which can be translated to the surface packing fraction $P_0 = 4/\pi\phi k_B T$, an interaction source $P_{int}^i = P_{int}$ which accounts for the pair interactions and it is the same as in equilibrium, and finally an active contribution $P_a^i = P_a$.

$$\begin{aligned}P_{int} =& \frac{1}{4L^2}\sum_{i,j}\left\langle \boldsymbol{F}_{ij}\cdot \Delta \boldsymbol{r}_{ij}\right\rangle \\ P_a =& \frac{v_0}{2\mu_t L^2}\sum_i \left\langle \hat{\boldsymbol{n}}_i \cdot \boldsymbol{r}_i\right\rangle = \rho\frac{v_0 v(\rho)}{2\mu_t D_r}\end{aligned} \tag{2.18}$$

For a system without pair interactions the active pressure P_a can be easily computed. The integration of the movement gives

$$\boldsymbol{r}_i(t) = \boldsymbol{r}_i(0) + v_0\int_0^t \hat{\boldsymbol{n}}_i(t') + \int_0^t \sqrt{2D_t}\boldsymbol{\xi} \tag{2.19}$$

Substituting the trajectory

$$P_a = \frac{v_0}{2\mu_t L^2} \sum_i \langle \hat{\boldsymbol{n}}_i \cdot \boldsymbol{r}_i(t) \rangle = \bar{\rho} \frac{v_0^2}{2\mu_t} \frac{1}{D_r} = \rho \frac{v_0^2}{2D_t D_r} k_B T \tag{2.20}$$

And from (**??**) we observe a enhanced diffusivity for a system of active particles $D = D_t + \rho v_0^2/(2D_r)$. Active Brownian Particles do not introduce torque in neither pair interactions nor wall collisions. This simple, and exclusive, characteristic of ABPs, and following the work of [Solon et al., 2015d, Solon et al., 2015b], we state that pressure is a state function, and thus, ideal to study MIPS for ABP.

2.3.1 Measures of the Pressure

We measure the total pressure of a system undergoing the MIPS transition. We quench a system in thermal equilibrium to a state at $Pe \neq 0$. In Figure 2.9 we show the quench and values for the instantaneous $\Pi(t)$.

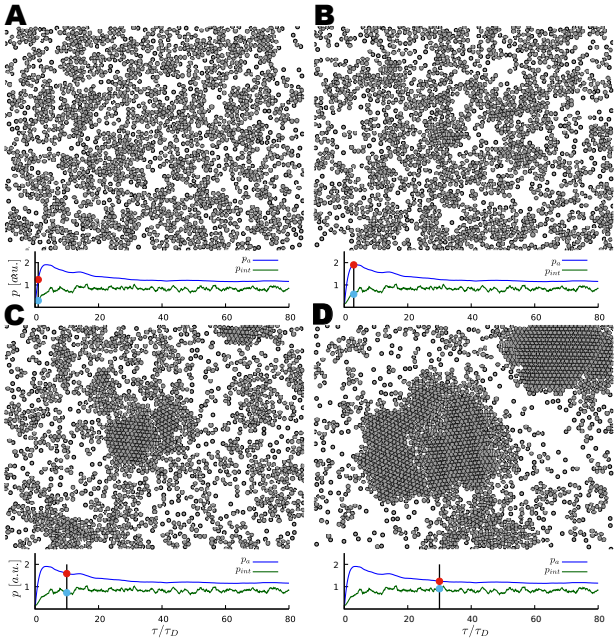

Figure 2.9 | Evolution of the total pressure during MIPS. Snapshots of the system at different time from the activity quench. We plot times $\tau/\tau_D = 1$, 3, 10, and 30 in **A**, **B**, **C**, and **D** respectively. In the first plot we observe a rapid increase of the activity pressure. Later the interaction pressure increases and stops the rise of P_a to the ideal gas value.

We observe an initial fast increase of the active pressure, active particles travel at unperturbed velocities close to v_0. As collisions occur the interaction pressure rises, local density increases and the $v(\rho)$ dependence triggers MIPS. We observe the decrease of active pressure, and its decay to the steady value.

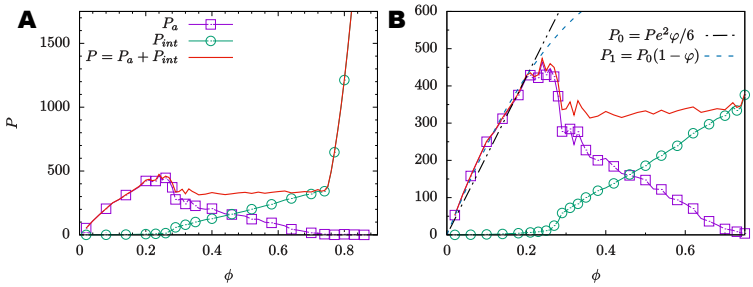

Figure 2.10 | Pressure across MIPS. Equation of state of ABP. Active, interaction and total pressure of the steady state after an activity quench to $Pe = 100$ for a system of $N = 1250$ ABP particles with $\epsilon = 250$, the onset of MIPS determines the pressure drom at $\phi_n \approx 0.3$. **A** divergence of the pressure at high ϕ indicate the crystal formation. **B** comparison with $P_0 = Pe^2\varphi/6$, and $P = P_0(1-\varphi)$ at the gas phase. Note the constant pressure across the MIPS coexistence.

2.3.2 Pressure across MIPS

The study the phase behaviour of MIPS by evolving the system from a homogeneous initial state at total packing density ϕ towards a steady state at a finite value of Pe, we quench the equilibrium system into the active system. We compare the results in systems confined between two parallel walls in y, and PBC in x, and systems with PBC in x, and y.

As previously mentioned, in an activity quench with PBC we observe a pressure drop around $\phi = \phi_n$, the transition is triggered and the active pressure drops. Beyond ϕ_n the active component of the pressure P_a diminishes as the interaction pressure increases P_{int}. The more particles in the dense region the lower the active pressure. Propulsion in the dense region is converted into interaction pressure and thus the exchange of pressure between P_a, and P_{int} while the total pressure is kept constant $P = P_a + P_{int}$.

Pressure, $P(\phi; Pe)$, as a function of density for different Péclet numbers can be found in Figure 2.12. For systems with $Pe < Pe_c \approx 16.7$ we observe a monotonous growth of P as a function of density, and computations in a confined system coincide with the results from a confined system. At higher activities, for PBC the pressure drops in the vicinity of MIPS. Pressure calculations in a confined system at low densities are blow their PBC counterpart; it diverts the PBC and follows a monotonous growth until ϕ_n where it saturates and coincides with the PBC situations. The presence of walls facilitates, and triggers MIPS below ϕ_n.

The equations of state in confined and PBC systems converge at large densities to a value close to the expected coexistence pressure. In equilibrium, finite-size

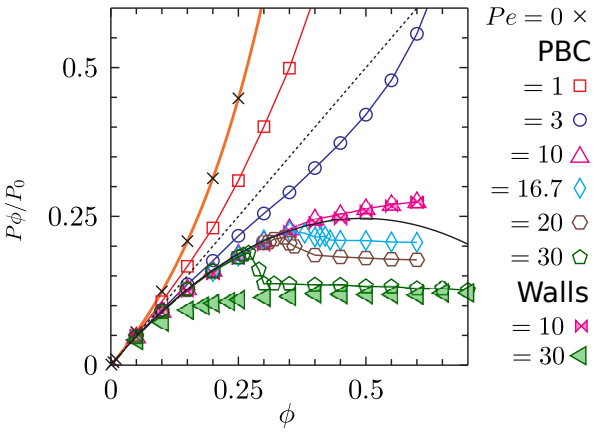

Figure 2.11 | Equations of State for . arg2

Figure 2.12 | Total pressure divided by the ideal ABP pressure. In hollow points the pressure calculations for PBC systems. In filled points the calculations for a system confined between two walls.

systems displat a pressure loop due to the formation of an interface between the two phases, while the loop arising in van der Waals theory is thermodynamically unstable [Mayer and Wood, 1965, Schrader et al., 2009]. Accordingly, $P(\phi)$ shows a peak when the dense phase develops, an effect that should disappear in the large N limit. The sharp pressure drop for ABP Hard Disks, and stiff ABPs indicates that interfacial fluctuations are considerably suppressed, ans suggests a large interface tension. Considering ABPs with lower values of ϵ the pressure drop is smoothed so is the structure of the dense phase, as it is clear from Figure 2.8. Hence, we interpret the pressure drop for PBC systems as a finite size effect. The idea behind this pressure jump is that MIPS involves a large, and persistent critical nucleus of size m_c to develop. Thus, systems are too small to phase separate close to the binodal low density and remain metastable.

The pressure drop has its origin in an excess of active pressure. The measure protocol, a high-activity quench, drives the system into a metastable gas phase which cannot be relaxed in a reasonable amount of time. For densities $\phi_{low} < \phi < \phi_n$ the system remains in the gas phase at ϕ instead of phase separating into ϕ_{low}, and ϕ_{high}. Then, $P(\phi; Pe)$ curves with the pressure drop do not correspond to Equations of State (EoS).

2.3.3 Metastability

To access the phase separated region for intermediate densities $\phi_{low} < \phi < \phi_n$ in a PBC geometry we propose a gradual succession of low-density quenches from an already phase separated system deep into MIPS. As we expand the system, nucleation is avoided since an interface between a dense and a low density phase is already present in the system. To enlarge the system in a PBC geometry we need to avoid splitting the dense phase. We prepare the initial configuration in a rectangular PBC box with a size ratio $L_x/L_y = 25/16$. The expansion is performed in the

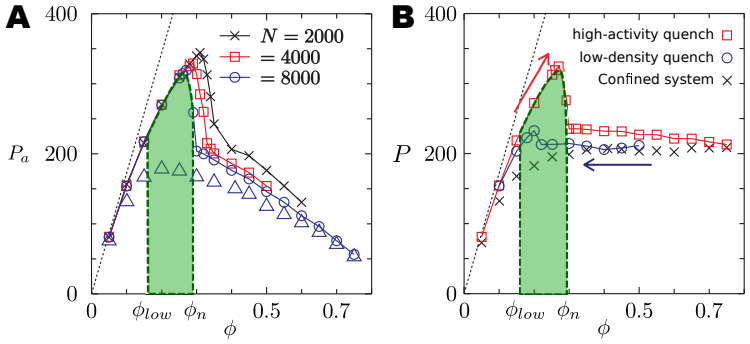

Figure 2.13 | A Active pressure at $Pe = 30$ for systems of $N = 2000$, 4000, and 8000 particles; pressure drop present in all systems. **B** Total pressure at $Pe = 30$ for a system of $N = 4000$ particles. In red squares the pressure at steady state for a high-activity quench. In blue circles the pressure at steady state for a low-activity quench. In black points the pressure with confining walls. The region between the low density ϕ_{low}, and the density of MIPS onset ϕ_n is green shadowed.

longest side so that the dense phase is not broken.

Following expansion protocol we present the pressure across MIPS in Figure 2.13**B**. For high-activity quenches, red points, we identify the pressure drop at ϕ_n. For low-density successive quenches, blue points, we obtain a constant value of the pressure which coincides with the calculations in the confined geometry for densities above the nucleation density $\phi > \phi_n$. Once below ϕ_n the pressure remains constant and the system phase separated. At low densities $\phi \approx_{low}$ the large density phase is evaporated and finally a gas remains. The $P(\phi; Pe)$ curves obtained by low-density quenches explore the phase separated region for $\phi_{low} < \phi < \phi_n$, and are the EoS of ABP.

According to classical nucleation theory (CNT), in the absence of a preferential site (homogeneous nucleation), phase separation can only be triggered by a rare event: the spontaneous formation of a critical nucleus of size larger than $m_c \propto \gamma/\Delta G_{homo}$, where γ is the interface tension and ΔG_{homo} the free energy difference. Since our system is not in equilibrium we cannot apply CNT directly. However, we borrow ideas from equilibrium systems. Redner *et al.* have developed an analogous theory to describe the kinetics of phase separation in ABP [Redner et al., 2016]. Within this framework, the critical nucleus size scales $m_c \propto \phi_{cp} \ln^2(Pe\phi_{low})$. Therefore, m_c is expected to be very large at high Pe. As shown in Figures 2.8, and 2.7 soft ABP suppresses the order of the dense phase and reduces the energy difference between phases. In turn, there is an observable increases of ϕ_{low}, as seen in Figure 2.5, thus m_c is smaller and so is the pressure drop in the onset of MIPS.

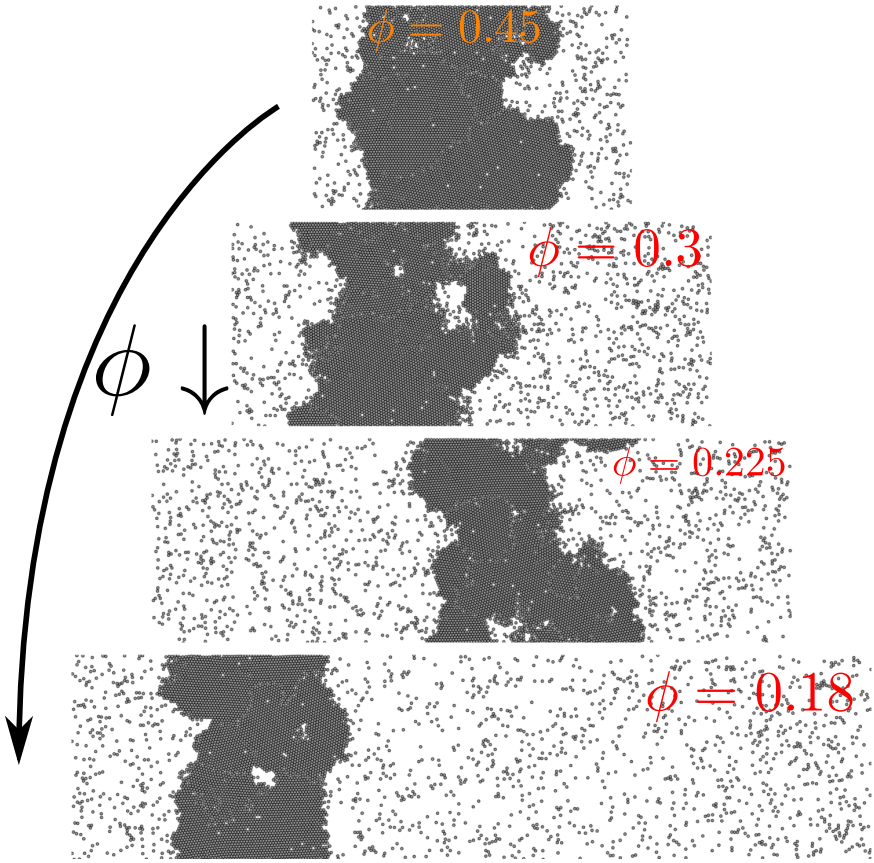

Figure 2.14 | Sequence of low-density quenches. From $\phi = 0.45$ we increase the size of the simulation rectangle to gradually reduce the density until $\phi = 0.18$ where the dense phase remains stable, and in coexistence with the gas phase.

After a series of low-density quenches, from an initial configuration at $\phi = 0.45$ we gradually descend to densities $\phi = 0.18$. In Figure 2.14 we have prepared an initial sample of $N = 6000$ particles at $Pe = 64$ density $\phi = 0.45$. The size of the dense phase is large and we shall not split it when we quench the system to lower densities, for this reason we start in a rectangular box of size ratio $L_x/L_y = (5/4)^2$, and low-density quench the system by increasing L_x to achieve the desired density ϕ.

At $Pe = 64$ the onset of MIPS for high-activity quenches is situated at $\phi \approx 0.25$. After three successive low-density quenches, at $\phi = 0.3$, $\phi = 0.225$, and $\phi = 0.18$ we observe the persistence, and stability of the already phase separated particles. We observe the typical exchange of particles within the dense and fluid phases and the breaking and reformation of huge chunks of the dense phase. Once formed and with a size higher than the critical size, the dense phase remains stable for $\phi_{low} < \phi < \phi_n$.

2.4 Conclusions and perspectives

In the development of this chapter we have exploited the recently develop formalism of the active pressure for ABP and the possibility to construct an equation of state to study and analyse the Motility Induced Phase Separation (MIPS). We have related the pressure drop previously identified as the onset of the phase separation. We have identified the metastability region and measured the pressure following different preparation protocols. By quenching an already phase separated system to lower densities we have accessed to phase separated systems for densities below the onset, ϕ_n, of MIPS obtained by high-activity quenches. Pressure calculations below ϕ_n reveal the continuity of the equation of state and the origin of the pressure drop.

In the absence of a preferential site for nucleation the triggering of the phase separation relies on a rare event, the formation of a cluster of a critical size m_c, and its stability for a finite time. By low-density quenches the dense phase separated ABP provide the nucleation site and MIPS is effectively sustained at $\phi_{low} < \phi < \phi_n$. The lower pressure of the phase separated system confirms it as the stable state of the system, and its pressure to the equation of state of ABPs. Total pressure of ABP stays approximately constant along MIPS, and confirms its role as the true EoS. The introduction of a solid wall triggers the phase separation and banishes the pressure jump associated to the dramatic onsef of MIPS since the particle accumulation on the walls is gradual as ϕ is increased.

We have considered the influence of the hardness of the repulsive interaction between Active Particles and its role in both the phase separation and the structure of the dense phase of ABPs. Soft WCA potentials allow large overlaps for of the ABP so that the crystalline order measured for Hard Spheres is completely lost. We then emphasize the role of repulsion in MIPS, the need for a rapidly decaying $v(\rho)$.

In this chapter we have presented the density phase separation introduced by the confinement with a wall. In the past it has been reported the wall accumulation for small Pe, and bulk densities in order to emphasize the abilities of the wall to generate a remarkable density profile, and particle accumulation. The structure and dynamic properties of the dense layer remain to be studied. Height fluctuations, and correlations $\langle h(x)h(x+\Delta x)\rangle$, and its interaction with the insertion of passive bodies, which is briefly introduced in Chapter 3.

The existence of a critical nucleation size has brought us to consider further simulations with metastable ABP gas preparations and crystalline Lennard-Jones seeds of different sizes. With a precursor for the density phase separation we can study the dynamics of the phase separation below the spinodal line defined by $\phi < \phi_n$.

Appendices

2.A Cluster distribution of ABPs

A long simulation of ABPs in the gas region would phase separate in the presence of an ABP cluster of a critical size. To study the timescales involved in the formation of such a macroscopic cluster we have analysed the cluster size distributions in an ABP metastable gas.

The predicted cluster size distribution $P(m)$ decays exponentially with an additional m^{-2} contribution [Redner et al., 2016].

$$P(m) = \exp(-m/m^*)/m^2 \tag{2.A.1}$$

In Figure 2.A.1 we present the results for $N = 2000$ ABPs at different Pe, and ϵ. We define a cutoff distace $r < r_c = 1.1\sigma$ to determine whether two neighbouring particles belong to the same cluster. Statistics is carried out in 2000 rotational diffusion times the sampling times larger than the translational time $\tau_t \approx Pe^{-1}$.

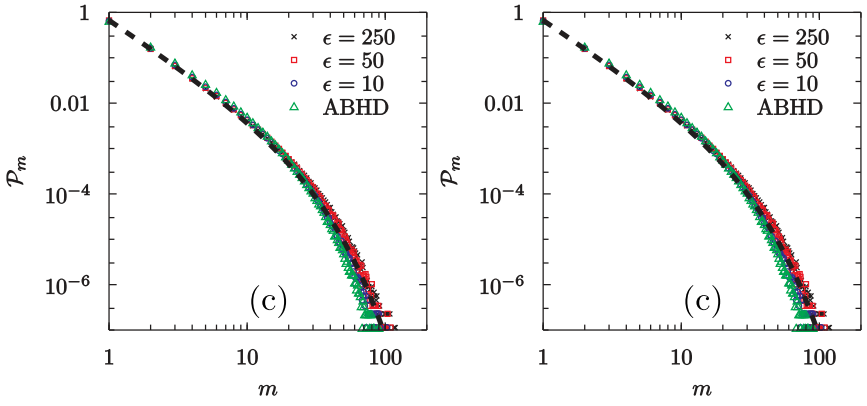

Figure 2.A.1 | Cluster size distribution for ABPs at the metastable gas region in a PBC box, $\phi = 0.2$. With $N = 2000$ particles we present A $Pe = 60$, and **B** $Pe = 100$. Black dotted line the theoretical fit $P(m)$ with fitting parameter $m^* = 14.5$

3

A Bath of Active Particles

In the previous chapter we have studied the emergent phenomenology in systems of Active Brownian Particles. For a system of purely repulsive ABP we described a density phase separation and the tools that have been recently developed. We now focus on the mechanical properties of a bath of active particles and their interaction between passive objects.

As briefly introduced in the Introduction to this thesis, the first approach to the interaction between active and passive systems was the seminal work of [Wu and Libchaber, 2000]. In their experiments, bacteria acted as active particles, and colloids where their passive counterpart. The persistence of swimming in the collisions with the passive objects were responsible of the enhanced diffusivity of the passive colloids. Then, [Angelani et al., 2011] presented numerical results for the structure of passive particles immersed in a bath of bacteria. The striking results of the simulations were an effective attraction between passive particles manifested in the pair correlation functions. More recently, [Speck and Jack, 2016, Harder et al., 2014b] have considered the problem for an inclusion in ABP suspensions.

Elongated particles, such as bacteria, introduce angular interactions between pairs. Relative orientation is not present in the majority of ABP models, except for some exceptions [Grossmann et al., 2012], in the literature. Alignment has recently been introduced in the form of a Kuramoto-like interaction between ABP [Martin-Gomez et al., 2018]. In this Chapter we introduce aligning active brownian particles (**AAP**) as a hybrid system that combines excluded volume interactions from ABPs, described in Chapter 2, and aligning interactions from Vicsek-like models.

In the first part of the Chapter, we study the bath in the absence of passive particles. We begin presenting a model of active particles with aligning interactions in 3.1. We motivate the need for an aligning interaction presenting a set of systems which naturally align: dumbbells, and swimmers. Once the model is defined and justified, we characterise the emergent structures in the active bath 3.2.3. Explore the differences between AAP and ABP.

In the second part of the chapter, we introduce passive particles and focus on the interaction between pairs of inclusions. We analyse the emergent forces and discuss their possible many-body consequences, and we measure them. Finally, and due to the importance of the confining walls in active systems [Levis et al., 2017] we repeat the measures in the vicinity of confining walls in 3.3.4, and 3.4.

3.1 Alignment in Active Particles

In the general introduction to this thesis we have commented on the emergent interactions that ABP particles induce on passive colloids [Harder et al., 2014b], and the apparent attraction between inclusions in a bacterial bath [Angelani et al., 2011]. In this sections we introduce a model for elongated particles, the dumbbells, and a model for swimming bacteria. Both models introduce the concept of angular interactions in the propulsion direction and justify the introduction in our model of aligning interaction between Active Brownian Particles in order to connect the aforementioned results on activity-induced of active particles in colloidal dispersions.

3.1.1 Active Dumbbells

We consider a dry active model, a model without hydrodynamics. Active dumbbells are a minimal model for elongated dry active particles, and can be easily extended to active self-propelling chains [Wensink and Löwen, 2008].

The specifics of the model are given in 3.B. A dumbbell is defined as a pair of brownian repulsive disks or spheres connected by an elastic constrain. Typically, the separation between centres, the rest length of the elastic force, corresponds to the diameter of the disks, disks are at contact.

3.1.2 Squirmers

The squirmer model firstly introduced by [Lighthill, 1952] and completed by [Blake, 1971] has widely been used for numerical studies involving suspensions of microswimmers. The squirmer model captures the hydrodynamics of a spherical particle whose propulsion mechanism consists in implementing a slip velocity along its surface. By moving cilia, and the generation of metachronal waves, paramecia swim at low Reynolds numbers.

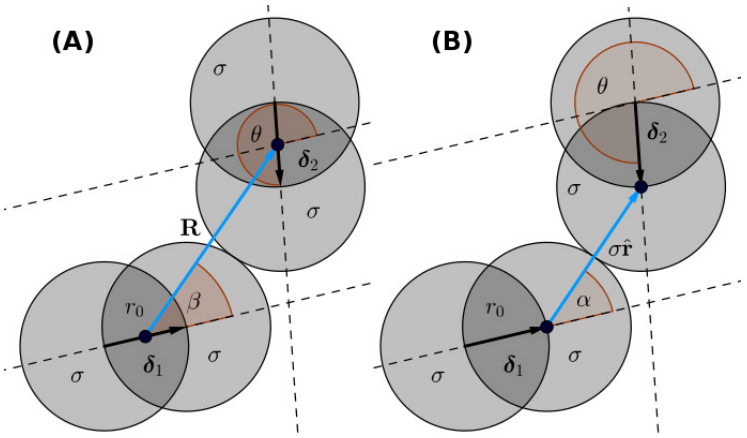

Figure 3.1 | Collision between a pair of dumbbells with director vectors $\hat{\boldsymbol{\delta}}_1$, and $\hat{\boldsymbol{\delta}}_2$. Vector $\boldsymbol{u} = \hat{\boldsymbol{\delta}}_2 - \hat{\boldsymbol{\delta}}_1$ defines the angle θ. **(A)** Interaction relative to the center of mass of each dumbbell, center-to-center vector $\boldsymbol{R}$ with norm d and angle β relative to θ_1. **(B)** Interaction relative to the center of each bead of the dumbbell with the angle α.

The squirmer model is a multipolar expansion which retains its first two terms B_1, and B_2. The velocity field generated by a squirmer at a position $\boldsymbol{r}$ away from its center of mass is given by

$$\boldsymbol{u} = \left(-\frac{1}{3}\boldsymbol{e} + \frac{\boldsymbol{e}\cdot\boldsymbol{r}}{r}\frac{\boldsymbol{r}}{r}\right)\left(\frac{R}{r}\right)^3 B_1 - \left[3\left(\frac{\boldsymbol{e}\cdot\boldsymbol{r}}{r}\right)^2 - \frac{\boldsymbol{r}}{r}\right]\left(\frac{R}{r}\right)^2 B_2 \tag{3.1}$$

The firt term B_1 is associated to the propulsion velocity of the particle in the direction $\boldsymbol{e}$ with velocity of the centre of mass $\boldsymbol{U} = 2/3B_1\boldsymbol{e}$. The second term, B_2, is associated to the stress generation. A squirmer of radius R in a fluid with viscosity η, generates a stresslet of strength $\boldsymbol{\Sigma} = 4/3\pi\eta R^2\,(3\boldsymbol{ee} - 1)$. The algae, bacteria, and self-propelled Janus particle can be modeled by squirmers [Bickel et al., 2013].

The squirmer model can also be introduced in a much more fundamental and compact way. The fundamental solutions of Stokes equations constitute a good basis to model a general swimmer. For each multipolar term can be interpreted as a body force, dipolar force, body torque, etc. A clear description of the multipolar expansion can be found in [Lauga and Powers, 2009]. For completeness we write down the equations for the velocity field generated by a squirmer in terms of different multipoles.

$$\boldsymbol{u} = \frac{R^3}{3}B_1\boldsymbol{D} - a^2 B_2\mathbf{G}_{\mathbf{D}} \tag{3.2}$$

In this way we can introduce microswimmers as a combination of multipoles, like the *Chlamydomonas reinhardtii* in Figure 3.2.

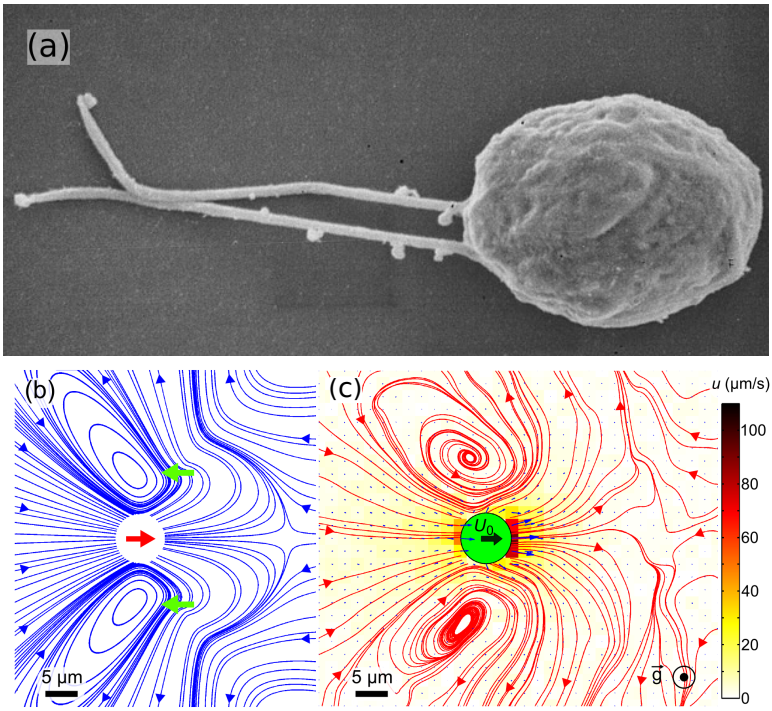

Figure 3.2 | The alga *Chlamydomonas reinhardtii* can be easily modelled as a combination of forces at different points. In **(a)** the image of a chlamy: the body and the two oars [Silflow and Lefebvre, 2001]. In **(b)** the three point force model with the extracted experimental data from **(c)** [Drescher et al., 2010]

Hydodynamic interaction between squirmers

The hydrodynamical description of the microswimmer naturally introduces interactions at a distance. The flow field developed by a particle interacts with the neighbouring objects in the fluid. A classical calculation given by Faxen's laws [Durlofsky et al., 1987] can be applied to compute the interaction between a squirmer pair. The relults from [Ishikawa et al., 2006] indicate the appearance of an interaction torque at short distances. However, the timescales associated to the reorientation when compared to the purely hydrodynamic repulsion were found to be negligible [Llopis and Pagonabarraga, 2010]. On the other hand, when swimming close to walls emergent torques are relevant and the swimmer-wall interaction introduces a torque to the swimmer.

The artificial jannus swimmers such as [Palacci et al., 2013b] develop a hydrodynamic field which can be expanded in terms of the squirmer model [Michelin and Lauga, 2014]. In those systems emergent hydrodynamic torques could be of a certain relevance, specially for heavy jannus colloids that swim close to the bottom

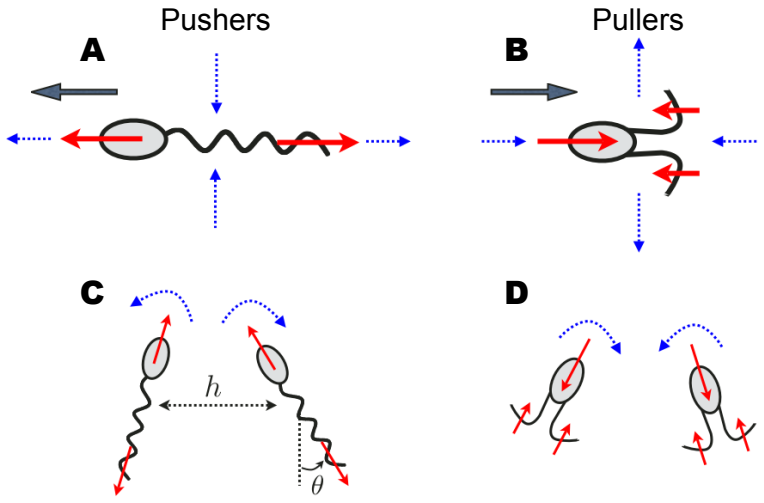

Figure 3.3 | Schematic representation of a pusher and puller squirmers. Red arrows represent the force dipoles exerted to the fluid and blue dotted arrows the qualitative direction of the fluid around the swimmer. A, and **B** depict a pusher and a puller, respectively. In **C** two pushers with converging trajectories reorient each other tending to a final configuration of the two agents swimming parallel. In **D** two pullers diverging from collision reorient towards an antiparallel configuration, image from [Lauga and Powers, 2009]

wall of the system.

3.2 Aligning Active Particles

In this section we present a model system for dry self-propelled disks interacting with pairwise repulsive and aligning potential interactions. Then, we reduce the parameters to a set of dimensionless magnitudes. Finally, we present the different emergent structures that develop in a system of Aligning Active Particles.

3.2.1 A Minimal model

We consider a two dimensional system, $L \times L$, with periodic boundaries (PBC) of colloidal self-propelled particles of diameter σ_a. The starting model for AAP departs from ABP, already presented in equations (2.3). Positions of AAP, $\boldsymbol{r}$ are evolved according to a Langevin equation of motion at a temperature T (3.3), and diffusion $D_t = k_B T \mu_t$. AAP interact with a repulsive conservative force $\boldsymbol{F}_i^c$, to account for excluded volume.

Activity is introduced by means of a constant velocity v_a acting on a direction $\boldsymbol{n} = (\cos\theta, \sin\theta)$. The new feature presented in (3.3) is the aligning interactions.

For AAP the equation for the orientation vector $\hat{\boldsymbol{n}}_i$ has two terms. The first one is a diffusive behaviour, with a rotational diffusion constant D_r. Rotational diffusion is ubiquitous in all models of the literature, from the original Vicsek Model in [Vicsek et al., 1995], to their variations [Czirók et al., 1997], and the subsequent ABP models [ten Hagen et al., 2011, Bialké et al., 2012]. While the second one is an aligning torque, ubiquitous in the "swimming together" models (3.3) but rarely explored in Active Bownian systems, until recently [Martin-Gomez et al., 2018]. The source of alignment is discussed later in Section 3.1. Its origin can be due to hydrodynamic interaction [Ishikawa et al., 2006], excluded volume interactions [Baskaran and Marchetti, 2008], or can emerge from a sensing [**?**], or taxis [Durham et al., 2009], of the micro-organisms or microcolloids.

$$\begin{cases} \dfrac{d\boldsymbol{r}_i(t)}{dt} = v_a \hat{\boldsymbol{n}}_i(t) + \mu_t \boldsymbol{F}_i^c(t) + \sqrt{2D_t}\boldsymbol{\xi}_i^t(t) \\ \dfrac{d\theta_i(t)}{dt} = \mu_r \Gamma_i(t) + \sqrt{2D_r}\nu_i^r \end{cases} \tag{3.3}$$

The interaction between particles is introduced in terms of a conservative pairwise repulsive potential $U(r)$, preferably a WCA potential with a forces described in (2.7) and a cut-off distance $r_c = 2^{1/6}\sigma_a$. Torque on each particle (3.4) aligns its orientation vector parallel to a generic unit vector $\boldsymbol{e}_j$ characteristic of the j-th particle. In a Kuramoto-like interaction we use $\hat{\boldsymbol{e}}_j = \hat{\boldsymbol{n}}_j$, *i-th* particle aligns with the orientation of the *j-th* particle. More biological motivated interactions for cells in tissues use $\hat{\boldsymbol{e}}_j = -\hat{\boldsymbol{r}}_{ij}$ [Smeets et al., 2016], where the orientation of the particle aligns in the opposite direction of the centre to centre unit vector.

$$\Gamma_i = -\frac{\Gamma_0}{\pi R_\theta^2} \sum_{j \neq i} (\boldsymbol{e}_j \times \hat{\boldsymbol{n}}_i) \cdot \hat{\boldsymbol{z}} = \frac{\Gamma_0}{\pi r_c^2} \sum_{j \neq i} \sin(\theta_{ij}) \tag{3.4}$$

Where Γ_0 is the strength of the torque and R_θ is the extend of the interaction. We introduce the torque in a vectorial form for polar interactions. In section 3.B.1 we introduce a nematic interaction which could be simplified to its 2d form $\sin 2\theta_{ij}$ instead of the general vectorial form. For the aligning active disks we set the interaction towards the neighbouring orientation vectors and extend the interaction in the range of the repulsive interaction given by $|\boldsymbol{r}_{ij}| < r_c = 2^{1/6}\sigma_a$.

Forces $\boldsymbol{F}_i$ and torques Γ_i are related to the velocities $\dot{\boldsymbol{r}}$, and torques $\dot{\theta}$ by the translational and rotational mobilities, μ_t and μ_r. The thermal bath is modelled by means of two stochastic terms $\boldsymbol{\xi}_i^t$ and ν_i. Noise is assumed to be gaussian with zero mean and variance proportional to the mobilities μ_t and μ_r. The addition of v_a breaks time reversal symmetry and thus detailed valance. To mantain the model as simple as possible, we hold the equilibrium relation between mobilities μ_r and μ_t through the size of the particle σ so that $\mu_t = \sigma^2 \mu_r / 3$.

3.2.2 Dimensionless relevant parameters

In Section 2.2.1 we presented the dimensionless relevant parameters for a system of ABPs. To extend this to AAP we need to identify the temporal scale associated to the alignment interactions in (3.4).

$$\tau_p = \frac{\sigma_a}{v_a}, \quad \tau_g = \frac{\pi R_\theta^2}{\mu_r \Gamma_0}, \quad \tau_t = \frac{\sigma_a^2}{D_t}, \quad \tau_r = \frac{1}{D_r} \tag{3.5}$$

Where we identify the timescales for: propulsion τ_p, alignment τ_g, diffusion τ_t, and angular diffusion τ_r. With this temporal scales the equations for AAP read,

$$\begin{cases} \dfrac{d\boldsymbol{r}_i(\tau)}{d\tau} = Pe\hat{\boldsymbol{n}}_i(\tau) + \dfrac{\epsilon}{3}\boldsymbol{F}_i^c(\tau) + \sqrt{2/3}\boldsymbol{\xi}(\tau) \\ \dfrac{d\theta(\tau)}{d\tau} = g\Gamma_i(\tau) + \sqrt{2}\nu_i(\tau) \end{cases} \tag{3.6}$$

Where we keep the definition for the Péclet Number $Pe = v_a/(\sigma D_r)$ that relates the propulsion time scale to the angular diffusion reorientation time. And the new Aligning Number $g = \Gamma_0/K_B T$ that compares the diffusion reorientation of the sphere to the aligning torque. In this Chapter we will essentially study the system under changes in Pe, and g at a fixed density of active particles.

3.2.3 Emergent structures in AAP

In the last chapter we introduced the motility induced phase separation (MIPS) which ABP at moderate densities undergo as activity increases. In a system of Aligning Active Particles the emergence of global ordering prevents the aggregation though a MIPS mechanism. Colliding particles will reorient and navigate in the same direction, eventually, at full speed v_a. In Figure 3.4 we compare a collision between ABPs and AAPs.

On one hand, collisions between ABP generate clusters whose centre of mass velocity $v_{cm} < v_a$. The lifespan of a cluster of a few particles depends on the diffusion of the orientations $\hat{n}_i$, and scales with the number of particles in the border of the cluster. On the other hand, collisions between AAP generate clusters whose centre of mass velocity v_{cm} increases as the respective orientations align in the same direction until saturation $v_{cm} \approx v_a$ for a polarized cluster. The lifespan of a cluster of aligned particles depends on the competition between aligning torque g and the diffusion of $\boldsymbol{n}$, and scales with the number of particles in the cluster.

To investigate the collective behaviour of aligning particles we need to stablish both a clustering and polarization criterion. We study the structure factor $S(q)$ to determine the density separation into a dense and diluted phases and global polar

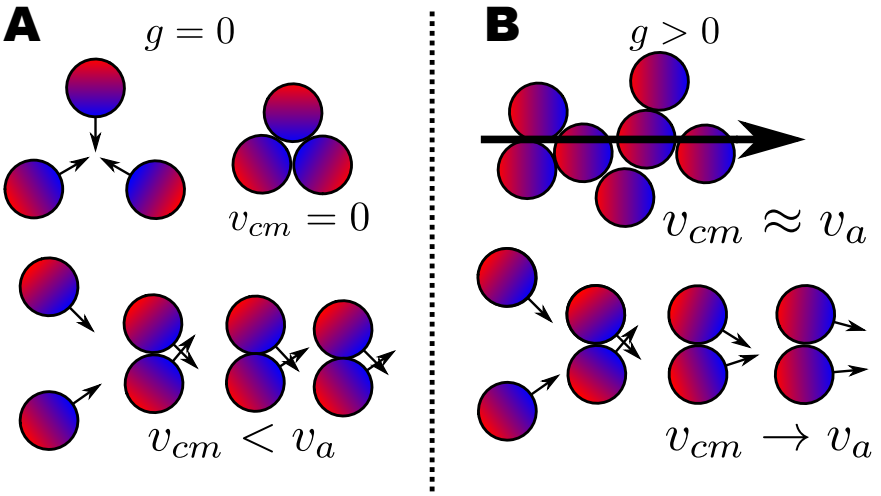

Figure 3.4| A. Interaction between ABP. A collision between a pair maintains the orientation of each particle until rotational diffusion allows them to escape. The velocity of the centre of mass of a large cluster of ABP $v_{cm} \approx 0$, since $v(\rho)$ goes to zero.**B** Interaction between AAP: in the interaction velocities reorient due to the aligning torque and the pair reaches the active velocity. Large clusters are characterized by a polarization that diffuses in time and move at $v_{cm} \approx v_a$

order parameter $\Psi(t)$, as defined in (3.7), to study the alignment of the system.

$$\Psi(t) = \frac{1}{N} \left\| \sum_{i}^{N} \hat{\boldsymbol{n}}_i(t) \right\| \tag{3.7}$$

The limiting values for the polar order parameter are $\Psi \approx 1/\sqrt{N}$ for a randomly oriented system, and $\Psi \approx 1$ for a system whose particles travel in the same direction. With the information of the structure factor we can distinguish between a phase in a cluster regime, and a density separated scenario which is then classified into a disordered static cluster for $\Psi \approx 0$, or a large travelling aligned cluster for $\Psi \approx 1$.

At a density of aligning particles $\phi = 0.1$ a system quenched from equilibrium to a finite Pe does not undego a Motility Induced Phase Separation. In the ABP phase diagram $\phi_g < \phi < \phi_n$, where $\phi(Pe)$ is the density in which the spinodal decomposition is triggered at a given Pe, and ϕ_b the density defined by the low-density binodal line. In [Martin-Gomez et al., 2018] authors distinguish between a Disordered state (D) situated at the left of the red squares in Figure 3.5. At the right side of the disordered phase, approximately above $g = 0.2$ the system develops a global order. It segregates into polar Flocks of particles. At the right side of the green circles in Figure 3.5 the system forms a macroscopic polar cluster. At high Pe the formation of the macroscopic cluster is suppressed and the system is constituted by microscopic polar clusters.

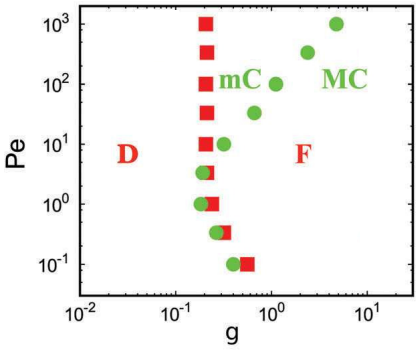

Figure 3.5 | Phase diagram for the aligning active particles at packing fraction $\phi = 0.1$ for various Pe, and g with $r_c \approx 2\sigma_a$. At $\phi_a = 0.1$ authors identify a Disordered state (D), and a Flocking regime (F). Between red and green dots the system develops global order but not a macroscopic cluster. Image courtesy of [Martin-Gomez et al., 2018]

In Figure 3.6 we present typical snapshots of the system at different regions of the pahse diagram (Pe, g). As compared to [Martin-Gomez et al., 2018] we use a shorter aligning range, $r_c = 2^{1/6}\sigma_a < 2\sigma_a$; the match of the aligning range with the repulsive range prevents the formation of an aligned macroscopic cluster at low values of Pe. We increased the density to $\phi = 0.18$, which is still below the MIPS spinodal decomposition. In (a) we observe an aligned suspension of AAP with several travelling clusters. In (b-c) we observe larger clusters but AAP are less compact and thus alignment does not completely align the whole structures. Finally, in (d) we observe a system at small g where collisions are stronger and does not align AAP, for a density $\phi > \phi_s$ the system would undergo a density separation controlled by MIPS. In the studied range we do not appreciate the formation of a large, and sole macroscopic cluster, travelling cluster due to the decrease of the aligning range.

We previously introduced the tools to quantify the state of the system. We analyse the structure factor and the global order parameter in Figure 3.7. We observe a q^{-2} divergence for systems (a-c) which is compatible with the cluster formation. The peak of $S(q)$ close to $q = 2\pi/\sigma$ is shifted to lower values of the wave vector for system (c), which is compatible with the increase of pair distances observed in the insets. Figure 3.7 shows the temporal evolution of global order. At large Pe the system rapidly reaches a stationary value. Particles travel fast and wipe and order the whole system. At low values of the Pe the competition between alignment and propulsion is dominated by alignment and particles orient before reaching interparticle distances close to σ_a. The repulsive potential easily separates the pair beyond aligning range and then thermal fluctuations disalign them. This process of formation and destruction introduce large fluctuations of $\Psi(t)$ in the steady state.

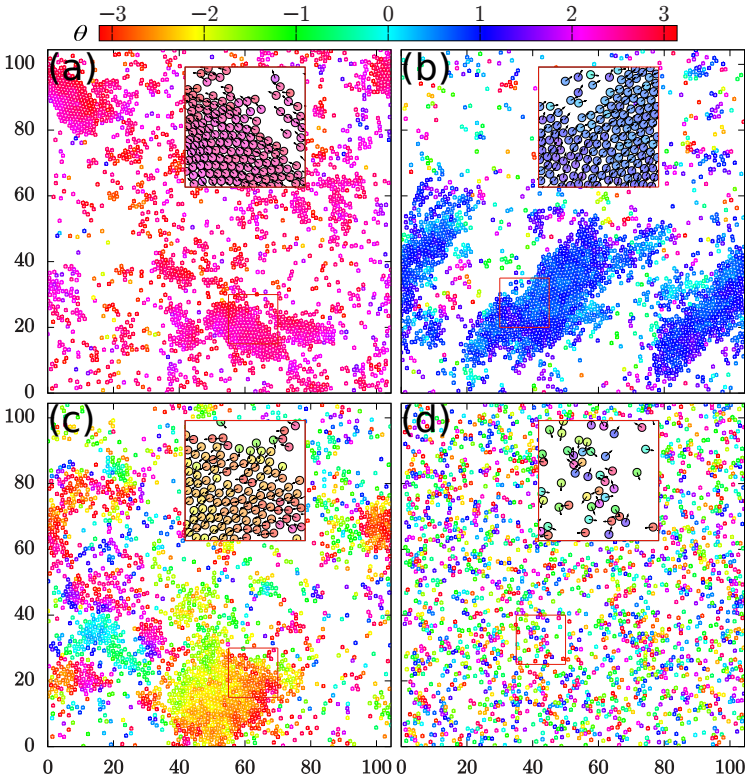

Figure 3.6 | Representative snapshots of the system for several parameters. Given the coordinates (Pe, g, ϕ); system (a) is $(50, 30, 0.18)$, system (b) is $(10, 30, 0.18)$, system (c) is $(3, 30, 0.18)$, and system (d) is $(30, 0.1, 0.18)$. Insets depict a magnified image of the high density region.

3.2.4 Comparison between ABP and AAP dense phases

In the last section we have included the analysis of the structure of a gas phase of ABP and AAP. The formation mechanism of the high density phase of AAP is completely different from the ABP separation, as we have already discussed. The local structure of ABP and AAP at high density regions has two major differences.

First, in ABP the local structure is hexagonal; though depends on the choice of ϵ. On the other hand, for AAP the local structure does not have a strong dependence on the repulsive strength ϵ; since the aggregation mechanism does not exclusively rely on the excluded volume but in the alignment with neighbours. The pair correlation functions for phase separated systems of ABP and AAP clearly show this feature in Figure 3.8.

In addition to the standard pair distribution function $g(r)$ which evaluates the

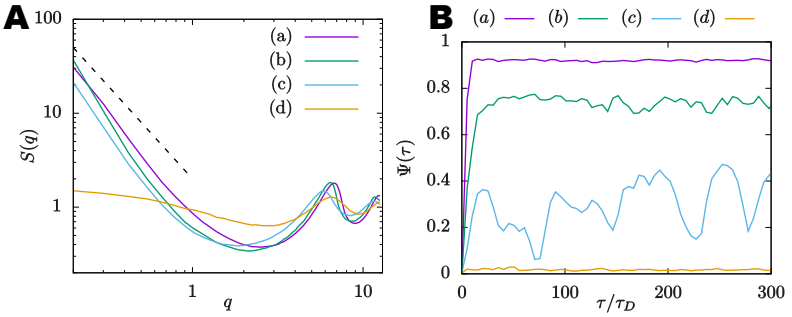

Figure 3.7 | System of $N = 2500$ AAP at $\phi = 0.18$ for the various combinations of Pe, and g introduced in Figure 3.6. **A** Long time average of the structure factor $S(q)$. **B** Temporal evolution of the global order parameter $\Psi(t)$

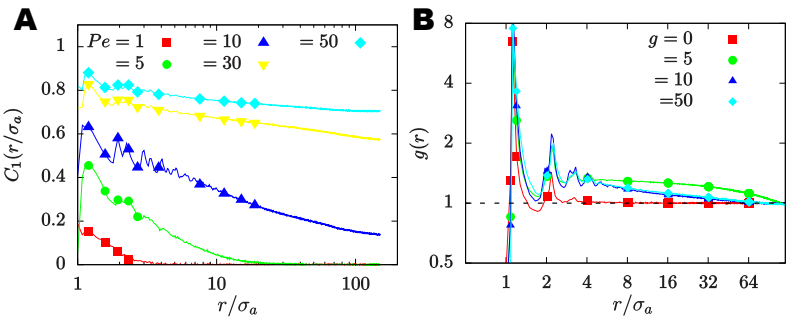

Figure 3.8 | System of $N = 20000$ AAP at $\phi = 0.18$ for various combinations of Pe, at $g = 10$. **A** Orientation correlator $C_1(r)$ at constant g. **B** Pair correlation function $g(r)$ at constant $Pe = 50$

probability to locate a pair of particles separated a distance r, we introduce two modified 2-dimensional $g(\boldsymbol{r})$, as defined in (3.8).

$$
\begin{aligned}
g(r,\varphi) &= \frac{2L^2}{N(N-1)} \sum_{i,j} \delta(r - r_{ij}) \delta(\theta - \widehat{\boldsymbol{n}_i, \boldsymbol{r}_{ij}}) \\
g(r,\theta) &= \frac{2L^2}{N(N-1)} \sum_{i,j} \delta(r - r_{ij}) \delta(\theta - \widehat{\boldsymbol{n}_i, \boldsymbol{n}_j})
\end{aligned}
\tag{3.8}
$$

The function $g(r,\theta)$ gives a two dimensional pair correlation function where the distance r denotes the distance between pairs of particles, and the angle θ the angle between the orientation and relative position vector. At contact θ is the angle that spans from the orientation vector to the collision site. The function $g(r,\varphi)$ gives the two dimensional pair correlation function where the distance r denotes the distance between pairs of particles, and angle φ the angle between orientations of the pairs. φ corresponds to the angular difference $\varphi = \theta_i - \theta_j$, where θ_i, and θ_j

are the orientations of the particles.

$$C_1(r) = \frac{\sum_{i,j} \hat{\boldsymbol{n}}_i \cdot \hat{\boldsymbol{n}}_j \delta(r - r_{ij})}{\sum_{i,j} \delta(r - r_{ij})} \tag{3.9}$$

Second, due to the formation mechanism, correlations of the orientations of pairs of ABP decay rapidly as a function of distance. Pair correlations are relevant in the interface of the dense drop since incoming particles have an orientation with a major component in the direction $-d\hat{\boldsymbol{n}}$ where $\hat{\boldsymbol{r}}$ is the unitary vector normal to the interface pointing towards the dilute phase, see Figure 2.3 in Chapter 1. On the other hand, pair correlations in the orientation of AAP extend to the whole length of the dense phase. Thus, the AAP dense cluster has a neat velocity. We define orientation pair correlations in (3.9), as the correlation of the first Legendre Polynomial.

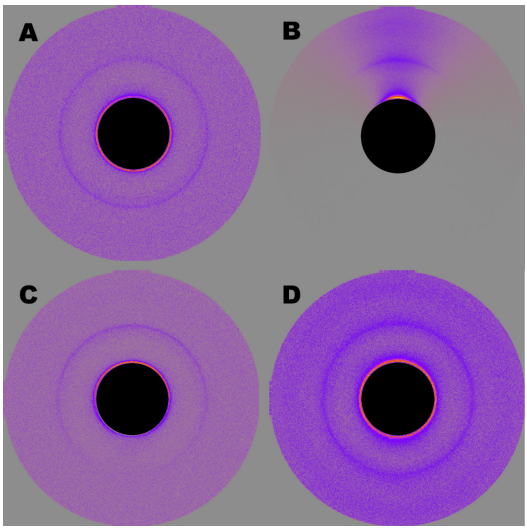

Figure 3.9 | Two dimenensional pair correlation functions for systems at $\phi < \phi_c$. **A**, and **B** introduce $g(r, \varphi)$ for $g = 0$, and $g \neq 0$ respectively. **C**, and **D** introduce $g(r, \theta)$ for $g = 0$, and $g \neq 0$ respectively. We observe accumulation particles in the direction of $\hat{n}$ for $g = 0$ (**C**), alignment of neighbours in the direction of $\hat{n}$ for $g \neq 0$ (**B**), and a randomization of neighbour orientations for $g = 0$ (**A**), and randomization of the interaction site relative $\hat{\boldsymbol{n}}$ for $g \neq 0$ (**D**)

3.3 Inclusions in an Active Bath

Now that we understand the emergent structures and the bath of active aligning particles we proceed to the main purpose of this Chapter, the introduction of passive colloids in an active bath. First, we study the influence of an inclusion in the bath of active particles. Second, we fix a pair of inclusions in the simulation box to study the relative forces between them. We study the distance dependence of the interaction emergent force from a mechanical measure of the interactions. And Finally, we consider the effects that arise in a mixture of active and passive particles when inclusions are not fixed in their initial positions.

Equations in (3.3) and (3.4) describe an active solvent in which passive particles will be immersed. Large passive colloidal particles, i.e. inclusions, of diameter σ_c, and centre of mass at positions $\boldsymbol{X}_i$ interact with the active particles repulsively and evolve by means of an over-damped Langevin equation.

$$\partial_t \boldsymbol{X}_i = -\frac{\sigma_a}{\sigma_c}\mu_t \boldsymbol{F}_i^{inc} + \sqrt{2\sigma_a/\sigma_c D_t}\boldsymbol{\eta}_i^t \tag{3.10}$$

Where we have already rescaled the equations using the Stokes relation between mobility coefficients. The drag on a sphere immersed in a viscous fluid is proportional to its size, thus μ_t is proportional to the inverse of the characteristic length of the particle σ. The mobility of a colloid of size σ_c is $\sigma_a/\sigma_c\mu_t$, where μ_t is the mobility coefficient for a colloid of size σ_a. The noise term $\boldsymbol{\eta}^t$ is Gaussian, and has zero mean and unit variance; the same statistical properties as $\boldsymbol{\xi}^t$. The force $\boldsymbol{F}^{inc}$ accounts for inclusion-inclusion and active particle-inclusion interactions.

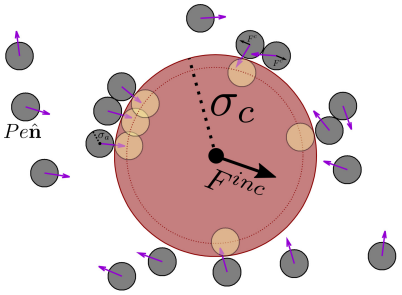

Figure 3.10 | Forces on an inclusion particle of diameter σ_c. Active particles swim in the direction defined by $\hat{\boldsymbol{n}}$. Repulsive interactions between AAP and inclusions follow equation (3.11) modelled by virtual image particles of size σ_a on the inside of the inclusion.

$$\boldsymbol{F}_i^{inc} = \sum_{i\neq j} f_{ij}^c\left(x-(\sigma_c-\sigma_a)\right)\hat{\boldsymbol{X}}_{ij} + \sum_{j\in\{\boldsymbol{r}_j\}} f_{ij}^c\left(R-(\sigma_c-\sigma_a)/2\right)\hat{\boldsymbol{R}}_{ij} \tag{3.11}$$

We introduce the interactions between particles with the same WCA repulsive potential (2.7). Note that interactions between passive particles occur at a shifted relative distance. In Figure 3.10 we plot virtual pale-yellow particles as the image particles of the colliding AAP. By means of virtual particles we guarantee the size of the inclusion and the degree of overlap given by the relation between propulsion Pe, and repulsion ϵ. Finally, we introduce the dimensionless number $\ell = \sigma_c/\sigma_a$ to characterize the size ratio between passive and active particles.

$$\frac{d\boldsymbol{X}_i(\tau)}{d\tau} = \ell^{-1}\frac{\epsilon}{3}\boldsymbol{F}_i^{inc}(\tau) + \sqrt{2\ell^{-1}/3}\boldsymbol{\eta}_i(\tau) \tag{3.12}$$

In a system of active and passive particles, we introduce the packing fractions of active and passive particles ϕ_a, and ϕ_c.

$$\phi_a = \frac{N_a\pi\sigma_a^2}{4L^2}, \quad \phi_c = \frac{N_c\pi\sigma_c^2}{4L^2} \tag{3.13}$$

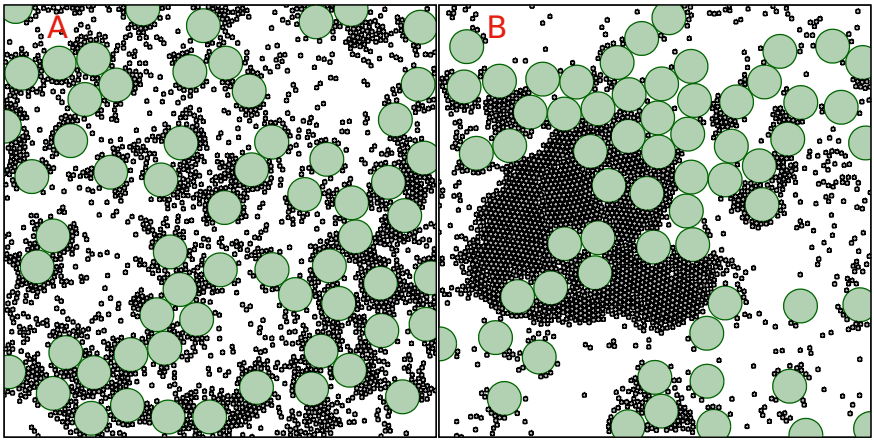

Figure 3.11 | Mixture of active and Passive particles at $\phi_a = 0.15$, and $\phi_p = 0.30$. The positions and orientations of active particles evolve with (3.6). The force exerted on each inclusion is the total contribution of the small particle interactions on its surface and their positions are evolved with (3.6).

Overall, we have introduced two parameters that characterize the propulsion and alignment of the active particles: Pe, and g; a parameter to define the interaction between particles ϵ; and three parameters to describe the composition of the system ℓ, ϕ_a, and ϕ_c.

3.3.1 One Inclusion

The first step into active-passive mixtures is to study the dynamics of an inclusion in an active bath as was first experimentally introduced by [Wu and Libchaber, 2000]. We have prepared a suspension of $N = 2000$ active particles at $\phi = 0.15$ and immersed several inclusions, with $\ell = \sigma_c/\sigma_a = 8$, within. To improve statistics we have immersed a total of $N_c = 9$ inclusions with a packing fraction $\phi_{inc} = 0.05$. We measure the mean squared displacement for the active suspension at $Pe = 30$, for both ABP ($g = 0$), and AAP ($g = 2$, 5, and 30).

The accumulation of active particles on the inclusion surface is strongly affected by the aligning properties of the active bath. At short times few active particles interact with inclusions and push them at maximum velocity v_a, and giving $MSD(\tau) \approx v_a^2\tau^2$. Beyond $\tau \approx 2 - 5$ the behaviour observes for ABP and AAP differentiate.

In the steady state, ABP tend to form a volatile dense layer around the inclusion, see the system sketch in Figure 3.12, and Figure 3.13 for an explicit form of the density profile of ABP surrounding an inclusion. ABP that collide with the surface

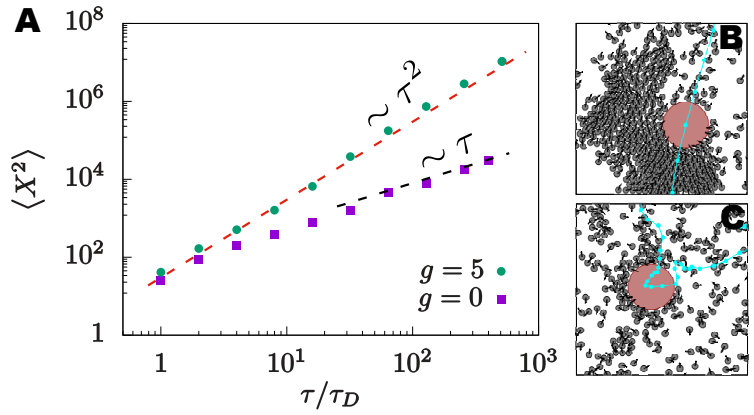

Figure 3.12 | Averaged MSD of inclusions at an active bath with $Pe = 30$, and $\phi_a = 0.15$. We average over 100 realizations of the process. **A** At $g = 0$ activity enhances diffusion by several orders of magnitude, $D_{inc} \propto Pe^2$ while $D^0_{inc} = \frac{\sigma_a}{\sigma_c} \approx 1/8$. For $g = 5$ we observe the ballistic regime for $MSD(\tau) \approx Pe^2\tau^2$.**B** For AAP with alignment set to $g = 5$, the macroscopic cluster drags the colloid at velocity v_a. **C** diffusive behaviour of the colloid immersed in an ABP suspension.

stay there until reorientation permits the escape from the inclusion. The presence of ABP interacting and pushing the inclusion introduces a random velocity to the centre of mass of the inclusion. This random velocities induce an enhancement of the spatial diffusion constant of the inclusion $D_{inc} = D_inc^{(0)} + D^{ac}_{inc}$. Where $D_inc^{(0)}$ is the thermal diffusuion, and D_inc^{ac} the diffusion induced by the active bath. For inclusions in a suspension of ABPs the long time limit of the mean squared displacement is then diffusive with a diffusion D_{inc}

$$\left\langle \boldsymbol{X}^2(\tau) \right\rangle = 4D_{inc}\tau \tag{3.14}$$

In the steady state, AAP form macroscopic travelling clusters at collective velocities approximately equal to the propulsion velocity of a single active particle. In this scenario, a passive particles in the way of the cluster gets transported at velocity v_a. Once they escape the travelling cluster, they diffuse at diffusion constant $D_inc^{(0)}$, this movement is negligible and can be considered to be almost zero when it is compared to the movements introduced by the macroscopic cluster. Ones the travelling cluster meets again the inclusion it continues pushing again at v_0. For slow dynamics of the macroscopic cluster we observe a ballistic behaviour for the MSD

$$\left\langle X^2(\tau) \right\rangle \approx v_a^2\tau^2 \tag{3.15}$$

At even longer timescales the global polarization of the cluster could diffuse. In a situation with a diffusion of the global polarization, D_p, of the travelling cluster the passive particle could recover a diffusive behaviour with a constant proportional to $v_0^2 D_p^{-1}$.

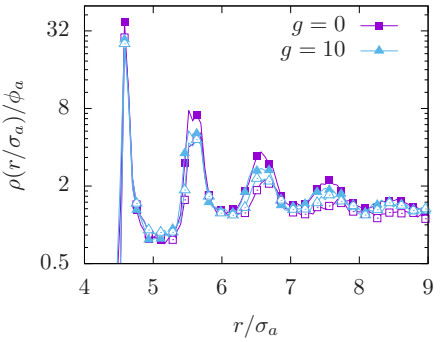

Figure 3.13 | Averaged density profile of active particles with $Pe = 30$, at a density $\phi = 0.15$ as a function to the distance to the surface of the inclusion. In solid points we plot the results for a fixed inclusion moving inclusions correspond to hollow points. ABP with a fixed inclusion show well definite shells while the local structure is rapidly lost for a moving inclusion. AAP at $g = 10$, in blue, show less structure surrounding the inclusion but show little variation for fixed and moving inclusions.

Additionally, we have extracted the density profiles of active particles surrounding inclusion in the case where inclusions move in the simulation box and when we set them in a fixed position. Figure 3.13 shows the formation of several structured layers of active particles surrounding an inclusion. The fixation of the inclusion has no appreciable effects in the formation of structures of AAP at $g = 10$. This independence is connected to the emergent travelling cluster constantly collides with the inclusion and defines a series of surrounding shells of active particles. With ABPs, however, the fixation of the inclusion permits the formation of more structured layers, the formation of structured shells is disfavoured when inclusions move. By fixing the inclusion we allow an inward flux of ABPs that entrap other ABPs close to the surface of the inclusion.

3.3.2 Two inclusions

To study the emergent interaction between passive particles we use a pair of inclusions. The reduction of the problem to a two body system simplifies the interpretation of results and gives a clear understanding of the interaction in terms of pair forces. Passive particles are immersed in a bath of active particles at surface density fraction $\phi_a = N_a \pi \sigma_a^2 / 4L^2$ always below the spinodal-decomposition line of the MIPS $\phi_a < \phi_c$. Inclusions are kept fixed at a centre to centre distance $\sigma_c + d$, we define d as the closest distance between inclusions, in the simulation box which has periodic boundary conditions. Figure 3.14 shows a sketch of the system. The strength for the particle collisions is chosen to be $\epsilon = 10$. Each simulation is run over 500 diffusion times and with at least 4 different initial conditions.

We measure the total force registered by inclusions. We compute the total force $\boldsymbol{F}_1^{inc}(\boldsymbol{X}_1)$ and $\boldsymbol{F}_2^{inc}(\boldsymbol{X}_2)$ acting on each inclusion. We project the relative force, $\boldsymbol{F}_2^{inc}(\boldsymbol{X}_2) - \boldsymbol{F}_1^{inc}(\boldsymbol{X}_1)$ on the center to center direction given by the unit vector $\hat{\boldsymbol{u}} = (\boldsymbol{X}_2 - \boldsymbol{X}_1) / \|\boldsymbol{X}_2 - \boldsymbol{X}_1\|$ as labelled in Figure 3.14. The outcome of this calculation is the interaction force f_r^-, as in equation (3.16). We can reproduce the computation to extract the forces acting on the centre of mass, and the forces acting on the direction normal to $\hat{\boldsymbol{u}}$. For symmetry, f_r^- is the only non-zero force.

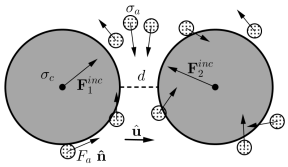

Figure 3.14 | Schematic representation of two inclusions immersed in a bath of active particles. The positions and orientations of particles evolve with (3.6). The force exerted on each inclusion is the total contribution of the active particle interactions on their borders. The total interacting force between the pair is computed according to (3.16)

$$F_r(d) = \left\langle \frac{\boldsymbol{F}_2^{inc}(\boldsymbol{X}_2) - \boldsymbol{F}_1^{inc}(\boldsymbol{X}_1)}{2} \cdot \hat{\boldsymbol{u}} \right\rangle_t = \left\langle f_r^- \right\rangle_t \tag{3.16}$$

The average of f_r^- over time, and different realizations of the process introduces the average relative force F_r, or effective interaction force. The sign of F_r determines an effective attractive-repulsive behaviour. For $F_r < 0$ the interaction is attractive ,and for $F_r > 0$ the interaction is repulsive.

We have set the density of active particles to $\phi_a = 0.18$ and simulated three qualitative different scenarios. Firstly, we simulated the system in thermal equilibrium, $Pe = 0$. Then we simulated two systems intrinsically out-of-equilibrium, $Pe = 30$: one with no aligning interactions corresponding to ABP with $g = 0$, and one with aligning interaction corresponding to AAP with $g > 0$. To better understand the interaction we have extracted the probability to measure a force f_r^-/F_a between inclusions. For the case $Pe = 0$ the active force $F_a = 0$, we then scale the interaction forces with the thermal force k_BT/σ_a. Histograms show a peaked value close to the mean value of the effective interaction force. In the active case the probability departs from Gaussianity.

In the equilibrium system the mean force at ($d = 0.875\sigma_a$) is attractive with $F_r = -0.33k_BT/\sigma_a$ and the variance is finite with value $\sigma_F = 0.33(k_BT/\sigma)^2$, this last feature is characteristic of the stochastic origin of the force.

Driving the system out-of-equilibrium gives a result that was not possible in equilibrium. For non-aligning particles the mean force is largely repulsive, $F_r = 9\ F_a$, the distribution of forces is not symmetric and disfavours attractive interactions. For aligning particles the interaction becomes attractive once again, with $F_r = -4\ F_a$. For the $Pe = 30$ the variance of the relative forces is dramatically increased, $\sigma_F = 8F_a$ and $\sigma_F = 4F_a$ respectively.

Dashed lines in Figure 3.15 correspond to the Gaussian curve for the mean and variance extracted from the raw data. For a suspension of ABP we observe a strong

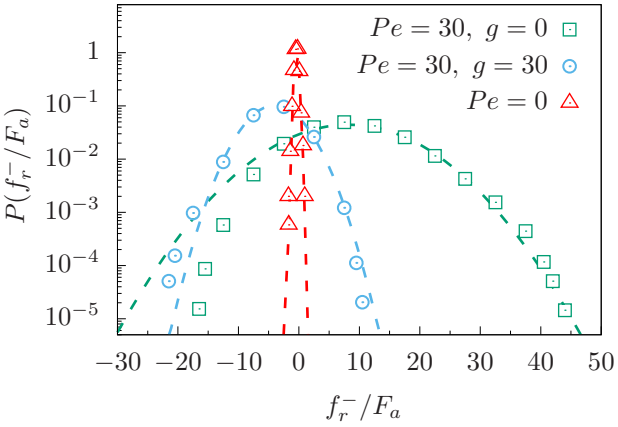

Figure 3.15 | Probability distribution of the value of the interacting force between the interactions at $d = 0.875\sigma_a$. In red triangles we plot the equilibrium case, $Pe = 0$, with a depletion attractive force. In blue circles and green squares we plot the PDF in the active case, $Pe = 30$. In a non aligning bath, $g = 0$ (green squares), the mean force is repulsive. In an aligning bath, $g = 30$ (blue circles), the emergent force is attractive. In dashed lines we plot gaussian functions with F_r/F_a, and σ_F/F_a.

deviation from gaussianity. The probability to measure a force separated $|\Delta F|$ from the average value is different for interactions above and beyond F_r. The statistical analysis of f_r^- conclude that the probability measure a force $f_r^- = F_r + |\Delta F|$ is larger than the probability to measure a force $f_r^- = F_r - |\Delta F|$. When the alignment is increased the probability to measure negative interactions increases, and for $g = 30$ we observe the attractive tail of $P(f_r^-)$ above the gaussian probability.

To understand the origin of the emergent force we have extracted the density field near the inclusions, as shown in Figure 3.16. In the equilibrium case we expect an homogeneous distribution of particles near the inclusions, only a small increase of the density near the walls in agreement with depletion forces [Mao et al., 1995].

In Figure 3.16 we present the density fields of active particles in the region close to the inclusion pair. Light yellow colours correspond to densities above the bulk values. The top plots correspond different realizations of a system of AAP at $Pe = 50$, and $g = 50$. Active particles form a travelling cluster that collides with the inclusion pair. The combination of the bright region, and the dark shadow indicates the collision angle between the travelling cluster and the inclusion pair. As a function of this angle the interaction is either attractive when the cluster intercepts the inclusion pair in a direction parallel to the centre to centre vector, or repulsive when the cluster intercepts the inclusion pair in the perpendicular direction.

Results for a bath of ABP particles, second row in Figure 3.16, indicate a different scenario. At low values of the separation distance d we appreciate the formation of brightly defined rings in the internal region of the inclusion pair. For a

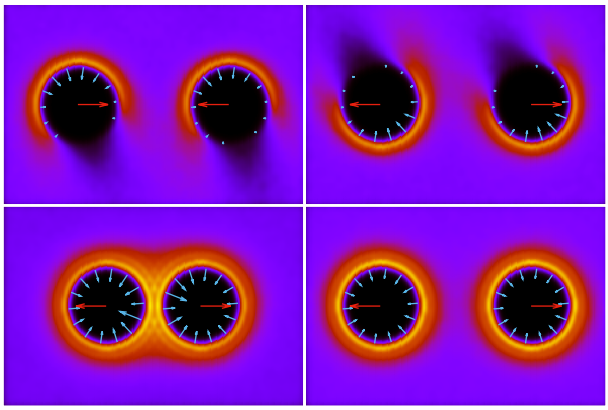

Figure 3.16 | Plot of the local density fields for three distinctive situations. Top figures are a system with $Pe = 50$, $g = 50$, and a separation distance of $d = 8\sigma_a$. Plots in the bottom are both at $Pe = 50$, and $g = 0$ for $d = 2\sigma_a$, and $d = 8\sigma_a$. Red arrows represent the averaged relative force in arbitrary units to appreciate the attractive/repulsive nature of the interaction. In blue arrows the force exherted on the inclusions at different surface angles.

suspension of ABPs this internal region behaves like a wedge that captures particles the ABP, a mechanism similar to [Kaiser et al., 2012]. The system is, on average, highly structured near the inclusion. In the wedge of the inclusions, the symmetry is broken and a neat repulsive force emerges.

3.3.3 Characterization of the Force

In this section we extended the analysis of forces over the separation distance d/σ_a for a systematic exploration of the Péclet and the alignment number g. We prepare systems with $L = 160\sigma_a$ with pairs of inclusions of diameter $\sigma_c/\sigma_a = 15$ separated a distance from surface to surface d. We have measured the relative interaction for ABPs with $Pe = 1$ to $Pe = 30$, and for AAP at $g = 10$ for $Pe = 10$ to $Pe = 30$. We reproduce the extracted effective force curves in Figure 3.17 and identify the common trends.

First, ee observe the repulsive behaviour of the interaction at low values of the alignment, $g \approx 0$, that matches quantitatively the results of [Harder et al., 2014b]. At low values of the alignment, an increase of the activity Péclet number increases the repulsive interaction.at $g = 0$ and $Pe = 1$ we obtain a result which is close to the depletion attraction. For increasing values of the activity we observe the gradual appearance of a repulsion force with maximum at $d = \sigma_a$. The effective force then decays to zero. We appreciate, though, that the interaction length of the decay increases with the value of the activity.

Second, at $g = 10$ the increase of the Pe induces a different behaviour of the relative effective interaction. The first effect is evident in the contact force, as Pe increases effective force at contact decreases and becomes more attractive. Then increasing the distance the force monotonously increases until $d = \sigma_a$, where it peaks. The second appreciable effect is beyond $d = 3\sigma_a$ where the observe the emergence of a slow decaying attractive interaction.

The measure of the force at $d = 0$, and σ_a reveals to be an indicator of the maximum attraction of the interaction, at contact, and the maximum in the repulsion for either APBs, and AAPs. Here we present a series of plots to show de dependence of force at contact $F_r(0)$, and the peak force $F_r(\sigma_a)$ on the activity parameters Pe, and g.

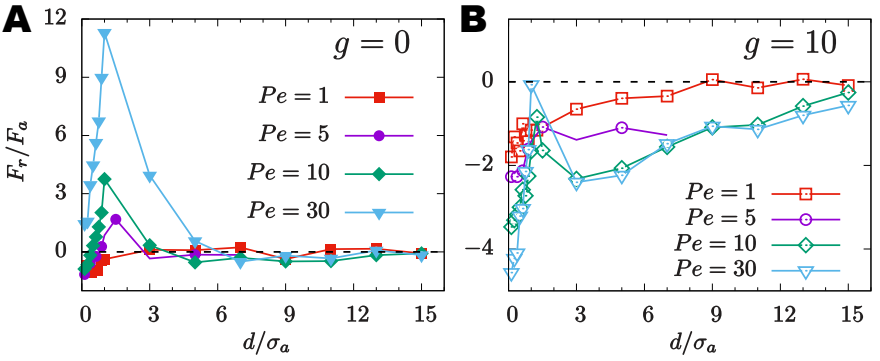

Figure 3.17 | Relative Force of interaction between inclusions at $\ell = 15$, and $\phi = 0.18$. In **A** we plot the strength of interaction for an ABP bath. In **B** we plot the strength of interaction for an AAP bath with $g = 10$. We observe the repulsion in the ABP case and the attraction and the emergence of a long range tail in the AAP suspension.

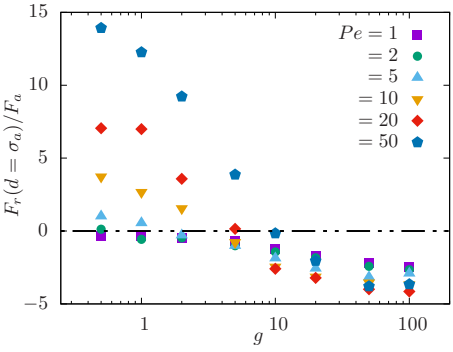

Figure 3.18 | Relative force at d/σ_a as a function of alignment for different Péclet and alignment strength g for a system at $\phi_a = 0.18$, and $\sigma_c/\sigma_a = 15$ at a distance maximum repulsion $d = \sigma_a$. Below a certain $g^\star$ we observe a strong repulsion that increases with Pe, beyond $g^\star$ the interaction becomes attractive and the dependence on Pe less relevant.

For increasing values of the alignment we typically observe the decrease of the peak force, see Figure 3.18. At low alignment the interaction strongly depends on the Pe, and the crossing from repulsion to attraction approximately occurs at

$g_{cross} \approx Pe/5$. For $g > g_{cross}$ the interaction force at the peak is more robust and less dependent on the value of the activity. We summarize this results, and the values of the force at contact in Figure 3.19 with a coloured plot to appreciate the magnitude of the interaction at contact, and at the peak force. We additionally interpolate the line of zero interaction force.

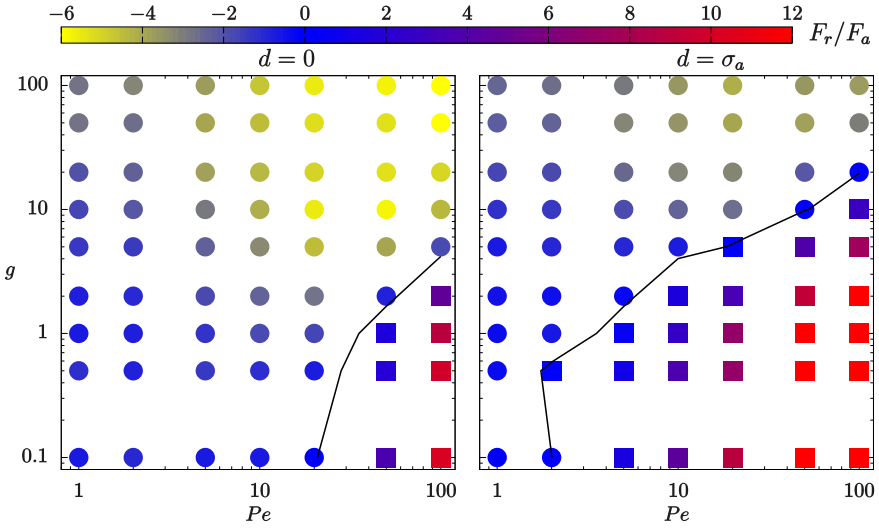

Figure 3.19 | Mean interaction force between inclusions of diameter $\sigma_c = 15\sigma_a$ in a suspension of active particles at packing density $\phi = 0.18$. We present the character and strength of the interaction for different distances $d = 0\sigma_a$, $d = \sigma_a$ respectively. We denote in squares the repulsive interaction and in circles otherwise. The black line follows the curve $F_r = 0$.

Formation energy We extend the concept of effective interaction force $F_r(d)$ to the concept of effective interaction and formation energies, $U(d)$, and U_F.

$$U(d) = \int_0^d F_r(r)dr, \quad U_F = \lim_{d\to 0} U(d) \tag{3.17}$$

The formation energy gives an interpretation of the overall interaction. For a system where the repulsive force is only positive or negative, as corresponds to ABP or AAP with hight g, the interpretation of the forces as attractive or repulsive is not clear since the interaction changes its behaviour as a function of the separation distances. The formation energy, U_F, gives a value proportional to the averaged value of the effective force on the whole range of interaction. In equilibrium, and in electrostatics, it measures the energy released by the formation of the dimer at contact from a pair of particles infinitely separated. For positive U_F an external agent needs to push the particles together so that they form a dimer at contact. In

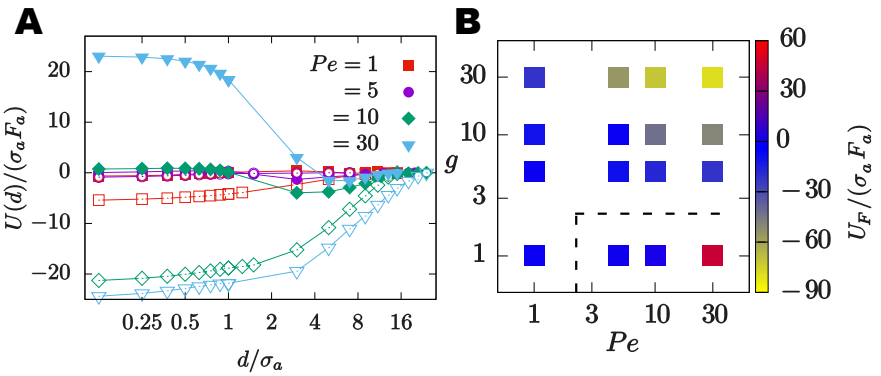

Figure 3.20 | Effective energy as defined in (3.17) for a system at $\phi_a = 0.18$, and $\ell = 15$ for various parameters of the active suspension. **A** Effective energy for ABP in solid dots as a function of the Pe, and effective energy of interaction for AAP at $g = 10$ for the hollow points at different Pe. **B** formation energy of a dimer at contact for the various pairs of Pe, and g considered. We plot in dashed lines the $U_F = 0$ line.

Figure 3.20 we plot the formation energy for a pair of dimers in ABP and AAP suspensions. Inclusions immersed in an ABP suspension present a negative formation energy at low Pe. The formation energy becomes positive at $1 < Pe < 3$ where the active repulsion overcomes equilibrium depletion forces, for $Pe > 3$ $U_F > 0$. For ABP suspensions where active depletion overcomes equilibrium depletion the effective interaction energy, $U(d)$, develops an attractive local minimum at large d and increases to a positive maximum as $d \to 0$, where inclusions collide. In a mixture of active and passive particles this will introduce a structure of passive particles separated by active particles but with few long range structure and density correlations.

Inclusions immersed in a suspension of AAP show repulsive interactions, even for $F_r(\sigma_a)$ for $g \gtrsim Pe/5$, as observed in Figure 3.18 where the curves intercept the line $F_r(\sigma_a) = 0$. In the previous situation the formation energy is clearly $U_F < 0$ and the effective energy $U(d)$ has a minimum at contact. In a mixture, passive particles will be pushed together with a larger correlation to develop a long range structure.

3.3.4 Two inclusions close to a wall

We repeat the previous calculations of the pair interaction for suspension of ABP in a system enclosed between two parallel walls. We have also explored the effect for finite values of the alignment and observed a complete capture of the active particles on the walls and the formation of structures typical for wetting. Before the study of the interactions between AAP and pairs of inclusions in confined systems we need to understand the dynamics and interactions of AAP in confined systems.

We define a wall at position $y = 0$, and $y = L$. The interaction between the walls and active particles is mediated by the pairwise conservative repulsive potential

$$U_W = \sum_i^N U_{WCA}(y_i) + U_{WCA}(L_y - y_i) \tag{3.18}$$

For a system of ABP confined between two parallel walls at a density $\phi > \phi_b$, where ϕ_b stands for the density of the low-density binodal line at a given Pe, the system phase separates into a dense phase $0.\phi_f \approx 0.9$, and a gas phase $\phi_g \approx 0.1$. The dense phase in the wall region, and the dilute phase in the central region of the box. A system at bulk density ϕ separates into two dense layers with approximate thickness given by

$$\left\langle \frac{h}{\sigma_a} \right\rangle \approx \frac{\phi - \phi_g}{\phi_f - \phi_g} \tag{3.19}$$

The introduction of a density phase separated system allows us to explore the interaction between passive particles in both the diluted and dense regimes. On one hand, walls guarantee phase separation for $\phi > \phi_g$ and the central region of the box has an averaged density ϕ_g well balanced by the dense phase on the walls that act as an active particle reservoir. On the other hand, walls maintain a dense layer of active particles which in PBC systems need to be nucleated, and sustained by the inclusions. The dense layer, though, is not homogeneous. The position of the interface is not fixed and the averaged orientation of ABP at the interface is perpendicular and inwards to it. Finally, close the wall inclusions experience an interaction mediated by the collisions between active particles and the walls.

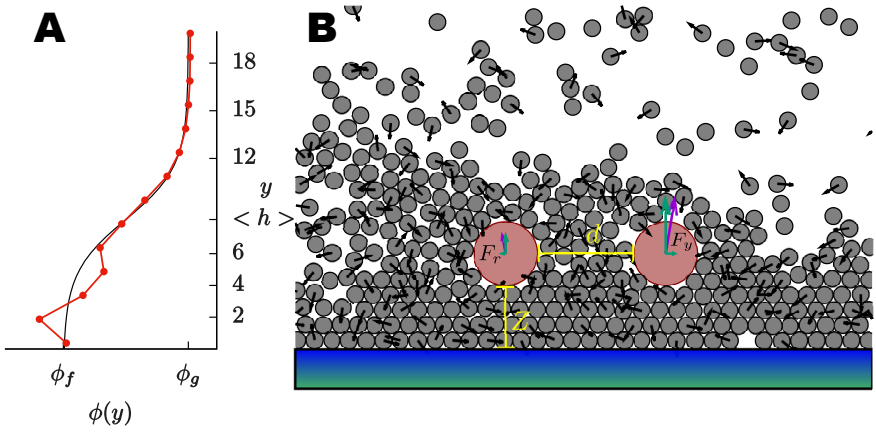

Figure 3.21 | A passive dimer close to a wall in a suspension of ABP. **A** density profile. Red curve the extracted profile and the black line equation (3.20) with $\phi_g = 0.13$, $\phi_f = 0.72$, $\langle h \rangle = 8.2\sigma_a$. **B** Snapshot of the system with $Z = 3\sigma_a$, and $d = 6\sigma_a$, we appreciate a positive perpendicular force F_y.

We use a typical hyperbolic density profile (3.20) to model the dense layer of ABP close to a wall. By a computation of the density profile along the direction perpendicular to the wall, y, we show a fit for $Pe = 30$, and $\phi = 0.3$ where Δ is the thickness of the wall, and y_0 the position of the interface.

$$\phi(y) = \phi_g + \frac{\phi_f}{2}\left[1 + \tanh\left(\frac{y - y_0}{\Delta}\right)\right] \tag{3.20}$$

Preparing a system at $\phi = 0.3$ introduces a pair of dense layers of active particles of average thickness $\langle h/\sigma_a \rangle = 8$; a detailed measure of the thickness reveals fluctuations of the position of the interface $\Delta h/\sigma_a = 3$. The forces acting on the inclusions define a relative interaction force F_r as defined in (3.16). In addition we introduce the total force on the dimer in the direction normal to the wall F_y (3.23), permitted by the symmetry breaking induced by the wall. A positive F_y describes an inclusion dimer that experience force that repels it from the wall, an expelling force, while $F_y < 0$ defines an attractive force towards the wall.

We now present the results from simulations with inclusions of diameter $\sigma_c = 4\sigma_a$, immersed in the dense layer $\langle h/\sigma_a \rangle = 8$ close to the wall. To characterize the inclusion dimer we introduce the minimum distance between the surface of each inclusion relative to the wall. For the sake of simplicity we introduce a dimer parallel to the wall with $Z_1 = Z_2 = Z$. For a more general scenario the dimer introduces an angle α relative to the wall and, at close distances, a torque on the pair.

Given the self-propelled nature of the active particles, the layer has some structure. The average of the projection of the ABP orientation, $\hat{\boldsymbol{n}}$, and the unit vector perpendicular to the interface $\hat{\boldsymbol{y}}$, $\langle \hat{\boldsymbol{z}} \cdot \hat{\boldsymbol{n}} \rangle$ is negligible negative for particles in the bulk of the dense region but for the interface $\langle \hat{\boldsymbol{z}} \cdot \hat{\boldsymbol{n}} \rangle < 0$.

We first test the effect the dense particles have in the interaction between passive colloids. We compare the results of the interaction force F_r in the dilute region, and the corresponding system with PBC at $\phi = \phi_g$. As expected the interaction in both the central region of the box and in the gas density with PBC match, as reported in red and black dots in Figure 3.22. Results are in correspondence with the ones obtained for larger inclusions in 3.3.2. The measured relative force is repulsive and has a maximum at $d = \sigma_a$, then it decays to zero without the appearance of long range interactions for $g = 0$.

We immerse the dimer into the dense phase by fixing the value of Z. In Figure 3.22 we distinguish two different scenarios. For $d < 2\sigma_a$ the relative interaction loses intensity and becomes attractive. But for non-integer values of the distance between inclusions the effective interaction is repulsive. Further than $d = 2\sigma_a$ the interaction develops an additional interaction, a long range effective force not present at the gas phase and associated to density fluctuations. For dimers close to the walls $Z < 4\sigma_a$, and deep into the dense layer the long range interaction is attractive. For $Z \geq 4\sigma_a$ the long range interaction develops a repulsive behaviour.

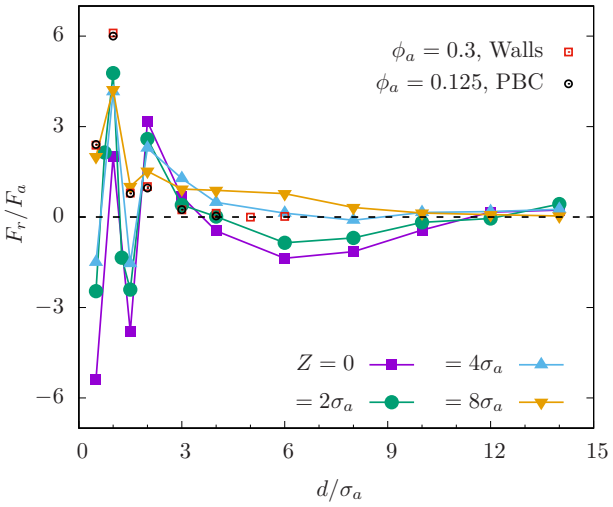

Figure 3.22 | Radial force between inclusions as a function of the separation distance d. In red and black squares we represent the reference interaction for a pair of inclusions in the middle of the box and a system at ϕ_g with PBC, respectively.

Interactions in the dense phase introduce long range effects due to the increase in the correlation lengths and density fluctuations as compared to a dilute system.

To study the normal force exerted to the inclusion we first present a simple theoretical estimation F_y^{est} of the orthogonal force $F_y^{(1)}$ acting on a single inclusion. An inclusion in an intermediate value of Z, on average, separates the gas from the dense phase. We qualitatively estimate the repulsion force as follows.

We assume the inclusion to be buoyant in the interface of the dense and the dilute regions. Being θ the polar angle which describes a point on the surface of the inclusion with $\theta = 0$ a point in the furthest right of the inclusion and $\theta = \pi$ a point in the furthest left, so the diameter that goes through $\theta = 0$, and $\theta = \pi$ is parallel to the wall. With this parametrization of the surface we distinguish between the region of the inclusion immersed in the gas phase with $0 < \theta\pi$, and the region in contact with the dense phase with $-\pi < \theta < 0$. The vertical force exerted by a particle with orientation φ relative to the normal at θ is $F_y = -F_a \sin\theta \cos\varphi$, for only the radial component of the propulsion force $F_a \cos\varphi$ contributes to the vertical force with its vertical component $-\sin\theta$.

The orientation of particles in the dense phase thermalizes and the distribution $P_\varphi = 1/(2\pi)$ is uniform. However, particles in the gas phase collide with $\varphi = 0$ and diffuse until escapement at $\varphi \approx \pm\pi/2$). The probability distribution for particles in the gas phase colliding with the inclusion is $P_\varphi = (2\pi)^{1/2} \exp\left(-\varphi^2/2\right)$. The total force on the inclusion is then the sum of the upwards force given by the

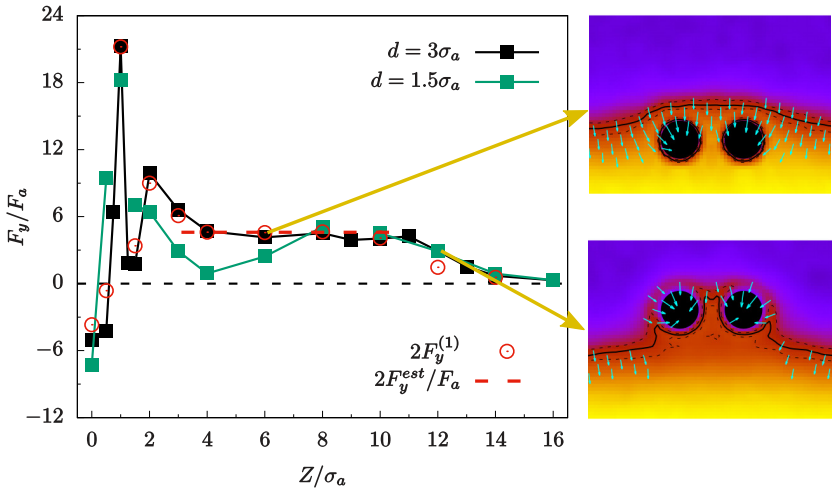

Figure 3.23 | Interaction force of the Active Brownian Particles on an inclusions dimer perpendicular to the wall at bulk density $\phi_a = 0.3$, and $Pe = 30$. In red circles we plot the interaction between a sole particle and the wall as a function of Z. The nonadditivity is manifested in the departure of F_y from $2F_y^{(1)}$ for $Z < 8\sigma_a$. Red dashed line define an estimate (3.21) of the repulsion force $2F_y^{est}$. On the right, density plots of ABPs with the contour line $\rho = 0.4$ for an inclusion separation $d = 3\sigma_a$ at $Z = 6\sigma_a$, and $Z = 12\sigma_a$. In green arrows the averaged orientation of active particles in the regions where $\psi(x, y) > 0.3$.

average $\phi_f \pi \sigma_c/2$ particles in the dense phase minus the sum of the downwards force given by the average $\phi_g \pi \sigma_c/2$ particles in the gas phase.

$$F_y^{est} = F_a \sigma_c \left(\phi_f - 0.65 \cdot \pi \phi_g\right) \approx 2.3 F_a \tag{3.21}$$

Where we have previously extracted the the densities from the density histogram and obtained $\phi_f \approx 0.8$, and $\phi_g \approx 0.12$. The integral of the orientation in the gas phase contains the non trivial integral

$$\frac{1}{\sqrt{2\pi}} \int_0^{\pi} \sin\theta d\theta \int_{-\pi/2}^{\pi/2} \cos\varphi \exp\left(-\varphi^2/2\right) \approx 2 \times 0.65 \tag{3.22}$$

For a single inclusion we measure the orthogonal force $F_y^{(1)}$. Results give a strong Z dependence at the the vicinity of the wall associated to the structure of the first layer of active particles. For distances $4\sigma_a < Z < 11\sigma_a$ the interaction converges to the estimate value F_y^{est} and then goes to zero as inclusions detach from the active dense fluid.

We proceed to compute the total force acting on a pair of inclusions, F_y, and the possible two body, nonadditive, effects on the equality $F_y = 2F_y^{(1)}$ associated to the interaction between inclusions.

$$F_y = \hat{\boldsymbol{y}} \left(\boldsymbol{F}_2^{inc} + \boldsymbol{F}_1^{inc} \right) \tag{3.23}$$

For a pair of particles at separation distance $d = 1.5\sigma_a$ we observe a weakening of the interaction for $Z > 2\sigma_a$, the short distance of the two inclusions introduces an effect when inclusions are completely or partially immersed in the dense phase. The interaction is nonadditive given its departure from $2F_y^{(1)}$. At distances $Z > \langle h \rangle$ the interaction finally follows $2F^{(1)}$. Finally, for a pair of particles at separation distance $d = 3\sigma_a$ we observe a good match with $F^{(1)}$. The interaction between inclusions is not manifested in the vertical force, and the wall interaction recovers additivity. In all cases we observe an interaction with the dense layer beyond $\langle h \rangle$. This is clearly seen in the density plots in Figure 3.23. The fluid-gas interface is deformed by inclusions as they get closer to the surface.

Finally, we quantify the the density and alignment of the active particles. We define a local density $\rho(x, y)$, and local alignment $\boldsymbol{\psi}(x, y)$ as follows:

$$\boldsymbol{\psi}(\boldsymbol{r}) = \frac{\sum_i \delta(\boldsymbol{r} - \boldsymbol{r}_i)\hat{\boldsymbol{n}}_i}{\sum_i \delta(\boldsymbol{r} - \boldsymbol{r}_i)} = \psi(x, y)\hat{\boldsymbol{p}}(x, y) \tag{3.24}$$

In Figure 3.23 we included the density field of active particles close to a wall with two inclusions separated a distance $d = 3\sigma_a$. We plot the orientation vector field for $\psi(x, y) > 0.3$ and observe that the averaged orientation $\hat{\boldsymbol{\psi}}$ is perpendicular to the interface. Deep inside the dense phase or the gas phase $\psi(x, y) < 0.3$.

3.4 Mixtures

The extraction of the interaction pair force is extremely dependent on the set-up. Both origin and behaviour of these out-of-equilibrium forces between passive particles depend on the structures that are formed around the particles. Structures are supported by the set-up. By fixing the passive particles we let the system to develop a structure which generates the final interaction. In the case of zero alignment this effect is extremely evident since the inclusions are fixed and the forces are repulsive.

In this section we present the results for suspensions of active and moving passive particles. We separate the results in two subsections. We first study the structure of the passive particles in a system with periodic boundary conditions. Finally we extend the analysis to a system with the usual periodic boundary conditions.

For a system confined between two walls we observe a strong influence of the wall. At low g we observe the formation of a dense layer of active particles that expel passive particles close to the walls, we already reported this effect for one and two inclusions. For $g > 2$ the effect of the wall is much more dramatic and completely dominates the dynamics of the system, active particles are completely

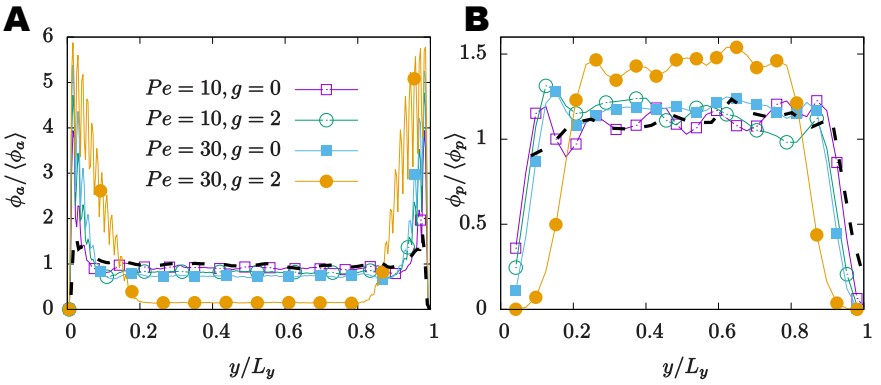

Figure 3.24| Density profile of particles in in a confined system at $\phi_a = 0.15$, and $\phi_p = 0.3$. In black dashed lines the equilibrium profiles. **A** Active particles for different activities and alignment, in dashed lines we observe the depletion accumulation of active particles close to the walls. **B** Passieve particles for different activities and alignment of the active bath, in dashed lines the equilibrium profile for a binary mixture (particles of diametre $\sigma_c > \sigma_a$)

captured by the walls, as seen in the density profiles 3.24. To optimize profile statistics, and specially for passive particles, we prepare systems in a rectangular box with $L_x/L_y = 2$, keeping $L_y \approx 75\sigma_a$.

For finite alignment, active aligning particles form a large structure and coexist with a very dilute gas of AAP. Inclusions are rapidly expelled from the dense part of the AAP and, thus, the interaction between AAP and inclusions takes place at the extremely diluted gas which does not show the typical collective phenomena discussed in bulk AAP, as seen both in Figures 3.24 and 3.25. For this reason, to compare the collective effects of the active bath on a finite density of inclusions, we must avoid walls, the most suited system to perform simulations is with Periodic Boundary Conditions.

3.4.1 Periodic Boundary conditions

We have prepared mixtures of $N_a = 2000$ aligning active particles at $\phi_a = 0.18$ and finite density $\phi_c = 0.3$ of passive particles and run a series of simulations with periodic boundary conditions at the pairs of Pe, and g values for which we extracted the effective forces in Figure 3.17.

To analyse the effect of the active bath we compute the pair distribution function of passive particles, $g(r)$. To simulate a system with $N_a = 2000$ active particles, and a statistically significant amount of passive particles we have decreased the size ratio to $\sigma_c/\sigma_a = 8$.

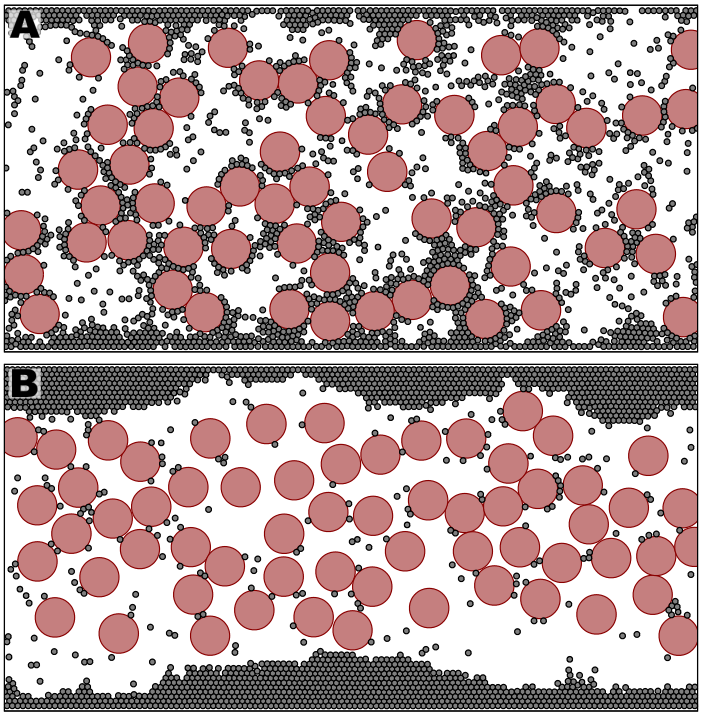

Figure 3.25 | Mixture of $N_a = 2000$ particles at packing fractions $\phi_a = 0.15$, $\phi_c = 0.3$, and $Pe = 30$. **A** For a system of ABP we observe wall accumulation of particles, a density phase separation. **B** For a system of AAP with $g = 2$ we observe a huge AAP depletion from the bulk and the formation of a density profile $h(x)$ on the walls.

After detailed analysis of Figure 3.26, systems with both $g = 0$, and $g = 10$ show a first peak at contact, $d = \sigma_c$. We observe, though, a second maximum at $d = \sigma_c + \sigma_a$ whose height is comparable to the first peak for $g = 0$ at large activities. The origin of the second peak lies in the short distance repulsion measured in section 3.3.2. For $g = 10$ we observe a strong increase of the first peak vale and the appearance of a second peak at $d = 2\sigma_c$, as compared to $g = 0$. The appearance of a second maximum at $d = 2\sigma_c$ which; both features are characteristic for an attractive interaction and compatible with the findings in section 3.3.2.

Snapshots of the system in Figure 3.27 show the density heterogeneities of active particles close to inclusions. On the left hand, ABP accumulate close to inclusions and promote repulsion between pairs but may introduce attractive triangular arrangements of passive particles surrounded by ABP. The overall arrangement of passive particles is rather homogeneous though density fluctuations are present in the system. On the right hand, AAP form a macroscopic travelling cluster that captures the passive particles and arranges them in a more heterogeneous and locally dense configuration. The travelling cluster collects and induces large density

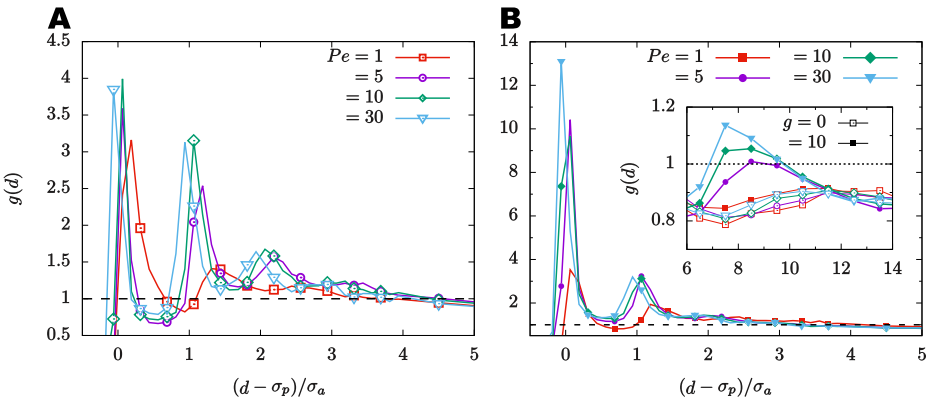

Figure 3.26 | Pair distribution function of passive particles for a mixture of active and passive particles at densities $\phi_a = 0.18$, and $\phi = 0.30$ and size ratio $\sigma_p/\sigma_a = 8$. **A** for Active Brownian Particles with $Pe = 30$, and **B** for Aligning Active Particles at $g = 10$, and $Pe = 30$. In the inset we show the position corresponding to $d = 2\sigma_c$, we distinguish ABP using hollow points and AAP using solid ones.

fluctuations on passive particles.

3.5 Conclusions and Perspectives

We have presented a model of active particles that account for aligning interactions respect to the swimming direction. We propose different aligning interactions that could be easily modelled, i.e. particles that align towards other particles, polar and nematic interactions or even alignment relative to external fields.

In the first place, we have identified dimensionless parameters to capture the intensity of both activity and alignment as compared to diffusive strengths, which we named Péclet, and aligning numbers. Such parameters and interactions determine the collective behaviour of the active particles. Once we understand the emergent phenomena in the active bath we introduced passive particles.

First, we analysed the movement of a single passive colloid to reproduce previous results on MSD enhancement, and then fixed a pair of passive particles in the active bath and explored the interaction strength between the colloids for different combination of the dimensionless relevant parameters.

Simulations show an emergent repulsive force between colloids as activity is increased and alignment is set to zero. The interaction strength can be then continuously converted from repulsion into attraction at short distances, $d \approx 0$, by increasing the alignment. As a consequence of the increase of alignment, we report the emergence of a long ranged interaction at distances up to $d/\sigma_c = 2$.

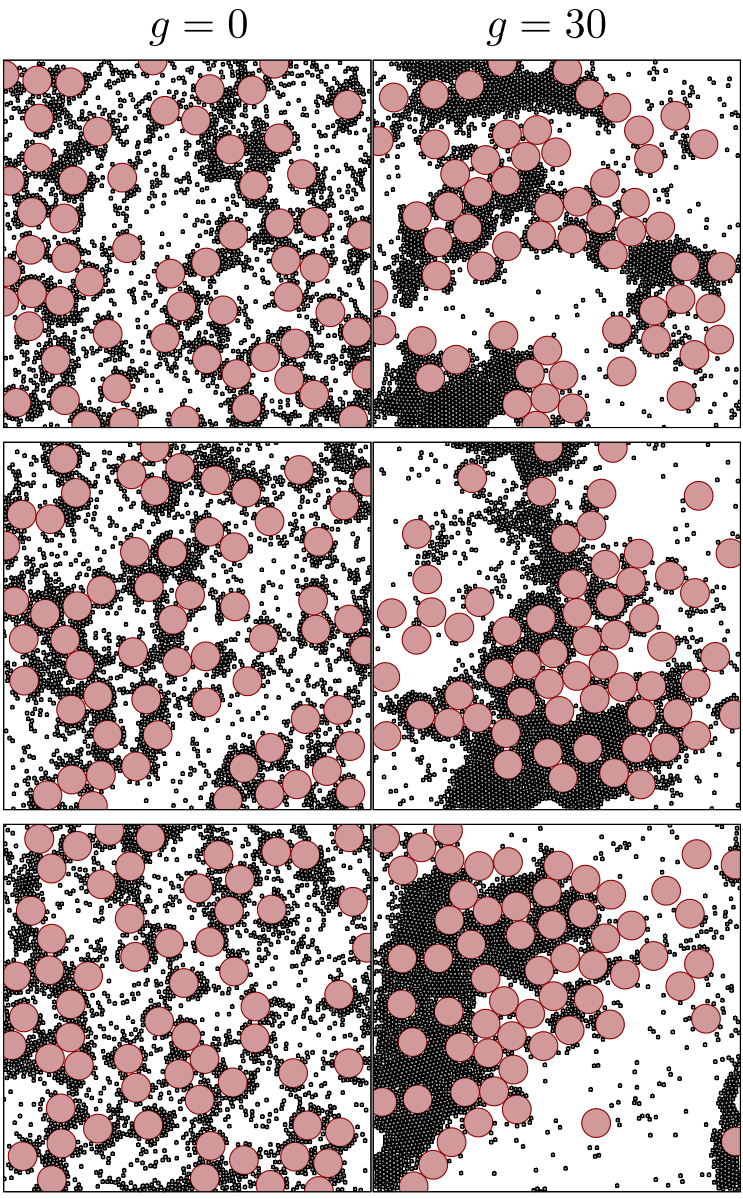

Figure 3.27 | Snapshots of a system at $Pe = 30$ and $\phi_a = 0.18$, and $\phi_p = 0.30$. Left column Active Brownian Particles ($g = 0$). Right column Aligning Active Particles ($g = 30$)

Considering the structure of the active particles around the passive particles we conclude that active torque-free particles get arrested in the wedges that form the inclusions and push the inclusions apart. Once we add torque, interacting particles

tend to travel together forming large polar aggregates. Travelling clusters intercept the inclusion dimer at different angles and show a force distribution $F_r(\alpha)$ which determines the angular averaged attractive behaviour.

We have presented active dumbbells and nematic interactions for circular active particles. We can extend the analysis of the induced interactions in such systems. In addition we may even consider the interaction of non-circular objects such as passive squares which have a well defined packing symmetry.

Second, we analysed the effect of confinement in the system. We describe the role of wall and the effect of alignment, further work is required to characterize the structures of AAP on the walls. For ABP the interaction between pairs of particles in the dense active fluid shows the extend of the interaction to distances larger than two active particles diameters. Fluctuations induced in the dense region activate long range interactions between passive particles. Moreover, we characterize the emergence of a body force on the inclusions that expels them from the dense phase close to walls. We estimate the force and test its additivity to pairs of particles. We show that additivity is lost for dimers separated by less than two particle diameters.

Third, we have studied the collective behaviour of a suspension of passive particles in an active bath. The effective repulsive behaviour extracted from pair interactions in a suspension of ABP translates into structures of passive particles separated by ABPs. New three-body effects emerge which need to be further studied. Finally, with AAP the long range attractive interactions, associated to a macroscopic travelling cluster, translate into large aggregates of passive particles pushed and segregated by travelling aligning active particles.

Appendices

3.A Hydrodynamic fields

We present a hydrodynamic model for a system of active particles and incorporate alignment. We coarse-grain the equations of motion in the formalism presented by [Dhont, 1996, Bialké et al., 2013, Speck et al., 2015] into dynamic equations for the coarse-grained density, polarization, and nematic field [Cates and Tailleur, 2013].

We define the equations that govern the motion of the particles. In this case the Langevin equations:

$$\partial_t \boldsymbol{r}_i = v_0 \hat{\boldsymbol{n}} - \mu \sum_{i \neq j} \boldsymbol{F}_{ij}^{cc} \frac{\boldsymbol{r}_i - \boldsymbol{r}_j}{|\boldsymbol{r}_i - \boldsymbol{r}_j|} + \sqrt{2D_0}\boldsymbol{\xi}_i \tag{3.A.1}$$

And the vectorial equation for the orientation vector. We introduce a torque that depends on the relative distance and orientation.

$$\partial_t \hat{\boldsymbol{n}}_i = \left(\sum_{j \neq i} \boldsymbol{\Gamma}_{ij} \left(\boldsymbol{r}_i, \hat{\boldsymbol{n}}_i; \boldsymbol{r}_i, \hat{\boldsymbol{n}}_j \right) + \omega_r \xi \hat{\boldsymbol{e}}_z \right) \times \hat{\boldsymbol{n}}_i \tag{3.A.2}$$

The evolution of the whole system is described by Ψ_N. This function measures the probability to find the system in a certain configuration of the microscopic variables (positions and orientations) at a certain time. The Smoluchowski equation relates the time evolution of Ψ_N to the momenta of the degrees of freedom.

$$\partial_t \Psi_N = \sum_k \nabla_{\boldsymbol{r}_k} \left(\mu \nabla_{\boldsymbol{r}_k} U - v_0 \hat{\boldsymbol{n}}_k + D \boldsymbol{\nabla}_{\boldsymbol{r}_k} \right) \Psi_N + \sum_k \left(\nabla_{\hat{\boldsymbol{n}}_k} V + \omega_r \nabla_{\boldsymbol{n}_k} \right) \Psi_N \tag{3.A.3}$$

Where $U\left(\boldsymbol{r}_1, ..., \boldsymbol{r}_N\right)$ is the repulsive potential and $V\left(\hat{\boldsymbol{n}}_1, ..., \hat{\boldsymbol{n}_N}\right)$ the aligning potential of interaction. Function $\Psi_N(\{\boldsymbol{r}\}, \{\hat{\boldsymbol{n}}\}; t)$ has $2N$ degrees of freedom for the spatial coordinates, N degrees of freedom for the orientations and an the temporal dependence on t. We can construct a one body function $\Psi_1(\boldsymbol{r}, \hat{\boldsymbol{n}}; t)$ with no approximations

$$\Psi_1 = N \int d\boldsymbol{r}_2 d...\boldsymbol{r}_N \int d\hat{\boldsymbol{n}}_1 ... d\hat{\boldsymbol{n}}_N \Psi_N(\boldsymbol{r}_1, ..., \boldsymbol{r}_N, \hat{\boldsymbol{n}}_1, ..., d\hat{\boldsymbol{n}}_N; t) \tag{3.A.4}$$

The pair body interactions that come from the potential need to be integrated weighted with the two-body distribution $\Psi_2(\boldsymbol{r}, \boldsymbol{r}', \hat{\boldsymbol{n}}, \hat{\boldsymbol{n}}')$. The one body froce $\boldsymbol{F}_1(\boldsymbol{r})$

$$\boldsymbol{F}_1 = -\int d\boldsymbol{r}' \partial_{\boldsymbol{r}'} U(\boldsymbol{r}, \boldsymbol{r}') \frac{\boldsymbol{r} - \boldsymbol{r}'}{|\boldsymbol{r} - \boldsymbol{r}'|} \Psi_2(\boldsymbol{r}, \boldsymbol{r}', \hat{\boldsymbol{n}}, \hat{\boldsymbol{n}}'; t) \tag{3.A.5}$$

There is a one body torque

$$\boldsymbol{\Gamma}_1 \cdot \hat{\boldsymbol{e}}_z = -\int d\boldsymbol{r}' \partial_\theta V(\boldsymbol{r}, \boldsymbol{r}') \frac{\boldsymbol{r} - \boldsymbol{r}'}{|\boldsymbol{r} - \boldsymbol{r}'|} \Psi_2(\boldsymbol{r}, \boldsymbol{r}', \hat{\boldsymbol{n}}, \hat{\boldsymbol{n}}'; t) \tag{3.A.6}$$

We now approximate the value of Ψ_2. We assume a stationary function that depends on the relative distance between positions $\boldsymbol{x} = \boldsymbol{r} - \boldsymbol{r}'$. We introduce angles ϕ as the angle between vectors $\boldsymbol{x}$ and $\boldsymbol{n}$, and θ as the angle between vectors $\boldsymbol{n}$, and $\boldsymbol{n}'$. The mean density of the system φ.

$$\Psi_2 \approx \varphi \Psi_1(\boldsymbol{x}) g(x, \phi, \theta) \tag{3.A.7}$$

With $g(x, \phi, \theta)$ the pair correlation function that includes the relative angle θ between active particles.

The computation of Ψ_1 introduce integrals over $v_0 \nabla_{\boldsymbol{r}} \boldsymbol{n} \Psi_N$. To proceed we introcuce the magnitudes ζ_p, and ζ_a

$$\boldsymbol{d} \cdot \boldsymbol{F}_1 = -\varphi \int_0^\infty x dx \int_0^{2\pi} d\phi \int_0^{2\pi} d\theta d\phi \cos(\phi) g(r, \phi, \theta) = -\varphi \Psi_1(\boldsymbol{r}) \zeta_p \tag{3.A.8}$$

$$M_1 = -\varphi \int_0^\infty x dx \int_0^{2\pi} d\phi \int_0^{2\pi} d\theta V'(\theta) g(r, \phi, \theta) = -\varphi \Psi_1(\boldsymbol{r}) \zeta_a \tag{3.A.9}$$

Vectors $\boldsymbol{n}$, and $\nabla \Psi_1$ define a non-orthornormal basis, $\langle \boldsymbol{n}, \nabla \Psi_1 \rangle$, of the cartesian plane. We now apply the Gram-Schmidt orthornormalization method to later extract independent projections on the relulting base $\{\boldsymbol{d}, \boldsymbol{v}_\perp\}$

$$\boldsymbol{v}_\perp = \nabla \Psi_1 - \frac{\boldsymbol{n} \cdot \nabla \Psi_1}{|\nabla \Psi_1|} \boldsymbol{n} \tag{3.A.10}$$

Now

$$\boldsymbol{F}_1 = (\hat{\boldsymbol{n}} \cdot \boldsymbol{F}_1) \hat{\boldsymbol{n}} + (\boldsymbol{F}_1 \cdot \boldsymbol{v}_\perp) \boldsymbol{v}_\perp / |\boldsymbol{v}_\perp|^2 \tag{3.A.11}$$

With vector $\boldsymbol{v}_\perp = \nabla \Psi_1 - \hat{\boldsymbol{n}} \cdot \nabla \Psi$. The modulus of the vector is easy to compute $|\boldsymbol{v}_\perp|^2 = |\nabla \Psi| \left(1 - |\hat{\boldsymbol{n}} \cdot \nabla \Psi_1|^2 / |\nabla \Psi_1|^2\right)$. The inverse is, to the first order in gradients $|\boldsymbol{v}_\perp|^{-2} = |\nabla \Psi_1|^{-2} \left(1 + \epsilon + \mathcal{O}(\epsilon^2)\right)$. Where $\epsilon < 1$ since it corresponds to the cosine of the angle defined by vectors $\hat{n}$, and $\nabla \Psi$. We do not consider $\epsilon = 1$ since this case corresponds to a case in which $\hat{\boldsymbol{n}}$ is parallel to $\nabla \Psi_1$ and the descomposition is nonsense.

$$(\boldsymbol{F}_1 \cdot \boldsymbol{v}_\perp) \boldsymbol{v}_\perp = \boldsymbol{F}_1 \cdot (\nabla \Psi_1 - \boldsymbol{n} \cdot \nabla \Psi_1 \boldsymbol{n}) (\nabla \Psi_1 - \boldsymbol{n} \cdot \nabla \Psi_1 \boldsymbol{n}) / |\nabla \Psi_1|^2 \tag{3.A.12}$$

$$(\boldsymbol{F}_1 \cdot \boldsymbol{v}_\perp)\, \boldsymbol{v}_\perp = \boldsymbol{F}_1 \left(\nabla\Psi_1 - \hat{\boldsymbol{n}} \cdot \boldsymbol{\nabla}\Psi_1 \hat{\boldsymbol{n}}\right) / \left|\nabla\Psi_1\right|^2 + \mathcal{O}(\left|\nabla\Psi_1\right|^2) \tag{3.A.13}$$

Using $D_0 + \frac{\nabla\Psi_1 - \hat{\boldsymbol{n}}\cdot\nabla\Psi_1\hat{\boldsymbol{n}}}{\left|\nabla\Psi_1\right|^2} \cdot \boldsymbol{F}_1 = D$ we write down the final equation for the one body probability field.

$$\partial_t \Psi_1 = -\nabla \cdot \left[\left(v_0 - \zeta_p \rho\right) \hat{\boldsymbol{n}} - D\nabla\right] \Psi_1 + \partial_\theta \left(\Gamma_0 \rho \zeta_a + D_r \partial_\theta\right) \Psi_1 \tag{3.A.14}$$

By a simple analogy between the terms $v_0 - \zeta\rho = v(\rho)$, and $\Gamma_a \rho \zeta_a$ we define $\Omega(\rho) = \Gamma_a \rho \zeta_a$. We are interesetd in fields that depend only in the position of measure. Thus, we need to integrate over the angles. To do so we project Ψ_1 onto Legendre Polynomials in $\hat{\boldsymbol{n}}$.

$$\Psi_1 = \rho + n_\alpha p_\alpha + \left(n_\alpha n_\beta - \frac{\delta_{\alpha\beta}}{2}\right) Q_{\alpha\beta} + \Theta[\Psi_1] \tag{3.A.15}$$

We may also define the equation in terms of the angle defined by $\hat{\boldsymbol{n}} = (\cos\theta, \sin\theta)$. We introduce Θ as the higher order multipoles of Ψ_1.

$$\Psi_1 = \rho + \begin{pmatrix} \cos\theta \\ \sin\theta \end{pmatrix} \cdot \boldsymbol{p} + \begin{pmatrix} \frac{1}{2}\cos 2\theta & \sin 2\theta \\ \sin 2\theta & -\frac{1}{2}\cos 2\theta \end{pmatrix} : \boldsymbol{Q} + \Theta[\Psi_1] \tag{3.A.16}$$

Projecting the equations on the Legendre Polynomials and using their definition we proceed to compute the dynamic equations for the coarse-grained fields:

$$\partial_t \rho = -\frac{1}{2}\partial_\alpha \left[v(\rho) p_\alpha\right] + \partial_\alpha D \partial_\alpha \rho \tag{3.A.17}$$

The angular contributions to the hydrodynamic equations come as follows. For the scalar field

$$f(\Omega) = \frac{1}{2\pi}\int_0^{2\pi} d\theta \partial_\theta \left(\Omega\rho\right) = 0 \tag{3.A.18}$$

For the vectorial field $\boldsymbol{g}(\Omega)$ we work with the components

$$g_x(\Omega) = \frac{1}{2\pi}\Omega \int_0^{2\pi} d\theta \cos\theta \partial_\theta \left(p_x \cos\theta + p_y \sin\theta\right) = \frac{1}{2}\Omega p_y \tag{3.A.19}$$

$$g_y(\Omega) = \frac{1}{2\pi}\Omega \int_0^{2\pi} d\theta \sin\theta \partial_\theta \left(p_x \cos\theta + p_y \sin\theta\right) = -\frac{1}{2}\Omega p_x \tag{3.A.20}$$

Introducing the skew-symmetrical tensor $S = \hat{\boldsymbol{e}}_x \otimes \hat{\boldsymbol{e}}_y - \hat{\boldsymbol{e}}_y \otimes \hat{\boldsymbol{e}}_x$ the equation for the change in polarization reads

$$\partial_t p_\alpha = -\partial_\alpha \left[v(\rho)\rho\right] - \omega_r p_\alpha + \partial_\beta D \partial_\beta p_\alpha - B_{\alpha\beta\gamma\delta}\partial_\beta \left(Q_\gamma \delta v(\rho)\right) + \frac{\Omega}{2} S_{\alpha\beta} p_\beta \tag{3.A.21}$$

Finally we compute the integrals for the magnetic order parameter projecting on $\cos 2\theta$, and $\sin 2\theta$

$$h_{xx}(\theta) = \frac{\Omega}{2\pi}\int_0^{2\pi} d\theta \cos 2\theta \partial_\theta \left(\sin 2\theta Q_{xy} + \sin 2\theta Q_{yx}\right) = \Omega \frac{Q_{xy} + Q_{yx}}{2} \tag{3.A.22}$$

To obtain

$$\partial_t Q_{\alpha\beta} = -\frac{1}{2}B_{\alpha\beta\gamma\delta}\partial_\gamma \left[v(\rho)p_\delta\right] - 4\omega_r Q_{\alpha\beta} + \partial_\gamma D \partial_\gamma Q_{\alpha\beta} + \frac{1}{2}\left(S_{\alpha\gamma}S_{\gamma\alpha} - Q_{\alpha\gamma}S_{\gamma\beta}\right) \tag{3.A.23}$$

Plus higher order fluxes $-\partial_\gamma J_{\alpha\beta\gamma}$.

3.B Aligning interactions in active dumbbells

In this section we motivate through a practical and common active matter system the presence of interaction torques between their constituting agents. Here we derive the appearance of a nematic interaction between colliding active particles without hydrodynamics.

Two bead systems are common in the active particle literature [Suma et al., 2014, Gonnella et al., 2014], even more general configurations such as active rods of multiple beads have been considered [Kaiser et al., 2013]. We define a dumbbell by the position of its centre of mass $\boldsymbol{r}_i$ and the vector that connects the centres of masses, the orientation vector $\boldsymbol{\delta}_i$. The beads of a dumbbell are defined by a pair of vectors $\boldsymbol{q}_i^\alpha$ with α where a stands for the head, and b for the tail.

$$\begin{cases} \boldsymbol{q}^a = \boldsymbol{r}_i + \boldsymbol{\delta}_i/2 \\ \boldsymbol{q}^b = \boldsymbol{r}_i - \boldsymbol{\delta}_i/2 \end{cases} \tag{3.B.1}$$

To keep δ_i within a range we introduce an elastic interaction $\boldsymbol{F}_i^{e,\alpha}$ at each constituent of the rod so that $\langle\delta\rangle = \delta_0$.

$$\begin{cases} \boldsymbol{F}^{e,a} = -K\left(\delta_i - \delta_0\right)\hat{\boldsymbol{\delta}}_i \\ \boldsymbol{F}^{e,b} = K\left(\delta_i - \delta_0\right)\hat{\boldsymbol{\delta}}_i \end{cases} \tag{3.B.2}$$

The simplest function to define the dumbbell is a linear spring which introduces a force proportional to the deviation relative to the rest value δ_0. In thermal equilibrium fluctuations of $\left\langle\delta^2\right\rangle$ are proportional to k_BT/K. It is common to choose a divergent potential, the FENE potential, with a characteristic length l_0.

$$F(r, l_0) = \frac{Kr}{1 - \left(r/l_0\right)^2} \rightarrow F(r < l_0, l_0) = Kr \tag{3.B.3}$$

We introduce an excluded volume interaction for pairs of dumbbells $F_{ij}^{\alpha\beta}$ in the direction of $\boldsymbol{r}_{ij}^{\alpha\beta} = \boldsymbol{q}_j^\beta - \boldsymbol{q}_i^\alpha$

$$F_{ij}^{\alpha,\beta} = 24\frac{\epsilon}{\sigma}\left[2\left(\frac{\sigma}{r}\right)^{13} - \left(\frac{\sigma}{r}\right)^7\right] \tag{3.B.4}$$

For simplicity we choose shifted Lennard-Jones potential truncated at $r = 2^{1/6}\sigma$. We tune the strength of the potential with ϵ. The total repulsive force acting on

monomer $\boldsymbol{q}_i^\alpha$

$$\boldsymbol{F}_i^\alpha = \sum_{j\neq i}\sum_\beta F_{ij}^{\alpha\beta}\hat{\boldsymbol{r}}_{ij}^{\alpha\beta} \tag{3.B.5}$$

From the dumbbell coordinates $\boldsymbol{r}$, and $\boldsymbol{\delta}$ the repulsion force introduces an interaction torque on $\boldsymbol{\delta}$.

$$2\boldsymbol{\Gamma}_i = \boldsymbol{\delta}_i \times \boldsymbol{F}_i^a - \boldsymbol{\delta}_i \times \boldsymbol{F}_i^b \tag{3.B.6}$$

Finally we introduce thermal fluctuations on $\boldsymbol{q}_i^\alpha$ with a characteristic strength $\sqrt{2D_0}$. With a random vector $\boldsymbol{\xi}_i^\alpha$ with fluctuations $\left\langle \boldsymbol{\xi}_j^\alpha(t)\boldsymbol{\xi}_j^\beta(t')a \right\rangle = \delta_{ij}\mathbf{I}\delta_{\alpha\beta}\delta(t-t')$. The Brownian equations for $\boldsymbol{q}_i^\alpha$ are

$$\frac{d\boldsymbol{q}_i^\alpha}{dt} = \mu\boldsymbol{F}_i^{e,\alpha} + \mu\boldsymbol{F}_i^\alpha + \sqrt{2D_0}\boldsymbol{\xi}_i^\alpha \tag{3.B.7}$$

The equations for the center of mass $\boldsymbol{r}_i$ will introduce the total force on the center of mass $\boldsymbol{\Phi}_i = \boldsymbol{F}_i^a + \boldsymbol{F}_i^b$ and an effective diffusion constant D_T. We introduce $\hat{\boldsymbol{\delta}}_i = (\cos\theta_i, \sin\theta_i)$.

$$\frac{d\boldsymbol{r}_i}{dt} = \mu_T\boldsymbol{\Phi}_i + \sqrt{2D_T}\boldsymbol{\xi}_i(t) \tag{3.B.8}$$

$$\frac{d\theta_i}{dt} = \mu_r\Gamma_i + \sqrt{2D_\theta}\nu_i(t) \tag{3.B.9}$$

The dynmic equation for the dimer separation introduces a noise $\zeta_i(t)$ which we do not specify.

$$\frac{d\delta_i}{dt} = -2\mu_d K\left(|\boldsymbol{\delta}_i| - \delta_0\right) + \mu_d\hat{\boldsymbol{\delta}}_i\cdot\left(\boldsymbol{F}^a - \boldsymbol{F}^b\right) + \zeta_i(t) \tag{3.B.10}$$

Now we have obtained the equations of motion for an equilibrium suspension of dumbbells. To drive the system out-of-equilibrium we need to introduce an additional force to each dumbbell. Now we introduce three different mechanisms "H", for a head propelled dumbbell adding $v_a\hat{\boldsymbol{\delta}}_i$ to $\dot{\boldsymbol{q}}_i^a$; "T" for a tail propelled dumbbell adding $v_a\hat{\boldsymbol{\delta}}_i$ to $\dot{\boldsymbol{q}}_i^b$, and "B" for a body propelled dumbbell adding $v_a\hat{\boldsymbol{\delta}}_i$ to both $\dot{\boldsymbol{q}}^\alpha$. With the propulsion, the final equation for the dumbbell now introduces

$$\frac{d\boldsymbol{r}_i}{dt} = v_a\hat{\boldsymbol{\delta}}_i + \mu_T\boldsymbol{\Phi}_i + \sqrt{2D_T}\boldsymbol{\xi}_i(t) \tag{3.B.11}$$

$$\frac{d\theta_i}{dt} = \mu_r\Gamma_i + \sqrt{2D_\theta}\nu_i(t) \tag{3.B.12}$$

In addition we can introduce wall to confine the system. If we introduce a wall at $y=0$, and $y=L$. The repulsive force that the walls introduce are

$$\boldsymbol{F}_i^{w,\alpha} = F_W(y_i^\alpha)\hat{\mathbf{y}} - F_W(L-y_i^\alpha)\hat{\mathbf{y}} \tag{3.B.13}$$

For simplicity we can define F_W to be a WCA repulsive force –the same that guarantees excluded volume.

Once again the interaction introduces a torque to each dumbbell.

$$2\boldsymbol{\Gamma}_i^w = \boldsymbol{\delta}_i \times \boldsymbol{F}_i^{w,a} - \boldsymbol{\delta}_i \times \boldsymbol{F}_i^{w,b} \tag{3.B.14}$$

3.B.1 Relative torque between dumbbells

We compute the torque between a pair of dumbbells. A particle with propulsion velocity v_a in the direction defined by the director $\boldsymbol{\delta}_1$ collides with a second dumbbell defined by the director $\boldsymbol{\delta}_2$. The interaction for two incoming dumbbells is between Head and Head or between Head and Tail.

For an acute Head to Head interaction the propulsion velocity that is not compensated by repulsion of both dumbbells gives a neat velocity to the centres of mass and so they travel together with an aligning torque, see plot **B** in Figure 3.B.1. In the absence of thermal fluctuations or interactions with other dumbbells the pair will align and travel together, forever. In the presence of thermal fluctuations – as a competition between angular diffusion, elongation, and propulsion – the couple can break. For Head to Tail interactions the aligning torque aligns the pair during the collision while the propulsion forces that are not compensated by the interactions – the projections on the direction perpendicular to $\hat{\boldsymbol{r}}$ – are antiparallel and thus, dumbbells will separate. In this situation torque bends the trajectories of incoming dumbbells, see plot **A** in Figure 3.B.1.

Now we compute the relative torque of interaction for a collision of two incomming dumbbells. The general Head-Head collision between dumbbells is depicted in Figure 3.B.1.

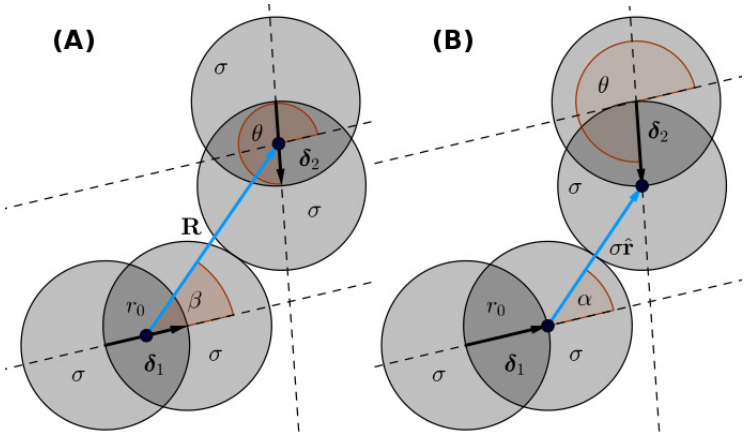

Figure 3.B.1 | Collision between a pair of dumbbells with director vectors $\hat{\boldsymbol{\delta}}_1$, and $\hat{\boldsymbol{\delta}}_2$. Vector $\boldsymbol{u} = \hat{\boldsymbol{\delta}}_2 - \hat{\boldsymbol{\delta}}_1$ defines the angle θ. **(A)** Interaction relative to the center of mass of each dumbbell, center-to-center vector $\boldsymbol{R}$ with norm d and angle β relative to θ_1. **(B)** Interaction relative to the center of each bead of the dumbbell with the angle α.

We introduce dumbbells with directors $\hat{\boldsymbol{\delta}}_1$, and $\hat{\boldsymbol{\delta}}_2$ with orientations θ_1, and θ_2 relative to the horizontal. Interaction is defined by vector $\hat{r}$ with orientation α relative to the horizontal. A bead of the dumbbell contributes to the interaction

if the projections $\boldsymbol{F}_1 \cdot \hat{\boldsymbol{r}} > 0$, and $\boldsymbol{F}_2 \cdot \hat{\boldsymbol{r}} < 0$. The overall interaction is $2F_r = (F_r^{(2)}\theta(\hat{\boldsymbol{\delta}}_2 \cdot \hat{\boldsymbol{r}}) - F_r^{(1)})\theta(-\hat{\boldsymbol{\delta}}_1 \cdot \hat{\boldsymbol{r}})$ with F_r the repulsive interaction acting on each bead. We now compute the case for two heads pushing.

$$F_r^{(1)} = F_a\hat{\delta}_1 \cdot \hat{\boldsymbol{r}}; \quad F_r^{(2)} = F_a\hat{\delta}_2 \cdot \hat{\boldsymbol{r}}; \qquad 2F_r = \left(F_r^{(1)} - F_r^{(2)}\right) \tag{3.B.15}$$

The repulsive force on the heads is $\boldsymbol{F}^{(1)} = -F_r\hat{\boldsymbol{r}}$, and $\boldsymbol{F}^{(2)} = F_r\hat{\boldsymbol{r}}$. We compute the torque at the center of mass of each dumbbell $\boldsymbol{\Gamma}_z^{(i)}$ – the position vector is $-\boldsymbol{\delta}_i/2$. Since the system lives in a two dimensional plane, the toque is in the direction of $\hat{\boldsymbol{z}}$.

$$\begin{aligned}\boldsymbol{\Gamma}^{(1)} =& -1/2\boldsymbol{\delta}_1 \times \boldsymbol{F}^{(1)} = -\frac{r_0F_a}{4}\left(\hat{\boldsymbol{\delta}}_1 - \hat{\boldsymbol{\delta}}_2\right) \cdot \hat{\boldsymbol{r}}\left(\hat{\boldsymbol{\delta}}_1 \times \hat{\boldsymbol{r}}\right)\\ \boldsymbol{\Gamma}^{(2)} =& 1/2\boldsymbol{\delta}_2 \times \boldsymbol{F}^{(2)} = \frac{r_0F_a}{4}\left(\hat{\boldsymbol{\delta}}_1 - \hat{\boldsymbol{\delta}}_2\right) \cdot \hat{\boldsymbol{r}}\left(\hat{\boldsymbol{\delta}}_2 \times \hat{\boldsymbol{r}}\right)\end{aligned} \tag{3.B.16}$$

The relative torque of interaction is given by $\boldsymbol{\Gamma}$. We define vector $\boldsymbol{u} = \hat{\boldsymbol{\delta}}_2 - \hat{\boldsymbol{\delta}}_1$ as the difference between orientation vectors.

$$\boldsymbol{\Gamma} = \frac{r_0F_a}{4}\left(\boldsymbol{u} \cdot \hat{\boldsymbol{r}}\right)\left(\hat{\boldsymbol{r}} \times \boldsymbol{u}\right) \tag{3.B.17}$$

Vector $\boldsymbol{u}$ is defined by the angle $\theta = \theta_2 - \theta_1$. The angle between $\boldsymbol{u}$, and $\hat{r}$ is $\omega = \theta - \alpha$. The relative torque of interaction is $\Gamma(\alpha, \theta) = -1/4r_0F_a\left|\boldsymbol{u}\right|^2 \sin\omega\cos\omega$

$$\hat{\boldsymbol{z}} \cdot \boldsymbol{\Gamma}(\alpha, \theta) = -\frac{r_0F_a}{2}\sin^2\left(\theta/2\right)\sin 2\left(\theta - \alpha\right) \tag{3.B.18}$$

This expression if valid for the range of parameters $\cos\alpha > 0$, and $\cos\Omega < 0$. On the other hand, the interaction has a specific range of angles in wich there is no overlap. We define $\alpha_c = \arccos\left(-r_0/(2\sigma)\right)$, and $\theta_c = \arccos\left(r_0/(2\sigma)\right)$. The interacion is allowed for $\alpha \in [-\alpha_c, \alpha_c]$, and $\theta \in [\alpha + \theta_c, \alpha + (2\pi - \alpha_c)]$.

To conclude, we introduce the interaction as a function of the center of mass of the dumbbell $\hat{\boldsymbol{r}} = \left(\boldsymbol{R} + \hat{\boldsymbol{u}}r_0/2\right)/\sigma$. We define $\Omega = \theta - \beta$ with $\boldsymbol{R} = d(\cos\beta\hat{\boldsymbol{x}} + \sin\beta\hat{\boldsymbol{y}})$.

$$\begin{aligned}\boldsymbol{\Gamma} =& \frac{F_ar_0}{4}\left[\boldsymbol{u} \cdot \left(\boldsymbol{R} + \boldsymbol{u}\frac{r_0}{2}\right)\right]\left[\left(\boldsymbol{R} + \frac{r_0}{2}\boldsymbol{u}\right) \times \boldsymbol{u}\right]\sigma^{-2} =\\ =& \frac{F_ar_0}{4}\left(\boldsymbol{u} \cdot \boldsymbol{R} + \boldsymbol{u}^2\frac{r_0}{2}\right)\left(\boldsymbol{R} \times \boldsymbol{u}\right)\sigma^{-2}\end{aligned} \tag{3.B.19}$$

Introducing $\boldsymbol{u}^2 = 2\left(1 - \cos\theta\right) = 4\sin^2(\theta/2)$ the equation reads

$$\hat{\boldsymbol{z}} \cdot \boldsymbol{\Gamma} = -\frac{r_0F_a}{4}\left(\left(\frac{d}{\sigma}\right)^2\sin^2(\theta/2)\sin 2\Omega + 16\frac{dr_0}{\sigma^2}\sin^4(\theta/2)\sin\Omega\right) \tag{3.B.20}$$

4 Granulars

4.1 Introduction

Granular matter has attracted some attention because of its different nature compared to the solid, liquid and gas state [Jaeger et al., 1996]. When shaken, it is brought out-of-equilibrium – there is a flux of energy from the container to the agents and dissipated in their contact interactions. A striking phenomena occurs in mixtures of particles where shaking may lead to species separation ranging from clusters to stripes [Ottino and Khakhar, 2000, Kudrolli, 2004, Aranson and Tsimring, 2006]. The best known manifestation of this granular separation is the so called Brazil nut effect [Godoy et al., 2008, Ciamarra et al., 2006b, Sanders et al., 2004]. For horizontally driven matter, gravity is no longer a relevant player, and a mixture can phase separate into stripes orthogonal to the shaking direction [Mullin, 2000, Pica Ciamarra et al., 2007], or even form clusters for swirling shaking [Aumaître et al., 2001b]. The ability to demix can be directly applied to industrial purposes or be used to explain stratification in terrestrial environments or may play a relevant role in asteroid or planetoid formation.

In the non-equilibrium state of shaking, granular matter has been reported to fluidize – for vertical and horizontal [Salueña et al., 1999, Pöschel et al., 2000, Ristow et al., 1997] forcing. In the fluidized regime density fluctuations have been reported and then Casimir-like scenarios [Kardar and Golestanian, 1999] open for internal interactions among grains [Cattuto et al., 2006].

In a granular system there is an interplay between its internal constituents and the boundaries of the system. The flow though a bottleneck, like the flow of sand in

a hourglass, can be spontaneously interrupted [Masuda et al., 2014, Lozano et al., 2012]. The nature of the interruption can change under shaking –the system can spontaneously unclog and flow until the next clog is formed. The formation of stable arch structures before the bottleneck has been correlated to the clogging of the system and it is a generic mechanism in many systems [Zuriguel et al., 2014].

The band segregation for a binary mixture of horizontally agitated granular matter has been explained [Ciamarra et al., 2006a] for attractive and anisotropic pairwise interactions between the intruders. In a dense system of poppy seeds and two metallic spheres it has been reported an effective attractive interaction [Lozano et al., 2015]. Spheres tended to stay together. This result has lead us to the simulation of the free movement of two intruders in a bed of granular particles. We have extracted the interaction forces that arise between intruders for different configurations and obtained not only anisotropic radial forces but long range interactions and aligning torques.

In this Chapter we introduce a dissipative granular media under horizontal shaking, see Section 4.2. In section **??**, we use the bed of driven granular particles to study the free movement of a pair of intruder particles and identify a long range, $\ln P(r) \sim 1/r$, decay of the probability to locate particles separated a distance r with a strong anisotropic character. To fully characterize the interaction force, in Section 4.6, we fix dimers in several configurations of distance and angle relative to the shaking. As a result, we are able to express the radial, long range, force as a function of the shaking amplitude and angle. Finally, we study the local fields of density and kinetic energy to find the appearance of a gradient in the kinetic energy along the axis of the dimer but not a deviation in the density. We then relate the energy and density profiles of a system of two particles to the density profile of a single intruder system.

4.2 Model

The experimental set-up considers a binary mixture of kidney shaped poppy seeds and bronze spheres on top of an oscillation tray, see Figure 4.1 **A**, and **B**. Grains, poppy seeds, are irregular in shape, see inset **D**, with typical diameters between $0.5\ mm$, and $1\ mm$, low density $\rho = 0.2\ g\ cm^{-3}$, and hence have a high friction with the flat bottom surface. We propose to two dimensional model for the poppy seeds and spheres lying on the tray. We introduce rains as disks of diameter σ_g, and a friction coefficient with the tray. Bronze spheres, as seen in **C**, are smooth and with a typical diameter $1.5\ mm$, high density $\rho \approx 8.8\ g\ cm^{-3}$, and easily rotate on a flat surface [Reis et al., 2004]. To model the excluded volume surrounding the spheres we propose to model them as disks of diameter σ.

The peculiarity of the system is the external driving, the horizontal shaking.

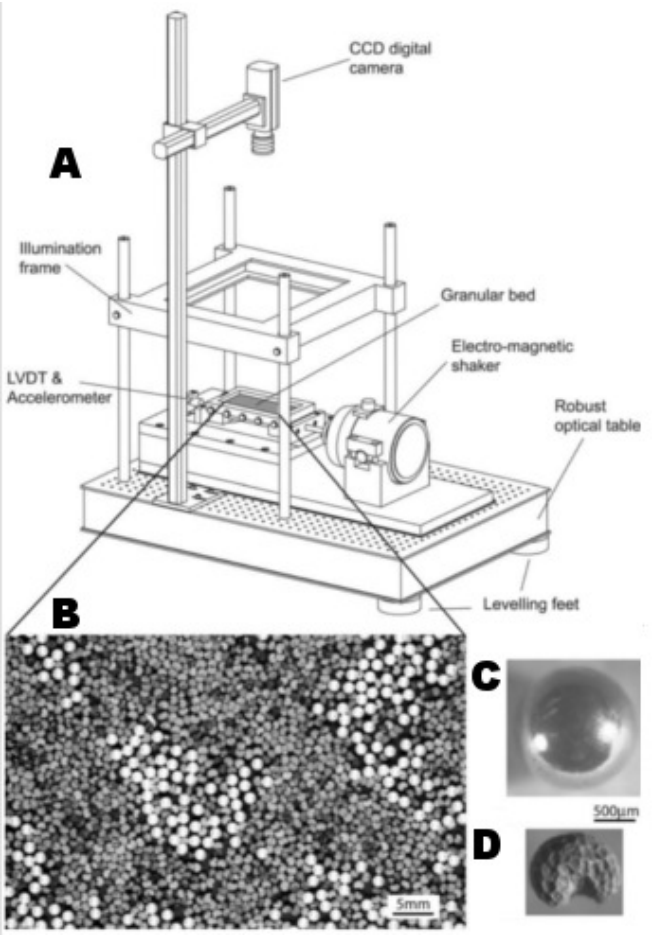

Figure 4.1 | Experimental set up. Experiments on granular segregation of spheres in a bed of poppy seeds from [Reis et al., 2006]. In **A** the experimental apparatus with the acquisition camera, the tray for the granular mixture, and the shaker. In **B** a capture of the granular bed with poppy seeds in gray, and spheres in white. Photograph of a sphere **C**, and a poppy seed **D**.

The bottom surface of the experiment is constantly horizontally vibrated, and we propose different responses for grains, and spheres. Irregularities in the poppy seed surface, large contact surface with the tray, introduce a friction coefficient with the tray, do not facilitate rotation, and thus follow the motor oscillations in contact with the tray. Spheres, however, present a contact point with the bottom surface and for a finite friction with the tray, and thus rotate to maintain the centre of mass at a constant position.

Then, we introduce excluded volume with repulsive forces. Collisions between cause an elastic deformation of the grains, problem initially posed by Hertz [Hertz, 1882], and treated again by [Love, 2013]. The collision in a viscoelastic material introduces a plastic deformation with a restitution coefficient proportional to the relative velocity [Kuwabara and Kono, 1987]. Interactions between particles incorporate an elastic repulsive force, and a velocity dependent dissipative force.

To account for shape irregularities and the roughness of grains we introduce random forces to both grains and inclusions. Random forces also account for three dimensional effects in the collisions, manifested in vertical velocities which a 2d model cannot cope with.

Altogether, we model the effects of horizontal periodic forcing of the tray on the grains and spheres. This model permits to measure the kinetic energy, and local density of the grains; it captures the dynamics of spheres in a bed of shaken grains; and, finally it also determines the forces acting spheres and grains.

4.2.1 Equations of motion

The temporal evolution of grains and spheres is determined by Newton's equations of motion in the laboratory frame of reference. Unlike the rest of the systems presented in this thesis, the system is not over-damped by a viscous fluid and we cannot neglect the inertial effect.

We introduce gains as N disks at position $\boldsymbol{x}$ in a 2d periodic square box of side L. Each grain with diameter σ_i, where σ_i are drawn from a uniform distribution with $\langle\sigma\rangle = \sigma_g$ and a dispersion of 10%. Grains have mass $m_i = m_0 \left(\sigma/\sigma_g\right)^3$. Spheres, also referred to as inclusions, are introduced as disks of diameter σ at with centre of mass at positions $\boldsymbol{X}$ and mass M[1].

$$m_i \frac{d^2\boldsymbol{x}_i}{dt^2} = -\gamma_{s,i}\left(\frac{d\boldsymbol{x}_i(t)}{dt} - \mathbf{v}_s(t)\right) + \boldsymbol{F}_i^c + \boldsymbol{F}_i^d + \boldsymbol{F}_i^r \tag{4.1}$$

$$M \frac{d^2\boldsymbol{X}_i}{dt^2} = -\gamma_s \frac{d\boldsymbol{X}_i(t)}{dt} + \boldsymbol{F}_i^c + \boldsymbol{F}_i^d + \boldsymbol{F}_i^r \tag{4.2}$$

[1]The mass ratio M/m is given by the density and size ratio of the particles

Where $\boldsymbol{v}_s$ is the tray velocity which follows the periodic form in the direction of $\hat{\boldsymbol{x}}$, $\boldsymbol{v}_s(t) = A_0\omega\sin(\omega t)\hat{\boldsymbol{x}}$, where A_0 is the oscillation amplitude, and $\omega/2\pi$ the shaking frequency of oscillation. The dissipation with the bottom surface of the container is introduced by γ_s. Grains follow the external forcing and dissipate energy for particle velocities relative to $\boldsymbol{v}_s$, as stated in the first term in the rhs of (4.1). Spheres, however, dissipate energy for displacements relative the laboratory frame of reference.

Interaction between pairs of grains incorporate an elastic repulsive force $\boldsymbol{F}^c$, and a dissipative force $\boldsymbol{F}^d$. Interactions activate when grains overlap [Hidalgo et al., 2009, Pöschel et al., 2000]. We introduce the compression [Pöschel and Schwager, 2005] of two particles, $\xi_{ij} = |\mathbf{x}_{ij}| - (\sigma_i + \sigma_j)/2$, to determine the interactions between pairs we introduce a linear spring-dashpot model for the interaction with $\boldsymbol{F}^c$

$$\boldsymbol{F}_i^c = \sum_i k_{eff}\xi_{ij}\theta(\xi_{ij})\,\hat{\mathbf{n}}_{ij} \tag{4.3}$$

the elastic force, with k_{eff} a material dependent parameter, and $\boldsymbol{F}^d$

$$\boldsymbol{F}_i^d = \sum_i \gamma(\mathbf{v}_{ij}\cdot\mathbf{n}_{ij})\,\theta(\xi_{ij})\,\mathbf{n}_{ij} \tag{4.4}$$

the dissipative force dependent on the relative velocity during the overlap $\boldsymbol{v}_{ij} = \boldsymbol{v}_i - \boldsymbol{v}_j$.

When particles collide and the relative velocity increases the overlap, the dissipative force acts in the same direction than the elastic force opposing to the relative velocity between particles, and dissipates kinetic energy. After the maximum of compression elastic energy pushes particles apart and changes the sign of the relative velocity. In the separation, the sign $\boldsymbol{F}^d$ is opposed to the elastic force and may lead to numerical artefacts, the two particles glued together by $\boldsymbol{F}^c$, and $\boldsymbol{F}^d$. To avoid this situation, and as proposed by [Pöschel and Schwager, 2005], we use the total force of interaction $\max(0, (\boldsymbol{F}^c + \boldsymbol{F}^d)\cdot\hat{\boldsymbol{n}})$.

Random force, $\boldsymbol{F}^r$, originated by irregularities in the grains and vertical movements is introduced by a Gaussian noise source for each component of the particle $\langle F_i^r(t)F_j^r(t')\rangle = \sqrt{2\Lambda_\alpha}\delta_{ij}\delta_{\alpha\beta}\delta(t-t')$. We generalize the noise so that fluctuations in the shaking direction Λ_x may be different than fluctuations in the perpendicular one.

4.2.2 Integration of the granular equations of motion

To integrate the of the equation of motion (4.1,4.2) for grains and inclusions, we have devised a numerical scheme to cope with the stochastic force, dissipation, and acceleration. Numerical integration of the equations of motion gives us access to

the evolution of positions, velocities, and forces of each particle to later extract relevant measures.

The integrator for the over-damped systems presented in the previous Chapters implemented a two-step Euler scheme. By an Euler step from t to $t + \Delta t$ we computed virtual positions for the particles. The average of forces at t, and $t + \Delta t$ gave the total force for the final Euler step. To solve the equations of motion with acceleration we write down the second order differential Langevin equation as a pair of first order differential equations for the momenta $\boldsymbol{p} = m\boldsymbol{v}$. The first equation corresponds to the definition of linear momentum of each particle

$$\frac{d}{dt}\boldsymbol{r}_i = \frac{1}{m_i}\boldsymbol{p}_i \tag{4.5}$$

And the second equation introduces the relevant forces acting on the particles. With $\boldsymbol{F}_i$ we denote the deterministic forces acting on a particle (conservative repulsion and contact dissipation); with $\boldsymbol{f}_i$ the stochastic forces of multiple origins. Finally, we account for the forcing of the system with the term $\boldsymbol{p}/m - \boldsymbol{v}_s$ where $\boldsymbol{v}_s$ is the velocity of the tray: typically a sinusoidal velocity.

$$\frac{d}{dt}\boldsymbol{p}_i = \boldsymbol{F}_i - \gamma\left(\frac{\boldsymbol{p}_i}{m_i} - \boldsymbol{v}_s\right) + \boldsymbol{f}_i \tag{4.6}$$

We integrate the equation for the positions a time step Δt to compute virtual positions at $t + \Delta t/2$.

$$\boldsymbol{r}_i(t + \Delta t/2) = \boldsymbol{r}_i(t) + \frac{\Delta t}{2}\frac{\boldsymbol{p}_i}{m_i} \tag{4.7}$$

To solve the equation for the momenta $\boldsymbol{p}_i$ we separate the terms that depend on $\boldsymbol{p}_i$ and the forces into deterministic $\boldsymbol{\Phi}_i = \boldsymbol{F}_i + \gamma_i\boldsymbol{v}_s$ and stochastic $\boldsymbol{f}_i$.

$$\left(\frac{d}{dt} + \frac{\gamma_i}{m_i}\right)\boldsymbol{p}_i = \boldsymbol{F}_i + \gamma_i\boldsymbol{v}_s + \boldsymbol{f}_i = \boldsymbol{\Phi}_i + \boldsymbol{f}_i \tag{4.8}$$

The liniear equation for $\boldsymbol{p}$ is direct and consists of a homogeneous and a particlular solution. The homogeneous solution for $\boldsymbol{p}_i(t + t_0)$

$$\boldsymbol{p}_i(t + \Delta t) = \boldsymbol{p}(t)\exp\left[\frac{\gamma_i}{m_i}\Delta t\right] \tag{4.9}$$

We propose an ansatz for the particular solution of the momenta introducing a function $\boldsymbol{\pi}(t)$, $\boldsymbol{p}_i^p = \boldsymbol{\pi}(t)\exp -\gamma_i/m_i t$. Inserting the particular solution into the equation for $\boldsymbol{p}_i$ gives the functional form of the auxiliary function $\boldsymbol{\pi}_i$.

$$\frac{d}{dt}\boldsymbol{\pi}_i(t) = \exp\left(\frac{\gamma_i}{m_i}t\right)(\boldsymbol{\Phi}_i + \boldsymbol{f}_i) \tag{4.10}$$

The term with the deterministic force $\mathbf{\Phi}_i$ gives

$$\boldsymbol{\pi}_i(t) = \boldsymbol{\pi}_i(t_0) + \frac{m_i}{\gamma_i}\left[\exp\left(\frac{\gamma_i \Delta t}{m_i}\right) - 1\right]\mathbf{\Phi}_i(t_0) + \int_{t_0}^{t} d\tau \exp\left[\frac{-\gamma_i\left(\Delta t - \tau\right)}{m_i}\right]\boldsymbol{f}_i(\tau) \tag{4.11}$$

To simplify further computations we define the following magnitudes. The dissipation of the momenta is introduced by $\Gamma_i = \exp\left(-\gamma_i \Delta t / m_i\right)$. A rescaled mobility coefficient for the deterministic force $\tilde{\mu}_i = \left(1 - \Gamma_i\right)/\gamma_i$. Finally, and effective diffusion coefficient $\tilde{D}_i = \left(\Gamma_i m_i/\gamma_i\right)^{1/2}\left(1 - \Gamma_i^2\right)^{1/2}$.

$$\boldsymbol{p}_i(t + \Delta t) = \Gamma_i \boldsymbol{p}_i(t) + \tilde{\mu}_i m_i \Phi_i + \tilde{D}_i \boldsymbol{\zeta}_i \tag{4.12}$$

To integrate the stochastic force we have computed the second moment $\sigma^2_{\alpha\beta ij} = \langle p_{i\alpha}(t) p_{j\beta}(t + \Delta t)\rangle - \langle p_{i\alpha}(t)\rangle \langle p_{j\beta}(t + \Delta t)\rangle$.

$$\sigma^2 = \int_0^{\Delta t} dt \int_0^{\Delta t} dt' \exp\left[-\frac{\gamma_i}{m_i}\left(\Delta t - t\right)\right]\exp\left[-\frac{\gamma_i}{m_i}\left(\Delta t - t'\right)\right]\langle f_{i\alpha} f_{j\beta}\rangle \tag{4.13}$$

$$\sigma^2_{ij\alpha\beta} = \frac{\Gamma_i m_i}{\gamma_i}\delta_{ij}\delta_{\alpha\beta}\left[1 - \exp\left(-\frac{2\gamma_i}{m_i}\Delta t\right)\right] \tag{4.14}$$

Then we introduced $\boldsymbol{\zeta}$ as a random Gaussian variable with zero mean and $\langle \zeta_{i,\alpha}(t)\zeta_{j,\beta}(t')\rangle = 2\Lambda_{i,\alpha}\delta_{ij}\delta_{\alpha\beta}\delta(t - t')$. We keep the possibility to introduce asymmetric fluctuations in the form of Λ.

Once we have a prediction for the evolution of the momenta of the particles we integrate the equations of motion with the information $\boldsymbol{p}(t)$, and $\boldsymbol{p}(t + \Delta t)$.

$$\boldsymbol{r}_i(t + \Delta t/2) = \boldsymbol{r}_i(t) + \frac{\Delta t}{2}\frac{\boldsymbol{p}_i(t)}{m_i} \tag{4.15}$$

$$\boldsymbol{p}(t + \Delta t) = \Gamma_i \boldsymbol{p}_i(t) + \tilde{\mu}_i m_i \mathbf{\Phi}_i(t) + \tilde{D}_i \boldsymbol{\zeta}_i(t) \tag{4.16}$$

$$\boldsymbol{r}(t + \Delta t) = \boldsymbol{r}_i(t + \Delta t/2) + \frac{\Delta t}{2m}\frac{\boldsymbol{p}_i(t) + \boldsymbol{p}_i(t + \Delta t)}{2} \tag{4.17}$$

4.2.3 System measurements

Numeric integration of the equations of motion gives access to the positions of grains and inclusions. Positions of particles provides the calculation the packing of particles, distributions of displacements after each cycle, and the Mean Squared Displacements for the bed of grains and inclusions. Measures of the velocity of particles provide information of the kinetic energy of the system, the characteristic energy of the granular bed. In experiments, positions and velocities are is accessible via image tracking.

In addition to positions and velocities, numeric integration of Newton's equations give the overall force on each particle. Total forces acting on the spheres, the

inclusions, reveal the interaction induced by the granular bed. Force measurements in experiments, though possible for static or slow moving configurations [Radjai et al., 1996, Løvoll et al., 1999, Majmudar and Behringer, 2005, Corwin et al., 2005], ar not available in shaken granular mixtures.

4.3 Zero inclusions

Shaking the system following $\boldsymbol{v}_s(t)$ introduces two possible definitions for the kinetic energy. An absolute kinetic energy $e_k(t)$, the kinetic energy of the particles relative to the laboratory frame of reference. Absolute kinetic energy introduces the total kinetic energy per grain of the system as measured from laboratory frame of reference. This energy is relevant for interactions with external bodies disconnected from the shaking. Relative kinetic energy $t_k(t)$, the kinetic energy of the particles relative to the tray frame of reference. Relative kinetic energy quantifies the sole strength of the random fluctuations, and the "thermalization" via collisions of the external energy influx of the velocity. The later is a relevant measure for granular interactions.

$$e_k(t) = \frac{1}{N_g} \int_t^{t+1} d\tau \sum_i \frac{1}{2} m \boldsymbol{v}_i^2 \tag{4.18}$$

$$t_k(t) = \frac{1}{N_g} \int_t^{t+1} d\tau \sum_i \frac{1}{2} m_i \left(\boldsymbol{v}_i - \boldsymbol{v}_s(\tau)\right)^2 \tag{4.19}$$

Computations of the kinetic energy at each shaking cycle are the average over the cycle. We use the period of oscillation as a computational time unit $(2\pi\omega)^{-1}$, the mean size of a grain as length unit σ_g and the mass of a grain of unit size σ_g as the mass unit m_0. In terms of these magnitudes we express the elastic constant k_{eff}, the dissipation constants γ and γ_s, and Λ_x to properly define the grains.

$$\phi = \frac{N_g \pi \sigma_g^2}{4L^2} \tag{4.20}$$

We characterize a granular bath at different shaking amplitudes for typical granular parameters found in the literature [Hidalgo et al., 2009, Salueña et al., 1999]. We have performed simulations of the granular bed at different shaking amplitudes A_0, packing density ϕ (4.20), and random noise Λ_x at either $\Lambda_x/\Lambda_y = 1$, and $\Lambda_x/\Lambda_y = 2$. We introduce the computations of kinetic energies to quantify the granular system at different packing densities, $\langle e_k \rangle$, and $t_k = \langle t_k \rangle$ are the time averaged energies over cycles.

In Figure 4.2 we plot the kinetic energies of the system for different shaking and noise amplitudes. As expected, by the addition of a dissipation constant the measured kinetic energy is below the expected value imposed by Λ. The average

kinetic energy keeps a constant value $\langle t_k \rangle \approx 0.9(\lambda_x \lambda_y)^{1/2}$ for $\phi_g < 0.6$. For higher packing fractions t_k decays, for particle collisions increase and so does the energy loss in interactions.

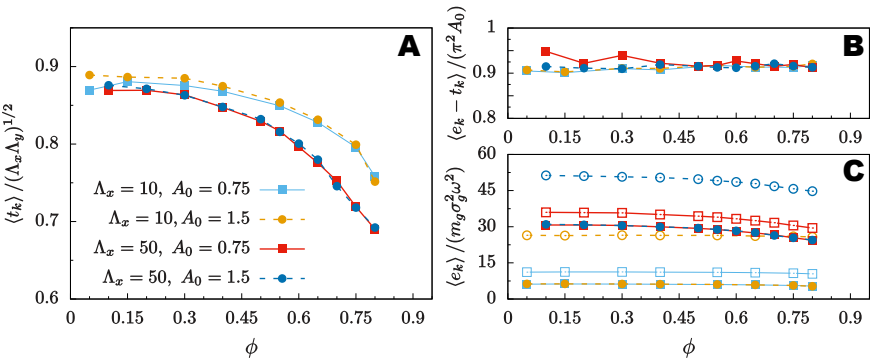

Figure 4.2 | Kinetic Energies of the granular bath. Kinetic energies as a function of the packing density for $\Lambda_x/\Lambda_y = 2$. **A** Relative kinetic energy scaled with the noise strength, Colours an line style indicate Λ_x, and shaking amplitude A_0. **B** Difference between the absolute and relative kinetic energies scaled with to the input forcing energy. **C** Kinetic energies as compared to the system units. Solid points indicate relative kinetic energy, and the absolute in hollow points.

As seen in Figure 4.2 the value of t_k does not depend on the shaking amplitude. The relation between the absolute kinetic energy $\langle e_k \rangle$ and the relative kinetic energy $\langle t_k \rangle$ is compatible with the *a priori* expectation

$$\langle e_k \rangle = \langle t_k \rangle + \int_0^1 d\tau \frac{1}{2} m_i \left(2\pi A_0\right)^2 \sin^2(2\pi\tau) \approx \langle t_k \rangle + \frac{1}{4}\pi A_0^2 m_g \qquad (4.21)$$

Absolute kinetic energy e_k increases as the shaking amplitude increases, as seen in **C** from Figure 4.2 but the difference $\langle e_k - t_k \rangle$ remains constant **B**.

The displacement of a particle after a complete shaking cycle, Δ, permits the measure of displacement distribution of granular particles. We track the displacement of granular particles after a shaking cycle. Gathering statistics over long times and all granular particles we obtain the distribution of displacements after a cycle $P(\Delta_x)$, and $P(\Delta_y)$. The distribution of displacements in Figure 4.3 shows a Gaussian behaviour for the displacements in th parallel and perpendicular directions for densities up to $\phi_g = 0.75$. This distribution originates a diffusive behaviour of particles at long times.

At $\phi_g = 0.80$, however, we observe a narrow distribution of displacements. This is associated to the formation of long lived structures trapping particles to undergo a subdiffusive process in the cages of the ordered structure. At large displacements, $1 < \Delta/\sigma_g < 2$, the probability widens. This situation corresponds

to jumps and exchange of particles in the structure.

We quantify the mobility of the grains, in the fluidized regime, with the diffusion coefficients extracted from the averaged mean squared displacements (MSD) in each dimension. For diffusive particles we expect a linear relation between the MSD, and time, $MSD_\alpha(\tau) = 2D_\alpha\tau$. At long times, we extract the D_x, and D_y as a function of the granular density, see Figure 4.4.

As a general rule, we observe a correlation between the diffusion coefficient scaled with the agitation noise D/Λ and the packing density. As density increases D/Λ diminishes. The correlation is high for D_x/Λ_x, and it is reduced in the case D_y/Λ_x. In Figure 4.4 we add a final plot with both D_x/Λ_x, and D_y/Λ_x for all densities, and shaking amplitudes to obtain an algebraic relation $D_x/\Lambda_x \sim (D_y/\Lambda_x)^\nu$. A logarithmic fit of the data gives an estimate of $\nu = 0.6$.

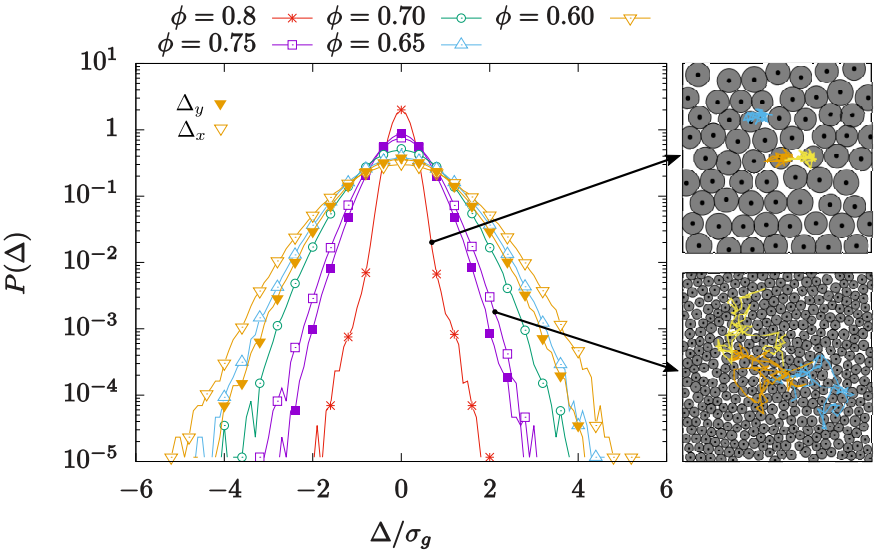

Figure 4.3 | Diplacement distribution after one cycle. $P(\Delta)$ for different concentration of grains. In solid points perpendicular displacements. We include snapshots of systems at $\phi_g = 0.75$, and $\phi_g = 0.80$ and trajectories of three particles.

4.4 One inclusion

In the last section have introduced the granular system, the bed of grains, and the measures of kinetic energy of the grains. The aim of this Chapter is to study the interaction between a pair of inclusions induced by external driving of the grains. Once the system has been characterized, the second step prior to introduce the pair

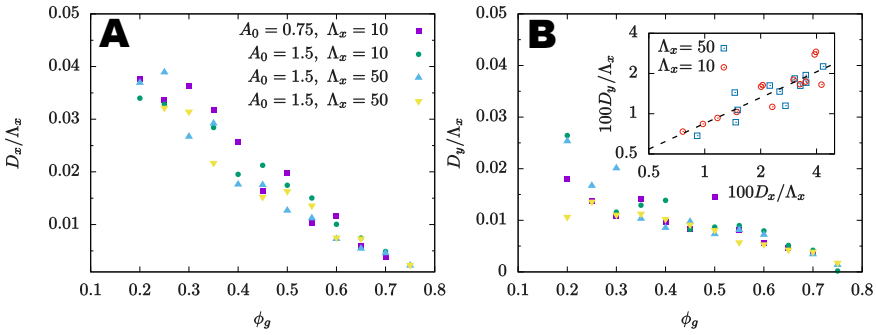

Figure 4.4 | Diffusion of grains. Parallel and perpendicular diffusion coefficients D_x, and D_y scaled to the noise strength Δ_x for different A_0, and Λ_x. In **A** the parallel diffusion shows a decay as density increases. In **B** the perpendicular diffusion D_y. In the inset the values of D_x, and D_y for the densities, and shaking amplitudes. The relation $D_y/\Lambda_x \sim (D_x/\Lambda_x)^\nu$ with $\nu = 0.6$

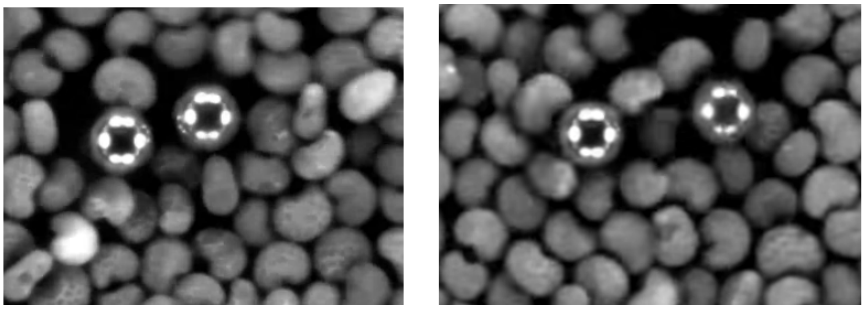

Figure 4.5 | Experimental inclusions. Experiments performed with bronze spheres in a dense bed of poppy seeds [Lozano et al., 2015].

of inclusions is to understand the dynamics of a single inclusion.

Experiments in mixtures of spheres and grains are usually performed in a regime of high density of grains [Reis et al., 2006, Lozano et al., 2015], see Figure 4.5. For further analysis on the effect of the granular bed on inclusions we have selected the packing densities $\phi = 0.60$, and $\phi = 0.75$ in the following sections. Finally, we fix the noise amplitude to $\Lambda_x = 50$ in system units. Active agents display a diffusive behaviour and so we expect passive bodies to follow it.

4.4.1 A free moving inclusion

In experiments [Lozano et al., 2015] placed metallic spheres in a bath of granular particles. We have considered the metallic sphere as a passive particle in an activated suspension. Under shaking and, in the presence of grains, we have simulated different solutions for the metallic sphere without moving into a full,

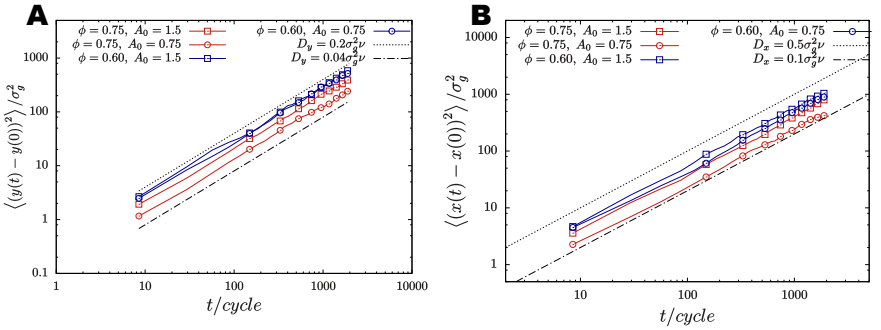

Figure 4.6 | Mean Squared Displacement of an inclusion. **A** the MSD in the shaking direction, and in **B** in the direction perpendicular to the shaking. We observe, in dashed lines, the expected diffusive behaviour for limiting values of D.

realistic, time consuming and too detailed simulation in three dimensions. First of all we introduced the sphere as a disk with different mass $M = 50m_g$, and a lower surface dissipation constant γ. Secondly, we tested with a disk of mass $m = 50m_g$ disconnected from the shaking of the tray. The disconnection from the shaking achieves a better modelling of the original problem of a sphere rolling on the tray. The sphere with a "single" point of contact with the tray rotates under shaking and, tries to stay at the same position in the laboratory frame of reference. This assumption lies on two main hypothesis: first the rotations are without slip, and second we assume that the stored rotational energy does have a strong influence in the interactions.

We introduce inclusions with vectors $\boldsymbol{X}_i$, and velocities $\boldsymbol{V}_i$ which follow granular equations (4.12). We have introduced repulsive dissipative potentials between inclusions, and between inclusions and grains such as (4.3,**??**). As we have previously discussed we disconnect the acceleration of the inclusions from the tray.

For granular packing densities $\phi = 0.6$, and $\phi = 0.75$, shaking amplitudes $A_0 = 0.75\sigma_g$, and $A_0 = 1.5\sigma_g$ we measure the diffusion of inclusions in the bath. We have averaged over hundreds of independent systems to obtain and guarantee a statistically good long time behaviour. Inclusions diffuse in the granular system even at large packing densities, $\phi = 0.75$, with a characteristic diffusive time $\tau_d = \sigma^2/D$. At high densities we observe a stronger influence of the shaking. The system has a larger diffusion constant the larger the shaking amplitude is. Mean squared displacement of inclusions in the parallel and perpendicular directions are presented in Figure 4.6. We observe a diffusive behaviour for several time decades.

Profiles

For a free moving inclusion we observe its diffusion and ability to explore the system. To study its effect in the granular bed we have fixed an inclusion in the simulation to measure the spacial dependence of granular magnitudes as a function of its distance to the inclusion surface. To fix the inclusion in the simulation box we freeze the updating of its position vector $\boldsymbol{X}_i$ but keep the dynamics on its velocity $\boldsymbol{V}_i$. We maintain the dynamics of the velocity of the inclusions because it plays an important role in the interactions with the grains.

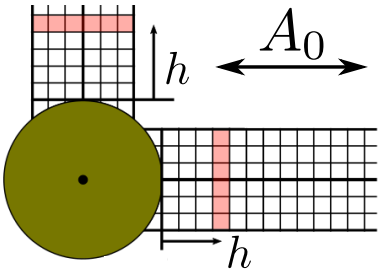

Figure 4.7 | Grid for the profile measures. At each cell we compute the local values of the density, and kinetic energies of the grains. Finally we average at constant h. $h = x$ in the direction of shaking and $h = y$ in the perpendicular direction.

To measure the profile we define a rectangular box that encloses the inclusion of size $L \times \sigma_g$ in the direction of the shaking and its perpendicular direction. We slice the box in boxes of width $\Delta x = 0.2\sigma$ and height $\Delta y = 0.2\sigma$.

We compute the local density, $\phi(x', y')$, and kinetic energies $e_k(x', y')$, and $t_k(x', y')$ at each cell with centre at position (x', y'). We average over 10^3 oscillation cycles for different initial conditions of the sea of grains. The result is then integrated in the vertical transverse direction to obtain the dependence on $h = x$ for the profile in the parallel direction, and on $h = y$ for the profile in the direction perpendicular to the shaking. To increase statistics we fold the data, we collect measures from both sides of the inclusion. Then we compute the relative measure as the local measure relative to the bulk values denoted by the average $\langle \cdot \rangle$

$$\delta e_k(h) = \frac{e_k(h) - \langle e_k \rangle}{\langle e_k \rangle}, \quad \delta t_k(h) = \frac{t_k(h) - \langle t_k \rangle}{\langle t_k \rangle} \tag{4.22}$$

Profiles, in Figure 4.8 show the disturbance that a fixed inclusion induces on bed of particles. The density profile $\phi(h)$ is not affected by the shaking. Kinetic energies, though, display a relative change close to the inclusion. The relative kinetic energy, $\delta t_k(h)$, at contact is positive, and asymptotically relaxes to zero, in both parallel and perpendicular directions. However, absolute kinetic energy, $\delta e_k(h)$, behaves differently for $\alpha = \pi/2$, when it is positive at short distances

$h \approx 1$ and relaxes to zero asymptotically; for $\alpha = 0$ it presents a minimum at contact and relaxes to zero.

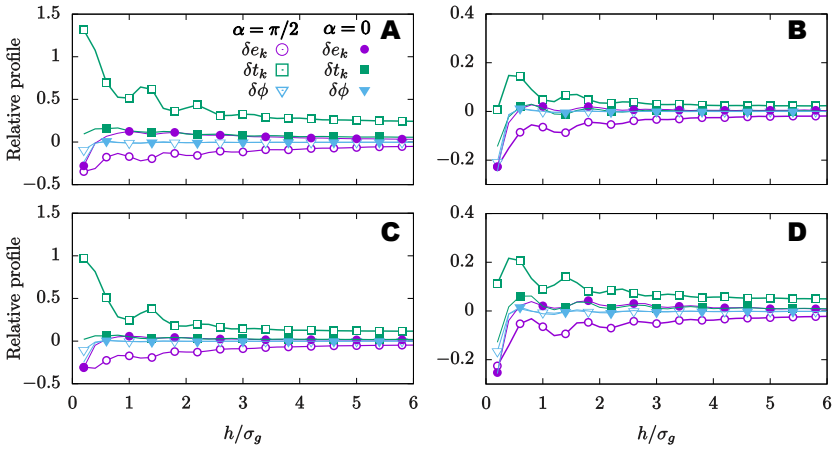

Figure 4.8 | Kinetic energy proifiles for one inclusion. Kinetic energy and density relative excess profiles the granular bed as a function of the distance to the surface of the inclusion. In the direction parallel to the shaking $\alpha = 0$ in solid points, and perpendicular $\alpha = \pi/2$ in hollow points. In **A** $A_0 = 1.5\sigma_g$, and $\phi = 0.75$, **B** $A_0 = 0.75\sigma_g$, and $\phi = 0.60$, **C** $A_0 = 1.5\sigma_g$, and $\phi = 0.60$, and **D** $A_0 = 0.75\sigma_g$, and $\phi = 0.75$

4.5 Two inlcusions

We are interested in the dynamics of a pair of intruder particles in a bed of shaken granular particles. We introduce a pair of intruder particles, in subsection 4.5.1, and define the relative coordinates that characterize the pair. In subsection 4.5.2 we extract the probabilities to measure the different configurations as a function of granular shaking and packing. Finally, 4.5.3 we visualise the probability to measure the pair separated a distance d and the relative orientation for both touching and distant pairs.

4.5.1 Dimer inclusions

In this subsection, we introduce a dimer of intruder particles of fixed diameter $\sigma = 1.5\sigma_g$, and mass per particle $m = 50\ m_0$. The centre of mass of each intruder is defined by the the 2d vector $\mathbf{R}^a$, and $\mathbf{R}^b$. To model the experimental set-up we introduce inclusions as disks disconnected from the oscillation of the tray; not moving solidarily to the tray resembles the 3d rotation of an inertial sphere on a moving platform. In section 4.2 we detail the Langevin equations for the grains an in 4.4.1 the dynamics of the inclusions and study the case of a sole inclusion of $\sigma = 1.5\sigma_g$ and mass $m = 50m_0$.

A doublet of intruders defines a dimer whose centre to centre vector is $\mathbf{r} = \boldsymbol{R}_a - \boldsymbol{R}_b$. The dimer vector, $\mathbf{r} = (r_x, r_y)$, is equally described by its modulus r and the angle α relative to the shaking direction $\boldsymbol{r} = r\,(\cos\alpha, \sin\alpha)$. We define the concept of "parallel" or "perpendicular" configurations of the dimer for the particular configurations $\alpha \approx 0$ and $\alpha \approx \pi/2$, respectively. For simplicity we use the minimal distance between the surface of inclusions $d = r - \sigma$ to define the dimer length.

To understand the dynamics of an intruder dimer we have prepared a large collection of granular beds with initial configurations of the dimer $d \in [4, 7]$ and $\alpha \in [0, 2\pi]$. We sample between 10^6 ($\phi = 0.60$) and $6\ 10^6$ ($\phi = 0.75$) shaking cycles for systems of box size $L = 32\sigma_g$, and compare the results for shaking amplitudes $A_0 = 0.75\sigma_g$ and $A_0 = 1.5\sigma_g$.

Energy is introduced by the external forcing with both parameters A_0, and ω. In the following sections we focus on the shaking amplitude A_0 to drive the system out of equilibrium. By changing A_0 we introduce a length scale that may lead to structural deformations of the system at distances $\sim 2A_0$. While changing ω we modify the dissipation rate of the granular system.

The absolute kinetic energy, see section 4.2.3, defines an energy scale $\langle e_k \rangle \approx \langle t_k \rangle + A_0^2\omega^2 m_g$ that depends on the shaking amplitude A_0, and the shaking frequency ω, and on the random forces characterized by the energy scale $\langle t_k \rangle$. Due to the robustness of the relative kinetic energy $\langle t_k \rangle$ to the changes in packing density of the grains ϕ, and the invariance for changes in the shaking amplitude A_0, shown in Figure 4.2, we choose $E = \langle t_k \rangle$ as the energy scale of the system.

4.5.2 Probability Landscapes

We define $\mathcal{P}(r_x, r_y)$ as the probability to measure the dimer in the configuration $r_x \in [r_x, r_x + \Delta x]$ and $r_y \in [r_y, r_y + \Delta y]$ – we use $\Delta x = \Delta y = 0.05\sigma_g$ in the following computations. We compute the probability landscape $-\ln \mathcal{P}\,(r_x, r_y)$. The probability landscape indicates the most probable relative distance between particles, it measures which are the most stable configurations of the dimer. If the system were in equilibrium, the probability landscape $-\ln \mathcal{P}$ would be proportional to the interaction energy $\mathcal{U}(r_x, r_y)$ of inclusions, the formation energy of the dimer.

To assist the interpretation of the probability landscapes in 4.9, and 4.10 we define the same colour scale for the different systems. We measure the probability density at large distances $r > 10\sigma$ in order to set $\ln \mathcal{P}(r \to \infty) \to 0$ to compare the different systems to the same reference configuration. In addition to the colour map, we introduce isocurves to guide the eye in the interpretation of the probability landscapes.

In this driven system we associate a minimum of the magnitude $-\ln P$ to a high

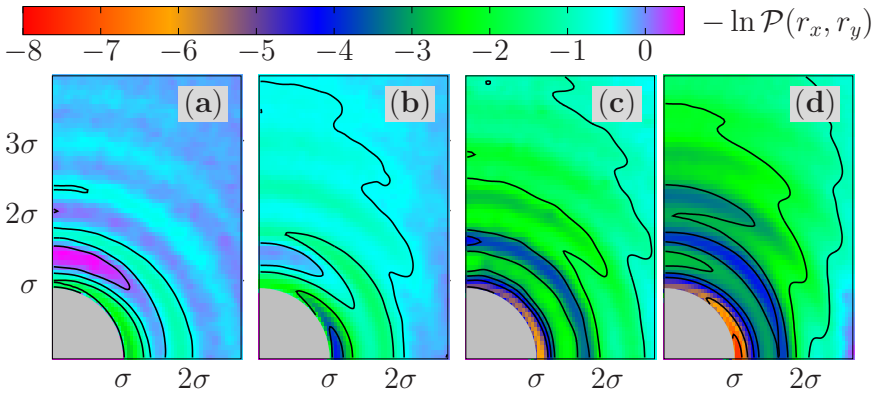

Figure 4.9 | Probability landscapes for a mobile inclusion dimer. Density plot of the measured joint probability landscape $-\ln \mathcal{P}(r_x, r_y)$ for the dimer configuration vector $\boldsymbol{r} = \boldsymbol{R}_a - \boldsymbol{R}_b$. From left to right we plot first the landscapes for low density granular beds at $\phi = 0.60$ (a) $A_0 = 0.75\sigma$, and (b) $A_0 = 1.5\sigma$. Second we plot the landscapes for high density granular beds at $\phi = 0.75$ (c) $A_0 = 0.75\sigma_g$, and (d) $A_0 = 1.5\sigma_g$.

probable configuration of the dimer, an attractive configuration of the inclusions. We extract the probability landscape for different packing densities and shaking amplitudes. We present $-\ln \mathcal{P}(r_x, r_y)$ in Fig. 4.9. We identify $r \approx \sigma$, and $\alpha \approx 0$ as the most probable configuration of the dimer. All four granular beds introduce an anisotropy for configurations at contact $r \approx \sigma$, see in Fig. 4.9 that, at contact, the probability is higher for $\alpha \approx 0$ rather than $\alpha \approx \pi/2$. The structure of the granular bath is clearly manifested in the probability landscape as a sequence of concentric rings surrounding $r = \sigma_g$.

However, in the case of high shaking amplitude $A_0 = 1.5\sigma_g$, and high packing fraction $\phi = 0.75$ the structure of the granular bed is rapidly lost in the direction $\alpha = 0$ and decays faster than at $\alpha = \pi/2$. Moreover, at large distances perpendicular configurations are favoured and an island of repulsion emerges centred at $r = 8\sigma_g$, and $\alpha = 0$, see Fig. 4.10 where we plot an extended region in the configuration space of the dimer configurations.

4.5.3 Averaged probability

The probability density $\mathcal{P}(r_x, r_y)$ in Cartesian coordinates can be translated into $\mathcal{P}(r, \alpha)$ in polar coordinates r, and α. In polar coordinates we define the averaged angular distribution $P(r)$ as the integral of $\mathcal{P}(r, \alpha)$ over the angle α. We have previously seen the emergent anisotropy in the configurations. The radial $P(r)$ averages on angles and gives an effective radial dependence of the probability.

We plot the probability as a function of the minimum distance between inclu-

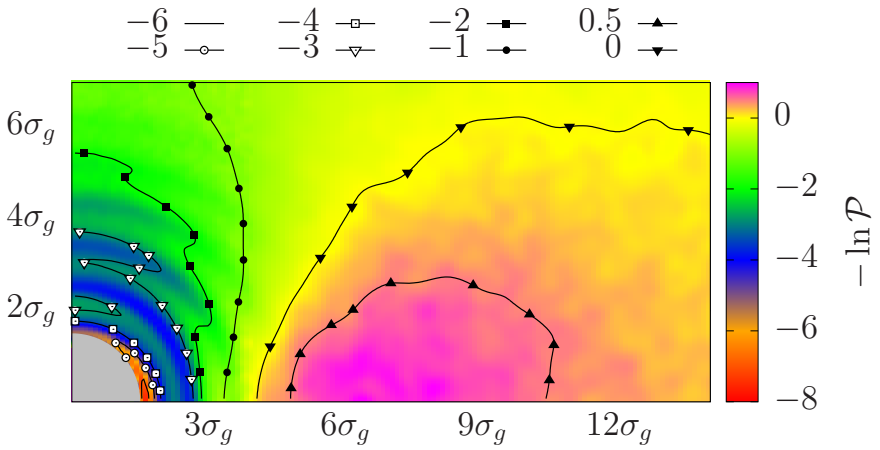

Figure 4.10 | Probability landscape at large A_0, and ϕ. Density plot of the probability landscape to measure the dimer configuration **r** for a system at $\phi = 0.75$, and $A_0 = 1.5\sigma_g$. We observe an exclusion zone, in magenta, where the probability to find the dimer is below the value of $\mathcal{P}$ at infinity.

sions in the dimer $d = r - \sigma$, so that $d = 0$ corresponds to the contact position $r = \sigma$. We identify three different features in the $P(r)$, shown in Fig. 4.11. First, at contact, $d = 0$, $-\ln P(d)$ has the lowest value, it is the preferred configuration. Second, the oscillations of $-\ln P(d)$ at short distances, $d < 3\sigma_g$, clearly show the structure of the bath, for the periodicity corresponds to the granular size. A separation of a whole grain between inclusions is more probable than being separated half a grain or a grain and a half. Images of the system reveal the grain in between inclusions. The surrounding of minima is locally stable and corresponds to an integer number of grains in between. Third, the oscillations are superimposed on a monotonous decay towards zero. The decay is stronger the more compact the system is – the signal is stronger at $\phi = 0.75$. In Figure 4.11 he show the algebraic decay of the probability by fitting a $-\ln P(d) \sim d^{-1}$ curve.

To measure the degree of anisotropy we introduce the projections $P_<(d;\alpha)$, and $P_>(d;\alpha)$ as are the integrals of $\mathcal{P}(r,\alpha)$ over r in the ranges $r \in (\sigma, d)$, and $r \in (d, \infty)$ for $P_<$ and $P_>$ respectively (4.23).

$$P_<(d;\alpha) = \int_\sigma^d r dr \mathcal{P}(r,\alpha), \qquad P_>(d;\alpha) = \int_d^\infty r dr \mathcal{P}(r,\alpha) \tag{4.23}$$

We quantify the anisotropy qualitatively seen in Fig. 4.9 with the angular distributions $P_>(d;\alpha)$, and $P_<(d;\alpha)$ see Fig. 4.12. An isotropic distribution in space corresponds to $P_{<,>}(d,\alpha) = 2/\pi \approx 0.64$. Values of $P_{<,>}(d,\alpha)$ above the isotropic value indicate preference for angular orientations α in that distance range, those angles are favoured. On $P_<(d = 2\sigma_g;\alpha)$ we observe a preference in parallel configurations, as $P_<$ is above the isotropic value for parallel configurations, and

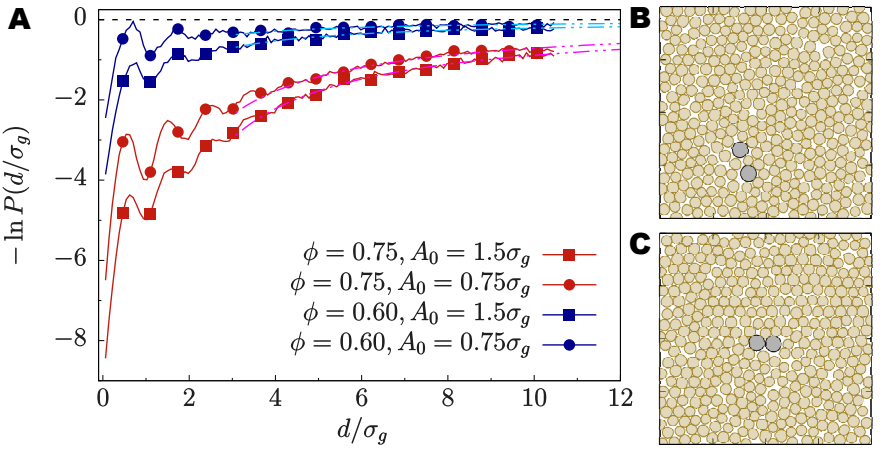

Figure 4.11 | Effective radial probability of a moving dimer. **A** Distance dependence of effective probability, $-\ln \mathcal{P}(d)$, of the relative distance between inclusions for different granular beds. In cyan and magenta dashed lines we plot an algebraic fit at large distances $-\ln P(d) = a/d$. **B**, and **C** Images of the system.

below for perpendicular configurations. The anisotropy in the configuration has a major dependence on the shaking amplitude A_0 rather than on the density, we do not observe great deviations for $\phi = 0.6$, and $\phi = 0.75$. Anisotropy at large distances, $P_>(d = 2\sigma_g; \alpha)$, favours perpendicular interactions, specially for $\phi = 0.75$, and $A_0 = 1.5\sigma_g$, as graphically seen in Figure 4.10.

If the system were in equilibrium, the interpretation of the probabilities would be straight forward. The minimum, and slow decay of the radial probability $-\ln P(D)$ would translate into an energy minimum at $r = \sigma$, and an emergent attractive long range interaction $U \sim d^{-1}$. The results in the anisotropy shown in Fig. 4.12 would imply the emergence of an aligning torque at short distances; a torque that would align the dimer in the shaking direction. However, the system is not in thermal equilibrium and thus, we cannot relate the probability to the interaction energy. But we identify effective attractive interactions and proceed to quantify in the next section.

4.6 Two Fixed inclusions

In this section we quantify the emergent interaction between inclusions. We fix the inclusions at relative coordinates (d, α) and measure the relative mean interactions, forces and torques. Then we propose a model that captures the radial force as a simple function of the shaking amplitude A_0, the relative angle α, and the distance between inclusions d. Finally, we introduce the computation of local measures of the granular bed along the axis of the dimer to comprehend the mechanism of the

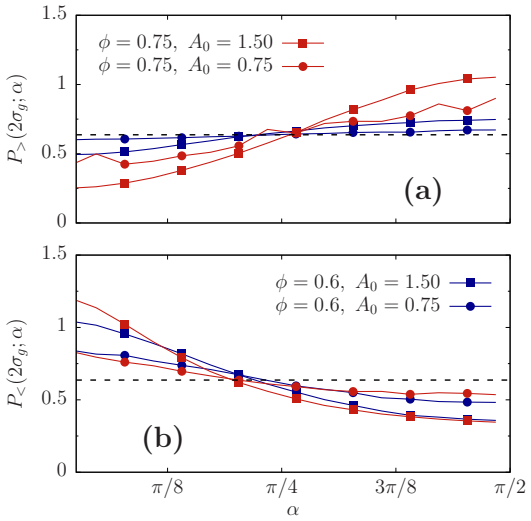

Figure 4.12 | Anisotropic orientation of the dimer. Anisotropy measures. (a) for distances below $2\sigma_g$. (b) for distances $d > 2\sigma_g$. In black dashed lines we plot the distribution function for an isotropic distribution in $P(\alpha) = 2/\pi$, above the dashed line the configuration α is favourable, below otherwise. In squares and circles the results for $A_0 = 1.5\sigma_g$, and $A_0 = 0.75\sigma_g$ respectively. In red and blue results for packing densities of the bed $\phi = 0.75$, and $\phi = 0.6$.

interaction.

4.6.1 Forces and Torques

In equilibrium statistical mechanics, the connection between free energy and probability is well established. The connection is given by $-\ln \mathcal{P}(d) = -\beta U_{eff}(d)$, where $U_{eff}(d)$ is the effective energy of interaction, and β the inverse of the thermal energy $k_B T$. In a dissipative driven system the connection is no longer valid since the system is not in equilibrium. For this reason we introduce a mechanical definition of relative force, torque and energy of interaction.

We fix the pair of inclusions [Zaeifi Yamchi and Naji, 2017, Harder et al., 2014b, Ni et al., 2015] at positions $\boldsymbol{R}_a$ and $\boldsymbol{R}_b$ but we maintain the evolution of the inclusions' velocity since the dissipation in the collisions depends on the relative velocity between interacting particles. The forces on the inclusions given by the granular bed are $\boldsymbol{F}_a$ and $\boldsymbol{F}_b$ on both particles. We define the effective interaction between inclusions by computing the relative force $\boldsymbol{F}_b(\boldsymbol{R}_b) - \boldsymbol{F}_a(\boldsymbol{R}_a)$. To extract the relevant information from the relative force acting on the dimer we project along the radial and tangential directions, $\hat{\boldsymbol{r}}$, and $\hat{\boldsymbol{t}}$
+

$$F_r(\alpha, d) = \left\langle \frac{\boldsymbol{F}_b(\boldsymbol{R}_b) - \boldsymbol{F}_a(\boldsymbol{R}_a)}{2} \cdot \hat{\boldsymbol{r}} \right\rangle \tag{4.24}$$

$$F_t(\alpha, d) = \left\langle (\boldsymbol{F}_b(\boldsymbol{R}_b) - \boldsymbol{F}_a(\boldsymbol{R}_a)) \cdot \hat{\boldsymbol{t}} \right\rangle \tag{4.25}$$

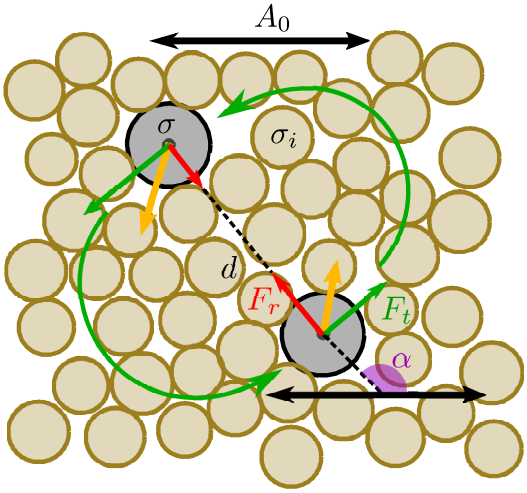

Figure 4.13 | Diagram for the force measurements. Sketch of the system with inclusions of diameter σ in grey, and grains of diameter σ_i in brown. Shaking direction is denoted by double headed arrows, and α the angle of the dimer relative to the shaking. In orange the force acting on each inclusion. We denote the relative interaction forces between passive particles, in red radial forces, and transverse forces in green, curved gren arrows give an intuition of the counter clock-wise torque.

Vectors $\hat{\boldsymbol{r}}$ and $\hat{\boldsymbol{t}}$ constitute an orthonormal basis of the plain, $\mathbb{R}^2$, the radial direction $\hat{\boldsymbol{r}} = (\boldsymbol{R}_b - \boldsymbol{R}_a) / |\boldsymbol{R}_b - \boldsymbol{R}_a|$ and, after rotating $\pi/2$ the transverse direction $\hat{\boldsymbol{t}} = \mathcal{R}_{\pi/2}\hat{\boldsymbol{r}}$. The brackets $\langle X \rangle$ denote the average of the magnitude X over cycles, and between 3 and 10 independent realizations of the system.

The projection $F_r(\alpha, d)$ define and characterize the interactions between inclusions. The forces in the radial direction define the strength and the attractive or repulsive nature of the interaction at particle d, and angle α of the centre-to-centre director relative to the shaking direction. The behaviour at short distances d reveal the interaction between inclusions induced by the local structure of the bath, while the behaviour at long distances d are associated to fluctuation induced interactions.

The sign of $F_r(\alpha, d)$ determines the nature of the interaction at a given distance and orientation angle. Attractive interactions are captured by negative values of F_r. Repulsive interactions, then correspond to $F_r > 0$. The transverse force, F_t, indicates the an emergent neat torque acting on the inclusion pair. Torques that induce a clock-wise rotation of the pair are identified by $F_t < 0$. Counter clock-wise rotations, then, are induced by $F_t > 0$. For a summary of the signs see Figure 4.14

The analysis of the granular bed as a function of the shaking amplitude, and density is performed in section 4.2.3. In there, a pair of kinetic energies are presented. On the one hand, the relative kinetic energy $\langle t_k \rangle$ does not depend either on the shaking amplitude A_0 nor the density of the system ϕ, it is best suited to compare forces in systems at different densities and shaking amplitudes. On the other hand, the absolute kinetic energy $\langle e_k \rangle$ does include the flux of energy that the shaking introduces to the grains. Even though both energies are suitable to define an energy scale we choose $\langle t_k \rangle$ for the sake of commensurability.

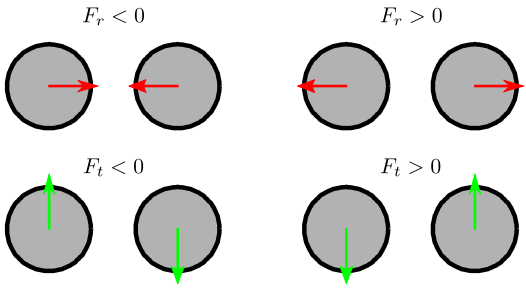

Figure 4.14 | Schematic representation of the relative forces and torques. Relative interactions between particles. F_r determines whether interactions are attractive, $F_r < 0$, or repulsive, $F_r > 0$. F_t determines the direction of rotation, either clockwise, $F_t < 0$, or counter-clockwise, $F_t > 0$.

In a squared box of side $L = 32\sigma_g$, and periodic boundary conditions, we fix inclusions at surface to surface distances in the range $d \in [0, 8]$. Given the anisotropy identified in Section 4.5.1, and the existence of a preferential direction, the shaking, we prepare the inclusions at different angles relative to the shaking, $\alpha \in [0, \pi/2]$. The angular exploration is performed in the first quadrant, for the symmetry of the problem condenses there all the meaningful information. We average on various sets with fixed parameters (α, d, A_0, ϕ) over 10^3 oscillation cycles, and independent realizations, to extract the averaged values F_r, and F_t.

The relative radial force F_r, and torque F_t, as defined in (4.24,4.25), and schematically represented in Figure 4.14 is presented in Figure 4.15 for granular baths with packing densities $\phi = 0.6$, and $\phi = 0.75$, and shaking amplitudes $A_0 = 0.75\sigma_g$, and $1.5\sigma_g$. Effective radial force shows the attractiveness of the interaction for a pair of inclusions at contact, at $d = 0$, for $F_r(0)$ is negative for all considered angles. The magnitude of effective attraction at contact depends on the orientation of the dimer relative to the shaking direction, the interaction is maximum at contact and decreases in the perpendicular direction. As distance increases, from $d = 0$ to $d = \sigma_g$ the force reaches a maximum peak before $d = \sigma_g$, and then presents a second minimum close to $d = \sigma_g$. Then F_r oscillates with decaying amplitude that reflects the local structure of the grains.

As a function of the dimer angle, α, the behaviour of the radial force changes. At perpendicular configurations the decaying oscillations reflect the structure of the bath for longer distances, shaking does not introduce relevant deformations in its orthogonal direction. As the angle is reduced, $\alpha < \pi/2$ the structure in the radial force is gradually destroyed –at large distances– while a neat attractive force appears for several inclusion diameters. Overall, shaking induces an effective attractiveness that increases as the dimer aligns relative to the shaking. In addition, a long range force $F_r \sim d^{-2}$ dominates the interaction at large distances. This aspect is analysed in further detail in the next section.

In addition to the central interaction F_r, a relative tangential force, F_t, appears for configurations with neither $\alpha \neq 0$, nor $\alpha \neq \pi/2$. Torque on the dimer reaches its maximum strength at $\alpha = \pi/4$. This non-central force is present in the system

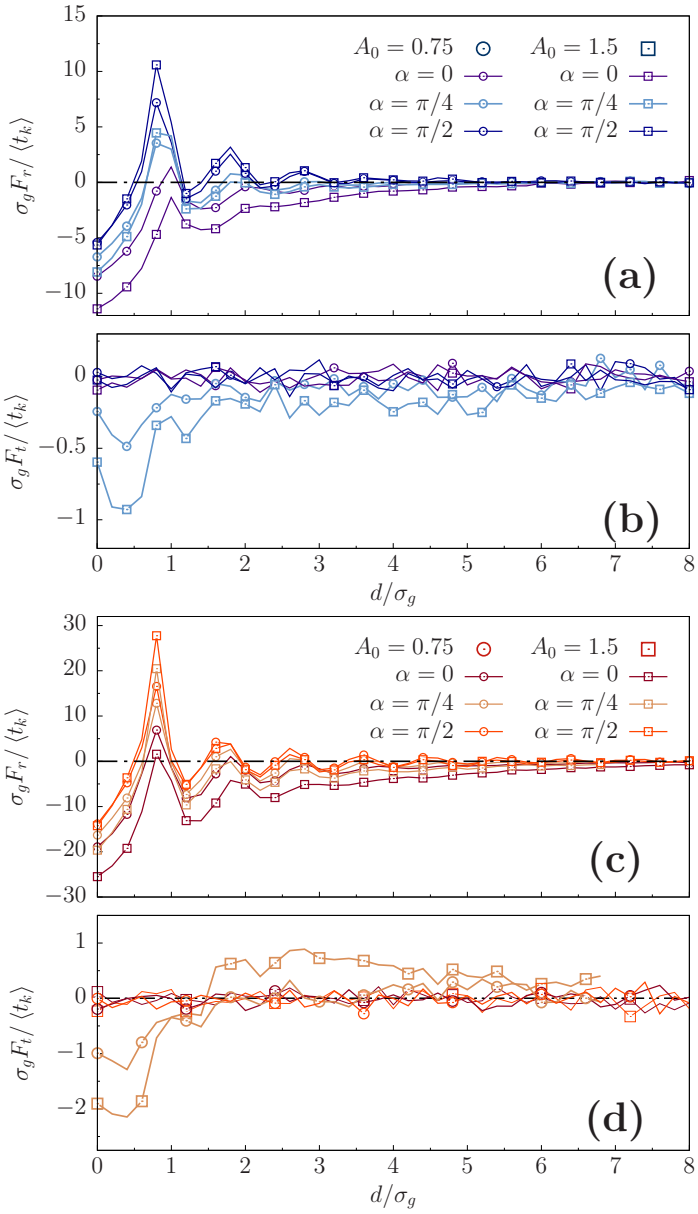

Figure 4.15 | Relative forces and torques between two inclusions. Mean relative force, F_r, and torque F_t as a function of distance. Plots (a,b) for densities $\phi = 0.60$ and F_t, and F_r, respectively. Plots (c,d) for densities $\phi = 0.75$ and F_t, and F_r, respectively. Different amplitudes are labelled by squares, $A_0 = 1.5\sigma_g$, and circles $A_0 = 0.75\sigma_g$. Different shades of colours identity the angle of the dimer relative to the shaking direction.

for short separation distances, $d \lesssim 2\sigma_g$. The negative sign of F_t indicates the emergence of torque that aligns the dimer towards the shaking direction. The torque decrease for low increments of the angle $\Delta F_t/\Delta\alpha < 0$ around $\alpha = 0$, indicates a stable configuration for $\alpha = 0$. The torque decrease for decreasing angles around $\alpha = \pi/2$, $\Delta F_t/\Delta\alpha < 0$, implies that configurations of the dimer $\alpha = \pi/2$ are dynamically unstable.

At $\phi = 0.75$, and $A_0 = 1.5$, however, a finite disaligning torque emerges at large distances $d \gtrsim 2\sigma_g$. The nature of torques shown in Figure 4.15 and is compatible with the anisotropy found in the probability $\mathcal{P}(r_x, r_y)$ for moving inclusions reported in Figures 4.9 and 4.12 in section 4.5.1. Moving inclusions, once in contact, had a strong tendency to be aligned in the direction of the shaking. For the dense configuration and large shaking amplitude, we reported an island of instability at large distances and $\alpha = 0$, consistent with the long range counter-clockwise torque in the force measurements for fixed dimers.

4.6.2 Long range interactions

At large distances the radial force decays towards zero in length scales larger than $10\sigma_g$. Even though we are not able to test the dependence over several decades in distance, we model the decay with an algebraic dependence. In granular media, long range algebraic forces have already been suggested [Cattuto et al., 2006]. However, for the given interaction range we cannot distinguish between an algebraic decay, with d^{-2}, and an exponential $\exp(-d/\lambda)$. For this reason, and given the oscillation of the interaction force at perpendicular configurations we propose an algebraic fit for its higher reliance fitting in the regime $\alpha \approx \pi/2$.

$$F_r(\phi, A_0, \alpha, d) = F_2(\phi, A_0, \alpha)\left(\frac{\sigma_g}{d}\right)^2 + F_0 \tag{4.26}$$

where F_2 gives the strength of the pair interaction, and F_0 the value of the relative effective force at infinity, which remains $F_0 \approx 0$.

To capture the full dependence on α, and A_0 on the strength of the long range emergent interaction $F_r(\phi, A_0, \alpha)$ we have systematically swept the space of parameters α, and A_0. The radial force presents an oscillating behaviour at large angles, $\alpha \approx \pi/2$, and a smooth one at lower values of α, see Figure 4.16. The strong oscillatory signal corresponds to an ordered structure of the granular bed surrounding each inclusion. The prevalence of the ordered structures around an inclusion is affected by the external forcing, the external displacement on the granular bed. At perpendicular configurations of the dimer the effect of external forcing is almost nonexistent. As the angle of the dimer increases the effect of the external forcing increases and the local structure is lost. What is even more, an effective interaction between particles emerge, and increases as the dimer gets aligned to the forcing.

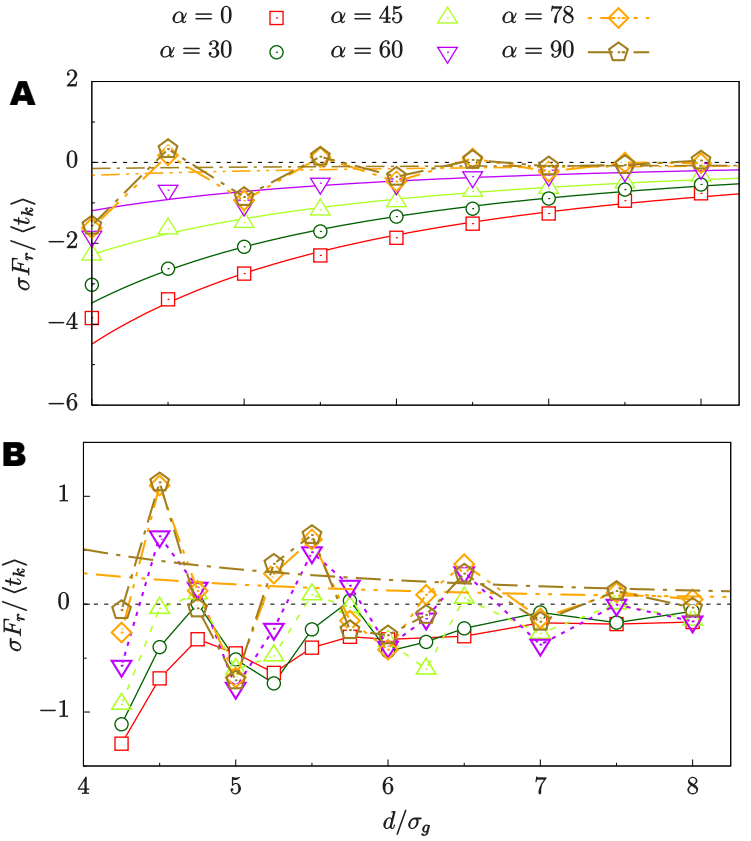

Figure 4.16 | Long range radial force between inclusions. Relative force, F_r between inclusions as a function of interparticle distance d/σ_g. **A** at shaking amplitude $A_0 = 1.5\sigma_g$ the external forcing is strong enough to destroy the internal structure of the grains at $\alpha < 60^{\circ}$. **B** at shaking amplitude $A_0 = 0.5\sigma_g$ the internal structure persists for angles $\alpha \gtrsim 30^{\circ}$.

The simplest interaction that satisfies the symmetry of the problem, the absence of polarity and a preferential direction, and the knowledge of extremal values of the interaction at $\alpha = 0$ (maximum), and $\alpha = \pi/2$ is $\cos^2 \alpha$. For this we introduce

$$F_2(\phi, A_0, \alpha) = B_2(A_0, \phi) \cos^2 \alpha \tag{4.27}$$

where B_2 is a function of the shaking amplitude and the density. In Figure 4.17 we present the values of the interaction strength F_2 for different shaking amplitudes as a function of the angle for $\phi = 0.75$, the case in which the signal is stronger. The linear behaviour on $\cos^2 \alpha$ validates the proposed model (4.27). The intensity of F_2 increases for greater shaking amplitudes A_0. In Figure 4.17 we present the fitted value of B_2 for increasing values of the shaking. B_2 presents two qualitative regimes. First, at low shaking amplitudes, the interaction is attractive at a constant value $\sigma_g B_2 / \langle t_k \rangle \approx -20$. Then, above $A_0 \approx 0.6$ B_2 remains no

longer constant and increases in magnitude, the interaction becomes more attractive. For the considered range the increase is linear on the shaking amplitude A_0 $\sigma_g B_2 / \langle t_k \rangle = 67(A_0 - 0.6\sigma_g)/\sigma_g$, for $A_0 > 0.6\sigma_g$.

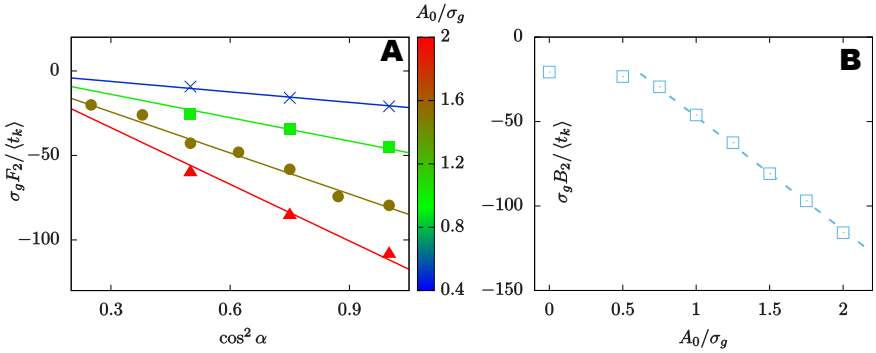

Figure 4.17 | Determination of the dependences of the strength of interaction $F_2(\phi, A_0, \alpha)$**. A** F_2 as a function of $\cos^2\alpha$ for different shaking amplitudes, and the dependence (4.27). **B** Value of the prefactor of $B_2(A_0, \phi)$ as a function of A_0/σ_g. The dashed line the relation $\sigma_g B_2/\langle t_k \rangle = 67\,(A_0/\sigma_g - 0.6) - 20$

In short, the results in Figures 4.16, and 4.17 indicate an emergent interaction between passive particles

$$F_r(\phi, A_0, \alpha, d) = F(\phi)\left(\frac{A_0 - A_0^c(\phi)}{\sigma_g} + B_0(\phi)\right)\cos^2\alpha\left(\frac{\sigma_g}{d}\right)^2, \quad \text{for } A_0 > A_0^c \tag{4.28}$$

where we have reduced the interaction force F_r at long distances to three density dependent functions. $F(\phi)$ quantifies the strength of interaction, and A_0^c, and B_0 the force, and shaking amplitudes at the onset of the amplitude dependence of the force.

4.6.3 Formation Energy

The measure of the force for a succession of distances between inclusions, presented in Figure 4.16, can be further exploited to define a mechanical formation energy of the dimer. We define the formation energy of a dimer as the integral of the radial force along a line at constant angle α relative to the shaking.

$$\mathcal{U}_\alpha(d) = \int_{d\to\infty} \boldsymbol{F}_{int} \cdot d\boldsymbol{l} = -\int_{\infty}^{d} F_r(r, \alpha) dr \tag{4.29}$$

For a system in equilibrium the relation between probability and energy is clear and direct, $\mathcal{U} = -\beta^{-1} \ln P$. In this system, the shaking introduces a flux of energy in such a way that the standard equilibrium relation $\mathcal{U} = -\beta^{-1} \ln P$ is no longer guaranteed. Moreover, the pinning of particles to extract measures of the interaction

force alters the structure of the sea of grains. The fact that grains are not able to separate the dimer, since d is fixed, may enhance interaction forces.

In section 4.4, for moving inclusions, we extracted the probability to find the dimer in the configuration (r_x, r_y), or in polar coordinates (r, θ), see Figure 4.11. With this data we proceed to check to which extend the relation between the formation energy, a mechanical measure, compares with an effective interaction energy whether the equilibrium relation $U = -\beta^{-1} \ln P$ held. We differentiate the mechanical formation energy in the direction α, $\mathcal{U}_\alpha$, to the effective averaged interaction energy extracted from the probability to locate particles at a given configuration, $U(d, \alpha)$.

With the data from the probability distribution $P(d)$, and the formation energy of the dimer $\mathcal{U}_\alpha(d)$ we define the a chi squared function which introduces an effective $\beta^{-1}(\alpha)$ a fitting parameter

$$\chi^2 = \sum_i \left[\mathcal{U}_\alpha \left(d_i \right) - \left(\beta^{-1}(\alpha) \ln P \left(d_i \right) + U_0(\alpha) \right) \right]^2 \tag{4.30}$$

First, we project the probability into a specific value of α, $P_\alpha(d, \alpha)$, to fit $\mathcal{U}_\alpha(d)$. The extreme behaviour of the pair probability at $\alpha = 0$, where a repulsion appears for $A_0 = 1.5\sigma_g$, and $\phi = 0.75$ is evident in Figure 4.18 and completely breaks an eventual energy connection to the probability since the formation energy presents a clear d^{-2} long tail. The perpendicular presents another striking characteristic. The formation energy presents a considerable humpback at short distances and rapidly decays to zero, in the special case of $\phi = 0.6$ following positive energies. This major difference with the probability, leads to small fitting values of β^{-1}, and even $\beta^{-1} < 0$. The effects of the pinning, the measure protocol, are evident at short distances.

Second, for angular dependences of the sort $\cos^2 \alpha$ the average value of the distribution corresponds to $\cos^2 \pi/4 = 1/2 = 2/\pi \int_0^{\pi/2} d\varphi \cos^2 \varphi$. Following this idea we compute the average formation energy as the angular average $\langle U_\alpha(d) \rangle_\alpha$, and the radial pair distribution function $P(r)$, previously presented in Figure 4.11. Given the nature of the decays in both $-\ln P(d)$, and $\langle \mathcal{U}_\alpha \rangle_\alpha$ we are able to fit an effective β^{-1} at large distances. The fitting, however, does not cover the close distance configurations, and thus the idea of an effective β^{-1} breaks down into pieces.

4.6.4 Granular Measures Profiles

It is important to understand the disturbance that inclusions introduce to the sea of grains. Fixing the inclusions allows us not only to measure the relative forces and torques but to capture the local variations of different magnitudes along the axis of the dimer.

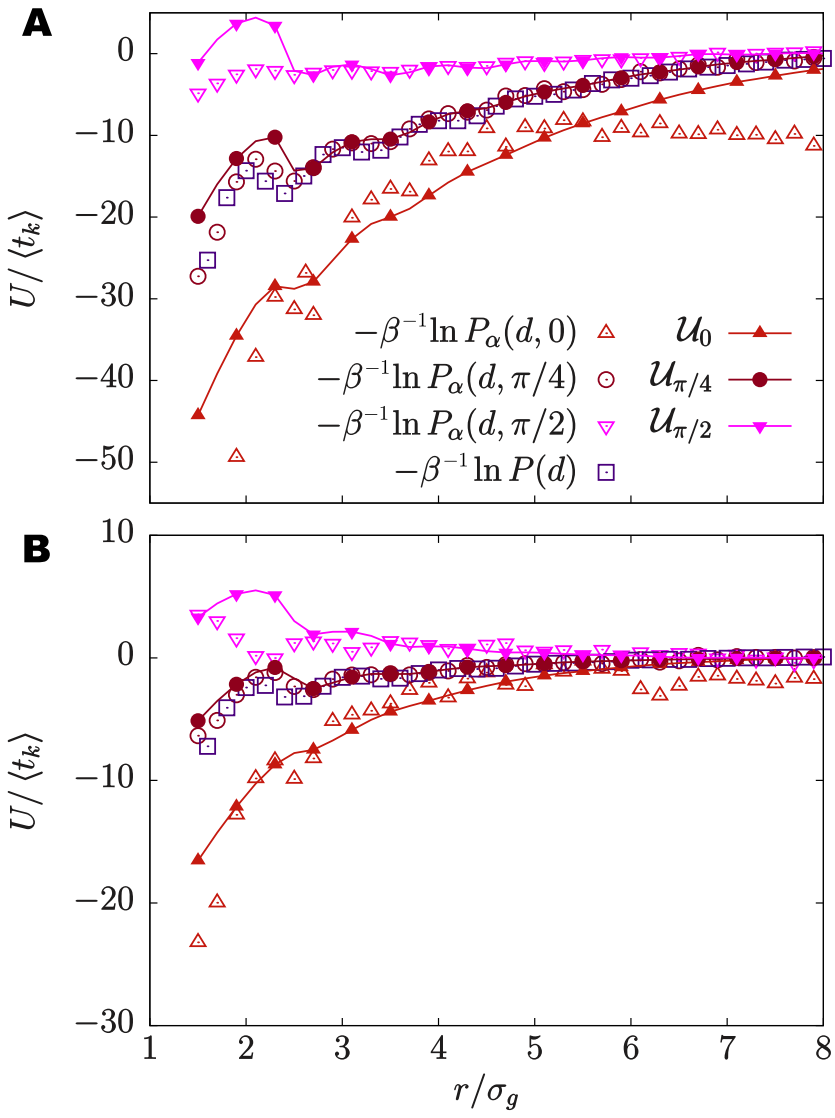

Figure 4.18 | Formation energy of an inclusion dimer. In solid lines the formation energy of the dimer in different directions. In points, we fit an effective β for the averaged probability $-\ln P_\alpha(r,\alpha)$ at different angles. Shaking amplitude $A_0 = 1.5\sigma_g$ and the density of the granular bed is set to $\phi = 0.75$ in **A**, and $\phi = 0.75$ in **B**

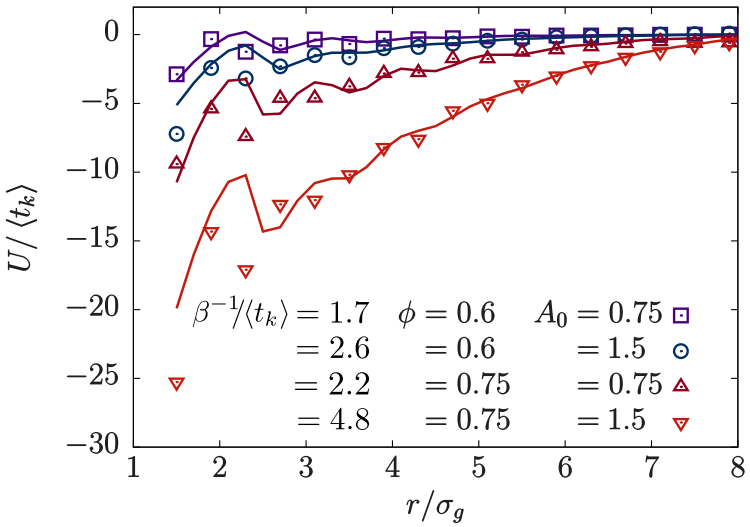

Figure 4.19 | Averaged formation energy of the inclusion dimer. Effective energy fit. Angular averaged pair probability, $-\beta^{-1} \ln\ P(d)$, and averaged mechanical energy $\langle \mathcal{U}_\alpha(d)\rangle_\alpha$.

To measure the profile we define a rectangular box that encloses the inclusions of size $L \times \sigma_g$ in the axis of the dimer, we follow the procedure introduced in Figure 4.7 in section 4.4.

We compute the local density, $\phi(x', y')$, and kinetic energies $e_k(x', y')$, and $t_k(x', y')$ at each cell with centre at (x', y'). We average over 10^3 oscillation cycles for different independent realizations of the sea of grains. The result is then integrated in the orthogonal dimension to the profile obtain the dependence on the distance from the inclusion h. To increase statistics we fold the data so that positive values correspond to profiles in the outer regions of the inclusions (i.e. $h' + L/2 + d/2 + \sigma_g \to h$, and $L/2 - d/2 - \sigma_g - h' \to h$). The inner region of the profile, between the inclusions, corresponds to negative values of the profile. We have not used the folded range but define $h \in [-d, 0)$ for a better visualization of the profiles.

In Figure 4.22 we plot the relative excess of density, and kinetic energies for $\phi = 0.75$, $A_0 = 1.5\sigma_g$ relative to the bulk values (4.22). We compute the profiles for different configurations of the dimer (parallel and perpendicular to the shaking) and different separation distances ($d = 2\sigma$ and $d = 6\sigma_g$).

For positive values of h/σ_g, the behaviour of each profile does change from the previously reported behaviour for a single inclusion, see 4.4.1. For negative values of h the deviations from bulk values follow the qualitative behaviour observed for

exterior profiles. The strength, though, increases. An appropriate description of the inner profiles considers the effects of each inclusion, and the join effect of the pair, a full description of a generic inner profile, g, at position $-h$ is

$$\delta g(h) = \delta g_1(-h) + \delta g_2(h_2 = d - h) + \delta g_{12}(h, d) \tag{4.31}$$

where δg_1, and δg_2 are the disturbances introduced by inclusions at positions $\boldsymbol{X}_1$, and $\boldsymbol{X}_2$, and $h_2 = d - h$ the position relative to inclusion $\boldsymbol{X}_2$. We introduce the two body contribution δg_{12} which depends on the distance h, and the dimer separation d. We sketch the two inclusion system in Figure 4.20.

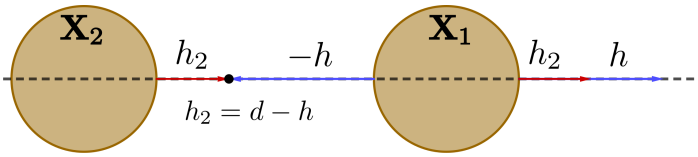

Figure 4.20 | Inclusion dimer geometry. The inner profile is at distances $-h$ from inclusion at $\boldsymbol{X}_1$, and distance h_2 from inclusion $\boldsymbol{X}_2$. We include the positive distances h, and h_2 from inclusion $\boldsymbol{X}_1$ in the exterior region.

We do not observe a significant deviation of the averaged density along the axis. The averaged density in the region between inclusions equals to the averaged density outside –except for the density at contact that decays due to grain size and the curvature of the disks. However, both kinetic energies –absolute, and relative– are not kept constant along h. On the one hand, the excess relative kinetic energy δt_k has a positive value at contact and relaxes towards zero. On the other hand, the absolute kinetic energy departs from a negative value at contact. For perpendicular configurations, $\alpha = \pi/2$, is suddenly increases to $\delta e_k > 0$ and relaxes to 0. For parallel configurations, e_k does not jump and the relaxation process occurs at negative values of e_k, as it corresponds to a single inclusion and reported in 4.4.1.

We test profile additivity, equation (4.31), by jointly plotting the inner measured profiles δe_k, and δt_k, and (4.31) considering $\delta g_{12} = 0$. In Figures 4.21, and 4.22 we present the inner and outer profiles for dimer distances $d = 6\sigma_g$, and $d = 2\sigma_g$, respectively. Results for the inner region show a good agreement with the additivity assumption for the energy profiles.

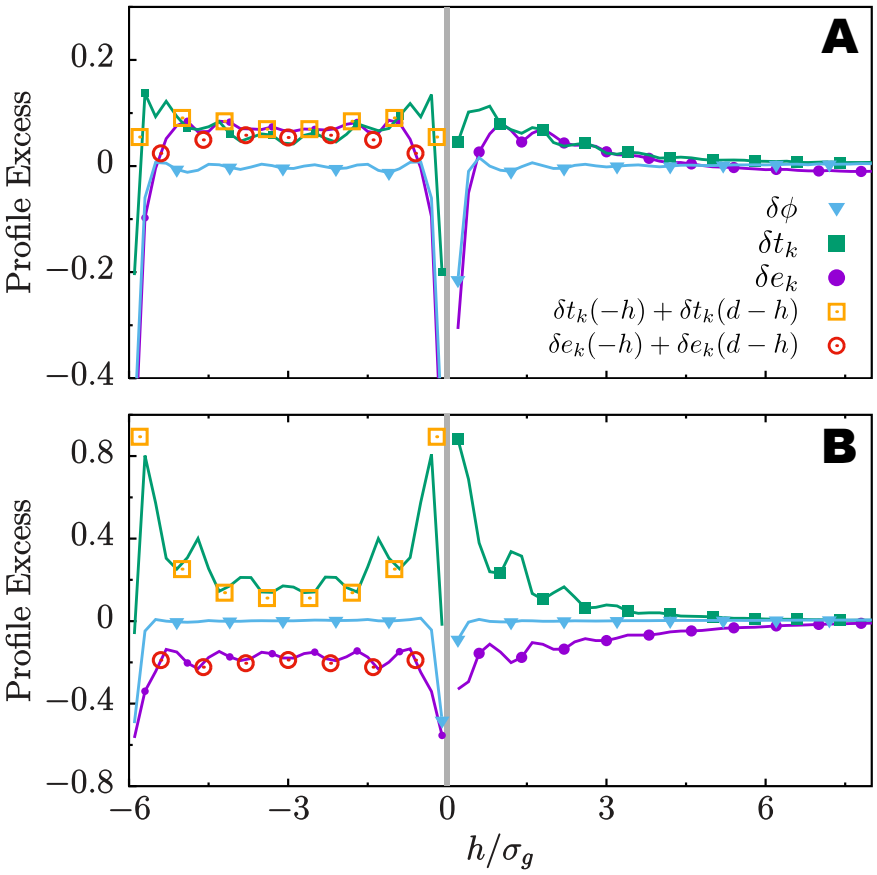

Figure 4.21 | Kinetic energy profiles for an inclusion dimer at $d = 6\sigma_g$**.** Excess kinetic energy and density of grains in a system at density $\phi = 0.75$, and shaking amplitude $A_0 = 1.5\sigma_g$ for different configurations of the dimer, and $d = 6\sigma_g$, and $\alpha = \pi/2$ in **A**, and $\alpha = 0$ in **B**. In orange squares and red circles we plot the result of combining two surfaces with origins at $h = 0$, and $h = -d$

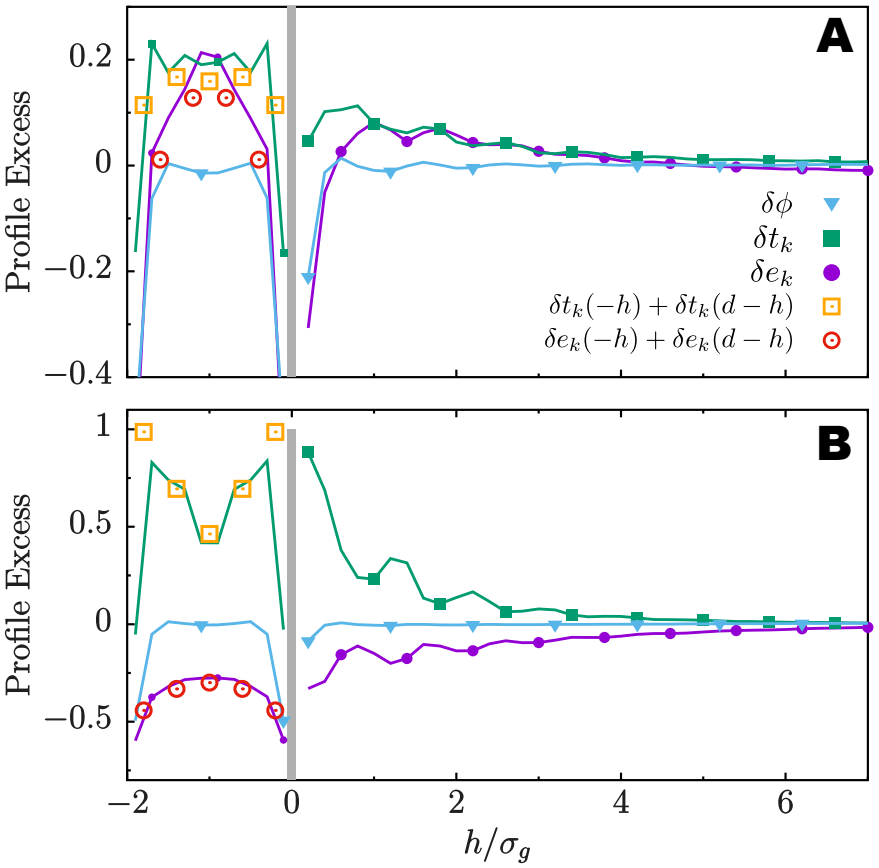

Figure 4.22 | Kinetic energy profiles for an inclusion dimer at $d = 2\sigma_g$. Excess kinetic energies and density of grains in a system at density $\phi = 0.75$, and shaking amplitude $A_0 = 1.5\sigma_g$ for different configurations of the dimer, and $d = 2\sigma_g$, and $\alpha = \pi/2$ in **A**, and $\alpha = 0$ in **B**. In orange squares and red circles we plot the result of combining two surfaces with origins at $h = 0$, and $h = -d$

4.7 Conclusions to this Chapter

In this chapter, we have proposed a model for horizontally vibrated granular matter. We presented kinetic energy measurements to characterize the granular bath and discussed the insertion of intruder particles. We analysed the dynamics of an inclusion and proceeded to introduce them in pairs. Previous experimental results from [Lozano et al., 2015] reported an effective interaction between pairs of inclusions via pair distribution functions.

Then, we introduced a pair of free moving moving inclusions to mimic the

experimental realization of the problem. We reported the tendency to stay at contact, and associated it to an effective emergent interaction. In addition, we reported the increase of the probability to obtain pairs of inclusions aligned with the shaking while at contact. At larger distances, and for high density packing fractions, pairs tend to align in the direction perpendicular to the shaking. We fixed the inclusions at different distances and relative angles to the shaking in order to measure their relative forces of interaction. Results evidence the emergence of a long range force, superimposed to the structure induced interactions, and its dependence with the aligning of the pair relative to the shaking. In parallel, we report the emergence of a relative aligning interaction torque between particles at short distances, and a disaligning torque at long distances for high densities, and shaking amplitudes. Results for fixed inclusions are consistent with the results for freely moving inclusions.

Further, a systematic exploration of the long range interaction in terms of system parameters has permitted us to compress the dependences of the pair distance, orientation relative to the shaking, and shaking amplitude into a simple expression with a sole dependence on the granular packing density. Combining the results of the mechanical forces and probabilities to measure free moving particles at given relative configurations has permitted us to check the impossibility to associate an effective temperature to connect energy and probabilities.

Altogether, we have prepared and characterized a computational framework to study the interaction of shaken granular bed with intruder particles via both mechanical and dynamical measures. The emergence of a disaligning torque at large distances, leads us to consider its implications in the stripe separation, perpendicular to the shaking direction, in mixtures of driven grains and inclusions.

Appendices

4.A Long Range Interaction

As briefly introduced the the body of this Chapter we fit the interaction data of the radial force between inclusions to an algebraic function for the distance between particles d^{-2}. We have extended the computation to boxes of size $L = 64\sigma_g$ to study a broader range of the inter particle distance in order to avoid the interactions with the image systems caused by the periodic boundary conditions, present at $d \approx L/2$.

The form of the interaction is either an algebraic function or an exponential

$$F_r = F_2 d^{-2}, \qquad F_r = G_2 \exp\left(-d/\lambda\right) \tag{4.A.1}$$

with F_2, and G_2 the strength of interaction, and λ the characteristic length of interaction.

Here

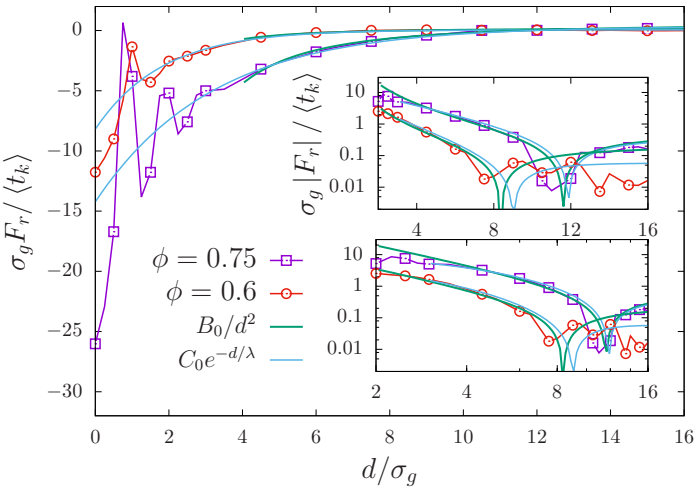

Figure 4.A.1 | Long range radial force decay, $\alpha = 0$. Effective radial force for a shaking amplitude $A_0 = 1.5\sigma_g$, and dimer orientation $\alpha = 0$. Insets in a semilorarithmic, and log-log scales.

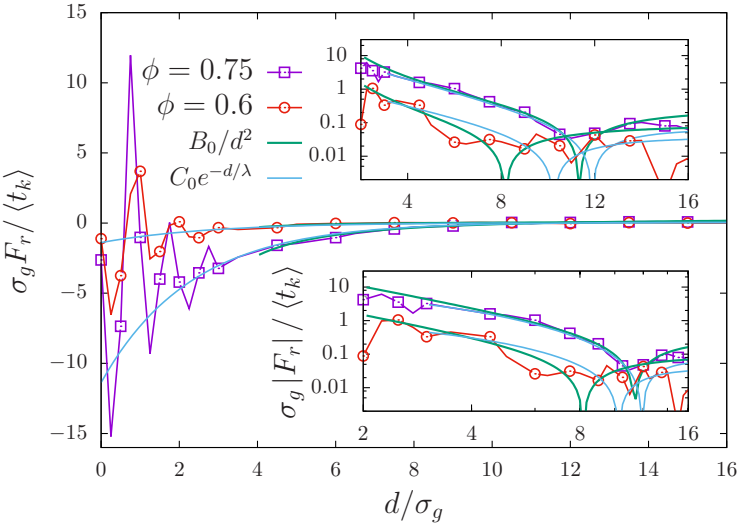

Figure 4.A.2 | Long range radial force decay, $\alpha = \pi/4$. Effective radial force for a shaking amplitude $A_0 = 1.5\sigma_g$, and dimer orientation $\alpha = \pi/4$. Insets in a semilorarithmic, and log-log scales.

5 Apolar Active Matter

5.1 Motivation

In the last two chapters we have focused on the interactions that a bath of self propelled particles induce on probe particles that behave like passive objects. The union link between systems presented in Chapters 3 and 4 are the force transmission mechanisms, contact forces, and the polar nature of the activity. Active Brownian Particles, Aligning Active Particles, and grains show a persistence of motion, and hence are polar active particles.

In this chapter we focus on novel system of active particles that differs from the aforementioned systems in different aspects. First, activity does not directly translate into a directed movement, there is no propulsion so we refer to the particles as Apolar Active Particles. Second, the activity mediated interaction between active and passive particles do not emerge from contact forces but from the intrinsic ability of apolar particles to generate steady chemical imbalances that extend to their surroundings. This works is founded in the theoretical framework proposed by [Soto and Golestanian, 2014b] to understand, and model, diffusophoretic interactions between colloidal particles in the microscale. In this Chapter we first introduce an experimental binary mixture of passive and apolar particles that give rise to diffusophoretic interactions. We develop a model to account for the relative interactions between particles of different sizes and activities. Then, we compare the theoretical predictions to experimental data to calibrate the strength of interaction. Finally we explore, computationally, the system for different concentrations of active and passive particles to later compare them to experimental aggregation processes.

Experiments performed in the Laboratory of Pietro Tierno in Barcelona showed an interesting aggregation mechanism in a mixture of hematite and silica particles. Previous experiments [Palacci et al., 2013a, **?**, **?**] reported attractive interactions for apolar photoactivated colloids and passive particles when it was immersed in a solution of hydrogen peroxide. With no illumination the system is in thermal equilibrium, but when it is shone by light, hematite particles catalyse the decomposition reaction $2H_2O_{2(aq)} \longrightarrow 2H_2O_{(l)} + O_{2(g)}$ on their surface. The local consumption and production of chemical products in the vicinity of hematite particles intrinsically drive the system out-of-equilibrium. The generation of gradients of chemical products leads to the development of fluid flows in the direction of gradient, as derived by [Anderson and Prieve, 1984].

At first experimentalists observed [Martinez-Pedrero et al., 2017] the appearance of a long range interaction in the form of a relative velocity between apolar and passive particles, and results shown in Figure 5.1. The aggregation occurred in helmatite dilute systems, with the formation of clusters similar to [Soto and Golestanian, 2014b], in such a way that a visual observation, and particle tracking, showed the emergence of a long range interaction which could extend to three or four Silica particle diameters. The interaction velocity between active and passive particles decays as the inverse of the square of the distance.

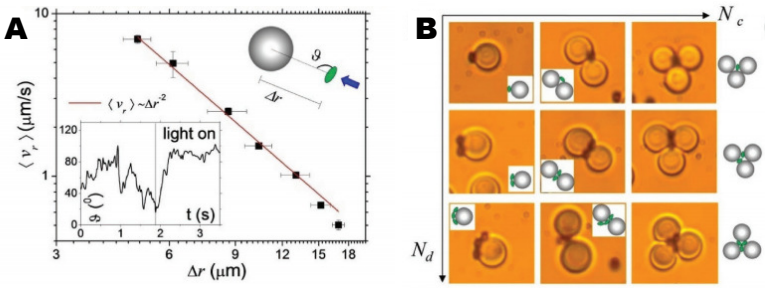

Figure 5.1 | Experimental diffusophoretic interactions. Experiments in a dilute binary mixture of active and passive particles immersed in a solution of hydrogen peroxyde and shone with blue light. In **A** the relative velocity of an apolar-passive pair with illumination. In the inset we observe the rapid reorientation of the particle with its long axis perpendicular to the centre to centre vector. **B** The formation of active-passive molecules with different numbers of active and passive particles. Images from [Martinez-Pedrero et al., 2017]

In dense systems experimentalists reported the emergence of structured Silica aggregates at even for very low fractions of hematite particles. The use of photoactivated particles to induce crystallization in colloidal aggregates has attracted our attention and consequently we have developed a model to computationally describe and work together with experimentalists in Pietro Tierno's Laboratory to characterize this active-passive mixtures.

The scope of this Chapter is to introduce a simple mechanism in section 5.2 to understand the emergent interaction between particles though the production and consumption of chemical products. This interaction is then used to construct a basic numerical model in section 5.3. In 5.4 we discuss the collective behaviour of the binary fluid and the emergence of different mesoscopic structures.

5.2 Diffusophoresis and hydrodynamics

The basic ingredients of this this problem are the chemical products and their coupling to the fluid. Since the works of J. Anderson [Anderson and Prieve, 1984, Anderson, 1989] the relation between gradients of chemicals and fluxes of fluids is well established by the relation (5.1).

$$\boldsymbol{v}(r,\theta,z) = \mu_d \vec{\nabla} c(r,\theta,z) \tag{5.1}$$

where a gradient of chemical product ∇c induces a velocity to the fluid $\boldsymbol{v}$ with a proportionality constant μ_d, the diffusophoretic mobility.

In this section we model the concentration fields of chemicals around active and passive particles in the framework developed by [Soto and Golestanian, 2014b, Soto and Golestanian, 2015]. The interaction of chemical fields results in gradients of chemicals on the surface of the particles. We exploit equation (5.1) to compute the flow field generated by each particle and the final effect on the neighbouring particles.

This diffusophoretic approach has been widely used [Golestanian et al., 2007], [**?**, **?**, **?**], and finally its use as polar dimers [Colberg and Kapral, 2017], [Huang et al., 2017].

5.2.1 Diffusion of chemicals

We model the concentration of chemicals with Laplace's equation for the chemical field c, with diffusion constant D_c, and production rate α on the active particles. We proceed to compute the effects on single field $c(r,\theta,\phi)$ using a spherical coordinate system.

$$\nabla c(r,\theta,\phi) = 0 \tag{5.2}$$

We consider a sphere of diameter $\sigma = 2R$. The production and consumption of chemicals occurs along the surface of the particle at a production/consumption rate α_c. Mathematically, it enters into the system though boundary conditions on $r = R$.

$$D_c \left.\frac{\partial c(r,\theta,\phi)}{\partial r}\right|_{r=R} = \alpha_c \tag{5.3}$$

We further simplify the problem by considering only the solutions with no dependence on ϕ. And we ask to the acceptable solutions must be bounded at infinity

$\lim_{r\to\infty} c(r,\theta) \to 0$.

$$c(r,\theta) = c_0 + \sum_{l=0}^{\infty} B_l \frac{P_l(\cos\theta)}{r^{l+1}} \tag{5.4}$$

Imposing the boundary condition (5.3) on (5.4) we obtain the concentration field generated by an apolar particle of a chemical product.

$$c(r,\theta) = c_0 + \frac{\alpha_c R^2}{D_c}\frac{1}{r} \tag{5.5}$$

The disturbance on the concentration field is a source/sink term – a monopole.

5.2.2 Velocity of a particle in a velocity field.

A spherical particle of radius $R = \sigma/2$ with a tangential hydrodynamic velocity field on its surface, $\boldsymbol{v}_{\parallel}(r,\theta,\phi)$. The total fluid velocity on the surface of the particle is directly related to the velocity of the centre of mass of the particle, $\mathbf{V}$, by the mass conservation of the fluid (5.6).

$$\mathbf{V} = -\frac{1}{4\pi R^2}\oint_{\partial\Omega} \boldsymbol{v}_{\parallel} dS \tag{5.6}$$

The functional form of the surface velocity $\boldsymbol{v}_{\parallel}$ defines the velocity of the particle. Here we switch to the specific case of diffusophoretic flows on spherical particles. The connection between the induced velocity $\mathbf{v}$ and the gradient is given in equation (5.1). As a consequence, a particle with a non-uniform density field on its surface generates a velocity field on its surface which potentially could propel the particle.

$$\mathbf{V} = -\frac{\mu_d}{4\pi R^2}\oint_{\partial\Omega} \nabla_{\parallel} c(r,\theta) dS \tag{5.7}$$

Equation (5.4) gives a complete description of the density field of chemical $c(r,\theta)$ with azimutal symmetry in the outer region of a spherical particle – the chemical field within the fluid region. We denote by β_p the multipolar components of the density field on a particle of radius R.

In spherical coordinates the parallel projection of the gradient relative to the surface $r = R$ is $\nabla_{\parallel} = R^{-1}\hat{\theta}\partial_\theta + (R\sin\theta)^{-1}\hat{\phi}\partial_\phi$, and simply $\nabla_{\parallel} = R^{-1}\hat{\theta}\partial_\theta$ when we omit for concentration fields with no ϕ dependence. It is convenient to introduce the derivative respect to the angle as $\partial_\theta = -\sin\theta\partial_{\cos\theta}$. Due to the revolution symmetry in the problem we compute the velocity projected on the $\hat{z}$ axis[1] $V_z = \mathbf{V}\cdot\hat{\mathbf{z}}$.

$$V_z = -\frac{\mu_d}{4\pi R^3}\oint_{\partial\Omega} \sin^2\theta \frac{\partial}{\partial\cos\theta}\sum_p \frac{\beta_p}{R^{p+1}} P_p(\cos\theta) dS \tag{5.8}$$

[1]The projection along the z axis introduces the projection $\hat{\mathbf{z}}\cdot\hat{\theta} = -\sin\theta$ which simplifies the computation which is no longer vectorial.

We integrate over the surface element $dS = R^2 d\phi d(\cos\theta)$, and the integral over ϕ is immediate

$$V_z = -\frac{\mu_d}{2R^2}\int_{-1}^{1} d(\cos\theta)\sum_p \beta_p R^{-p}(1-\cos^2\theta)\frac{\partial}{\partial\cos\theta}P_p(\cos\theta) \tag{5.9}$$

We introduce the relation $(1-x^2)P_n'(x) = nP_{n-1}(x) - xnP_n(x)$, and introduce x and 1 as a function of the Legendre Polynomials to the later use of the orthogonality relationships $\langle P_m(x)|\, P_n(x)\rangle = 2/(2m+1)\delta_{mn}$.

$$V_z = -\frac{\mu_d}{2R^2}\sum_p \beta_p R^{-p}\int_{-1}^{1} dx\,[-pP_1(x)P_p(x) + pP_{p-1}(x)P_0(x)] \tag{5.10}$$

As a consequence of the orthogonality of the Legendre Polynomials, the only term in the concentration field that is able to induce a neat velocity on the particle is the the polar defined by the magnitude of β_1.

$$V_z = -\frac{\mu_d}{2R^2}\sum_p \beta_p R^{-p}\left(-\frac{2}{3}+2\right)\delta_{p1} = \frac{2}{3}\frac{\mu_d\beta_1}{R^3} \tag{5.11}$$

An active particle with homogeneous catalytic properties on its surface, $\alpha(\theta) = \alpha$, generates a monopolar concentration field with the only non zero term β_0. An apolar particle is not able to swimm. A half coated particle, however, $\alpha = 0$ for $\theta < \pi/2$, and $\alpha \neq 0$ for $\theta > \pi/2$ generates a chemical field with non-zero polar component, $\beta_1 \neq 0$, and thus swims.

In the next section we explain how the presence of an apolar colloid generates a polar chemical field on the surface of a neighbouring particle.

5.2.3 Response field induced by an Apolar Particle

The study of an isolated particle results in a simple monopolar field with nothing else. In a situation with a second particle, a reflector (R), separated a distance r from the source particle (S) experiences a concentration difference on opposite sides in the direction towards the source. A simple calculation from the source predicts a concentration difference $\delta c = c(r-R) - c(r+R) \approx 2R\beta_0^{(S)}/r^2$. A finite polar contribution to the field in the reflector particle $\beta_1^{(R)}$ generates a concentration difference $\delta c = 2\beta_1^{(R)}/R^2$. Equating both δc we obtain a first estimation of the polar field on the reflector particle of magnitude $\beta_1^{(R)} \approx \beta_0^{(S)} R^3/r^2$.

From this qualitative computation the source particle induces a neat velocity on the reflector particle of magnitude v proportional to $\mu_d\delta_0 r^{-2}$. From this simple result we conclude that a source particle induces a long range decaying velocity $v \sim r^{-2}$ on other particles –regardless on their ability to catalize chemicals. The velocity does not depend on the diameter of the receptor particle; if the interaction

where to come from an energy potential the force, F, would be proportional to the size of the receptor particle. $F \propto R$.

To proceed with the exact calculation we define the system, and the coordinates involved in the computation, in Figure 5.2. The source particle (S) is located at position $\mathbf{r_S}$ which corresponds to the origin of the basis $\mathcal{B}_S$ whose coordinates are denoted by (r', θ', z'). The reflector particle (R) is located at position $\mathbf{r_R}$ and defines the origin of the basis $\mathcal{B}_R$ whose coordinates are denoted by the triad (r, θ, z). The distance between particles is given by the vector $\mathbf{z} = |\mathbf{r}_S - \mathbf{r}_R|\,\hat{\mathbf{z}} = z\hat{\mathbf{z}}$, where $\hat{\mathbf{z}}$ is an element of the basis $\mathcal{B}_R$. The position vector in which the field is computed, $\mathbf{r}' = \mathbf{r}_p - \mathbf{r}_S$, from the origin of the basis $\mathcal{B}_S$ can be also computed from the basis $\mathcal{B}_R$ as $\mathbf{r}' = \mathbf{r} - \mathbf{z}$.

A common computation is $1/|\mathbf{r}'|$. From the basis $\mathcal{B}_S$ the calculation is trivial hence $1/|\mathbf{r}_p| = 1/r'$. However, from $\mathcal{B}_R$

$$\frac{1}{|\mathbf{r}'|} = \frac{1}{z}\sum_{p=0}^{\infty}\left(\frac{R_R}{z}\right)^p (-1)^p P_p(\cos\theta) \tag{5.12}$$

Where we have already restricted $|\mathbf{r}| = R_R$ on the surface of particle R. In addition we include the $(-1)^p$ to account for the fact that we have introduced $\pi - \theta'$ instead of θ' in the calculations.

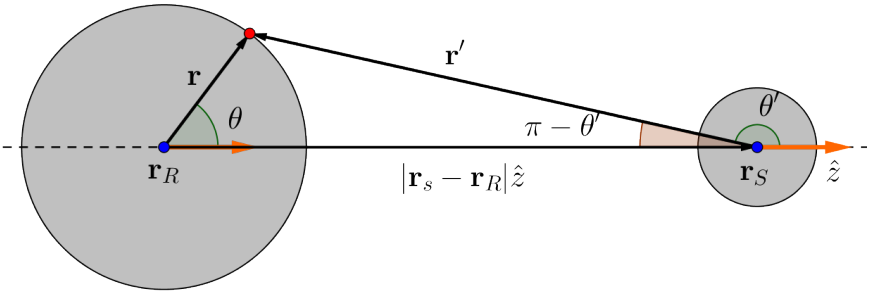

Figure 5.2 | Physical portrait on the system. A cut of the plain $\phi = 0$ shows the pair of spheres as a pair of disks. The source particle generates a field $c_S(r', \theta')$ which needs to satisfy boundary conditions on the sphere centred at $\mathbf{r}_R$.

We introduce a the source (S) and reflector (R) particles as spheres of radii R_S, and R_R respectively. The source generates a chemical field (5.13) characterized by the l-th multipolar term of the Laplace expansion. Given the linearity of the differential equations governing diffusion, a linear combination of the l-th multipoles

gives the general solution to the problem.

$$c_S(r',\theta') = B_l \frac{P_l\big(\cos(\theta')\big)}{(r')^{l+1}} \tag{5.13}$$

The field c_S as a function of the coordinates (r,θ) must satisfy both Laplace equation and the boundary condition on $r' = R_S$, and on $r = R_R$. To impose the boundary conditions on the reflector particle centered at $\boldsymbol{r}_R$ we need to determine the coefficients β_m from the general expression:

$$c_R(r,\theta) = \sum_m \beta_m \frac{P_m(\cos\theta)}{r^{m+1}} \tag{5.14}$$

In cylindrical coordinates the differentiation respect to z generates multipoles of higher order. In our system the z coordinate corresponds to the centre-to-centre line.

$$\frac{\partial}{\partial z}\frac{P_l(\mu)}{r^{l+1}} = -(l+1)\frac{P_{l+2}(\mu)}{r^{l+2}} \tag{5.15}$$

We use this property to relate (5.13) to a source monopole.

$$\frac{P_l(\mu)}{r^{l+1}} = \frac{-1}{l}\frac{\partial}{\partial z}\frac{P_{l-1}(\mu)}{r^l} = \ldots = \frac{(-1)^l}{l!}\frac{\partial^l}{\partial z^l}\frac{1}{r} \tag{5.16}$$

To expand $c_S(r',\theta')$ in the coordinates of $\mathcal{B}_R$. We need (5.12)

$$c_S(r'(r,\theta),\theta') = \frac{(-1)^l}{l!}B_l\frac{\partial^l}{\partial(z')^l}\frac{1}{r'} = \frac{(-1)^{l+m}B_l}{l!}\frac{\partial^l}{\partial z^l}\frac{1}{z}\sum_{m=0}^{\infty}\left(\frac{r}{z}\right)^m P_m(\cos\theta) \tag{5.17}$$

The total field on the surface of (R) $c = c_R(r,\theta) + c_S(r,\theta)$ needs to satisfy the boundary conditions $\partial_r c(r,\theta)|_R = \alpha_R/D_c$

$$c(r,\theta) = \sum_{m=0}^{\infty}\left[\frac{(-1)^{l+m}B_l}{l!}\frac{\partial^l}{\partial z^l}\frac{r^m}{z^{m+1}} + \beta_m\frac{1}{r^{m+1}}\right]P_m(\cos\theta) \tag{5.18}$$

The term $m = 0$ needs special consideration since it is the only nonbanishing element in RHS of the boundary condition $P_0 = 1$.

$$\beta_0 = \frac{\alpha_R R_R^2}{D_c} \tag{5.19}$$

It is not surprising that this term coincides with the monopole generated by its surface properties. However, expressions with $m \neq 0$ are now possible since $B_l \neq 0$.

$$\beta_m^{(l)} = (-1)^{m+1}\frac{m\,(m+l)!}{l!(m+1)!}B_l R_R^{2m+1}\frac{1}{z^{m+l+1}} \tag{5.20}$$

The only relevant contribution of β that leads to propulsion is β_1. The fist source contribution is $B_0 = \alpha_S R_S^2/D_c$. We set $l = 0$, and $m = 1$.

$$\beta_1^{(0)} = -\frac{1}{2}R_R^3\frac{\alpha_c R_S^2}{D_c}\frac{1}{z^2} \tag{5.21}$$

We obtain a dipolar velocity field around the reflector that decays quadratically with the distance to the source. We may compute, once again, the effect of the induced dipolar field on the source. Now $l = 1$, and $m = 1$ with B_1 the previous result.

$$\beta_1^{(1)} = \frac{1}{2} R_S^3 R_R^3 \frac{\alpha_S R_S^2}{D_c} \frac{1}{z^5} \tag{5.22}$$

The next step is to consider higher order terms. It is not relevant for the scope of this thesis but, since the quadrupolar term of the velocity field is widely used in the squirmer model $B_2 \neq 0$ we compute the lower order contributions to β_2.

$$\beta_2^{(0)} = \frac{2R_R^5}{3} \frac{\alpha_0 R_S^2}{D_c} \frac{1}{z^3} \tag{5.23}$$

$$\beta_2^{(1)} = -R_S^5 R_R^3 \frac{\alpha_c R_S^2}{D_c} \frac{1}{z^6} \tag{5.24}$$

5.2.4 Interaction velocities

As previously seen in subsection 5.2.2, for a spherical particle, the only contribution of the multipolar expansion of the chemical field that is able to generate a propulsion (5.11) by diffusophoresis is $l = 1$, the dipolar.

For a system composed by two species: one active, and one passive. The interaction velocities that particle x induces on particle y in the radial direction, $v^{x\to y}$ are:

$$v^{a\to a} = -\frac{2\alpha_S \mu_d^a}{3D_c} \frac{R_a^2}{z^2} + \frac{2\alpha_S \mu_d^a}{3D_c} \frac{R_a^5}{z^5} \tag{5.25}$$

$$v^{a\to p} = -\frac{2\sigma_S \mu_d^p}{3D_c} \frac{R_a^2}{z^2} \tag{5.26}$$

$$v^{p\to a} = \frac{2\alpha_S \mu_d^a}{3D_c} \left(\frac{R_p}{R_a}\right)^3 \frac{R_a^5}{z^5} \tag{5.27}$$

By means of a chemical velocity $V_0 = \alpha_a \mu_d^a \sigma_a^2/(12D_c)$ we rewrite the equations for the relative velocity for pairs of particles:

$$v^{a,a} = -2V_0 \left(\frac{\sigma_a}{z}\right)^2 + \frac{1}{4} V_0 \left(\frac{\sigma_a}{z}\right)^5 \tag{5.28}$$

Using μ_d^p/μ_d^a to define a μ^*

$$v^{a,p} = -V_0 \mu^* \left(\frac{\sigma_a}{z}\right)^2 + \frac{1}{8} V_0 \left(\frac{\sigma_p}{\sigma_a}\right)^3 \left(\frac{\sigma_a}{z}\right)^5 \tag{5.29}$$

5.2.5 Newton's Third Law

The interaction between an active and a passive particle has been computed in terms of velocities. Since the interaction is not understood as fundamental interactions; we are omitting the presence of the fluid and the ulterior movements of the chemical products; we obtain the effective force of interaction between particles through the stokes formula for a sphere. A sphere moving at velocity U experiences a drag force F, $F = 6\pi\eta RU$. If the interaction where to come from a force the relative velocity between particles would be:

$$v_{rel} = 2\mu F_{int} \tag{5.30}$$

Assuming Newton's Third Law of motion $|\mathbf{F}_{12}| = |\mathbf{F}_{21}| = F_{int}$. The imposition of such an interaction gives.

$$v_{rel} = v_a + v_p = \mu(R_a)F_{int} + \mu(R_p)F_{int} = \mu(R_a)F_{int}\left(1 + \frac{\mu(R_a)}{\mu(R_p)}\right) \tag{5.31}$$

For thermal mobilities $\mu \sim R^{-1}$. The relative velocity is shared among interacting particles according to the ratio between radii.

$$v_a = v_{rel}\left(1 + \frac{R_a}{R_p}\right)^{-1} = \frac{R_p v_{rel}}{R_a + R_p}; \qquad v_p = \frac{R_a v_{rel}}{R_a + R_p} \tag{5.32}$$

For simplicity we define $\lambda = R_p/(R_a + R_p)$, then $(1 - \lambda) = R_a/(R_a + R_p)$.

As previously seen the computed diffusophoretic interactions do not share the same dependencies over distance. $v^{a\to p} \sim z^{-2}$ while the reaction velocity $v^{p\to a} \sim z^{-5}$. We define a parameter ζ which connects from a scenario in which Third Law is satisfied ($\zeta = 0$) to a scenario in which it is fully broken ($\zeta = 1$). Assuming a relative velocity $v_{rel} = v^{a\to p} + v^{p\to a}$

$$v_p = v^{a\to p}\zeta + (1-\zeta)(1-\lambda)v_{rel}; \quad v_a = v^{p\to a}\zeta + \lambda(1-\zeta)v_{rel} \tag{5.33}$$

5.3 Computational model

Active particles in the experimental realizations are ferromagnetic hematite ellipsoids [Martinez-Pedrero et al., 2017]. In all experiments ellipsoids are characterized by a long axis $a = 1.8 \pm 0.1\ \mu m$ and a short axis $b = 1.3 \pm 0.1\ \mu m$. We model the ellipsoids by means of a dumbbell, a dimer. We define a dimer as a pair of disks of diameter $\sigma_a = 1.3\mu m$ connected by a spring of size $r_0 = 0.5\mu m$ and spring constant k. When we introduce a diffusion D_0 to each monomer the centre of mass of the dimer diffuses with a total translational diffusion constant of $D_T = 2D_0$, and a rotational diffusion constant $D_R = 2D_0/r_0^2$[2].

[2]The rotational diffusion constant is a relevant parameter for polar active matter since the Péclet number relates the characteristic running time to the rotation diffusion time.

5.3.1 Equilibrium Interactions

We build the model for the mixture of active and passive particles on an equilibrium model for the system. Active particles are described by dimers of two disks. The dimer breaks the polar symmetry of the apolar particle and its short axis is used as director of the magnetic permanent moment. Passive particles are described by disks. In order to avoid overlaps between disks we introduce a repulsive WCA (2.7) potential between particles.

Dimers

To determine the spring constant we ask the elongation fluctuations $\Delta x/r_0$ to be below 5% – the approximate dispersion in sizes of experimental particles. The characteristic energy of the spring is $k\Delta x^2$ and needs to be equated to the thermal fluctuations $b_B T$. Then we choose a spring constant $k = 400 k_B T/r_0^2$.

Dimers are located by the position vector $\boldsymbol{r}_i$. The two disks that constitute the dimer are given by the position vectors $\boldsymbol{q}_i^a$, and $\boldsymbol{q}_i^b$. Hence $\boldsymbol{r}_i = \left(\boldsymbol{q}_i^a + \boldsymbol{q}_i^b\right)/2$ and we define the dimer vector $\boldsymbol{\delta}_i = \boldsymbol{q}_i^b - \boldsymbol{q}_i^a$. To fully characterize the dimers we need to introduce a normal vector to $\boldsymbol{\delta}$. We introduce a $\boldsymbol{t}_i = \mathcal{R}_{\pi/2}\boldsymbol{\delta}_i$.

Magnetic dimers

Hematite particles have a magnetic permanent moment $m_0 = 2 \times 10^{-16} Am^2$ in the direction of its short axis; each dimer has $\boldsymbol{m}_i = m_0 \hat{\boldsymbol{t}}_i$. Once immersed in a mixture of water and hydrogen peroxide ellipsoids sediment close to the glass substrate of the experimental chamber – where they remain in a two dimensional confinement.

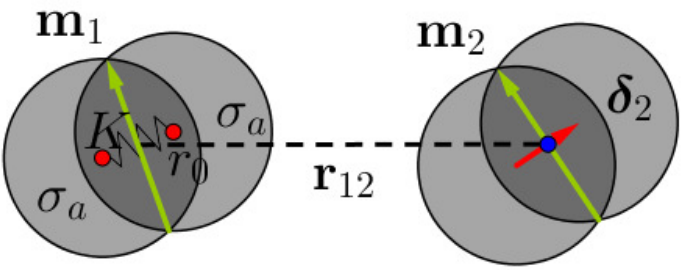

Figure 5.3 | Sketch of a pair of dimers with the magnetizations $\boldsymbol{m}_1$, and $\boldsymbol{m}_2$ parallel to the short axis and the dipolar vector δ connecting the centres of each disk, in red in the left dimer – joining them a spring of rest length r_0, and constant K.

A magnetic dipole of magnitude m_0 generates a magnetic field $\boldsymbol{B}$

$$\boldsymbol{B}(\boldsymbol{r}) = \frac{\mu_0 m_0}{4\pi r^3}\left(3\left(\hat{\boldsymbol{m}}\cdot\hat{\boldsymbol{r}}\right)\hat{\boldsymbol{r}} - \boldsymbol{m}\right) \tag{5.34}$$

In such a field a second magnetic dipole experiences a torque $\boldsymbol{T} = \boldsymbol{m}\times\boldsymbol{B}$. Given particles at positions $\boldsymbol{r}_1$, and $\boldsymbol{r}_2$ with position vector $\boldsymbol{r} = \boldsymbol{r}_2 - \boldsymbol{r}_1 = -\boldsymbol{r}'$ the torques experienced by de dipoles are

$$\boldsymbol{T}^{(1)} = \frac{\mu_0 m_0^2}{4\pi r^3}\left[3\left(\hat{\boldsymbol{m}}_1\cdot\hat{\boldsymbol{r}}\right)\left(\hat{\boldsymbol{m}}_2\times\hat{\boldsymbol{r}}\right) - \hat{\boldsymbol{m}}_2\times\hat{\boldsymbol{m}}_1\right] \tag{5.35}$$

$$\boldsymbol{T}^{(2)} = \frac{\mu_0 m_0^2}{4\pi r^3}\left[3\left(\hat{\boldsymbol{m}}_2\cdot\hat{\boldsymbol{r}}\right)\left(\hat{\boldsymbol{m}}_1\times\hat{\boldsymbol{r}}\right) + \hat{\boldsymbol{m}}_2\times\hat{\boldsymbol{m}}_1\right] \tag{5.36}$$

The total torque $T = T^{(1)} + T^{(2)} = 0$, since there is no external magnetic field. The relative torque is $\boldsymbol{\Gamma} = T^{(1)} - T^{(2)}$ which depends on the angle difference between the dipoles $\sin\theta = \hat{m}_2\times\hat{m}_1$

$$\boldsymbol{\Gamma} = \frac{\mu_0 m_0^2}{4\pi r^3}\left(\hat{\boldsymbol{m}}_1\times\hat{\boldsymbol{m}}_2\right) \tag{5.37}$$

To compare[3] the angular diffusion to the magnetic torque we divide $|\boldsymbol{\Gamma}|$, which has units of energy to over the thermal fluctuations with an energy scale $k_B T$. For $\beta|\boldsymbol{\Gamma}| > 1$ thermal fluctuations are negligible while for $\beta|\boldsymbol{\Gamma}| < 1$ thermal fluctuations dominate and a pair of dimers remain alligned.

$$\beta|\boldsymbol{\Gamma}| < \frac{4\times10^{-7}\times10^{-32}}{4.14\times10^{-21}\left(10^{-6}\right)^3}(r/1\mu m)^{-3} \approx \left(\frac{1\mu m}{r}\right)^3 \tag{5.38}$$

As seen in equation (5.38) magnetic alignment dominates below $1\mu m$. Thermal hematite particles will spontaneously form chains in the direction of the short axis since $\sigma_a \approx 1\mu m$.

The magnetic interaction between dimers introduces an attractive/repulsive force on the centre of mass of each dimer; the vectorial form of the force is:

$$\boldsymbol{F}_{ij}^m = \frac{3\mu_0 m_0^2}{4\pi r^4}\left[\left(\hat{\boldsymbol{r}}\cdot\hat{\boldsymbol{m}}_i\right)\hat{\boldsymbol{m}}_j + \left(\hat{\boldsymbol{r}}\cdot\hat{\boldsymbol{m}}_j\right)\hat{\boldsymbol{m}}_i + \hat{\boldsymbol{r}}\left(\hat{\boldsymbol{m}}_i\cdot\hat{\boldsymbol{m}}_j\right) - 5\hat{\boldsymbol{r}}\left(\hat{\boldsymbol{r}}\cdot\hat{\boldsymbol{m}}_i\right)\left(\hat{\boldsymbol{r}}\cdot\hat{\boldsymbol{m}}_j\right)\right] \tag{5.39}$$

To avoid overlapping of particles we introduce a repulsive WCA potential (2.7) between disks from different dimers. The strength of the interaction depends on ϵ which we fix at a moderate value $\epsilon = 24k_B T$.

The interaction of a monomer of a dimer needs to be computed for each monomer α of the other dimers. The distance between monomers α, and β of

[3] A more accurate argument the Langevin dynamical equation of the angle $\partial_t\theta = \beta D_r|\boldsymbol{\Gamma}| + \sqrt{2D_r}\xi$ leads to the same result.

dimers i, and j respectively is $\boldsymbol{q}_{ij}^{\alpha\beta} = \boldsymbol{q}_i^{\alpha} - \boldsymbol{q}_j^{\beta}$

$$\boldsymbol{F}_i^a = \frac{1}{2}K\left(r_0 - |\boldsymbol{\delta}_i|\right)\hat{\boldsymbol{\delta}}_i + \sum_{j\neq i}\sum_{\alpha} F^c\left(q_{ij}^{a,\alpha}, \sigma_a\right)\hat{\boldsymbol{q}}_{ij}^{a,\alpha} + \frac{1}{2}\boldsymbol{F}_i^m - \frac{|\boldsymbol{\Gamma}_i|}{2\,|\boldsymbol{\delta}_i|}\hat{\boldsymbol{m}}_i \quad (5.40)$$

$$\boldsymbol{F}_i^b = -\frac{1}{2}K\left(r_0 - |\boldsymbol{\delta}_i|\right)\hat{\boldsymbol{\delta}}_i + \sum_{j\neq i}\sum_{\alpha} F^c\left(q_{ij}^{b,\alpha}, \sigma_a\right)\hat{\boldsymbol{q}}_{ij}^{b,\alpha} + \frac{1}{2}\boldsymbol{F}_i^m + \frac{|\boldsymbol{\Gamma}_i|}{2\,|\boldsymbol{\delta}_i|}\hat{\boldsymbol{m}}_i \quad (5.41)$$

Where K is the elastic constant of the dimer spring, α sweeps the monomer labels (a, and b), and $\boldsymbol{F}_i^m$ is the contribution of the forces acting on the centre of mass – magnetic forces. Finally we introduce the magnetic torque $\boldsymbol{\Gamma} = \boldsymbol{\delta} \times \boldsymbol{F}/2 - \boldsymbol{\delta} \times \boldsymbol{F}/2 = |\boldsymbol{\delta}|\,|\boldsymbol{F}|$ as forces in the direction perpendicular to the dimer vector, hence in the direction of the magnetic moment.

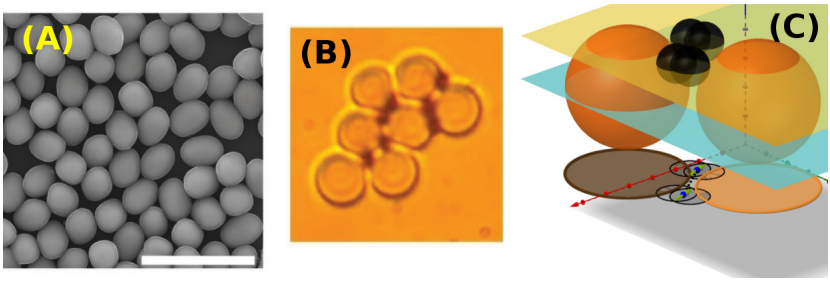

Figure 5.4 | (A) SEM image of a suspension of hematite particles. (B) Images of a mixture of hematite and silica particles. Active particles are located in the interstitial region of the silica aggregate "overlapping" the silica particles. (C) 3D sketch with hematite and silica particles in different planes and the projection on the same plane showing overlap.

Passive colloids

We introduce passive particles, inclusions of diameter σ_p as disks with centres at position $\boldsymbol{R}_i$. Disks introduce an additional repulsive force on each monomer $\boldsymbol{q}_i^{\alpha}$. Repulsion is introduced by a non-additive WCA pair potential. For a pair of passive particles we define $\sigma = (\sigma_p + \sigma_p)/2$, for active disks we use $\sigma = (\sigma_p + \sigma_p)/2$, and for a pair of active and passive disks we use $\sigma = \sigma_{WCA} = (\sigma_p + \Delta\sigma_a)/2$, where $\Delta \in [0, 1]$. With such a force, the interaction between active and passive particles allows a certain overlap – up-to half an active particle for $\Delta = 1$. The overlap of disks in the simulation plane could effectively model the dynamics of the passive and active particles located at different planes.

The total force acting on an apolar particle is

$$\boldsymbol{f}_i^{\alpha} = \boldsymbol{F}_i^{\alpha} - \sum_{j\in\{R_j\}} F^{WCA}(z_{ij}^{\alpha}, \sigma_{WCA})\frac{\boldsymbol{R}_j - \boldsymbol{q}_i^{\alpha}}{|\boldsymbol{R}_j - \boldsymbol{q}_i^{\alpha}|} \quad (5.42)$$

Where we use $\boldsymbol{z}_{ij}^{\alpha} = \boldsymbol{R}_j - \boldsymbol{q}_i^{\alpha}$. The repulsion forces acting on a passive particle $\boldsymbol{F}_i^{int}$ are

$$\boldsymbol{F}_i^{int} = \sum_{j\neq i}\sum_{\alpha} F^{WCA}(R_{ij},\sigma_p)\hat{\boldsymbol{R}}_{ij} + \sum_{j\in\{R_j\}} F^{WCA}(z_{ij}^{\alpha},\sigma_{WCA})\hat{\boldsymbol{z}}_{ij}^{\alpha} \tag{5.43}$$

5.3.2 Chemical Interaction Velocities

The model presented in 5.3.1 introduces elongated particles and magnetic forces in thermal equilibrium. We have previously developed a model for out-of-equilibrium interactions between particles when light is turned on. Contrary to the equilibrium models we introduce the non-equilibrium interactions as interaction velocities, $\boldsymbol{v}_i^{\alpha}$.

In an overdamped Langevin equation velocities are proportional to forces though mobility coefficients. In this subsection we introduce the non-equilibrium velocities modulated by a parameter ζ that connects a scenario with no Action-Reaction ($\zeta = 1$) to an Action-Reaction scenario ($\zeta = 0$).

$$\dot{\boldsymbol{q}}_i^{\alpha} = D_0\beta\boldsymbol{f}_i^{\alpha} + \sqrt{2D_0}\boldsymbol{\xi}_i^{\alpha} + \boldsymbol{v}_i^{\alpha} \tag{5.44}$$

$$\dot{\boldsymbol{R}}_i = D_0\beta\frac{\sigma_a}{\sigma_p}\boldsymbol{F}_i^{int} + \sqrt{2D_0}\left(\frac{\sigma_a}{\sigma_p}\right)^{1/2}\boldsymbol{\xi}_i + \boldsymbol{V}_i \tag{5.45}$$

$$\boldsymbol{v}_i^{\alpha} = \sum_{j\neq i}\sum_{\beta} v^{a\to a}\hat{\boldsymbol{q}}_{ij}^{\alpha\beta} + \sum_{j\in\{R_j\}}\left[\lambda\left(1-\zeta\right)\left(v^{p\to a}+v^{a\to p}\right)+\zeta v^{p\to a}\right]\hat{\boldsymbol{z}}_{ij}^{\alpha} \tag{5.46}$$

$$\boldsymbol{V}_i = \sum_{\alpha}\sum_{j\in\{q_j^{\alpha}\}}\left[\left(1-\lambda\right)\left(1-\zeta\right)\left(v^{a\to p}+v^{p\to a}\right)+\zeta v^{a\to p}\right]\frac{\boldsymbol{R}_i-\boldsymbol{q}_j^{\alpha}}{\left|\boldsymbol{R}_i-\boldsymbol{q}_j^{\alpha}\right|} \tag{5.47}$$

Characteristic times

The dynamics introduce several time scales. We define the following time scales for the active particles. The equivalent characteristic time for a passive particle the passive particle time is $(\sigma_p/\sigma_a)^3$ times the active time.

$$\tau_d = \frac{\sigma_a^2}{D_0} \qquad \tau_r = \frac{\sigma_a^2}{\beta D_0\epsilon} \qquad \tau_d = \frac{\sigma_a^2}{\beta D_0 K} \qquad \tau_p = \frac{\sigma_a}{V_0} \tag{5.48}$$

By means of the apolar diffusion time σ_a^2/D_0, and the apolar characteristic length σ_a we introduce the characteristic velocity $V_T = D_0/\sigma_a \approx 0.3\mu m\ s^{-1}$.

Experimental Calibration

In equations (5.28), and (5.29) we derived the dependence of the relative velocity between pairs on the relative distance between particles. By means of tracking experiments we can measure the relative distance between particles. Averaging over trajectories we obtained the curves $V_{rel} = \langle v_{rel}(r) \rangle$ for pairs of active-passive and active-active particles, see Figure 5.5.

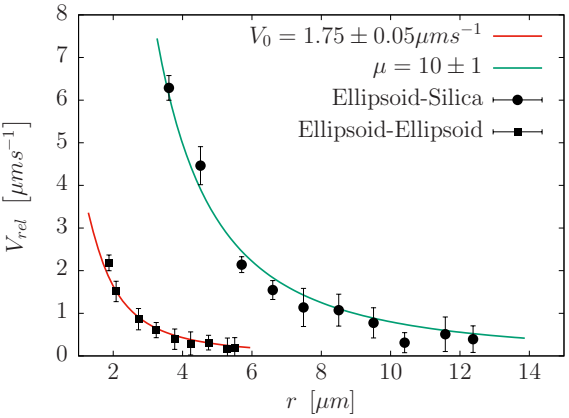

Figure 5.5 | Calibration fits for the pair of parameters V_0, and μ. We obtain a characteristic velocity $V_0 = 1.75 \pm 0.05 \mu m\ s^{-1}$ and a mobility coefficient $\mu = 20 \pm 1$.

In experiments we track the positions of the centres of mass of pairs of active and passive particles. For an active-passive with relative velocities v^a, and v^b for the monomers, and V for the passive particle we can extract the relative velocity

$$V_{rel} = (v^a + v^b)/2 + V \approx \frac{1}{8} V_0 \left(\frac{\sigma_p}{\sigma_a}\right)^3 \left(\frac{\sigma_a}{r}\right)^5 - 2V_0 \mu^* \left(\frac{\sigma_a}{r}\right)^2 \tag{5.49}$$

For an active-active pair the relative velocity is computed in the same way

$$V_{rel} = -2V_0 \left(\frac{\sigma_a}{r}\right)^2 + \frac{1}{4} V_0 \left(\frac{\sigma_a}{r}\right)^5 \tag{5.50}$$

5.4 Zeta = 0 – Action Reaction

We introduce a series of simulation for the mixture of active and passive particles. For a rationalization of the mixture we have defined the packing densities of passive particles Φ_p, and packing density of active particles as follows Φ_a. Using N_p as the number of passive particles, N_a the number of apolar dimers, and L the longitudinal dimensions of a squared simulation box with periodic boundary conditions.

$$\Phi_p = \frac{N_p \pi \sigma_p^2}{4L^2}, \qquad \Phi_a = \frac{2N_a \sigma_a^2 (\pi - c)}{4L^2} \tag{5.51}$$

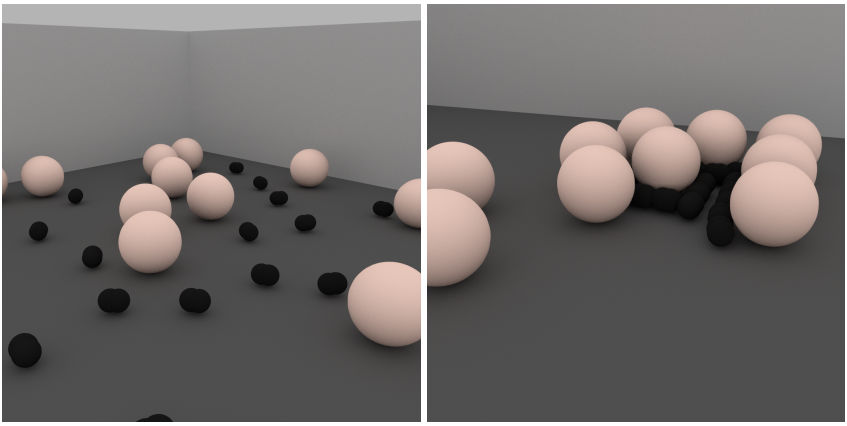

Figure 5.6 | Artistic representation of a binary mixture of active and passive particles. **A** the system evolving in equilibrium before the activity quench. **B** the system after the activity quench. Passive particles are nucleated around apolar particles which form a chain due to the join action of the diffusphoretic, and magnetic interactions.

where the measure of the overlap between monomers of the dimer is given by the factor $c = \arccos(r_0/\sigma_a) - \frac{r_0}{\sigma_a}\sqrt{1 - {r_0}^2/{\sigma_a}^2}$.

The model above for the dynamics of active and passive particles has a special feature. It naturally breaks action reaction for the interactions between species. This is not a common scenario for molecular dynamics. As previously seen, the interaction between particles can be understood as a relative interaction fulfilling action-reaction (5.44-5.47) setting the parameter $\zeta = 0$. In this conditions the interaction velocities are split into each pair as a function of the ratio between diameters.

In this work we do not investigate the interactions mediated by pure hydrodynamics. As computed before, at each particle appears a tangential velocity field in the fluid. The surface velocity field propagates into the bulk and induces hydrodynamic interactions on other particles. A good exercise for the future is to map each particle into the effective squirmer, introduced first by [Lighthill, 1952] and later corrected by [Blake, 1971]. The squirmer model introduces $B_1 = \beta_1$, and $B_2 = \beta_2$ as the tangential components of the surface velocity. More recently, [Llopis and Pagonabarraga, 2010] studied the detailed hydrodynamics of the interaction between pairs of squirmer.

5.4.1 Emergent structures

In this section we study the macroscopic arrangement of active and passive particles for system at different densities. We have prepared an array of systems with passive

particle's density in the range $\Phi_p = 0.1$ to $\Phi_p = 0.6$, and active particles in the range $\Phi_a = 0.02$ to $\Psi_a = 0.3$.

The initial configuration is obtained by evolving the system in thermal equilibrium to a steady state. For the configurations with large quantities of both active and passive particles we have followed the following procedure. First, we introduce $2/3$ of the passive particles in de box. Second, we introduce a large fraction of the apolar particles. Third, we turn on attraction between apolar and passive particles in order to generate empty spaces. Forth, we introduce the remaining $1/3$ of passive and active particles. Fifth, we equilibrate the system.

For a system in equilibrium we quench it to the state with a finite V_0, and μ interaction, and finite magnetic interactions. In experiments, the apolar particles showed a certain structure reminiscent of their alignment relative to the terrestrial magnetic field. In simulations we activate the magnetic interactions between apolar particles a few time units prior to the activity quench, so there is a certain structure although we do not introduce an external magnetic field – such as the terrestrial.

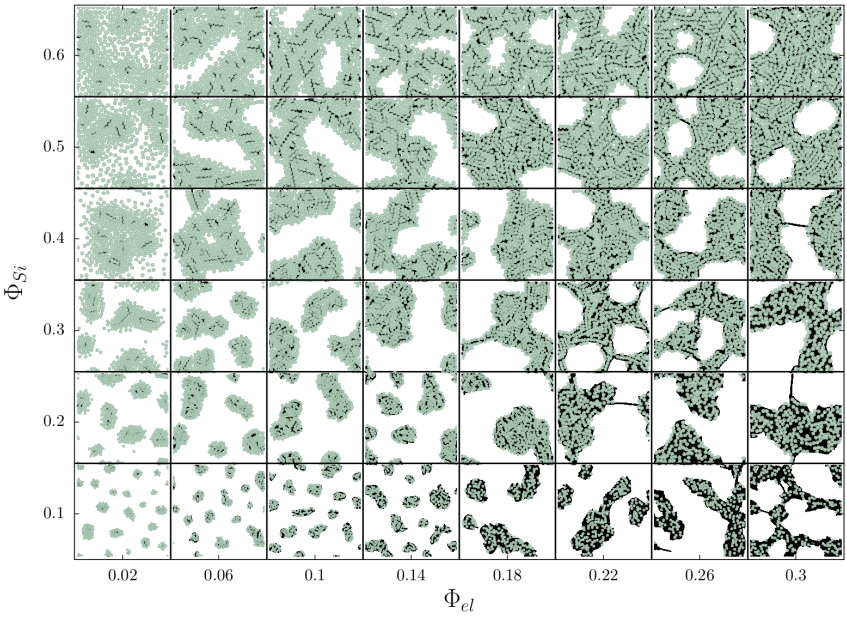

Figure 5.7 | Lattice of snapshots of computational system. The mixture at different densities and after $\tau = 1000$ after the activity quench.

In Figure 5.7 we present in a grid the typical structures that emerge in the mixture after the activity quench. From the image, taken at $\tau/\tau_d = 1000$ after the activity quench, we appreciate different morphologies. At large densities of passive

particles we observe percolating structures of passive colloids. At low densities of active particles we observe the formation of clusters, and separating both regimes we observe the formation of gel like structures. In the following section we stablish a quantitative to sort the different morphologies.

5.4.2 Structure Diagram

To identify different structures in the system we introduce the cluster analysis presented in [Baumgartl et al., 2007] and define the averaged gyration radii of active and passive particles. We detail the computation of the averaged gyration radii, $\langle r_g \rangle$, in Appendix 5.A. The magnitude $\langle r_g^a \rangle$ defined for active particles, $\langle r_g^p \rangle$ for passive particles give a quantitative description of the structures of the system. The comparison of $\langle r_g \rangle$ with the system size gives a criterion to define percolation in the system. A structure is said to percolate when its average gyration radius is comparable to half a system size. Then, we define the percolation threshold for the passive particles $r_c^p/L = 0.5$, and $r_c^a/L = 0.4$ per the active particles to take into account the emergence of magnetic bridges connecting different structures, and thus the reduction in the threshold.

The relation between radii of gyration determine the different structures appreciated in Figure 5.7. For gyration radii below the percolation threshold we define the cluster phases. The Cluster I structure is numerically classified by $\langle r_g^p \rangle > \langle r_g^p \rangle$. The Cluster I structures correspond to clusters of passive particles with central seeds of active particles. At low concentration of active particles the Cluster I phase is in coexistence with a gas phase of passive particles that are not attached to active particles, see section 5.4.4. The Cluster II structure is numerically classified by $\langle r_g^p \rangle < \langle r_g^p \rangle$. The system is constituted by clusters of of passive particles held together by a network of active particles, active particles envelop and percolate in the cluster of passive particles.

For gyration radii above the percolation threshold we encounter three different scenarios. The Gel I structure characterized by $\langle r_g^p \rangle / L > r_c^a$, and $\langle r_g^a \rangle < r_c^a$. Where we observe a percolating structure of passive particles held together by localized chains of active particles. The Gel II structure is formed when both radii of gyration exceed the percolation threshold. In Gel II passive particles percolate, and the active chains cover the whole structure acting as a structural scaffold. Finally, the Gel III structure is characterized by the percolation of the active particles $\langle r_g^a \rangle / L > r_c^a$ but $\langle r_g^p \rangle / L < r_c^p$, and the formation of clusters of passive particles. Unstructured passive particles are arrested in a aggregates of active particles which, at high density of apolar particles, connected by active particle's bridges. The results of this classification are shown in Figure 5.8. We identify the different structures in different colours, and introduce a pair of constant Φ_p lines in order to illustrate the evolution of the gyration radii for increasing concentration of apolar particles. At Figure 5.9 we observe the change in the macroscopic arrangement of the system for increasing density of active particles.

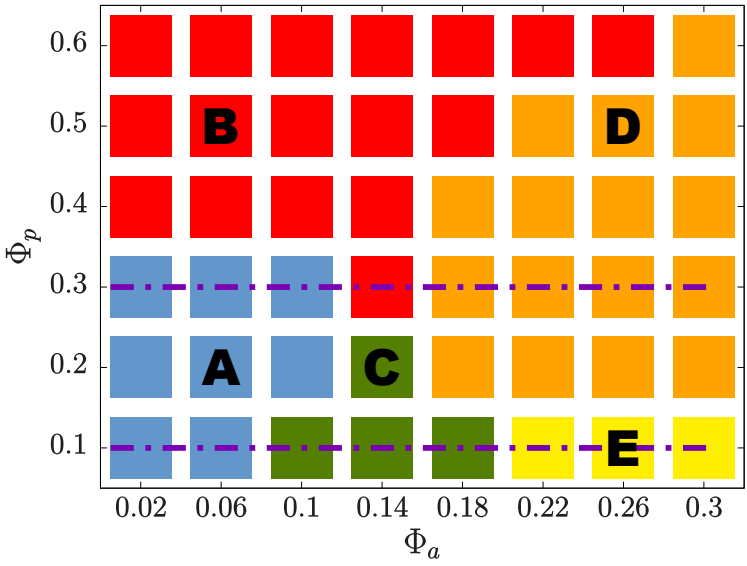

Figure 5.8 | Computational structural diagram of the system as a function of densities for $Pe = 2$, $\mu = 20$, and $M = 36$. Denoted by **A**, and **C** Cluster I and II structures in blue, and green, respectively. Denoted by **B**, **D**, **E** Gels I, II, and III in red, orange, and yellow, respectively. Horizontal dashed lines are the constant Φ_p lines used to exemplify the radii of gyration calculations in Figure 5.9

The increase of active particles in a diluted suspension of passive particles, $\Phi_p = 0.1$, follows this succession of stages. First, at low concentrations of apolar particles the system forms clusters of passive particles held together by chains of apolar particles. Then, the increase of apolar particles in the system maintains the clusters of passive particles but apolar particles are gradually entangled in the core of clusters, until they cover them, entering in the Cluster II region. Finally, for increasing densities of apolar particles the apolar particles form large bundles of chains which may connect the passive clusters in the system.

The increase of active particle in suspension of passive particles at an intermediate density of passive particles, $\Phi_p = 0.3$, follows different structures. First, the system resides in a cluster phase with chains holding the passive clusters. With the increase of apolar particles, the activity quench my lead to a percolating cluster of passive particles held together by several chains of apolar magnetic particles. Finally, for larger densities of apolar particles the chains that give structure to the passive aggregate connect in a percolating network. In the percolating structures there is a competition between the asymmetry of magnetic interactions and the attractive diffusophoretic induced interactions which results in the formation of an apolar scaffold that supports the attractive collapse of the diffusophoretic interactions.

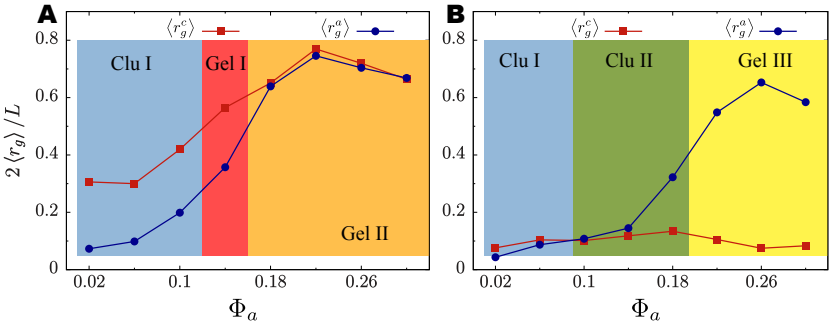

Figure 5.9 | Gyration radius of the active and passive clusters, for increasing density of active particles, Φ_a, at fixed Φ_p. Cluster I, and Cluster II in blue, and green. Gel I, Gel II, and Gel III in red, orange, and yellow. **A** at $\Phi_p = 0.3$. **B** at $\Phi_p = 0.1$

5.4.3 Experimental Structures

The theoretical description of a mixture of active apolar particles with magnetic interactions, and passive colloids presented in this Chapter has been motivated by experiments in mixtures of silica particles, and hematite ellipsoids. In the laboratory, experimentalists have analysed the activity quench of a silica-hematite mixture for different densities of active, and passive particles. Here, we present experimental results showing the appearance of different aggregation structures.

The catalysis of hydrogen peroxide from the hematite particles once the illumination is turned on generates oxygen in a gas form. The formation of gas in the experimental sample leads to the formation of growing bobbles. This growing of bobbles usually interferes with the observation field, and thus destroys the experiment. In experiments, the temporal observation window is limited by the amount of hematite colloids, and the intensity of the interaction. Typical experiments span for tens of minutes, which correspond to $\tau \approx 200\tau_d$.

In Figure 5.10 we list the emergent structures and visually classify them in the structures that we presented in Figure 5.8. For low density of silica, and hematite particles, **A**, we observe the formation of passive clusters with high hexagonal order with active particles in the centres, this structures have the same characteristics as the Cluster I phase identified in simulations. Increasing the density of ellipsoids, **B**, we first observe the formation of silica clusters covered by long silica chains, the clusters completely covered by hematite particles loose the hexagonal order, this is similar to the Cluster II scenario. Finally, for even larger concentrations of magnetic ellipsoids, **C**, we observe the joining of the silica clusters by magnetic bridges, like in the Gel III structures.

At larger concentrations of silica particles, we observe the formation of a large

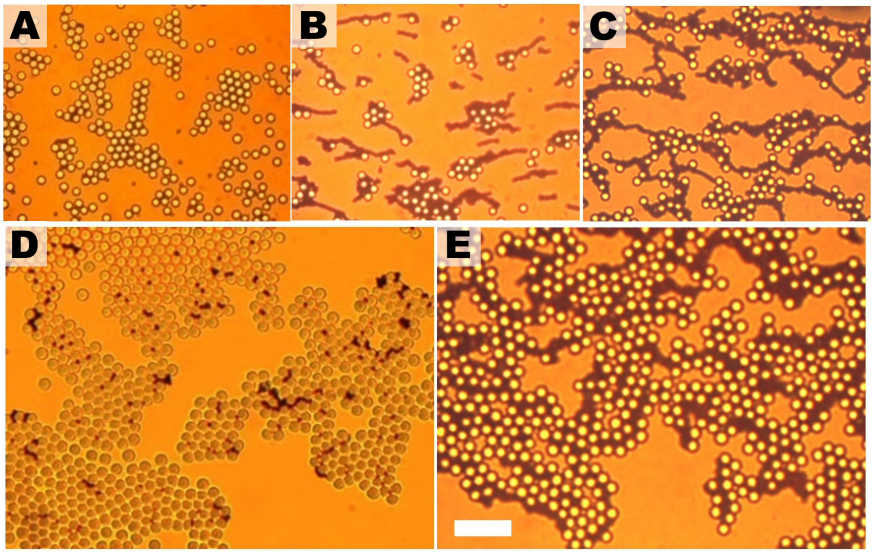

Figure 5.10 | Experimental Structures. Experiments in in the laboratory for different silica (light particles), and hematite ellipsoids (dark particles) concentrations. **A** Distribution of clusters with apolar cores, Cluster I structures. **B** Distribution of clusters with covered by ellipsoids, Cluster II. **C** Distribution of clusters of silica particles connected by a percolating network of magnetic particles, Gel III. **D** Percolating network of silica particles with clusters of silica particles, Gel I. **E** Double percolation of silica, and hematite particles, Gel II.

percolating cluster of silica beads. At low densities of apolar particles, **D**, the large silica structure is held together by clusters of hematite ellipsoids, like in the Gel I structures. Finally, once the density of magnetic ellipsoids is larger, and comparable to the number of silica particles, we observe the formation of a chain of magnetic particles that goes across the silica cluster, like in the Gel II structures.

5.4.4 Analysis of the Structures

For a passive system of WCA repulsive particles $\Phi_p < 0.6$ we expect a fluid phase behaviour for the particles. In this section we prepare a binary mixture of active and passive particles with $0 < \Phi_p \leq 0.6$, and $0 < \Phi_a \leq 0.3$ in equilibrium. After the activity quench the system evolves into different macroscopic structures. In Figure 5.7 we have plotted intermediate configurations of the system and summarized grouped them following the radius of gyration criterion into five distinctive phases, shown in Figure 5.8. In this section we present the general features of the cluster, and percolating structures.

A. Cluster Phases

At low densities of active, and passive particles, $\Phi_a < 0.1$ and $\Phi_p < 0.4$, we find the Cluster I, and Cluster II morphologies. Active particles attract passive particles to form dynamic clusters with hexagonal order, see Figure 5.11. In this region we encounter situations where the clusters of passive particles are in coexistence with a gas of passive particles, for the number of active particles is not sufficient to capture all passive particles. In Cluster II morphologies the cluster is completely wrapped by active particles.

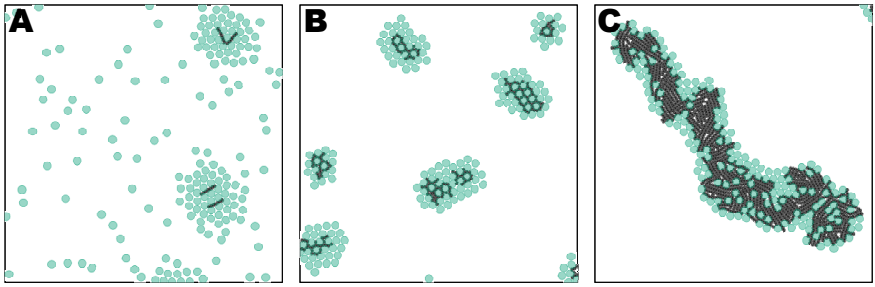

Figure 5.11 | Detail cluster structures. In **A-B** the central core of active particles forms a chain and holds together passive particles which exhibits an ordered hexagonal structure. In **A**, $\Phi_a = 0.005$, clusters are in coexistence with a gas phase. In **B**, $\Phi_a = 0.02$, the gas phase disappears and the excess of active particles start to entangle in the passive clusters. In **C**, $\Phi_p = 0.12$, the central core of apolar particles forms a bundle of chains that percolate in the passive cluster.

The hexagonal structure of the passive particles in the cluster is evident from the structure factors shown in Figure 5.13. The gas of passive particles in the simulations at $\Phi_a = 0.005$ decrease the contrast of the hexagonal structure but the peaks corresponding to the hexagonal lattice are still visible. The structure of the active particles presents a different behaviour in both situations. For systems with a gas of passive particles, active particles accumulate in the centres of the passive clusters disposed in chains, this translates to the structure factor with a q^{-1} divergence at low wave vectors. For the apolar saturated sample, $\Phi_a = 0.02$ the excess of apolar particles induces the formation of rings surrounding the passive structure and the $1/q$ divergence in the structure of apolar particles factor is lost.

In Figure 5.12 we present the large scale temporal evolution of a Cluster I structure with a gas phase of passive colloids. We observe the formation of clusters with cores of apolar particles. Additionally, we present the evolution of the structure factors for times from $\tau = 100$ to 3000 from the activity quench. For the passive particles we observe a first maximum at $q^\star(t) \approx 0.1$ that moves to lower values of the wave vector at increasing times. This wave vector corresponds to characteristic distances $2\pi/q^\star \approx 10\sigma_p$, the typical distance between clusters.

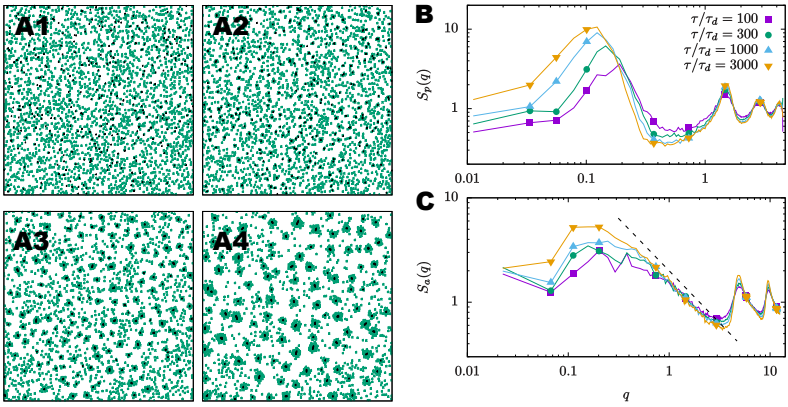

Figure 5.12 | Cluster I structure, system with $\Phi_p = 0.1$, and $\Phi_a = 0.005$. The system evolves from the activity quench at $\tau = 0$. In **A** the evolution at times 100, 300, 1000, and 3000. In **B**, and **C** the structure factor for passive, and active particles respectively. In a dotted line $S_a(q) \sim q^{-1}$ as a guide to the eye.

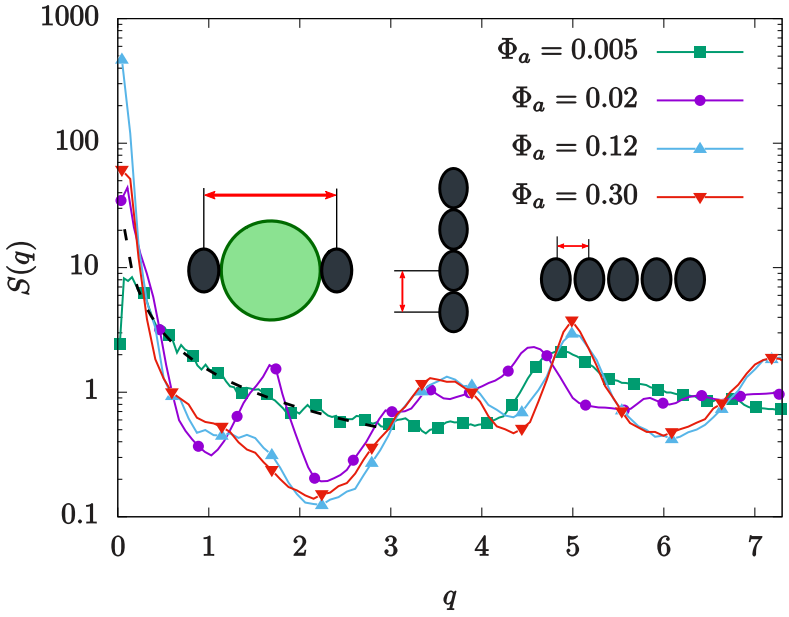

Figure 5.13 | Structure factors of active particles for $\Phi_p = 0.1$ at different Φ_a. Green squares correspond to a Cluster I structure in equilibrium with a gas. In purple circles a Cluster I structure without passive gas. In red and blue triangles percolating structures of active particles. We schematically illustrate the typical structures that correspond to the different peaks.

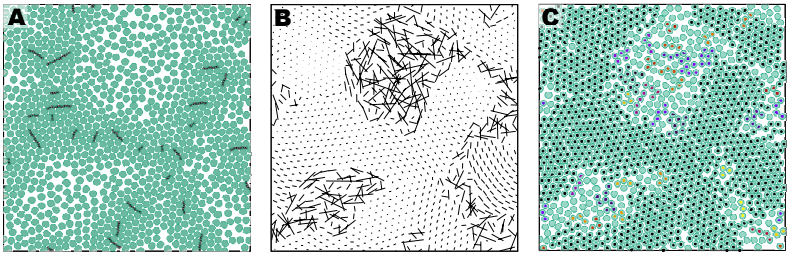

Figure 5.14 | Gel I, system at $\Phi_a = 0.02$, and $\Phi_p = 0.595$. **A** short active chains holding the percolating structure. **B** Particle jumps for a time difference $\Delta\tau = 500\tau_d$, we appreciate the percolating structure from the coexisting gas. **C** Clusters with $n > 2$ particles labelled by the pertinence to each cluster.

B. Percolating Structures

Percolating structures of passive particles typically appear for densities of passive particles $\Phi_p > 0.3$. At low density of active particles we observe the formation of a macroscopic cluster in coexistence with free passive particles. Chains of active particles generate a cohesive region in the passive particles and form a percolating structure. In Figure 5.14 we have different plots that show the main characteristics of this structures, the Gel I structures. First, we observe the elongated distribution of chains along the passive structure in **A**. The passive particles in the low density region correspond to a dense diffusing phase. In **B** we plot the displacement of passive particles in a time interval of $\tau = 500\tau_d$. The particles in the percolating structure define small coordinated movements corresponding to the reorganization of the aggregate. The free passive particles define a series of random displacements which exhibit their diffusive motion. Finally, in **C** we observe the clusters in the system with more than two particles labelled by different colours. The cluster clearly exhibits its percolating nature.

At higher densities of passive particles we observe the formation of ramified structures with holes in the interior, this constitutes the Gel II structures with a double percolation of passive and active particles. Magnetic chains cover the system and hold the collapse. In Figure 5.7 we observe the formation of holes in the Gel II structures. We have simulated a system in the Gel II phase with $N_p = 1000$ particles at densities $\Phi_a = 0.22$, and $\Phi_p = 0.30$. We have computed the density of passive particles at different times from the activity quench and present the evolution of the local density field of passive particles, computed as presented in Appendix 5.A, in Figure 5.15.

Density plots of a Gel II structure in Figure 5.15 reveal the merging of the empty holes in the structure and the slow dynamics of the system. The coarse local grained densities have been computed for the passive particles, and thus, so that the internal regions of de dense phase at low values of the local density correspond to the entangled network of magnetic particles. The competition between the attraction

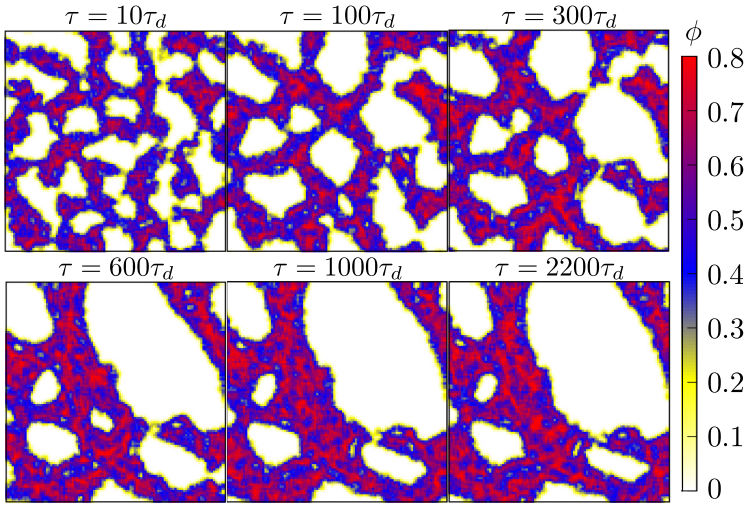

Figure 5.15 | Coarse grained local density for the Gel II structures. Density plots for a system at $\phi_p = 0.22$, and $\Phi_a = 0.30$ at times form $\tau = 10\tau_d$ to $\tau = 2200\tau_d$ from the activity quench.

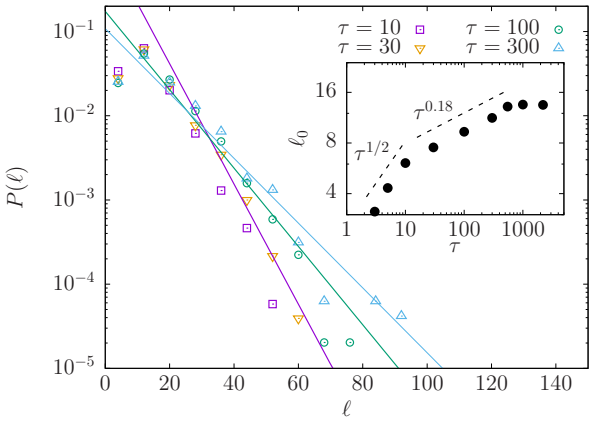

Figure 5.16 | Plot of the cord length distributions of dense regions for a system at $\Phi_p = 0.3$, and $\Psi_a = 0.22$ at different times τ after the activity quench. In the inset we plot the value of the characteristic domain length ℓ_0 as extracted from an exponential fit $P(\ell) \sim \exp(-\ell/\ell_0)$ as a function of time. We plot $\ell \sim \tau^{1/2}$, and $\tau_d^{0.18}$ as a guide to the eye.

and the bending resistance of the magnetic chains governs the dynamics of the holes in the structure.

To study the growth of the dense domains in the system we present the chord length distribution [Testard et al., 2014], presented in Appendix 5.A. To summarise, we draw cords in the system and measure the length, ℓ, of the cord which is between two consecutive interfaces. The chord length distribution has gives information of the detailed structure of the dense region of the system, and decays exponentially at large values ℓ. The characteristic decay length ℓ_0 gives a good estimate of the

average size of the dense domains.

The determination of the average domain size ℓ_0 at different times from the quench, Figure 5.16, reveals an initial domain growth of the system $\ell_0 \sim \tau^{1/2}$, after this fast dynamics the growth is slowed down to $\ell \sim \tau^{0.18}$, and finally the structure is arrested.

5.4.5 Temporal Correlations

To characterize the global dynamics of the systems we introduce the dynamic structure factor $F_q(\Delta t)$, and the relaxation of the local hexagonal order of the system $C_\Psi(\Delta t)$. The definition of the temporal measurements is presented in Appendix 5.A. The dynamic structure factor measures the temporal evolution of the density field for a given wave vector. The use of F_q is largely extended in the study of gels [Zaccarelli, 2007]. For two dimensional systems [Flenner and Szamel, 2015] reported that the typical plateau in three dimensional gels was less evident in two dimensional systems, and proposed the measure of the bond-orientational correlation function C_Ψ.

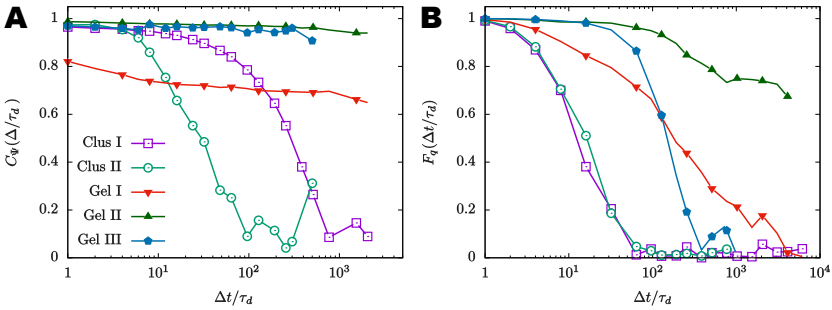

Figure 5.17 | Structural relaxation for passive particles. Measures performed in the different structures. **A** Local hexagonal order correlation. **B** Dynamic Structure Factor, F_q, measured at the wave vector $q \approx 2\pi/\sigma_p$ corresponding to the peak of the static structure factor $S(q)$.

The analysis of the dynamic structure factor at the peak of the $S(q)$ presents a fast decaying behaviour for systems in the Clusters phases. The behaviour of the F_q for the percolating structures requires further attention. For the Gel I structure the decay is slow but constant in time. The origin of this continuous decay is the coexistence of the arrested structure with a diffusing gas of particles. A detailed separated analysis of both phases could reveal major differences in the decay of the density correlations in the Gel I structure. The Gel II structure consists in a percolating structure of passive particles with entangled network of active magnetic particles. The competition between the attraction induced by activity and the rigidity of the magnetic chains prevents the system from collapse and gives rise to an

arrested gel structure. The arrested nature of the structure is revealed in the slow decay of F_q to a plateau at long times. Finally, the Gel III structure shows a high correlation for long times and suddenly drops to zero. This Gel III structures are characterized by the formation of a network of magnetic particles that connect clusters of passive particles. The slow movements and reconfigurations of the magnetic network together with the low structure at $q \approx 2\pi/\sigma_p$ revealed by the structure factors measured in the Gel III phase may be the origin of the rapid decay at long times.

The second correlation measure that we introduced, the local hexagonal order correlation, presents different characteristic decay times for the Cluster phases. The structure factors measure in the Cluster phases reveal a local hexagonal for passive particles the Cluster I phase and an amorphous distribution of passive particles in the Cluster II structures. This difference facilitates the reorientation of passive particles in Cluster II hases as compared to the Cluster I phase. The Gel structures II, and III do not present an appreciable decay for C_Φ, which corresponds to the stable structure formation observed in simulations. However, Gel I structures coexist with a dense fluid of free diffusing passive particles. The diffusion of passive particles introduce a first fast decay of C_Ψ and then orientations in the high-density hexagonal prevail to longer times and thus the slow decay of C_Ψ.

5.5 Conclusions

In this Chapter we have proposed a model to reproduce and extend an experimental system that jointly combines active magnetic particles and passive particles. In this system active particles are not of a polar nature but generate an isotropic disturbance, in the form of production of chemical gradients, to the medium. We have theoretically modelled the diffusophoretic pair interaction that emerge between pairs of particles in the neighbourhood of an active particle. This interactions are introduced in terms of relative velocities of interactions.

Then, we have compared the analytical dependences of the interaction velocities with experimental results and confirmed the d^{-2} algebraic decay for the compared distance range. With the experimental data we obtain a calibration of the interaction to prepare mixtures of active and passive particles at different densities. This leads to the determination of various segregation morphologies and structures: from clusters to gels. Gel phases are identified by the percolation of either passive particles, magnetic active particles, and both species together. In the double percolation of active, and passive particles, the anisotropy in the magnetic interaction is revealed to be essential in the formation of magnetic chains that percolate the internal structure of the gel and act as a structural scaffold that prevents the system from a complete collapse.

Meanwhile, in the laboratory the experimentalists have proceeded to perform a series of experiments to determine the emergence of the defined structures. At

low concentration of active apolar particles they identify a cluster phase for low densities of passive particles and the percolating crystal at higher concentrations of passive particles. The doping of active particles induces the formation of crystalline structure in a passive colloidal dispersion.
At higher concentration of active particles, experiments confirm the total surrounding of clusters of passive particles by entangled networks of hematite colloids. At higher concentrations of active particles, such entangled networks, span from cluster to cluster and introduce a Gel III like structure. At higher concentrations of passive particles we observe the double percolation of a network of active magnetic particles covering a crystal of passive particles.

Finally, we have studied the temporal relaxation of the structures and measured the slow decay of density correlations for wave vectors associated to passive-passive particle's distances. The gel structures are associated to a slow decay of the correlations. The bond orientation correlations reveal the arrested dynamics of the different gel structures, and succeeds to distinguish the cluster structures.

To conclude, we have presented a novel model to study the collective behaviour and segregation in mixture of apolar diffusophoretic particles and passive particles. We are able to reproduce the different morphologies obtained in the laboratory, and extend the simulations to temporal windows beyond reach in experiments and avoiding the external drifts caused by the generation of gas bubbles.

Appendices

5.A Analysis of the mixture

In this Appendix we present the set of measure tools that we have used to characterize the different structures observed in this Chapter and summarized together to help the reader to locate them at the same section of the Thesis.

5.A.1 Spatiotemporal correlations

To study structural properties of the mixture we introduce several measures of the system. We introduce the dynamic structure factor $F_q(t,t')$ as the pair correlations of particles $\{r_i(t)\}$ at initial time t, and particles $\{r_i(t')\}$ at time t' in the position Fourier space. The definition of $F_q\,(t,t')\,0$ for the wave vector $\boldsymbol{q}$.

$$F_{\boldsymbol{q}}(t,t') = \frac{\left\langle \sum_j \sum_{k\neq j} \exp\left[-i\left(\boldsymbol{r}_j(t) - \boldsymbol{r}_k(t')\right)\cdot \boldsymbol{q}\right]\right\rangle}{\left\langle \sum_{j\neq k} \exp\left[-i\left(\boldsymbol{r}_j(t) - \boldsymbol{r}_k(t)\right)\cdot \boldsymbol{q}\right]\right\rangle} \tag{5.A.1}$$

This computation over pairs of particles can be simplified with the definition of the particle density ρ in Fourier space $\boldsymbol{k}$

$$\rho_{\boldsymbol{q}}(t) = \sum_{j=1}^{N} \exp\left(-i\boldsymbol{q}\cdot\boldsymbol{r}_i(t)\right) \tag{5.A.2}$$

Now the calculation is reduced to the product of the density and its complex conjugate. The denominator is, up to a factor N, the static structure factor measured at time t. Or alternatively the product of the density at wave vector $\boldsymbol{q}$ and at $-\boldsymbol{q}$

$$F_{\boldsymbol{q}}(t,t') = \frac{\left\langle \rho_{\boldsymbol{q}}(t)\rho^{\dagger}_{\boldsymbol{q}}(t')\right\rangle}{\left\langle \rho_{\boldsymbol{q}}(t)\rho^{\dagger}_{\boldsymbol{q}}(t)\right\rangle} = \frac{\langle \rho_{\boldsymbol{q}}(t)\rho_{-\boldsymbol{q}}(t')\rangle}{\langle \rho_{\boldsymbol{q}}(t)\rho_{-\boldsymbol{q}}(t)\rangle} \tag{5.A.3}$$

Periodic boundaries in the system introduce a lower bound for q, $dq = 2\pi/L$. The set of wave vectors is now discrete with $\boldsymbol{q}(l,h) = (l,h)\,dq$ with l, and h integer values. The structural correlations in two dimensional glassy systems needs to be computed with a high accuracy since its behaviour generally differs from standard results in three dimension, as reported by [Flenner and Szamel, 2015]. To improve the statistics of the measure we take measures for $q = |\boldsymbol{q}|$. In the $\boldsymbol{q}$ space we set

$\Delta q = 0.1$ to define the pairs (l, h) for which $|\boldsymbol{q}(l,h) - q| < \Delta q$. In Figure 5.A.1 we observe a typical picture of the wave vectors that constitute Fourier space and the coronas of pairs (l, h) that identify each wave vector modulus q.

In the quest for statistics we assume the intermediate scattering to be a function of the time difference $\Delta t = t' - t$. Being a function of Δt we can take the average over different initial times t.

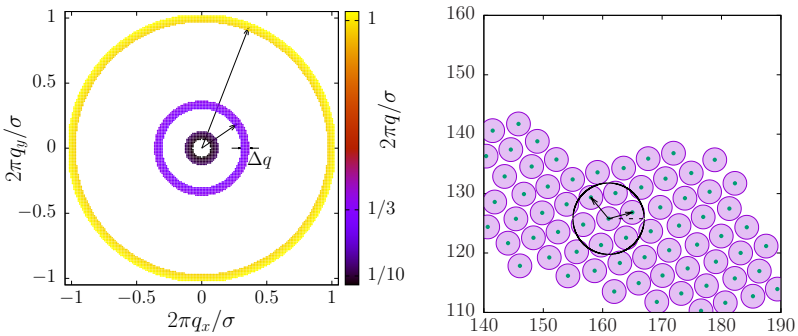

Figure 5.A.1 | A Plot in the $\boldsymbol{q}$-space for the determination of the $(l,\ h)$ values that define different $q \pm \Delta q$ for the computation of $F_q(\Delta t)$. **(B)** Illustration of the system with a circle of radius r_c centred at particle $\boldsymbol{r}_n$. The angle between the horizontal and the director of the centre-to-centre vector between particles n, and a its neighbours j define the angle θ_{nj} used in the computation of Ψ_6^n.

A second structural and time dependent correlation function is the time correlation of the local hexagonal order. For each particle in the system we define the local order parameter Ψ_6^n. We locate the n_b neighbouring particles of n_b^n of each particle n, particles j whose distance with particle n, $r_{nj} < r_c$, is smaller than a certain cut-off r_c, we typically use $r_c = 1.5\sigma$, being σ the diameter of the particles.

$$\Psi_6^n = \frac{1}{n_b^{(n)}} \sum_{j \in \{n_b\}}^{n_b^{(n)}} \exp\left(-6i\theta_{nj}\right) \tag{5.A.4}$$

The angle θ_{nj} is easily defined as $\theta_{ij} = \text{Atan2}\left[\boldsymbol{r}_{ij} \cdot \hat{\boldsymbol{y}}, \boldsymbol{r}_{ij} \cdot \hat{\boldsymbol{x}}\right]$. Where $\text{Atan2}(y, x)$ gives the value of $\arctan(y/x)$ in either the $(-\pi, \pi]$. The we define the temporal correlation of the local hexagonal order of the system $C_\Psi(t, t')$ as

$$C_\Psi(t,t') = \frac{\left\langle \sum_n \Psi_6^n(t) \Psi_6^{n\dagger}(t') \right\rangle}{\left\langle \sum_n \Psi_6^n(t) \Psi_6^{n\dagger}(t') \right\rangle} \tag{5.A.5}$$

The temporal evolution of the system typically shifts the peaks of the structure factor in case the system domains are growing or typical neighbouring distance

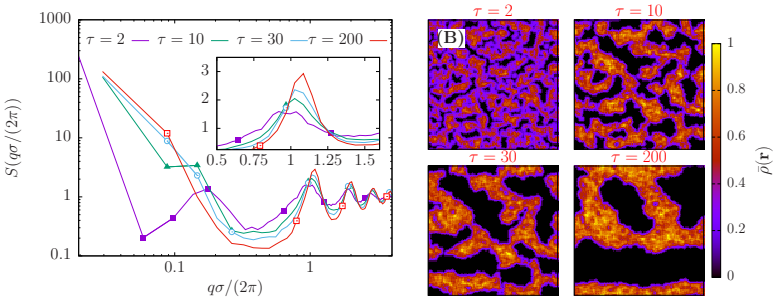

Figure 5.A.2 | For a system at densities $\Phi_a = 0.22$, and $\Phi_p = 0.3$ evolving. **(A)** Plot of the structure factor for different times. The inset shows the maximum of $S(q)$ shifting to large q's as a function of time. **(B)** Coarse grained density $\bar{\rho}$ for the system at different times.

change in time. In Figure 5.A.4 we present the temporal evolution of the structure factor $S(q)$ of passive particles for the evolutuion of an apolar mixture of particles the Gel II phase, see Section 5.4.4. The intensity of the structure factor at the wave vector of magnitude $q = 2\pi/\sigma$ slowly shifts to higher q. The density field defined by (5.A.7) in the $S(q)$ measure times indicates the formation of large structures at long times and the compaction of the passive particles, as indicated by the increase of denser regions.

To study the temporal growth of the structure in the system we define the chord length, and cluster distributions. The first measure is of great use in systems that percolate and lead to the hole formation in the structure, while the second measure is of great utility in systems that evolve into cluster phases.

5.A.2 Chord Length distributions

In the case the system undergoes a separation it is important to characterize the temporal evolution of characteristic lengths of the separated domains of the system. As introduced by [Testard et al., 2014] the chord length distribution is a robust and simple measurement of characteristic sizes for particulate domains and even for holes in the system. The fundamental idea of the method is to draw cords across the system and extract the distribution of length of cords that cover a domain, the length of chords with either particles or holed define the chord length distributions of particles and holes $P(\ell)$, and $P_h(\ell)$ respectively.

In order to extract the chord length distribution of the system we introduce a density field on a lattice of site width ξ. We define an additional distance ξ_b. In the computation of the density field boxes with centres at $\boldsymbol{r} = (x, y)\xi$ within a distance below ξ_b to the centre of any particle $\boldsymbol{r}_i$ contribute to $\rho(\boldsymbol{r})$ an amount $1/4\pi\xi_b^2$.

$$\rho(\boldsymbol{r}) = \frac{1}{4\pi\xi_s^2}\sum_i \theta\left(|\boldsymbol{r}-\boldsymbol{r}_i| - \xi_s\right) \tag{5.A.6}$$

where $\theta(x)$ is the Heaviside step function. Now we coarse-grain the density $\rho(\boldsymbol{r})$ into $\bar{\rho}(\boldsymbol{r})$ over the surrounding boxes.

$$\bar{\rho}(\boldsymbol{r}) = \frac{1}{6}\left[2\rho(\boldsymbol{r}) + \rho(\boldsymbol{r}+\hat{\boldsymbol{x}}\xi) + \rho(\boldsymbol{r}-\hat{\boldsymbol{x}}\xi) + \rho(\boldsymbol{r}+\hat{\boldsymbol{y}}\xi) + \rho(\boldsymbol{r}-\hat{\boldsymbol{y}}\xi)\right] \tag{5.A.7}$$

Following [Testard et al., 2014] we define $\xi = \sigma/2$, and $\xi_b = \sigma$. The grid spacing is the radius of the particle and the coarse-grained field introduces the effects of the neighbouring cells. With the density field on a lattice the computation of the probability distribution of the local densities of the fluid, $P(\bar{\rho})$, is direct. By a visual analysis of $P(\bar{\rho})$ we can identify a density ρ_c below which the system is in the gas phase and above which the system is dense. With this criterion the lattice sites with $\bar{\rho} > \rho_c$ as those belonging to the fluid phase and $\bar{\rho} < \rho_c$ as those belonging to the empty or gas phase. The definition of the gas-fluid interface is now the collection of dense grid cells neighbouring a gas grid cell.

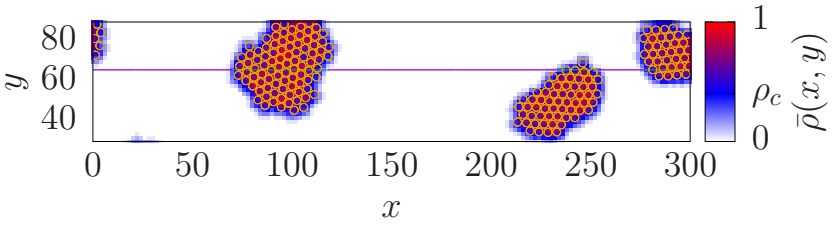

Figure 5.A.3 | Coarse grained density $\bar{\rho}(\boldsymbol{r})$ for a dilute system. We coarse grain the disk off-lattice into a lattice $\bar{\rho}(\boldsymbol{r})$. The interface (in blue) separates the dense and dilute regions.

Once the coarse-grained density is computed on the lattice we define a cord parallel to either $\hat{\boldsymbol{x}}$ or $\hat{\boldsymbol{y}}$ and measure the length of chords in the fluid or in the empty region between interfaces. We repeat this procedure for the entire lattice to obtain the overall $P(\ell)$ for either chords in the gas/empty phase and the fluid phase. A representative $P(\ell)$ curve is presented in Figure 5.16. The distribution shows a first maximum corresponding to the most probable chord length and then a decay with an exponential tail $\exp(-\ell/\ell_0)$ which defines the characteristic length ℓ_0. The temporal evolution of ℓ_0 determines the growth kinetics of the structures in the system.

5.A.3 Cluster Distribution

A pair of particles belong to the same cluster if their relative distance, r_{ij}, is below a cut-off $r_{ij} < r_c$. Given r_c we sort particles in clusters of size n. For a system in which particles aggregate in n_c clusters we are able to define the cluster distribution

function $P(n)$. This distribution is defined by the probability to find a cluster with n particles in the system. Typically the cut-off radius r_c is defined close to the first maximum of the pair distribution function, $g(r)$ of the system. The $g(r)$ gives the probability to measure a relative distance r between a pair of particles, it gives the average local structure surrounding a particle. For a system of volume Ω we have $N(N-1)/2$ pairs of particles. Using $d\Omega$ as the volume element of the system we define the pair distribution function[4].

$$g(r)d\Omega = \frac{2\Omega}{N(N-1)} \sum_{i \neq j} \delta(|\boldsymbol{r}_{ij}| - r) \tag{5.A.8}$$

Each cluster can be further studied. A typical measure is the gyration radius of the cluster r_g, a measure widely used to characterize polymers [Doi and Edwards, 1988] and particulate aggregates [Meakin, 1983].

The system of active and passive particles can be understood as a binary fluid. In this situation we are able to define clusters of active and passive particles separately. We define an averaged radius of gyration of the system $\langle r_g \rangle$ as previously presented [Baumgartl et al., 2007]. For a system of N particles and n_c clusters. Each cluster k is constituted by n_k particles.

$$\langle r_g \rangle = \frac{1}{N} \sum_{k=1}^{n_c} n_k \left(\frac{1}{n_k} \sum_{j}^{n_k} \left(\boldsymbol{r}_j^k - \boldsymbol{r}_{cm}^k \right) \right)^{1/2} \tag{5.A.9}$$

were $\boldsymbol{r}_{cm}$ is the position of the centre of mass of each cluster. The mean radius of gyration is then defined for both active $\langle r_g^a \rangle$, and passive particles $\langle r_g^p \rangle$. The comparison between $\langle r_g \rangle$ and the simulation box size, L, gives a criterion for the percolation threshold of the clusters, $r_c^a = 0.4$, and $r_c^p = 0.5$. A structure is said to percolate when $\langle r_g \rangle / L > r_c$, and to be in a cluster phase otherwise.

Cluster properties

The definition of averaged measure on a cluster usually require the prior determination of the centre of mass of the cluster, $\boldsymbol{r}_{cm}$. In this subsection we present an algorithm to compute the position of the centre of mass of the cluster in a system with periodic boundary contitions.

The centre of mass of a cluster is located at coordinates $\boldsymbol{r}_{cm} = (x_{cm}, y_{cm})$. The proceeding to compute x_{cm} and y_{cm} is independent and identical for either x_{cm}, and y_{cm}. So with no loss of information we compute x_{cm}. For each particle of the cluster with x coordinate x_j we define $\theta_j = 2\pi x_j / L_x$. The angle[5] θ_j defines the

[4] Computationally we approximate dr for a finite Δr and the Delta function for a step function that activates for $abs(|\boldsymbol{r}_{ij}|) - r < \Delta r/2$.

[5] The system defined by the PBC lies on the surface of a torus. The pair of angles θ determined by the x, and y coordinates univocally translate the coordinates on the box to the coordinates on the torus.

complex number $z_j = \exp(i\theta_j)$. The position of the centre of mass corresponds to the average on the complex numbers $\bar{z} = \langle z \rangle$. In exponential form $\bar{z} = \exp(i\bar{\theta})$ defines the position of the centre of mass in the real x space $x_{cm} = \bar{\theta} L_x/(2\pi)$, in the determination $0 \leq Arg(z) < 2\pi$ in the case we define $x \in [0\ , 2\pi\ )$.[6]

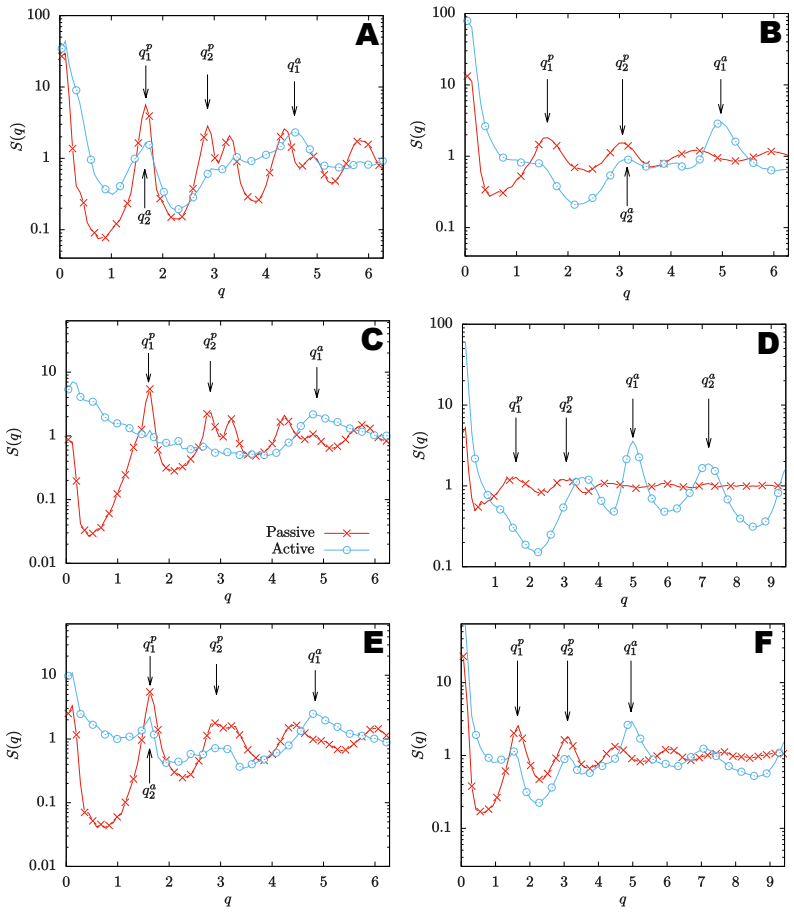

Figure 5.A.4 | Stucture Factors for the different structures. **A** Cluster I corresponds to $\Phi_a = 0.02$, and $\Phi_p = 0.1$. **B** Cluster II corresponds to $\Phi_a = 0.15$, and $\Phi_p = 0.15$. **C** Gel I corresponds to $\Phi_a = 0.02$, and $\Phi_p = 0.595$. **C** Gel III corresponds to $\Phi_a = 0.3$, and $\Phi_p = 0.1$. **D** Gel II corresponds to $\Phi_a = 0.2$, and $\Phi_p = 0.595$. **E** Gel II corresponds to $\Phi_a = 0.22$, and $\Phi_p = 0.3$.

[6] For coordinates $x \in [-L/2, L/2)$ the determination for complex numbers needs to be $-\pi \leq Arg(z) < \pi$.

6

Conclusions and perspectives

This thesis has addressed the emergence of effective interactions between passive particles immersed in an active bath. Here, we summarize the main conclusion (•) and future perspectives (⋆) for each chapter.

In Chapter 1 we focused in the general properties of an active suspension modelled by ABP, from which we extract the following conclusions:

- The stiffness of the repulsive interaction controls the local structure of the dense phase, and the MIPS appearance.
- The pressure drop previously found in the EoS of ABP in the MIPS onset is the result of measures in a metastable state of ABPs.
- The preparation protocol, low-density quenches instead of high-activity quenches give access to the coexistence state of MIPS at densities below the spinodal.
- ⋆ Study the MIPS phase separation dynamics for densities below the spinodal line by means of precursor seeds in the system.
- ⋆ ABP phase separation has been already discussed at low values of Pe, and ϕ. Extend the calculations beyond MIPS onset.
- ⋆ Model the density phase separation on walls for AAP, or dumbbells, and the structure of the dense region.

In Chapter 2 we included angular interactions in an ABPs to model Aligning Active Particle (AAP). First, we characterized the emergent structures in a bath of AAP. Second, we introduced passive particles and characterized the interactions induced by the active bath. From this study, we conclude:

- The MIPS transition is supressed as the alignment between particles appears.
- As a consequence, instead of a large, and static, crystalline aggregate, alignment favours the formation of travelling polarized clusters with a neat velocity.
- The interaction between a pair of inclusions and ABP is repulsive at large propulsion velocities. However, as alignment between particles increases, the formation of large structures of travelling AAP changes the behaviour of the force to an attractive, and long ranged effective force.
- The interaction of wall confined ABP and inclusions introduces an attractive effective component in the pair interaction.
- The wall confinement introduces a perpendicular force on the pair which we captured by a simple approximation. This interaction is found to be additive except for pair distances $d < 2\sigma_a$
- The predictions for the collective behaviour are identified in the structure of the inclusions captured in the pair correlation functions.
- ⋆ For ABPs we identify the formation of stable trimers of inclusions, and thus pair interactions are not additive. We need to extend the force calculations to trimers of inclusions.
- ⋆ Interactions ABP close to walls show additional effects in the relative interaction. It is expected to encounter additional interaction features for AAP aggregated on a wall

Chapter 3 studies the emergent interactions in shaken granular media. In mixtures of grains and spheres. Spheres are introduced as grains disconnected from the external forcing. Combining measures on fixed, and on moving inclusions we arrive at the following conclusions:

- Moving pairs of inclusions have a tendency to stay in contact and in the direction of the external forcing. This corresponds to an effective attractive interaction and aligning torques in the the direction of the external forcing.
- The force measurements fixing the inclusions confirm the emergence of the effective interactions between pairs.
- The effect of fixed inclusions in the granular bed has an effect on the internal ordered structure of the bed and translates into a long range attractive interaction between pairs. Long range interactions have a clear dependence on the shaking amplitude, relative orientation, and distance of the pair.
- For dense systems and moderate shaking amplitudes at long distances between inclusions the orientation parallel to the shaking becomes unstable.

- The measures of both formation energies computed for fixed inclusions, and the pair distribution probabilities do not satisfy the equilibrium Boltzmann relation, not even with an effective temperature.

⋆ Study of the escape rates for inclusions and their relation with the Kramers Escape problems.

⋆ The instability of parallel configurations at long distances may lead to the perpendicular stripe separation for a mixture.

In Chapter 4, we present a system of passive particles in a mixture with apolar active particles. The interactions are mathematically modelled and derived to focus on the resulting structures in mixtures. From the results presented, we conclude:

- The activation of a chemical reaction generates attractive interactions between active-passive pairs and active-active pairs.

- The introduction of magnetic interactions between active particles promotes chain formation and their structuring in a network.

- Percolation structures arrest the system. Percolation of passive particles, and active particles, and join percolation of active and passive is found.

- Experiments have reported the emergence of percolating, and arrested networks.

⋆ Refine the model to account for a density dependent interaction strength of the active particles.

⋆ Introduce the non-symmetric interactions on each pair to explore the structure formation when active-passive interactions do not fulfil action-reaction.

Globally, this thesis illustrates the emergence of interactions of a new nature in passive systems mediated by the intrinsic out of equilibrium properties of the active baths. Thus, it encourages to extend the results to many body scenarios, and in the vicinity of confining walls, as it is the case in experimental realizations of the aforementioned out-of-equilibrium systems.

Resum de la Tesi en Català

Aquesta tesi presenta l'estudi d'interaccions emergents entre partícules passives en el si d'un bany actiu, fora de l'equilibri, per a diferent sistemes model de la física de la matèria tova, sistemes col·loïdals i medis granulars. Aquest tesi s'estructura en una introducció general a la matèria tova i en quatre capítols en què es desenvolupa el contingut de la tesi. Cada un d'ells se centra en els diferents aspectes considerats.

Al Capítol 1 presentem una introducció al camp de la materia tova i els sistemes paradigmàtics que on es desenvolupa el contingut de la tesi. Despés s'introdueixen les interaccions típiques en l'equilibri termodinàmic presents en aquests sistemes. Després introduïm les dues grans famílies de sistemes model per a partícules microscòpiques fora de l'equilibri, els models de Vícsek i eñs models de partícules Brosnianes actives (ABP). Finalment, es presenten resultats novedosos d'intereaccions que emergeixen entre les partícules quan els sistemes es porten lluny de l'equilibri per la introducció de suspensions de partícules intrínsecament fora de l'equilibri.

Al Capítol 2 presentem un sistema model de matèria tova fora de l'equilibri basat en partícules amb volum excòs i autopropulsió. La introducció de l'autopropulsió fa que el sistema perdi la invariància sota simetries temporals, i per tant, deixi d'estar en l'equilibri termodinàmic. Com a resultat d'una competició entre l'autopropulsió i els efectes repulsius de les partícules, a densitats suficientment grans, un sistema d'ABPs se separa en dues fases, una de densa i una de diluïa. Recentment s'ha proposat una extensió del càlcul de la pressió per tal d'incorporar-hi l'activitat. S'ha demostrat, també, que en absència d'interaccions angulars aquesta pressió defineix una equació d'estat per al sistema, i per tant permet de descriure la transició de fase.

En aquest context, la tesi exposa l'origen d'una discontinuïtat àmpliament coneguda en el valor de la pressió a la densitat a partir de la qual el sistema se separa en les dues fases. Proposem que aquest salt abrupte de la pressió és degut a la preparació del sistema i que fins ara s'ha estat calculant la pressió corresponent a l'estat metastable i que aquest introdueix un excés de pressió al sistema. La persistència del sistema a l'estat metastable està lligada a la necessitat que el sistema formi una llavor suficientment gran per tal d'iniciar el procés de separació, un esdeveniment que no se succeeix en temps de simulació raonable.

Hem comprovat que el sistema es manté separat quan es construeix la condició inicial per a la simulació a partir de sistemes prèviament separats mitjançant

un canvi d'una densitat alta a la densitat més baixa en la qual volem prendre les mesures de pressió. La pressió calculada mitjançant aquest mètode es manté a un valor inferior als calculats fins ara la pressió deixa de tenir una singularitat en el punt en què el sistema comença a separar-se. L'existència d'aquest cicle en un diagrama pressió volum recorda als cicles d'histèresi observat prèviament en transicions de fase de primer ordre en sistemes d'equilibri. En aquest capítol, doncs, resolem la problemàtica del salt de pressió en l'equació d'estat de les partícules actives brownianes.

Al Capítol 3 proposem un conjunt de partícules brownianes actives, introduït al capítol 2, com a bany model fora de l'equilibri. A més a més, introduïm un segon aspecte fonamental en els sistemes de partícules actives, l'alineació d'orientacions de propulsió, àmpliament estesa en els sistemes de fora d'equilibri, com ara nedadors i animals. L'alineació és típica de sistemes amb hidrodinàmica, la qual nosaltres no considerem, i sistemes de forma allargada, tals com bastons. La intensitat relativa de la propulsió i l'alineació donen lloc a diferents escenaris col·lectius: en primer lloc una fase de desordre i de tipus gas, una escenari de MIPS a alineacions baixes i finalment un escenari d'agregats que viatgen a velocitats no nul·les al llarg del sistema.

Amb aquests banys caracteritzats procedim al gruix del capítol que consisteix en introduir partícules passives i estudiar-ne les forces, mecànicament, que emergeixen entre elles com a conseqüència de la presencia de les partícules actives, les partícules intruses de diàmetre unes 10 vegades més gran que les partícules que constitueixen el bany actiu. Per un parell de partícules intruses, o partícules de prova, observem l'aparició de forces atractives de depleció a distàncies curtes i baixa intensitat de la propulsió, aquest és el cas típic d'equilibri. En el moment en què mantenim l'alineació entre les partícules actives baixa i n'augmentem la propulsió mesurem un canvi qualitatiu de la força que passa a ser repulsiva entre les partícules de prova. Finalment, quan augmentem la intensitat de l'alineació la força torna a recuperar un caràcter atractiu juntament amb un augment de l'abast de la interacció a llargues distàncies, de fins a més d'un diàmetre de les partícules intruses. Al final del capítol discutim l'origen de les forces basant-nos amb les estructures emergents que hem estudiat en la feina prèvia de caracterització del bany actiu. La captura de les partícules en banys amb baixa alineació és responsable la la repulsió entre les partícules intruses: les partícules actives queden atrapades a l'embut definit per les parets en contacte de les partícules passives. Amb l'augment de les interaccions d'alineament es fomenta l'aparició d'agregats que viatgen al llarg del sistema, n'emergeixen forces de llarg abast: típicament de les dimensions de l'agregat actiu.

Per acabar estenem els resultats a mescles de partícules actives i passives i mitjançant les correlacions de distància entre les partícules passives podem extreure que, qualitativament, l'efecte col·lectiu per a partícules passives respon prou bé als resultats obtinguts per la mesura directa de les forces.

Al Capítol 4 introduïm un sistema diferent pertanyent també al camp de la matèria condensada tova i basat en els experiments previs realitzats a la Universitat

de Navarra en sistemes granulars vibrats, sistemes constituïts per llavors de rosella. Proposem un sistema dissipatiu de grans de diferents diàmetres disposars formant una monocapa en un pla amb un forçament extern en una direcció horitzontal al pla. En aquest sistema discutim el comportament d'una esfera metàl·lica i com aquesta es comporta com l'equivalent d'una partícula granular desconnectada del forçament extern. Les similituds del problema amb el que hem plantejat al Capítol 3 ens duen a un tractament amb les eines de mesures desenvolupades per les intrusions en banys actius. En aquest sistema, però, hi ha una direcció preferencial al pla i, per tant, hem considerat i mesurat l'aparició de parells de força sobre parelles de partícules de prova que indueixen rotacions. Hem caracteritzat els moviments relatius de les inclusions lliures i hem constatat que una parella tendeix a alinear-se en la direcció del forçament extern i a estar en contacte. Els càlculs de les forces relatives i parells de forçes sobre les partícules fixades són compatibles amb una atracció a curt abast i l'alineació de la parella en la direcció d'oscil·lació.

A més a més, identifiquem l'aparició de forces de llarg abast degudes al trencament de l'estructura granular a la regió entre les partícules però amb un efecte menys notable a la regió externa, les fluctuacions de velocitat presenten magnituds diferents dins i fora i, de manera anàloga a les forces de Casimir, resulten en una atracció de llarg abast. Finalment, hem expressat les dependències de la intensitat de l'atracció en funció dels paràmetres que descriuen l'estat del sistema: l'amplitud del forçament extern, l'angle for forma la parella respecte la direcció d'oscil·lació i la distància relativa de la parella.

Al Capítol 5 presentem un sistema experimental que connecta l'activació de reaccions químiques amb l'establiment de fluxos químics i del fluid de les superfícies col·loïdals basats en els experiments del grup de Pietro Tierno a la Universitat de Barcelona. La presència de les partícules en el medi on hi ha consum i generació de productes químics genera interaccions entre les partícules del sistema. Tant si participen en les reaccions químiques com si només experimenten els perfils de concentració generats per les partícules veïnes s'estableixen unes velocitats relatives d'interacció. A la primera part del capítol plantegem el model que ens permet d'extreure les dependències funcionals de les interaccions per a poder construir un model computacional i explorar l'ensamblatge de les mescles per a diferents valors de les concentracions de partícules actives i passives.

A partir de dades experimentals obtenim els coeficients que caracteritzen les intensitats de les reaccions i explorem les configuracions i estructures que emergeixen en mescles de partícules actives i passives a diferents concentracions. Essencialment distingim ente un règim en què preval la formació d'agregats controlats per nuclis centrals de partícules actives, i un règim en què es formen agregats que s'extenen de manera contínua en tot el conjunt del sistema, estructures percolants i amb els aspectes morfològics típics dels gels.

L'addició d'interaccions magnètiques, asimètriques, entre les partícules actives permeten l'establiment d'estructures linials percolants que s'estenen en tota l'extensió del sistema. Les cadenes magnètiques basteixen i sustenten les estructures donant lloc a estructures de tipus gel. Finalment, hem caracteritzat les estrucures

resultants no només morfològicament sinó que també hem estudiat la relaxació, que esdevé a unes escales de temps més lentes que les associades a la difusió lliure de les partícules.

Aquests resultats, per a partícules actives que no s'autopropulsen, contrasten amb els resultats existents fins al moment en què si bé s'havia considerat el dopatge amb agents actius aquests eren de naturalesa polar i autopropulsada.

En resum, en aquesta tesi hem considerat diferents sístemes tipus del camp de la matèria activa, medis granulars i dispersiona col·loidals, i els hem disposat en el si de medis intrinsecament fora de l'equilibri termodinàmic. La naturalesa de no equilibri dels banys, indueixen un sèrie d'interaccions efectives entre les partícules passives que hem caracteritzat en el tranascurs dels capítols de la tesi.

Bibliography

[Anderson, 1989] Anderson, J. L. (1989). Colloid transport by interfacial forces. *Annual Review of Fluid Mechanics*, 21(1):61–99.

[Anderson and Prieve, 1984] Anderson, J. L. and Prieve, D. C. (1984). Diffusiophoresis: Migration of colloidal particles in gradients of solute concentration. *Separation and Purification Methods*, 13(1):67–103.

[Angelani et al., 2009] Angelani, L., Di Leonardo, R., and Ruocco, G. (2009). Self-starting micromotors in a bacterial bath. *Physical Review Letters*, 102(4):1–4.

[Angelani et al., 2011] Angelani, L., Maggi, C., Bernardini, M., Rizzo, A., and Di Leonardo, R. (2011). Effective interactions between colloidal particles suspended in a bath of swimming cells. *Physical review letters*, 107(13):138302.

[Aranson and Tsimring, 2006] Aranson, I. S. and Tsimring, L. S. (2006). Patterns and collective behavior in granular media: Theoretical concepts. *Reviews of Modern Physics*, 78(2):641–692.

[Aumaître et al., 2001a] Aumaître, S., Kruelle, C. A., and Rehberg, I. (2001a). Segregation in granular matter under horizontal swirling excitation. *Phys. Rev. E*, 64:041305.

[Aumaître et al., 2001b] Aumaître, S., Kruelle, C. A., and Rehberg, I. (2001b). Segregation in granular matter under horizontal swirling excitation. *Phys. Rev. E*, 64:041305.

[Baskaran and Marchetti, 2008] Baskaran, A. and Marchetti, M. C. (2008). Enhanced diffusion and ordering of self-propelled rods. *Phys. Rev. Lett.*, 101:268101.

[Baumgartl et al., 2007] Baumgartl, J., Dullens, R. P. A., Dijkstra, M., Roth, R., and Bechinger, C. (2007). Experimental observation of structural crossover in binary mixtures of colloidal hard spheres. *Phys. Rev. Lett.*, 98:198303.

[Bechinger et al., 2016] Bechinger, C., Di Leonardo, R., Löwen, H., Reichhardt, C., Volpe, G., and Volpe, G. (2016). Active particles in complex and crowded environments. *Reviews of Modern Physics*, 88(4).

[Berg, 2008] Berg, H. C. (2008). *E. coli in Motion*. Springer Science & Business Media.

[Beysens and Estève, 1985] Beysens, D. and Estève, D. (1985). Adsorption phenomena at the surface of silica spheres in a binary liquid mixture. *Phys. Rev. Lett.*, 54:2123–2126.

[Bialké et al., 2013] Bialké, J., Löwen, H., and Speck, T. (2013). Microscopic theory for the phase separation of self-propelled repulsive disks. *EPL (Europhysics Letters)*, 103(3):30008.

[Bialké et al., 2012] Bialké, J., Speck, T., and Löwen, H. (2012). Crystallization in a dense suspension of self-propelled particles. *Phys. Rev. Lett.*, 108:168301.

[Bickel et al., 2013] Bickel, T., Majee, A., and Würger, A. (2013). Flow pattern in the vicinity of self-propelling hot janus particles. *Phys. Rev. E*, 88:012301.

[Blake, 1971] Blake, J. R. (1971). A spherical envelope approach to ciliary propulsion. *Journal of Fluid Mechanics*, 46(1):199–208.

[Briand and Dauchot, 2016] Briand, G. and Dauchot, O. (2016). Crystallization of self-propelled hard discs. *Phys. Rev. Lett.*, 117:098004.

[Casimir, 1948] Casimir, H. B. (1948). On the attraction between two perfectly conducting plates. In *Proc. Kon. Ned. Akad. Wet.*, volume 51, page 793.

[Cates and Tailleur, 2013] Cates, M. and Tailleur, J. (2013). When are active brownian particles and run-and-tumble particles equivalent? consequences for motility-induced phase separation. *EPL (Europhysics Letters)*, 101(2):20010.

[Cates, 2012] Cates, M. E. (2012). Diffusive transport without detailed balance in motile bacteria: does microbiology need statistical physics? *Reports on Progress in Physics*, 75(4):42601.

[Cates and Tailleur, 2015] Cates, M. E. and Tailleur, J. (2015). Motility-induced phase separation. *Annu. Rev. Condens. Matter Phys.*, 6(1):219–244.

[Cattuto et al., 2006] Cattuto, C., Brito, R., Marconi, U. M. B., Nori, F., and Soto, R. (2006). Fluctuation-induced casimir forces in granular fluids. *Physical review letters*, 96(17):178001.

[Cavagna et al., 2010] Cavagna, A., Cimarelli, A., Giardina, I., Parisi, G., Santagati, R., Stefanini, F., and Viale, M. (2010). Scale-free correlations in starling flocks. *Proceedings of the National Academy of Sciences*, 107(26):11865–11870.

[Ciamarra et al., 2006a] Ciamarra, M. P., Coniglio, A., and Nicodemi, M. (2006a). Dynamically induced effective interaction in periodically driven granular mixtures. *Phys. Rev. Lett.*, 97:038001.

[Ciamarra et al., 2006b] Ciamarra, M. P., Vizia, M. D. D., Fierro, A., Tarzia, M., Coniglio, A., and Nicodemi, M. (2006b). Granular species segregation under vertical tapping: Effects of size, density, friction, and shaking amplitude. *Phys. Rev. Lett.*, 96:058001.

[Colberg and Kapral, 2017] Colberg, P. H. and Kapral, R. (2017). Many-body dynamics of chemically propelled nanomotors. *Journal of Chemical Physics*, 147(6).

[Corwin et al., 2005] Corwin, E. I., Jaeger, H. M., and Nagel, S. R. (2005). Structural signature of jamming in granular media. *Nature*, 435(7045):1075–1078.

[Czirók et al., 1997] Czirók, A., Stanley, H. E., and Vicsek, T. (1997). Spontaneously ordered motion of self-propelled particles. *Journal of Physics A: Mathematical and General*, 30(5):1375.

[Daniels et al., 2009] Daniels, L. J., Park, Y., Lubensky, T. C., and Durian, D. J. (2009). Dynamics of gas-fluidized granular rods. *Physical Review E - Statistical, Nonlinear, and Soft Matter Physics*, 79(4):1–8.

[de Gennes, 1981] de Gennes, P.-G. (1981). Suspensions colloïdales dans un mélange binaire critique. *CR Acad. Sci. B*, 292(279):9.

[de Groot and Mazur, 1984] de Groot, S. R. and Mazur, P. (1984). *Non-equilibrium Thermodynamics*. Courier Corporation.

[Delmotte et al., 2015] Delmotte, B., Keaveny, E. E., Plouraboué, F., and Climent, E. (2015). Large-scale simulation of steady and time-dependent active suspensions with the force-coupling method. *Journal of Computational Physics*, 302:524–547.

[Deseigne et al., 2010] Deseigne, J., Dauchot, O., and Chaté, H. (2010). Collective motion of vibrated polar disks. *Physical Review Letters*, 105(9):1–4.

[Dhont, 1996] Dhont, J. K. (1996). *An introduction to dynamics of colloids*, volume 2. Elsevier.

[Di Leonardo et al., 2010] Di Leonardo, R., Angelani, L., Dell'Arciprete, D., Ruocco, G., Iebba, V., Schippa, S., Conte, M. P., Mecarini, F., De Angelis, F., and Di Fabrizio, E. (2010). Bacterial ratchet motors. *Proceedings of the National Academy of Sciences*, 107(21):9541–9545.

[Dinsmore et al., 1997] Dinsmore, A. D., Warren, P. B., Poon, W. C., and Yodh, A. G. (1997). Fluid-solid transitions on walls in binary hard-sphere mixtures. *Europhysics Letters*, 40(3):337–342.

[Doi and Edwards, 1988] Doi, M. and Edwards, S. F. (1988). *The theory of polymer dynamics*, volume 73. oxford university press.

[Drescher et al., 2010] Drescher, K., Goldstein, R. E., Michel, N., Polin, M., and Tuval, I. (2010). Direct measurement of the flow field around swimming microorganisms. *Phys. Rev. Lett.*, 105:168101.

[Dreyfus et al., 2005] Dreyfus, R., Baudry, J., Roper, M. L., Fermigier, M., Stone, H. A., and Bibette, J. (2005). Microscopic artificial swimmers. *Nature*, 437(7060):862.

[Dunkel et al., 2013] Dunkel, J., Heidenreich, S., Drescher, K., Wensink, H. H., Bär, M., and Goldstein, R. E. (2013). Fluid dynamics of bacterial turbulence. *Phys. Rev. Lett.*, 110:228102.

[Durham et al., 2009] Durham, W. M., Kessler, J. O., and Stocker, R. (2009). Disruption of vertical motility by shear triggers formation of thin phytoplankton layers. *Science*, 323(5917):1067–1070.

[Durlofsky et al., 1987] Durlofsky, L., Brady, J. F., and Bossis, G. (1987). Dynamic simulation of hydrodynamically interacting particles. *Journal of Fluid Mechanics*, 180:21–49.

[Elgeti and Gompper, 2009] Elgeti, J. and Gompper, G. (2009). Self-propelled rods near surfaces. *Epl*, 85(3).

[Elgeti and Gompper, 2013] Elgeti, J. and Gompper, G. (2013). Wall accumulation of self-propelled spheres. *EPL (Europhysics Letters)*, 101(4):48003.

[Ellis et al., 2017] Ellis, P. W., Pearce, D. J. G., Chang, Y.-W., Goldsztein, G., Giomi, L., and Fernandez-Nieves, A. (2017). Curvature-induced defect unbinding and dynamics in active nematic toroids. *Nature Physics*, 14:85 EP –. Article.

[Fisher and Gennes, 1978] Fisher, M. E. and Gennes, P. (1978). Wall phenomena in a critical binary mixture. *Comptes Rendus Hebdomadaires Des Seances De L Academie Des Sciences Serie B*, 287(8):207–209.

[Flenner and Szamel, 2015] Flenner, E. and Szamel, G. (2015). Fundamental differences between glassy dynamics in two and three dimensions. *Nature Communications*, 6:7392 EP –. Article.

[Galajda et al., 2007] Galajda, P., Keymer, J., Chaikin, P., and Austin, R. (2007). A wall of funnels concentrates swimming bacteria. *Journal of bacteriology*, 189(23):8704–8707.

[Galajda et al., 2008] Galajda, P., Keymer, J., Dalland, J., Park, S., Kou, S., and Austin, R. (2008). Funnel ratchets in biology at low Reynolds number: Choanotaxis. *Journal of Modern Optics*, 55(19-20):3413–3422.

[Gallas et al., 1992] Gallas, J. A. C., Herrmann, H. J., and Sokolowski, S. (1992). Convection Cells in Vibrating Granular Media. *Phys. Rev. Lett.*, 69(9).

[Gambassi et al., 2009] Gambassi, A., MacIołek, A., Hertlein, C., Nellen, U., Helden, L., Bechinger, C., and Dietrich, S. (2009). Critical Casimir effect in classical binary liquid mixtures. *Physical Review E - Statistical, Nonlinear, and Soft Matter Physics*, 80(6):1–27.

[Ginot et al., 2015] Ginot, F., Theurkauff, I., Levis, D., Ybert, C., Bocquet, L., Berthier, L., and Cottin-Bizonne, C. (2015). Nonequilibrium equation of state in suspensions of active colloids. *Phys. Rev. X*, 5:011004.

[Godoy et al., 2008] Godoy, S., Risso, D., Soto, R., and Cordero, P. (2008). Rise of a brazil nut: A transition line. *Phys. Rev. E*, 78:031301.

[Golestanian et al., 2007] Golestanian, R., Liverpool, T., and Ajdari, A. (2007). Designing phoretic micro-and nano-swimmers. *New Journal of Physics*, 9(5):126.

[Gomez-Solano et al., 2017] Gomez-Solano, J. R., Samin, S., Lozano, C., Ruedas-Batuecas, P., Van Roij, R., and Bechinger, C. (2017). Tuning the motility and directionality of self-propelled colloids. *Scientific Reports*, 7(1):1–12.

[Gonnella et al., 2014] Gonnella, G., Lamura, A., and Suma, A. (2014). Phase segregation in a system of active dumbbells. *International Journal of Modern Physics C*, 25(12):1441004.

[Grossmann et al., 2012] Grossmann, R., Schimansky-Geier, L., and Romanczuk, P. (2012). Active brownian particles with velocity-alignment and active fluctuations. *New Journal of Physics*, 14(7):073033.

[Hagan and Baskaran, 2016] Hagan, M. F. and Baskaran, A. (2016). Emergent self-organization in active materials. *Current Opinion in Cell Biology*, 38:74 – 80. Cell architecture.

[Harder et al., 2014a] Harder, J., Mallory, S., Tung, C., Valeriani, C., and Cacciuto, A. (2014a). The role of particle shape in active depletion. *The Journal of Chemical Physics*, 141(19):194901.

[Harder et al., 2014b] Harder, J., Valeriani, C., and Cacciuto, A. (2014b). Activity-induced collapse and reexpansion of rigid polymers. *Phys. Rev. E*, 90:062312.

[Hernández-Rojas et al., 2016] Hernández-Rojas, J., Chakrabarti, D., and Wales, D. (2016). Self-assembly of colloidal magnetic particles: energy landscapes and structural transitions. *Physical Chemistry Chemical Physics*, 18(38):26579–26585.

[Hertlein et al., 2008] Hertlein, C., Helden, L., Gambassi, A., Dietrich, S., and Bechinger, C. (2008). Direct measurement of critical Casimir forces. *Nature*, 451(7175):172–175.

[Hertz, 1882] Hertz, H. R. (1882). Uber die beruhrung fester elastischer korper und uber die harte. *Verhandlung des Vereins zur Beforderung des GewerbefleiBes, Berlin*, page 449.

[Hidalgo et al., 2009] Hidalgo, R. C., Zuriguel, I., Maza, D., and Pagonabarraga, I. (2009). Role of particle shape on the stress propagation in granular packings. *Phys. Rev. Lett.*, 103:118001.

[Howse et al., 2007] Howse, J. R., Jones, R. A., Ryan, A. J., Gough, T., Vafabakhsh, R., and Golestanian, R. (2007). Self-Motile Colloidal Particles: From Directed Propulsion to Random Walk. *Physical Review Letters*, 99(4):8–11.

[Huang et al., 2017] Huang, M.-j., Scho, J., and Kapral, R. (2017). Chemotactic and hydrodynamic effects on collective dynamics of self- diffusiophoretic Janus motors Chemotactic and hydrodynamic effects on collective dynamics of self-diffusiophoretic Janus motors. *New Journal of Physics*, pages 0–13.

[Huang et al., 2011] Huang, R., Chavez, I., Taute, K. M., Lukić, B., Jeney, S., Raizen, M. G., and Florin, E. L. (2011). Direct observation of the full transition from ballistic to diffusive Brownian motion in a liquid. *Nature Physics*, 7(7):576–580.

[Huerta et al., 2005] Huerta, D. A., Sosa, V., Vargas, M. C., and Ruiz-Suárez, J. C. (2005). Archimedes' principle in fluidized granular systems. *Physical Review E - Statistical, Nonlinear, and Soft Matter Physics*, 72(3):1–5.

[Hunter, 2001] Hunter, R. J. (2001). *Foundations of colloid science*. Oxford university press.

[Ishikawa et al., 2006] Ishikawa, T., Simmonds, M. P., and Pedley, T. J. (2006). *Hydrodynamic interaction of two swimming model micro-organisms*, volume 568.

[Jaeger et al., 1996] Jaeger, H. M., Nagel, S. R., and Behringer, R. P. (1996). Granular solids, liquids, and gases. *Reviews of modern physics*, 68(4):1259.

[Kadanoff et al., 1967] Kadanoff, L. P., Götze, W., Hamblen, D., Hecht, R., Lewis, E. A. S., Palciauskas, V. V., Rayl, M., Swift, J., Aspnes, D., and Kane, J. (1967). Static phenomena near critical points: Theory and experiment. *Rev. Mod. Phys.*, 39:395–431.

[Kaiser et al., 2014] Kaiser, A., Peshkov, A., Sokolov, A., Ten Hagen, B., Löwen, H., and Aranson, I. S. (2014). Transport powered by bacterial turbulence. *Physical Review Letters*, 112(15):1–5.

[Kaiser et al., 2013] Kaiser, A., Popowa, K., Wensink, H. H., and Löwen, H. (2013). Capturing self-propelled particles in a moving microwedge. *Phys. Rev. E*, 88:022311.

[Kaiser et al., 2015] Kaiser, A., Sokolov, A., Aranson, I. S., and Löwen, H. (2015). Motion of two micro-wedges in a turbulent bacterial bath. *European Physical Journal: Special Topics*, 224(7):1275–1286.

[Kaiser et al., 2012] Kaiser, A., Wensink, H. H., and Löwen, H. (2012). How to capture active particles. *Phys. Rev. Lett.*, 108:268307.

[Kardar and Golestanian, 1999] Kardar, M. and Golestanian, R. (1999). The "friction" of vacuum, and other fluctuation-induced forces. *Reviews of Modern Physics*, 71(4):1233.

[Keber et al., 2014] Keber, F. C., Loiseau, E., Sanchez, T., DeCamp, S. J., Giomi, L., Bowick, M. J., Marchetti, M. C., Dogic, Z., and Bausch, A. R. (2014). Topology and dynamics of active nematic vesicles. *Science*, 345(6201):1135–1139.

[Kudrolli, 2004] Kudrolli, A. (2004). Size separation in vibrated granular matter. *Reports on Progress in Physics*, 67(3):209.

[Kümmel et al., 2015] Kümmel, F., Shabestari, P., Lozano, C., Volpe, G., and Bechinger, C. (2015). Formation, compression and surface melting of colloidal clusters by active particles. *Soft Matter*, 11(31):6187–6191.

[Kuwabara and Kono, 1987] Kuwabara, G. and Kono, K. (1987). Restitution coefficient in a collision between two spheres. *Japanese Journal of Applied Physics*, 26(8R):1219–1223.

[Lambert et al., 2010] Lambert, G., Liao, D., and Austin, R. H. (2010). Collective escape of chemotactic swimmers through microscopic ratchets. *Phys. Rev. Lett.*, 104:168102.

[Lauga, 2011] Lauga, E. (2011). Life around the scallop theorem. *Soft Matter*, 7:3060–3065.

[Lauga and Powers, 2009] Lauga, E. and Powers, T. R. (2009). The hydrodynamics of swimming microorganisms. *Reports on Progress in Physics*, 72(9):096601.

[Levis and Berthier, 2014] Levis, D. and Berthier, L. (2014). Clustering and heterogeneous dynamics in a kinetic monte carlo model of self-propelled hard disks. *Physical Review E*, 89(6):062301.

[Levis et al., 2017] Levis, D., Codina, J., and Pagonabarraga, I. (2017). Active brownian equation of state: metastability and phase coexistence. *Soft Matter*, 13(44):8113–8119.

[Lighthill, 1952] Lighthill, M. J. (1952). On the squirming motion of nearly spherical deformable bodies through liquids at very small reynolds numbers. *Communications on Pure and Applied Mathematics*, 5(2):109–118.

[Llopis and Pagonabarraga, 2010] Llopis, I. and Pagonabarraga, I. (2010). Hydrodynamic interactions in squirmer motion: Swimming with a neighbour and close to a wall. *Journal of Non-Newtonian Fluid Mechanics*, 165(17-18):946–952.

[Love, 2013] Love, A. E. H. (2013). *A treatise on the mathematical theory of elasticity*. Cambridge university press.

[Løvoll et al., 1999] Løvoll, G., Måløy, K. J., and Flekkøy, E. G. (1999). Force measurements on static granular materials. *Physical Review E - Statistical Physics, Plasmas, Fluids, and Related Interdisciplinary Topics*, 60(5):5872–5878.

[Lozano et al., 2012] Lozano, C., Janda, A., Garcimartín, A., Maza, D., and Zuriguel, I. (2012). Flow and clogging in a silo with an obstacle above the orifice. *Phys. Rev. E*, 86:031306.

[Lozano et al., 2015] Lozano, C., Zuriguel, I., Garcimartín, A., and Mullin, T. (2015). Granular Segregation Driven by Particle Interactions. *Phys. Rev. Lett.*, 114(17):178002.

[Lu et al., 2015] Lu, B. S., Dean, D. S., and Podgornik, R. (2015). Out-of-equilibrium thermal Casimir effect between Brownian conducting plates. *Epl*, 112(2).

[Lushi et al., 2017] Lushi, E., Kantsler, V., and Goldstein, R. E. (2017). Scattering of biflagellate microswimmers from surfaces. *Phys. Rev. E*, 96:023102.

[Majmudar and Behringer, 2005] Majmudar, T. S. and Behringer, R. P. (2005). Contact force measurements and stress-induced anisotropy in granular materials. *Nature*, 435(7045):1079–1082.

[Mao et al., 1995] Mao, Y., Cates, M. E., and Lekkerkerker, H. N. (1995). Depletion force in colloidal systems. *Physica A: Statistical Mechanics and its Applications*, 222(1-4):10–24.

[Marchetti et al., 2013] Marchetti, M. C., Joanny, J. F., Ramaswamy, S., Liverpool, T. B., Prost, J., Rao, M., and Simha, R. A. (2013). Hydrodynamics of soft active matter. *Reviews of Modern Physics*, 85(3):1143–1189.

[Martin-Gomez et al., 2018] Martin-Gomez, A., Levis, D., Diaz-Guilera, A., and Pagonabarraga, I. (2018). Collective motion of active brownian particles with polar alignment. *Soft Matter*, 14:2610–2618.

[Martinez-Pedrero et al., 2017] Martinez-Pedrero, F., Massana-Cid, H., and Tierno, P. (2017). Assembly and transport of microscopic cargos via reconfigurable photoactivated magnetic microdockers. *Small*, 13(18).

[Martinez-Pedrero et al., 2015] Martinez-Pedrero, F., Ortiz-Ambriz, A., Pagonabarraga, I., and Tierno, P. (2015). Colloidal microworms propelling via a cooperative hydrodynamic conveyor belt. *Physical review letters*, 115(13):138301.

[Masuda et al., 2014] Masuda, T., Nishinari, K., and Schadschneider, A. (2014). Critical bottleneck size for jamless particle flows in two dimensions. *Phys. Rev. Lett.*, 112:138701.

[Mayer and Wood, 1965] Mayer, J. E. and Wood, W. W. (1965). Interfacial tension effects in finite, periodic, two-dimensional systems. *The Journal of Chemical Physics*, 42(12):4268–4274.

[Meakin, 1983] Meakin, P. (1983). Diffusion-controlled cluster formation in two, three, and four dimensions. *Phys. Rev. A*, 27:604–607.

[Michelin and Lauga, 2014] Michelin, S. and Lauga, E. (2014). Phoretic self-propulsion at finite péclet numbers. *Journal of Fluid Mechanics*, 747:572–604.

[Möbius et al., 2001] Möbius, M. E., Lauderdale, B. E., Nagel, S. R., and Jaeger, H. M. (2001). Size separation of granular particles. *Nature*, 414:270 EP –.

[Mullin, 2000] Mullin, T. (2000). Coarsening of self-organized clusters in binary mixtures of particles. *Physical Review Letters*, 84(20):4741–4744.

[Ni et al., 2015] Ni, R., Cohen Stuart, M. A., and Bolhuis, P. G. (2015). Tunable long range forces mediated by self-propelled colloidal hard spheres. *Phys. Rev. Lett.*, 114:018302.

[Ni et al., 2013] Ni, R., Stuart, M. A. C., and Dijkstra, M. (2013). Pushing the glass transition towards random close packing using self-propelled hard spheres. *Nature communications*, 4:2704.

[Ottino and Khakhar, 2000] Ottino, J. M. and Khakhar, D. V. (2000). Mixing and segregation of granular materials. *Annual Review of Fluid Mechanics*, 32(1):55–91.

[Palacci et al., 2014] Palacci, J., Sacanna, S., Kim, S.-H., Yi, G.-R., Pine, D. J., and Chaikin, P. M. (2014). Light-activated self-propelled colloids. *Philosophical Transactions of the Royal Society of London A: Mathematical, Physical and Engineering Sciences*, 372(2029).

[Palacci et al., 2013a] Palacci, J., Sacanna, S., Steinberg, A. P., Pine, D. J., and Chaikin, P. M. (2013a). Living crystals of light-activated colloidal surfers. *Science*, 339:936.

[Palacci et al., 2013b] Palacci, J., Sacanna, S., Vatchinsky, A., Chaikin, P. M., and Pine, D. J. (2013b). Photoactivated colloidal dockers for cargo transportation. *Journal of the American Chemical Society*, 135(43):15978–15981.

[Paladugu et al., 2016] Paladugu, S., Callegari, A., Tuna, Y., Barth, L., Dietrich, S., Gambassi, A., and Volpe, G. (2016). Nonadditivity of critical Casimir forces. *Nature Communications*, 7(7):11403.

[Patch et al., 2017] Patch, A., Yllanes, D., and Marchetti, M. C. (2017). Kinetics of motility-induced phase separation and swim pressure. *Physical Review E*, 95(1):1–8.

[Pica Ciamarra et al., 2007] Pica Ciamarra, M., Coniglio, A., and Nicodemi, M. (2007). Phenomenology and theory of horizontally oscillated granular mixtures. *The European Physical Journal E*, 22(3):227.

[Pöschel and Schwager, 2005] Pöschel, T. and Schwager, T. (2005). *Computational granular dynamics: models and algorithms*. Springer Science & Business Media.

[Pöschel et al., 2000] Pöschel, T., Schwager, T., and Salueña, C. (2000). Onset of fluidization in vertically shaken granular material. *Phys. Rev. E*, 62:1361–1367.

[Purcell, 2014] Purcell, E. M. (2014). Life at low reynolds number. In *Physics and our world: reissue of the proceedings of a symposium in honor of Victor F Weisskopf*, pages 47–67. World Scientific.

[Radjai et al., 1996] Radjai, F., Jean, M., Moreau, J. J., and Roux, S. (1996). Force distributions in dense Two-Dimensional granular systems. *Physical Review Letters*, 77(2):274–277.

[Ray et al., 2014] Ray, D., Reichhardt, C., and Reichhardt, C. J. O. (2014). Casimir effect in active matter systems. *Phys. Rev. E*, 90:013019.

[Redner et al., 2016] Redner, G. S., Wagner, C. G., Baskaran, A., and Hagan, M. F. (2016). Classical nucleation theory description of active colloid assembly. *Phys. Rev. Lett.*, 117:148002.

[Reis et al., 2004] Reis, P. M., Ehrhardt, G., Stephenson, A., and Mullin, T. (2004). Gases, liquids and crystals in granular segregation. *Europhysics Letters*, 66(3):357–363.

[Reis et al., 2006] Reis, P. M., Sykes, T., and Mullin, T. (2006). Phases of granular segregation in a binary mixture. *Physical Review E - Statistical, Nonlinear, and Soft Matter Physics*, 74(5):1–13.

[Reynolds, 1885] Reynolds, O. (1885). Lvii. on the dilatancy of media composed of rigid particles in contact. with experimental illustrations. *The London, Edinburgh, and Dublin Philosophical Magazine and Journal of Science*, 20(127):469–481.

[Ristow et al., 1997] Ristow, G. H., Straßburger, G., and Rehberg, I. (1997). Phase diagram and scaling of granular materials under horizontal vibrations. *Phys. Rev. Lett.*, 79:833–836.

[Salueña et al., 1999] Salueña, C., Pöschel, T., and Esipov, S. E. (1999). Dissipative properties of vibrated granular materials. *Phys. Rev. E*, 59:4422–4425.

[Sanders et al., 2004] Sanders, D. A., Swift, M. R., Bowley, R. M., and King, P. J. (2004). Are brazil nuts attractive? *Phys. Rev. Lett.*, 93:208002.

[Scala et al., 2007] Scala, A., Voigtmann, T., and De Michele, C. (2007). Event-driven brownian dynamics for hard spheres. *The Journal of chemical physics*, 126(13):134109.

[Schnautz et al., 2005] Schnautz, T., Brito, R., Kruelle, C. A., and Rehberg, I. (2005). A horizontal Brazil-nut effect and its reverse. *Physical Review Letters*, 95(2):1–4.

[Schrader et al., 2009] Schrader, M., Virnau, P., and Binder, K. (2009). Simulation of vapor-liquid coexistence in finite volumes: A method to compute the surface free energy of droplets. *Physical Review E*, 79(6):061104.

[Schweitzer et al., 1998] Schweitzer, F., Ebeling, W., and Tilch, B. (1998). Complex motion of brownian particles with energy depots. *Phys. Rev. Lett.*, 80:5044–5047.

[Silflow and Lefebvre, 2001] Silflow, C. D. and Lefebvre, P. A. (2001). Assembly and motility of eukaryotic cilia and flagella. lessons from chlamydomonas reinhardtii. *Plant physiology*, 127(4):1500–1507.

[Smeets et al., 2016] Smeets, B., Alert, R., Pešek, J., Pagonabarraga, I., Ramon, H., and Vincent, R. (2016). Emergent structures and dynamics of cell colonies by contact inhibition of locomotion. *Proceedings of the National Academy of Sciences*, 113(51):14621–14626.

[Solon et al., 2015a] Solon, A. P., Fily, Y., Baskaran, A., Cates, M. E., Kafri, Y., Kardar, M., and Tailleur, J. (2015a). Pressure is not a state function for generic active fluids. *Nature Physics*, 11(8):673.

[Solon et al., 2015b] Solon, A. P., Fily, Y., Baskaran, A., Cates, M. E., Kafri, Y., Kardar, M., and Tailleur, J. (2015b). Pressure is not a state function for generic active fluids. *Nature Physics*, 11(8):673–678.

[Solon et al., 2015c] Solon, A. P., Stenhammar, J., Wittkowski, R., Kardar, M., Kafri, Y., Cates, M. E., and Tailleur, J. (2015c). Pressure and phase equilibria in interacting active brownian spheres. *Physical Review Letters*, 114(19):198301.

[Solon et al., 2015d] Solon, A. P., Stenhammar, J., Wittkowski, R., Kardar, M., Kafri, Y., Cates, M. E., and Tailleur, J. (2015d). Pressure and phase equilibria in interacting active brownian spheres. *Physical review letters*, 114(19):198301.

[Son et al., 2013] Son, K., Guasto, J. S., and Stocker, R. (2013). Bacteria can exploit a flagellar buckling instability to change direction. *Nature physics*, 9(8):494.

[Soto and Golestanian, 2014a] Soto, R. and Golestanian, R. (2014a). Self-assembly of catalytically active colloidal molecules: tailoring activity through surface chemistry. *Physical review letters*, 112(6):068301.

[Soto and Golestanian, 2014b] Soto, R. and Golestanian, R. (2014b). Self-assembly of catalytically active colloidal molecules: Tailoring activity through surface chemistry. *Phys. Rev. Lett.*, 112:068301.

[Soto and Golestanian, 2015] Soto, R. and Golestanian, R. (2015). Self-assembly of active colloidal molecules with dynamic function. *Phys. Rev. E*, 91:052304.

[Speck and Jack, 2016] Speck, T. and Jack, R. L. (2016). Ideal bulk pressure of active brownian particles. *Physical Review E*, 93(6):062605.

[Speck et al., 2015] Speck, T., Menzel, A. M., Bialké, J., and Löwen, H. (2015). Dynamical mean-field theory and weakly non-linear analysis for the phase separation of active brownian particles. *The Journal of chemical physics*, 142(22):224109.

[Suma et al., 2014] Suma, A., Gonnella, G., Marenduzzo, D., and Orlandini, E. (2014). Motility-induced phase separation in an active dumbbell fluid. *EPL (Europhysics Letters)*, 108(5):56004.

[Szabó et al., 2006] Szabó, B., Szöllösi, G. J., Gönci, B., Jurányi, Z., Selmeczi, D., and Vicsek, T. (2006). Phase transition in the collective migration of tissue cells: Experiment and model. *Physical Review E - Statistical, Nonlinear, and Soft Matter Physics*, 74(6):1–5.

[Tailleur and Cates, 2008] Tailleur, J. and Cates, M. (2008). Statistical Mechanics of Interacting Run-and-Tumble Bacteria. *Physical Review Letters*, 100(21):218103.

[Takatori and Brady, 2016] Takatori, S. C. and Brady, J. F. (2016). Forces, stresses and the (thermo?) dynamics of active matter. *Current Opinion in Colloid & Interface Science*, 21:24 – 33.

[Takatori et al., 2014] Takatori, S. C., Yan, W., and Brady, J. F. (2014). Swim pressure: stress generation in active matter. *Physical review letters*, 113(2):028103.

[ten Hagen et al., 2011] ten Hagen, B., van Teeffelen, S., and Löwen, H. (2011). Brownian motion of a self-propelled particle. *Journal of Physics: Condensed Matter*, 23(19):194119.

[Testard et al., 2014] Testard, V., Berthier, L., and Kob, W. (2014). Intermittent dynamics and logarithmic domain growth during the spinodal decomposition of a glass-forming liquid. *The Journal of Chemical Physics*, 140(16):164502.

[Tierno et al., 2008] Tierno, P., Golestanian, R., Pagonabarraga, I., and Sagués, F. (2008). Magnetically actuated colloidal microswimmers. *The Journal of Physical Chemistry B*, 112(51):16525–16528.

[Uchida, 2001] Uchida, N. (2001). Casimir effect in fluids above the isotropic-lamellar transition. *Phys. Rev. Lett.*, 87:216101.

[Vicsek et al., 1995] Vicsek, T., Czirók, A., Ben-Jacob, E., Cohen, I., and Shochet, O. (1995). Novel type of phase transition in a system of self-driven particles. *Phys. Rev. Lett.*, 75:1226–1229.

[Vicsek and Zafeiris, 2012] Vicsek, T. and Zafeiris, A. (2012). Collective motion. *Physics Reports*, 517(3-4):71–140.

[Vizsnyiczai et al., 2017] Vizsnyiczai, G., Frangipane, G., Maggi, C., Saglimbeni, F., Bianchi, S., and Di Leonardo, R. (2017). Light controlled 3d micromotors powered by bacteria. *Nature communications*, 8:15974.

[Vnuk, 1983] Vnuk, F. (1983). Phase equilibria in binary mixtures. part 2. miscibility gap with two critical temperatures (closed-loop phase diagram). *Journal of the Chemical Society, Faraday Transactions 2: Molecular and Chemical Physics*, 79(1):57–64.

[Volpe et al., 2011] Volpe, G., Buttinoni, I., Vogt, D., Kuemmerer, H.-J., and Bechinger, C. (2011). Microswimmers in Patterned Environments. pages 8810–8815.

[Weber et al., 2016] Weber, S. N., Weber, C. A., and Frey, E. (2016). Binary mixtures of particles with different diffusivities demix. *Physical review letters*, 116(5):058301.

[Wensink and Löwen, 2008] Wensink, H. and Löwen, H. (2008). Aggregation of self-propelled colloidal rods near confining walls. *Physical Review E*, 78(3):031409.

[Winkler et al., 2015a] Winkler, R., Wysocki, A., and Gompper, G. (2015a). Virial pressure in systems of spherical active brownian particles. *Soft matter*, 11(33):6680–6691.

[Winkler et al., 2015b] Winkler, R. G., Wysocki, A., and Gompper, G. (2015b). Virial pressure in systems of spherical active brownian particles. *Soft matter*, 11(33):6680–6691.

[Wu and Libchaber, 2000] Wu, X.-L. and Libchaber, A. (2000). Particle diffusion in a quasi-two-dimensional bacterial bath. *Physical Review Letters*, 84(13):3017.

[Yang et al., 2014] Yang, X., Manning, M. L., and Marchetti, M. C. (2014). Aggregation and segregation of confined active particles. *Soft matter*, 10(34):6477–6484.

[Zaccarelli, 2007] Zaccarelli, E. (2007). Colloidal gels: Equilibrium and non-equilibrium routes. *Journal of Physics Condensed Matter*, 19(32).

[Zaeifi Yamchi and Naji, 2017] Zaeifi Yamchi, M. and Naji, A. (2017). Effective interactions between inclusions in an active bath. *The Journal of Chemical Physics*, 147(19):194901.

[Ziherl and Muševič, 2001] Ziherl, P. and Muševič, I. (2001). A note on observability of fluctuation-induced structural interaction in a nematic mesophase. *Liquid Crystals*, 28(7):1057–1062.

[Ziherl et al., 1999] Ziherl, P., Podgornik, R., and Žumer, S. (1999). Wetting-driven casimir force in nematic liquid crystals. *Phys. Rev. Lett.*, 82:1189–1192.

[Zöttl and Stark, 2014] Zöttl, A. and Stark, H. (2014). Hydrodynamics determines collective motion and phase behavior of active colloids in quasi-two-dimensional confinement. *Physical Review Letters*, 112(11):1–5.

[Zuriguel et al., 2014] Zuriguel, I., Parisi, D. R., Hidalgo, R. C., Lozano, C., Janda, A., Gago, P. A., Peralta, J. P., Ferrer, L. M., Pugnaloni, L. A., Clément, E., et al. (2014). Clogging transition of many-particle systems flowing through bottlenecks. *Scientific reports*, 4:7324.